From Detector Layout to Signal Analysis: Geometry Optimization and Neutron-Gamma Tagging in Plastic Scintillator Detectors

DISSERTATION

ZUR ERLANGUNG DES GRADES

“Doktor der Naturwissenschaften”

AM FACHBEREICH PHYSIK, MATHEMATIK UND INFORMATIK
DER
JOHANNES GUTENBERG UNIVERSITÄT

MAINZ

This manuscript has been authored by Fermi Forward Discovery Group, LLC under Contract No. 89243024CSC000002 with the U.S. Department of Energy, Office of Science, Office of High Energy Physics.

Asa Nehm

Mainz, 2026

Acknowledgements

First and foremost, I want to thank my supervisor, Alfons Weber, for supporting me throughout my PhD. Whether I was having difficulties at work or in my private life, I knew I could always count on you to help me out. I also want to thank you for your guidance whenever I needed feedback on the direction my projects should take. Thanks for giving meaning to the German word for PhD supervisor, 'Doktorvater' (PhD father). Thank you for accepting who I am and making an effort to make me feel heard, seen, and respected.

I am also grateful to be part of a working group with wonderful, amazing people. I would like to thank you all – Asit Srivastava, Cloe Girard-Carillo, Dorina Zundel, Gioele Reina, Ioana Caracas, Liam O'Sullivan, Lukas Koch, Stefan Schoppmann, and Susanna Wakely – for your support and guidance throughout the last four years.

I want to acknowledge the work of the TMS consortium. Especially for the preparation and contributions of Clarence Wret, Jeffrey Kleykamp, Liam O'Sullivan, Magnus Handley, Xiaoyan Huang, and Kiyoung Jung. Thanks to Hugh Gallagher, the consortium leader, for giving me the opportunity to pursue my project, and to all the people in the consortium for supporting me and providing valuable insights and feedback.

I am thankful to have been part of the DUNE collaboration, with many people who share my vision of a welcoming work environment, and to have been able to conduct my research in a fulfilling way. Thanks to Alex Booth and Mike Dolce for the technical support, and to many collaborators, especially from Young DUNE, for making collaboration meetings exciting and wonderful to attend.

I also want to thank the people that I worked with locally. Without the incredible efforts of Antoine Laudrain and Sebastian Ritter, I would not have been able to successfully conduct the neutron and gamma tagging study. Thanks also to Volker Buescher and Lucia Masetti for their feedback and support with this study. The many long discussions we had during our meetings were very helpful in understanding things I hadn't initially considered and in expanding my knowledge.

Last but not least, I have to thank my family, especially my mom, for supporting and believing in me throughout my journey. Thanks for always trying to understand what I am working on, even though you could never really grasp it. Thanks for being there for me when it got hard. Also, thanks to all my friends for the emotional support and for making sure I stay sane and well over the last four years.

Abstract

Neutrinos are elementary particles with many properties still unknown. Their masses so far have only upper and lower limits. Still, due to neutrino oscillations, it is clear that they are not massless, as stated by the Standard Model of Elementary Particles. Neutrinos are also present in the Universe in vast amounts, but they rarely interact with the surrounding matter. Their abundance makes them very interesting for many theories beyond the Standard Model, e.g., dark matter searches and charge-parity symmetry violation in the leptonic sector, which could be (partially) responsible for the observed matter-antimatter asymmetry in today's Universe.

The Deep Underground Neutrino Experiment (DUNE) is a next-generation accelerator-based neutrino oscillation experiment that will study neutrinos with unprecedented precision and may answer many open questions. DUNE uses a powerful neutrino beam from Fermilab. It consists of a Near Detector complex to measure neutrinos before oscillation, and a Far Detector complex 1300 km away to measure them after oscillation. As part of the Near Detector complex, measurements are also possible with different angles to the neutrino beam. This enables excellent control of systematic uncertainties of e.g., neutrino cross section measurements.

One detector in the near detector complex is The Muon Spectrometer, an extension of a Liquid Argon detector that measures the charge and momentum of muons produced in neutrino interactions within the Liquid Argon. The design of this detector, which consists of alternating layers of steel and plastic scintillator bars, must be optimized for the expected muon energies.

In this thesis, a study of the optimal module orientation plan is presented, which is necessary for the physics performance of the near detector complex and, by extension, DUNE. As part of this study, the event reconstruction was also developed and improved. Simulated muons are then reconstructed, and the performance of different module orientation plans is tested.

As a second part, a study of neutron and gamma tagging using a pulse shape discrimination plastic scintillator is presented. The properties of this material allow particle differentiation based on the temporal distribution of emitted light. A novel approach to using the individual light signals was successfully tested using data from a small, local test setup.

Contents

List of Figures

List of Tables

Acronyms

ACE-BR Accelerator Complex Evolution Booster Replacement. 26

ACE-MIRT Accelerator Complex Evolution Main Injector Ramp and Target. 26

AmBe Americium Beryllium. 77, 78, 80, 100, 102

APA anode plane assembly. 18, 19

BSM Beyond the Standard Model. 15, 16, 22, 23

CC charged-current. v, 1, 3, 4, 10, 11, 29, 45

CP charge-parity. ii, 2, 5, 10, 15, 16, 21, 29

CPA cathode plane assembly. 18

CRP charge readout plane. 19–21

CRU charge-readout unit. 19

DUNE Deep Underground Neutrino Experiment. ii, v, 15–18, 21–24, 26, 48

DUNE-PRISM DUNE Precision Reaction-Independent Spectrum Measurement. 22–25, 29

FC field cage. 18, 19

FD Far Detector. ii, v, 15–18, 21–23, 25, 28, 29

FN false negative. 58

FP false positive. 58

FSI Final-State Interactions. 22

FWHM full width half maximum. 39

GAr Gaseous Argon. 26

GArTPC Gaseous Argon TPC. 26, 27

HD horizontal drift. 18–20

JUNO Jiangmen Underground Neutrino Observatory. 15

LAr Liquid Argon. ii, 20, 23–29

LArTPC Liquid Argon TPC. 18, 20, 23, 28

MSW Mikheyev-Smirnow-Wolfenstein. 7, 16

NC neutral-current. v, 1, 3, 4, 11, 22

ND Near Detector. ii, 15, 16, 20–24, 29, 30, 45

ND-GAr GAr near detector. 27

ND-LAr LAr near detector. 20, 23–25, 27, 29, 30, 45, 48–51, 53, 54, 69, 73

PCB printed circuit board. 19, 78, 80

PD photon detection. 19, 20

PID particle identification. 19

PMNS Pontecorvo-Maki-Nakagawa-Sakata. 5, 15, 16

PMT photomultiplier tubes. 26, 78, 79, 82–84, 101–103

PSD pulse shape discrimination. ii, vii, viii, 77, 78, 80, 82, 83, 101–103

QCD quantum chromodynamics. 22

QE quasi-elastic. 22

R&D Research and Development. 26–28

RHC Reverse Horn-Current. 29, 30, 33

SAND System for on-Axis Detection. 22, 25–28

SBND Short-Baseline Near Detector. 18

SiPM Silicon Photo-Multiplier. 19, 24, 26–28, 31, 37, 77, 78, 80, 83, 85, 91, 102

SN Supernova. 16

SNO Sudbury Neutrino Observatory. 3, 4

SURF Sanford Underground Research Facility. 15

TMS The Muon Spectrometer. ii, 23–26, 29–31, 33, 36, 42, 43, 45, 46, 48–50, 53, 54, 58, 62, 64, 65, 67, 69, 72–74, 103

TN true negative. 58

TP true positive. 58

TPC Time Projection Chamber. 18, 27

VD vertical drift. 18, 19, 28

WLS wavelength-shifting. 24, 27, 31

1 Introduction

This chapter provides an overview of neutrinos: how they were discovered, the solar and atmospheric neutrino problems that led to the discovery of neutrino oscillation, details of neutrino oscillation, and how neutrinos interact with matter. Also, the kinematics of charged pion decays and their effect on neutrino energies are discussed. Finally, an overview of the different energy-loss mechanisms for charged particles is provided.

1.1 The Standard Model and Weak Interaction

The Standard Model, shown in Figure 1, describes the interactions of elementary particles via the strong, weak, and electromagnetic forces. It was developed in the 1960s by Sheldon Glashow [1], Steven Weinberg [2], and Abdus Salam [3], among others.

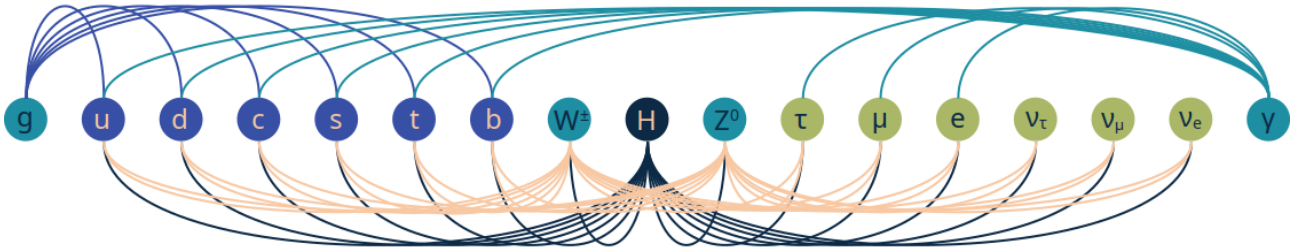

Figure 1: Sketch of the Standard Model of Particle Physics with connections for possible interactions

The elementary particles are grouped into the fermions, with half spins, and bosons, with integer spins. Fermions come in two types: quarks and leptons, each with three generations. From lightest to heaviest, the quarks are the up and down quarks in the first mass generation, the strange and charm quarks in the second, and the bottom and top quarks in the third generation. The leptons are, again from lightest to heaviest, the electron, the muon, and the tau. Each of these leptons has a corresponding neutrino; more on them in the following Section.
The bosons consist of the gauge bosons with spin 1 and a scalar boson with spin 0. The gauge bosons of the strong interaction are the gluons, which have 8 different colors. The gauge boson of the electromagnetic interaction is the photon. The weak-interaction bosons are the $W^{\pm}$ for the charged-current (CC) and the Z^0 for the neutral-current (NC). The scalar boson is the Higgs boson and is responsible for the masses of the gauge bosons of the weak interaction and the fermions.
The electromagnetic and weak interactions have been unified into the electroweak interaction with a $SU(2) \times U(1)$ symmetry. The $SU(2)$ group is for the weak interaction. It corresponds to interactions with the weak gauge bosons $W^{\pm}$ and Z^0[1]. The $U(1)$ group describes the electromagnetic interaction and interactions with photons. Only left-handed, where the direction of the spin and motion are opposite, neutrinos participate in weak interactions and, therefore, are the only ones described in the Standard Model so far. The leptons are therefore grouped into left-handed doublets

$$\begin{pmatrix} \nu_e \\ e \end{pmatrix}_L , \begin{pmatrix} \nu_\mu \\ \mu \end{pmatrix}_L , \begin{pmatrix} \nu_\tau \\ \tau \end{pmatrix}_L$$

and right-handed, where the direction of the spin and motion are the same, singlets e_R , μ_R , τ_R.

[1] The $W^{\pm}$ and Z^0 bosons do not directly relate to the $SU(2)$ group, as there is no exact $SU(2)$ after symmetry breaking. The bosons are states after the symmetry breaking, though.

The Lagrangian of the electroweak interaction, for an example of only electron and electron-neutrino, is

$$\begin{aligned}\mathcal{L} =& e \cdot \bar{e}\gamma^{\mu} Q_e e A_{\mu} \\ &- \frac{e}{\cos\theta_W \sin\theta_W} \cdot [g_L^e \bar{e}_L \gamma^{\mu} e_L + g_R^e \bar{e}_R \gamma^{\mu} e_R + g_L^{\nu} \bar{\nu} \gamma^{\mu} \nu] \cdot Z_{\mu} \\ &- \frac{e}{\sqrt{2}\sin\theta_W} [\bar{\nu}\gamma^{\mu} e_L W_{\mu}^{+} + \bar{e}_L \gamma^{\mu} \nu W_{\mu}^{-}]\end{aligned} \tag{1}$$

with the left- and right-handed couplings of the fermion $g_L = I_3 - Q\sin^2\theta_W$ and $g_R = -Q\sin^2\theta_W$.
The first line in the Lagrangian describes the coupling of the electron to the photon, the second line of both leptons to the Z^0 boson, and the third line of both leptons to the $W^{\pm}$ bosons. Here, $g = e/\sin\theta_W$ is the weak coupling constant, e is the electromagnetic coupling constant, γ^{μ} the γ-matrices, A_{μ} is the photon, θ_W is the Weinberg or weak mixing angle, I_3 is the third component of the weak isospin, and Q is the electric charge of the electron.
Even though neutrinos are considered massless in the Standard Model, it was proven experimentally via the detection of neutrino oscillation that neutrinos have non-zero masses. Neutrino masses can be introduced into the Standard Model in the same way as for quarks, using the conjugate Higgs doublet. The gauge invariant Dirac mass term would then be $\mathcal{L}_D = -m_D(\bar{\nu_R}\nu_L + \bar{\nu_L}\nu_R)$, after spontaneous symmetry breaking. Right-handed neutrinos would only interact gravitationally if this is the origin of neutrino masses.
Another way to add neutrino masses into the Lagrangian is possible without breaking the gauge invariance of the Standard Model. For this, only right-handed neutrinos and left-handed antineutrinos are added to the Lagrangian with the left-handed antineutrinos as the charge-parity (CP) conjugate field for the right-handed neutrinos ν_R^c. The Majorana mass term would then be $\mathcal{L}_M = -1/2M(\bar{\nu_R^c}\nu_R + \bar{\nu_R}\nu_R^c)$. As this provides a direct coupling between a particle and an antiparticle, this would only be possible if neutrinos are their own antiparticles and violate the lepton number conservation, referred to as Majorana neutrinos [4]. Currently, it is still unclear whether neutrinos are Dirac or Majorana particles, and many experiments are aiming to answer this question.

1.2 Neutrinos

1.2.1 Historic Introduction to Neutrinos and Neutrino Oscillation

1.2.1.1 The Discovery of the Neutrino

Neutrinos are uncharged leptons and only interact via the weak interaction and gravity, and come in three different flavors: electron-neutrinos (ν_e), muon-neutrinos (ν_μ), and tau-neutrinos (ν_τ) [4]. These flavors are also called the weak eigenstates, as they are associated with the charged leptons e, μ, and τ. Neutrinos were first postulated by Pauli after observing the non-discrete electron energy spectrum of beta decays [5]. The first, although indirect, evidence for the existence of neutrinos came from an electron capture measurement in ^{37}Ar atoms in 1952 [6]. In a nuclear recoil experiment, the interaction $^{37}Ar + e^- \rightarrow {}^{37}Cl + \nu_e + 816$ keV showed a recoil of the produced ^{37}Cl nucleus, only explicable with the existence of neutrinos.
The direct discovery of neutrinos was made later using the inverse beta decay $\bar{\nu}_e + p \rightarrow e^+ + n$, shown in Figure 2, with a kinematic threshold of 1.8 MeV with the Cowan-Reines neutrino experiment in 1955/6 [7]. A nuclear reactor served as the source of antineutrinos. The positron emitted in the interaction could be measured promptly via the annihilation, and the production of two photons with 511 keV. The neutron was detected with a delay, with the neutron captured on ^{113}Cd producing gamma signals.
That neutrinos come in different flavors was only discovered in 1962 with the Alternating Gradient Synchrotron (AGS) experiment and the discovery of the muon-neutrino [9]. Using neutrinos created in proton collisions with a ^4Be target, the rates of muons and electrons, produced in the subsequent neutrino in-

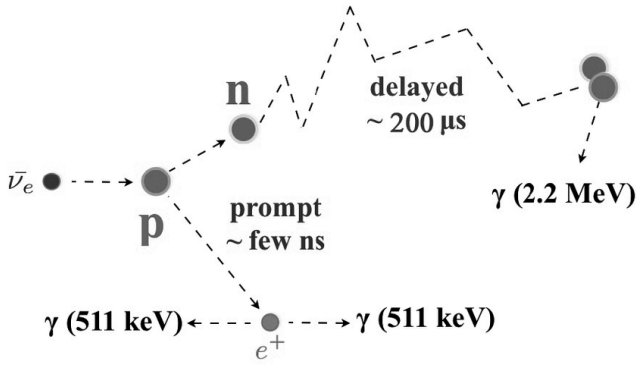

Figure 2: The inverse beta decay reaction of the anti-electron neutrino. The neutron in the picture is captured by a proton, producing a gamma signal of 2.2 MeV (credit: [8])

teractions $\nu_\mu + n \rightarrow \mu^- + p$ and $\nu_\mu + n \rightarrow e^- + p$, would be identical if neutrinos did not have different flavors. Therefore, the rates of muons and electrons, detected and identified with a spark chamber, were measured and found to differ, proving the existence of electron- and muon-neutrino flavors.
The existence of the tau-neutrino flavor could be determined indirectly with the Z_0 resonance measurement with the Large Electron-Positron Collider (LEP) in 1990 [10]. The width of the resonance Γ_Z is the sum of the widths of all different decay modes of the Z_0 boson $\Gamma_Z = \Gamma_{had} + \Gamma_{inv} + 3\Gamma_l$. A precise measurement of the total width, therefore, allowed for the determination of the width of the invisible decay mode $\Gamma_{inv} = N_\nu \Gamma_\nu$ into neutrinos under the assumption of lepton universality. This then allowed for the calculation of the number of light ($m_\nu < m_Z/2$) active neutrinos. The experimentally obtained resonance width of $N_\nu = 2.9841 \pm 0.0083$ agreed perfectly with the $N_\nu = 3$ hypothesis, proving the existence of three active light neutrino flavors.

1.2.1.2 The Solar Neutrino Problem

Electron neutrinos are produced in large quantities during nuclear fusion in the Sun. Many different fusion processes produce neutrinos, with the dominant one being the pp chain (99%) (see Figure 7 and discussed in detail in Section 1.2.2.3). In the first step of this, two protons (or positively charged hydrogen atoms) fuse to build a deuterium nucleus and also produce a positron and an electron-neutrino.
The Homestake experiment [11] was designed to measure the neutrino flux from the Sun. The experiment was conducted by R. Davis in the 1960s and used a tank containing 380 m^3 of tetrachloroethylene (C_2Cl_4). The electron-neutrinos were interacting, above the energy threshold of 814 keV, with ^{37}Cl and producing ^{37}Ar along with electrons in the interaction $\nu_e + ^{37}Cl \rightarrow e^- + ^{37}Ar$. The measured flux, determined from the number of ^{37}Ar atoms, was only about a third of the expected neutrino flux [12]. This difference became known as the 'solar neutrino problem' [4].
Later on, the Superkamiokande [13] and Sudbury Neutrino Observatory (SNO) [14] experiments also measured the solar neutrino flux via different processes: elastic scattering on electrons ($\nu_e e^- \rightarrow \nu_e e^-$) for Superkamiokande with a detection of the electrons, and ν_e charged-current (CC) and ν_l neutral-current (NC) weak interactions on deuterons for SNO. The respective interactions are shown in Figures 3 and 4.
Both detectors use the Cherenkov effect in water to detect the leptons produced in the neutrino interactions via the inverse beta decay. The detection threshold in both Superkamiokande (a pure Water-Cherenkov detector) and SNO (a pure heavy Water-Cherenkov detector) was about 5 MeV. Water-Cherenkov detectors also allow measurement of the direction of the original neutrino and, compared to the Homestake experiment, where the number of ^{37}Ar atoms produced by neutrino interactions was determined every few weeks, provide real-time measurements.
While Superkamiokande confirmed the deficit of solar electron-neutrinos, SNO was also able to measure the other neutrino flavors and found the expected neutrino flux to be correct when also considering the

ν_μ and ν_τ fluxes from the NC interactions. SNO's measurement was consistent with the theoretical expectation, but rather than consisting solely of electron-neutrinos, the other two flavors also have significant components. These different flavors cannot be produced in the nuclear fusion processes, which provided clear evidence for neutrino flavor transformations.

1.2.1.3 The Atmospheric Neutrino Problem

With the solar neutrino problem solved, a new problem was discovered, this time for atmospheric neutrinos (see more details in Section 1.2.2.4). The Superkamiokande experiment, among others, measured the fluxes of muon-neutrinos and electron-neutrinos and compared their ratio. The expected ratio was 2 : 1 for ν_μ against ν_e from charged pion decays (more details on this in Section 1.2.2.4) into a muon and a muon-neutrino ($\pi^+ \rightarrow \mu^+ + \nu_\mu$) and the subsequent muon decay into an electron along with neutrinos of both flavors ($\mu^+ \rightarrow e^+ + \bar{\nu}_\mu + \nu_e$). For neutrinos originating from directly above the experiment, this expected ratio was found to hold for energies below 1 GeV; for neutrinos from the opposite side of the Earth, on the other hand, this ratio was not confirmed. Here, a deficit in ν_μ was measured, which was consistent with a transformation into the hard-to-measure ν_τ [15]. The measurements also showed a dependence of the transformation on both the neutrino's energy and path length. This provided clear evidence that the flavor transformation was due to neutrino oscillation between different flavors [4].
The observation of flavor transformation also demonstrated that neutrinos have mass [4]. The flavor oscillation is possible only with phase differences arising from mass differences between the states. Mass differences cannot exist with only massless ($m = 0$) particles; therefore, some neutrino flavors must be massive.

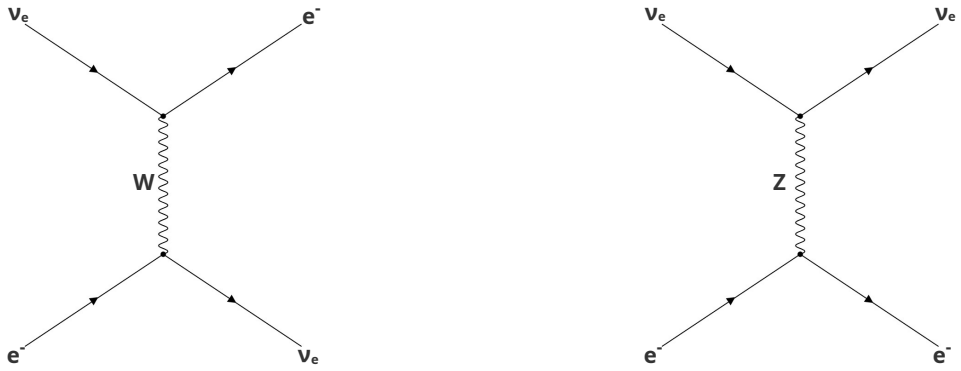

Figure 3: The two Feynman diagrams contributing to $\nu_e e^- \rightarrow \nu_e e^-$ scattering, as detected in Superkamiokande [4]

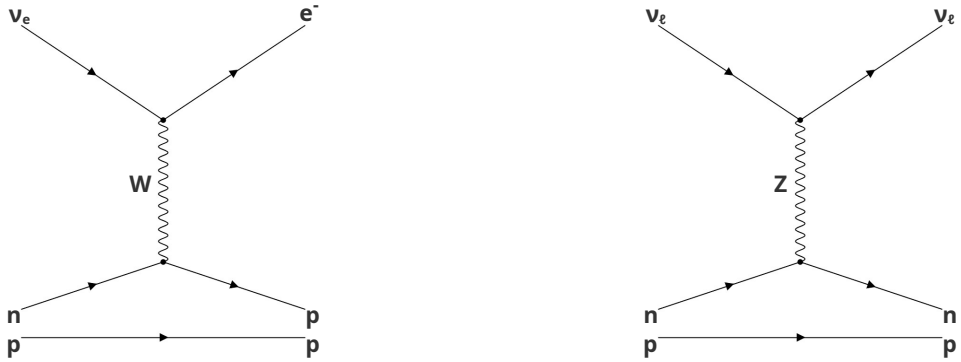

Figure 4: The Feynman diagrams contributing to the ν_e CC and ν_l NC weak interactions with the deuteron in SNO [4]

1.2.2 Neutrino Oscillation

While the weak eigenstates of neutrinos appear during weak interactions, neutrinos propagate in the mass eigenstates ν_1, ν_2, ν_3 [4]. The weak eigenstates $|\nu_\alpha\rangle$, $\alpha = e, \mu, \tau$, are linear combinations of the mass eigenstates $|\nu_i\rangle$, $i = 1, 2, 3$

$$|\nu_\alpha\rangle = \sum_{i=1}^{n} U^*_{\alpha i} |\nu_i\rangle$$

with U as the unitary mixing matrix, analogous to the CKM matrix in the quark sector [16]. U is given by Equation 2, where $c_{ij} = \cos\theta_{ij}$, $s_{ij} = \sin\theta_{ij}$, $\delta = \delta_{CP}$.

$$U_{PMNS} = \begin{pmatrix} U_{e1} & U_{e2} & U_{e3} \\ U_{\mu 1} & U_{\mu 2} & U_{\mu 3} \\ U_{\tau 1} & U_{\tau 2} & U_{\tau 3} \end{pmatrix} = \begin{pmatrix} c_{12}c_{13} & s_{12}s_{13} & s_{13}e^{-i\delta} \\ -s_{12}c_{13} - c_{12}s_{13}s_{23}e^{i\delta} & c_{12}c_{23} - s_{12}s_{13}s_{23}e^{i\delta} & c_{13}s_{23} \\ s_{12}s_{23} - c_{12}s_{13}c_{23}e^{i\delta} & -c_{12}s_{23} - s_{12}s_{13}c_{23}e^{i\delta} & c_{13}c_{23} \end{pmatrix} \times diag(e^{i\eta_1}, e^{i\eta_2}, 1) \tag{2}$$

The θ_{ij} are the mixing angles θ_{12}, θ_{23}, and θ_{13} between the neutrino eigenstates. Only if neutrinos are Majorana particles, insinuating that they are their own antiparticles, do the phases η_1 and η_2 exist. These are irrelevant for oscillation and matter effects, though, because oscillation experiments are not sensitive to them. In the Dirac case, where neutrinos are not their own antiparticles, the Majorana phases (η_1 and η_2) can be absorbed in the wave functions. For values of the phase δ unequal to 0 or π, the mixing matrix is complex and charge-parity-invariance is violated in the lepton sector [17]. The mixing matrix is usually referred to as the Pontecorvo-Maki-Nakagawa-Sakata (PMNS) matrix.
The PMNS matrix can also be parametrized as in Equation 3, where the first matrix describes mixing for long-baseline or atmospheric neutrinos, the second for short-baseline reactor neutrinos, the third for long-baseline reactor neutrinos, and the fourth matrix only for the Majorana case.

$$U_{PMNS} = \begin{pmatrix} 1 & 0 & 0 \\ 0 & c_{23} & s_{23} \\ 0 & -s_{23} & c_{23} \end{pmatrix} \cdot \begin{pmatrix} c_{13} & 0 & s_{13}e^{-i\delta} \\ 0 & 1 & 0 \\ -s_{13}e^{i\delta} & 0 & c_{13} \end{pmatrix} \cdot \begin{pmatrix} c_{12} & s_{12} & 0 \\ -s_{12} & c_{12} & 0 \\ 0 & 0 & 1 \end{pmatrix} \cdot \begin{pmatrix} e^{i\eta_1/2} & 0 & 0 \\ 0 & e^{i\eta_2/2} & 0 \\ 0 & 0 & 1 \end{pmatrix} \tag{3}$$

As the masses of the different mass eigenstates are different, proven by the existence of neutrino oscillation, phase differences arise between the different linear components until they interact and collapse into a weak eigenstate, producing an observable charged lepton of the corresponding flavor. This lepton, produced in the second interaction, can then have a different flavor than the corresponding lepton from the initial weak neutrino eigenstate at the time of production.
For neutrino propagation in vacuum, the oscillation probability $P_{\alpha\beta}$ from weak eigenstate α to weak eigenstate β can be calculated from the time evolution of the mass eigenstates $\left|\nu_\alpha(\vec{x}, t)\right\rangle = \sum_{i=1}^{n} U^*_{\alpha 1} |\nu_i\rangle e^{-i\phi_i}$ with $\phi_i = p_i \cdot x_i = (E_i t - \vec{p}_i \cdot \vec{x})$ as shown in Equation 4 [16].

$$P_{\alpha\beta} = |\left\langle \nu_\beta \middle| \nu_\alpha(\vec{x}, t) \right\rangle|^2 = \delta_{\alpha\beta} - 4\sum_{i<j}^{n} \mathrm{Re}[U_{\alpha i}U^*_{\beta i}U^*_{\alpha j}U_{\beta j}] \sin^2 X_{ij} + 2\sum_{i<j}^{n} \mathrm{Im}[U_{\alpha i}U^*_{\beta i}U^*_{\alpha j}U_{\beta j}] \sin 2X_{ij} \tag{4}$$

$$X_{ij} = \frac{(m_i^2 - m_j^2)L}{4E} = 1.267\Delta m^2_{ij}[\mathrm{eV}^2]\frac{L[\mathrm{m}]}{E[\mathrm{MeV}]} \tag{5}$$

For the example of oscillation from muon-neutrinos to electron-neutrinos, the probability

$$P(\nu_\mu \to \nu_e) \approx \sin^2 2\theta_{13} \sin^2\theta_{23} \sin^2 (1.267\Delta m^2_{23}[eV^2]\frac{L[m]}{E[MeV]})$$

in leading order.
An example for the oscillation probability of muon-neutrinos is shown in Figure 5[2].

[2]The values for the mixing parameters used to calculate the probabilities are different than the ones given in Table 1.

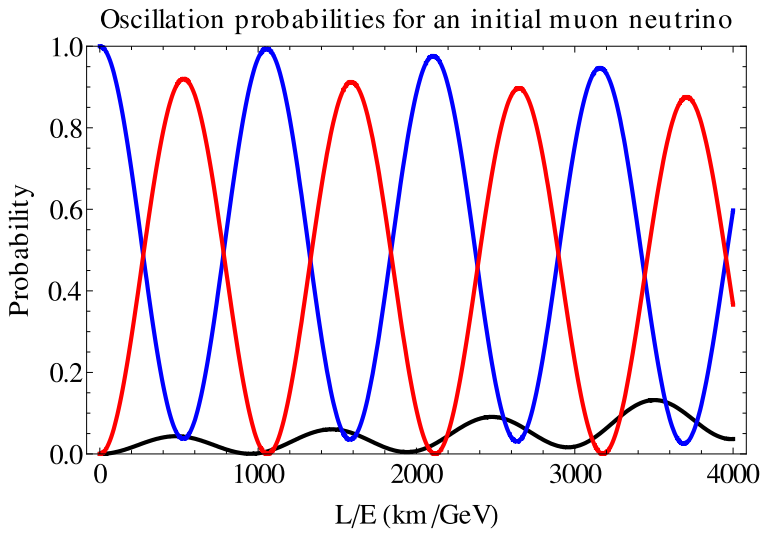

Figure 5: Muon neutrino oscillation probability. The blue line refers to muon neutrinos, the red line to tau neutrinos, and the black line to electron neutrinos. (credit: [18])

1.2.2.1 Neutrino Mass Ordering

For the Standard Model case of massless neutrinos, neutrino oscillation cannot occur as the terms are dependent on the mass difference Δm^2_{ij}. Since oscillation has been observed, neutrinos must have a mass, albeit small. Oscillation experiments are sensitive only to the squared mass difference and therefore cannot determine the actual neutrino mass.

The two different mass-squared differences, though, can and have been measured. The values are shown in Table 1, along with the current measured mixing angles. The two mass-squared differences allow for two distinct neutrino mass orderings, as shown in Figure 6. For Δm^2_{31}, $\Delta m^2_{32} > 0$, the mass ordering is called 'normal' with $m_1^2 < m_2^2 < m_3^2$. In the case of Δm^2_{31}, $\Delta m^2_{32} < 0$, the mass ordering is called 'inverted' with $m_3^2 < m_1^2 < m_2^2$. Currently, there is no strong preference for either mass ordering [19].

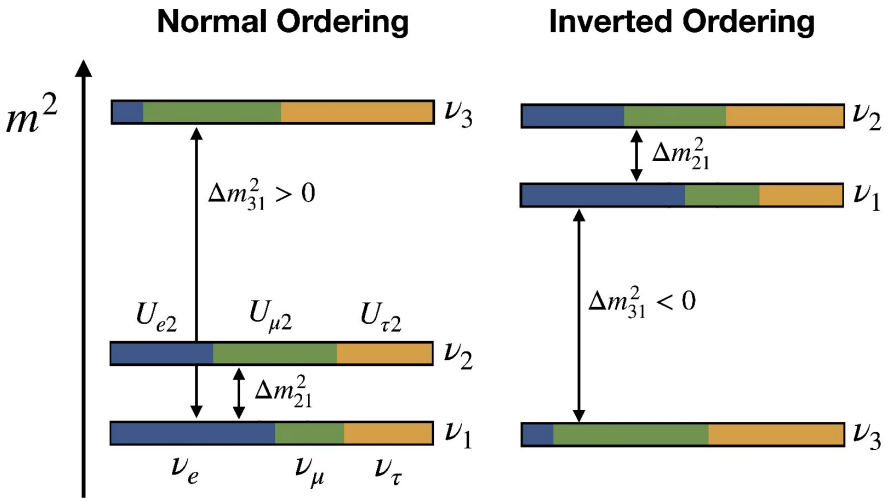

Figure 6: Diagram showing the normal and inverted mass ordering (credit: [20])

1.2.2.2 Neutrino Oscillation in Matter

For neutrino propagation in matter, the dense medium affects the neutrino phase velocity, due to inelastic scattering with the nuclei and coherent or forward scattering in the matter [16]. This effect is also

dependent on the specific neutrino flavor. The effective potential at point x, with the electron density $n_e(x)$ and the Fermi constant G_F is

$$V = diag(\pm\sqrt{2}G_F n_e(x), 0, 0)$$

with + for neutrinos and − for antineutrinos. This potential changes the oscillation probability in the chosen example of oscillation from muon-neutrinos to electron-neutrinos in the first order, as shown in Equation 6 [17].

$$\begin{aligned} P(\nu_\mu \to \nu_e) \approx \sin^2\theta_{23}\sin^2 2\theta_{13}\frac{\sin^2(\Delta_{31}-aL)}{(\Delta_{31}-aL)^2}\Delta_{31}^2 \\ + \sin 2\theta_2 3\sin\theta_{13}\sin 2\theta_{12}\frac{\sin(\Delta_{31}-aL)}{(\Delta_{31}-aL)}\Delta_{31}\frac{\sin aL}{aL}\Delta_{21}\cos(\Delta_{31}+\delta_{CP}) \\ + \cos^2\theta_{23}\sin^2 2\theta_{21}\frac{\sin^2 aL}{(aL)^2}\Delta_{21}^2 \end{aligned} \tag{6}$$

where $\Delta_{ij} = \Delta m_{ij}^2 L[\text{km}]/4E_\nu[\text{GeV}]$ and $a = G_F n_e(x)/\sqrt{2}$.

$\sin^2\theta_{12}$	$0.307^{+0.013}_{-0.012}$	
Δm_{21}^2	$(7.53 \pm 0.18)\times 10^{-5}$ eV^2	
$\sin^2\theta_{23}$	$0.553^{+0.016}_{-0.024}$ (inverted)	$0.558^{+0.015}_{-0.021}$ (normal)
Δm_{32}^2	$(-2.529 \pm 0.029)\times 10^{-3}$ eV^2 (inverted)	$(2.455 \pm 0.028)\times 10^{-3}$ eV^2 (normal)
$\sin^2\theta_{13}$	$(2.19 \pm 0.07)\times 10^{-2}$	

Table 1: Current values for the neutrino mixing parameters [21]

1.2.2.3 Solar Neutrinos

As mentioned before, the Sun produces electron-neutrinos in its fusion processes. These occur mainly in the core and can be categorized into two main types: the pp chain and the CNO cycle. The pp chain is dominant for light(er) stars and produces about 99% of our Sun's energy. The CNO cycle, on the other hand, is dominant for heavier stars and makes less than 1% of our Sun's energy [22].

The pp chain and CNO cycle are depicted in Figure 7 and their respective neutrino energies in Figure 8. The energies of solar neutrinos depend on the specific fusion process and range up to about 11 MeV for the ^8B (shown in green) and Hep (shown in gray) processes.

The baseline for solar neutrinos is the distance between the Sun and Earth, which is given by the astronomical unit 1 AU $\approx 1.5 \cdot 10^8$ km [16]. With this baseline and these energies, solar neutrinos can be used to study the oscillation parameters $|\Delta m_{21}^2|$ and θ_{21}. They can also be used to study the metallicity of the Sun, with different models of the Sun's metallic[3] content predicting different neutrino fluxes. A higher metallicity of the Sun implies more neutrinos from the CNO cycle due to a higher abundance of these elements. A lower metallicity has a higher abundance of Hydrogen and Helium, with more neutrinos from the pp chain. The neutrinos produced in fusion reactions also provide proof that nuclear fusion actually occurs in the Sun and can be used to test energy production and loss mechanisms by comparing the optical and neutrino luminosities, as they escape promptly from the dense core, unlike photons. For photons, it takes $\sim 10^5$ yrs to escape.

Using the matter density of the Sun, matter effects such as the Mikheyev-Smirnow-Wolfenstein (MSW) effect (see [16] for details) can also be studied and confirmed. These effects also allow studies for new physics, especially in the transition region of P_{ee} where sterile (meaning non-active) neutrinos could be observed [22].

[3] Metals are considered all elements with a higher atomic number than Helium.

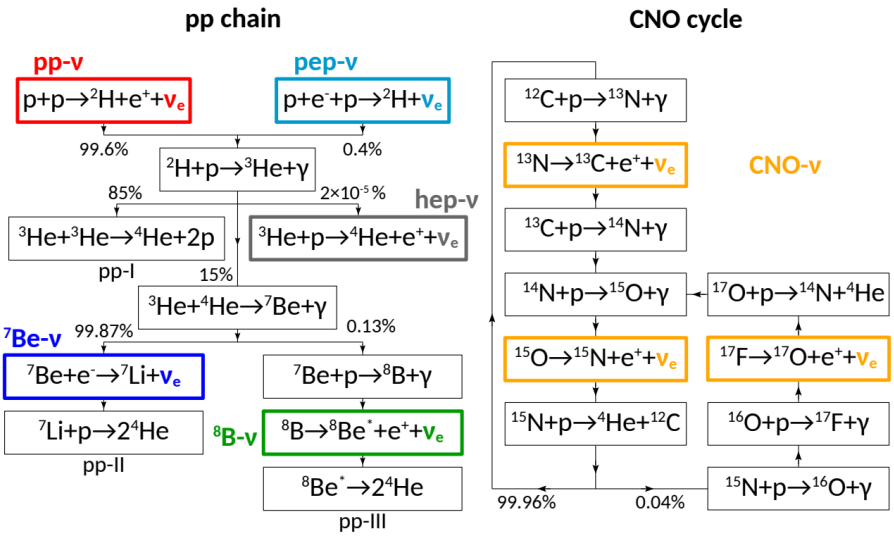

Figure 7: Neutrinos from the pp chain (pp, pep, hep, ^7Be, and ^8B) and CNO cycle [22]

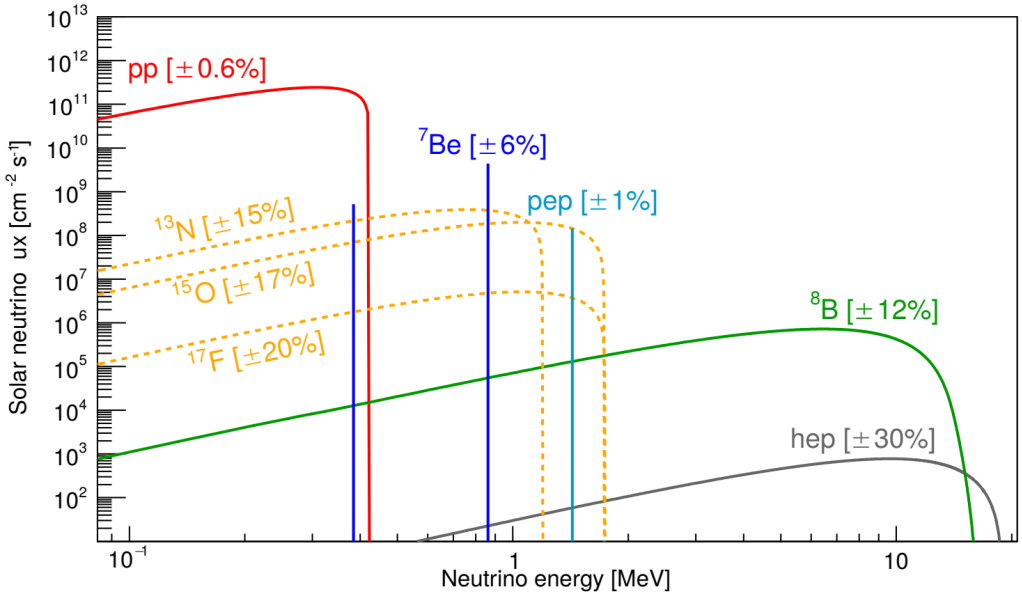

Figure 8: Energy spectrum of solar neutrinos of the different fusion processes in the Sun [22]

1.2.2.4 Atmospheric Neutrinos

Atmospheric neutrinos originate, as solar neutrinos, from space, but in this case, only indirectly. Cosmic rays, originating from galactic and extragalactic sources, can interact with nuclei in Earth's atmosphere and produce muons through the subsequent decay of the produced charged pions $\pi^{\pm} \rightarrow \mu^{\pm} + \nu_{\mu}/\bar{\nu}_{\mu}$. In addition, atmospheric neutrinos can be ν_e from the subsequent muon decay. A sketch of the neutrino production in cosmic ray interactions can be seen in Figure 9.

The neutrino energy is usually low with $E_{\nu} < 1$ GeV, but can be very high as well in rare cases. The energy range is therefore $0.1 - 100,000$ GeV [24]. Atmospheric neutrinos are usually produced at the top of the atmosphere, but as they can traverse the Earth fully as well, the baseline is between 10 and 10,000 km. With these energies and baselines, atmospheric neutrinos can be used for measurement of the mass difference $|\Delta m^2_{32}|$, the mixing angle θ_{23}, the sign of this mass difference ($sign(\Delta m^2_{32})$), as well as the angle δ_{CP}.

1.2.2.5 Reactor Neutrinos

In fission reactions, anti-electron-neutrinos are produced in β-decays. This occurs in large numbers in

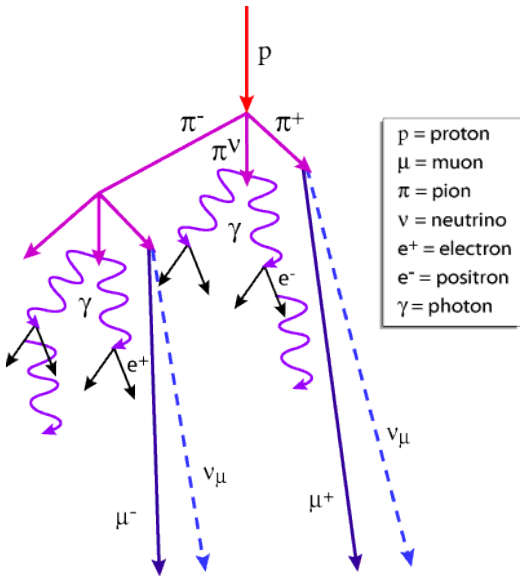

Figure 9: Production of a cosmic-ray extensive air shower [23] creating atmospheric neutrinos

nuclear reactors, hence these anti-electron-neutrinos are referred to as reactor neutrinos. The primary elements used in the reactors are ^{235}U, ^{238}U, ^{239}Pu, and ^{241}Pu. Each fission reaction releases $6\overline{\nu}_e$, which makes reactors the strongest neutrino source on Earth. Their energies, on the other hand, are on the lower side with 2 MeV as the energy threshold for detection and up to 10 MeV [25], as shown in Figure 10.

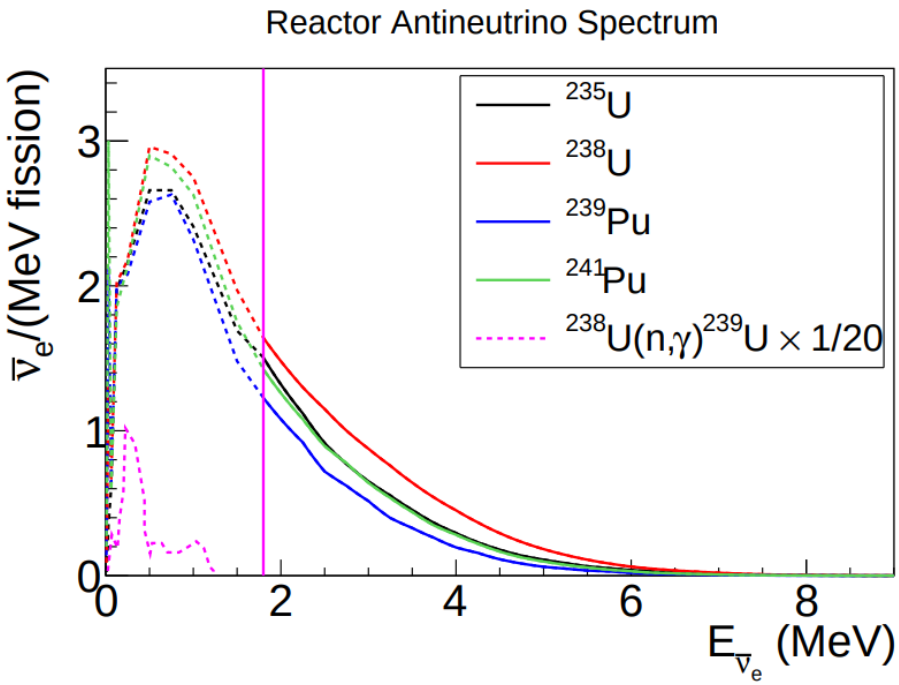

Figure 10: The $\overline{\nu}_e$ energy spectra for ^{235}U, ^{238}U, ^{239}Pu, and ^{241}Pu fissions. The inverse beta decay threshold for detection is marked by the vertical line (credit: [26])

The baseline for measurement of reactor neutrinos can be freely chosen[4] and is therefore tunable to the 'use'-case. There are experiments with very short baselines of less than 500 m, which usually look for the existence of sterile neutrinos [27], short baselines of $1-2$ km for the study of θ_{13} [25], and longer baselines of $50-60$ km for the study of the mass ordering [28] and 260 km for the study of Δm^2_{12} [29].

[4] Legal implications have to be considered, though.

Especially the determination whether $\theta_{13} \neq 0$ is important in light of the study of the neutrino mass ordering and CP violation [25].
In addition to these, reactor neutrinos could also be used to study θ_{12}, $|\Delta m^2_{32}|$, and the sign of this mass difference ($sign(\Delta m^2_{32})$) [28].

1.2.2.6 Accelerator Neutrinos

Neutrinos from accelerators offer precise knowledge of energy and baseline, as both can be freely chosen and tuned to the specific needs of an experiment. Accelerator neutrinos are produced in proton collisions and the subsequent $\pi^{\pm}$ decays (more details on this in Section 2.2.1). The resulting neutrinos are predominantly ν_μ.
With accelerator neutrinos θ_{13}, θ_{23}, $|\Delta m^2_{32}|$, $sign(\Delta m^2_{32})$, and δ_{CP} can be studied.

1.2.3 CP Violation in Neutrino Oscillation

The charge-parity (CP) violation in the leptonic sector, for $\delta_{CP} \neq 0, \pi$, could be observed in the comparison of the oscillation processes $\nu_\mu \rightarrow \nu_e$ and $\bar{\nu}_\mu \rightarrow \bar{\nu}_e$. For this case, however, both δ_{CP} and $a = G_F n_e(x)/\sqrt{2}$ change their signs, meaning that both the CP violation as well as the matter effect play a role in an observed difference of the two processes. The asymmetry from the matter effect increases with baselines, making experiments with longer baselines more sensitive to neutrino mass ordering. For baselines beyond 1200 km the degeneracy between CP violation effects and matter effects can be resolved [17].
The impact of the CP violation in the leptonic sector can be expressed by the Jarlskog invariant [30]

$$J^{PMNS}_{CP} \equiv \mathrm{Im}(U_{\mu 3} U^*_{e3} U_{e2} U^*_{\mu 2}) = \frac{1}{8} \sin 2\theta_{12} \sin 2\theta_{13} \sin 2\theta_{23} \cos\theta_{13} \sin\delta_{CP}$$

which is $0.033 \sin\delta_{CP}$ with current values for the oscillations $\nu_\mu \rightarrow \nu_e$ and $\bar{\nu}_\mu \rightarrow \bar{\nu}_e$, hinting at CP violation due to the value not being 0.
CP violation would be an important process to explain the matter-antimatter asymmetry from big bang nucleosynthesis [17], according to the Sakharov conditions:

- lepton or baryon number violation
- charge and charge-parity violation
- interactions out-of-equilibrium

The first condition could be satisfied in the presence of right-handed neutrino Majorana masses, and the third by the expansion of the Universe. CP violation in the leptonic sector could then generate the matter-antimatter asymmetry through leptogenesis [30].

1.2.4 Neutrino Interactions

To detect neutrinos, they must interact with matter, producing a particle signal that detectors can measure. The most important[5] interactions for this (analog for antineutrinos) are shown in Figure 11.
For the CC interactions, the resulting lepton can be detected.[6] In some cases and depending on the energy of the neutrino, though, as shown in Figure 13, other interaction types (deep-inelastic scattering (DIS), resonance Δ production (RES)) than the quasi-elastic (QE) scattering can also occur, which may result in additional final state particles, as seen in Figure 14.
Quasi-elastic (QE) scattering is the interaction between a neutrino and a nucleon (proton or neutron)

[5] For the DUNE case, see the next chapter.
[6] The for CC interactions newly produced quark in CC interactions can, in some cases, be detected as either a new proton or neutron. These can be emitted or stay in the nucleus.

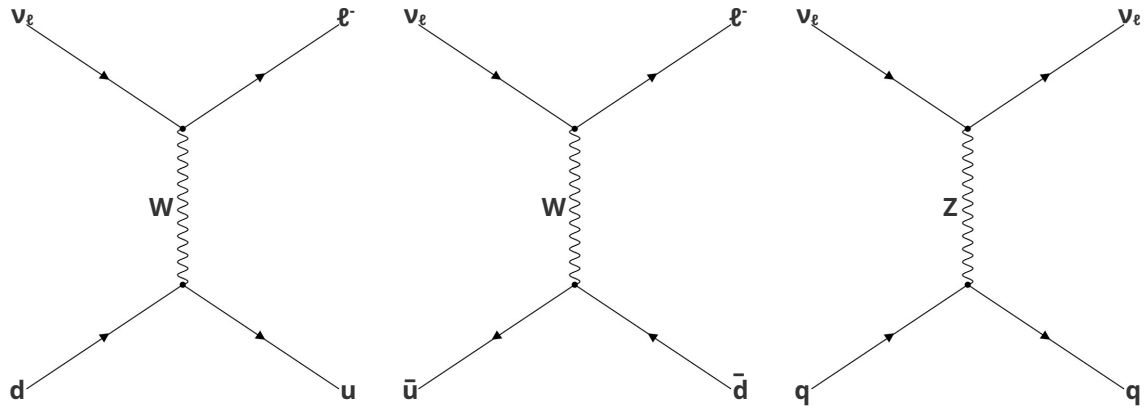

(a) CC on d (b) CC on $\bar{u}$ (c) NC

Figure 11: The Feynman diagrams for CC and NC neutrino interactions in matter [4]

within a nucleus, exchanging a W boson as shown in Figures 11a or 11b. The energy for QE (at the maximum of the distribution, see Figure 13) is not high enough to probe the internal structure of nucleons and nuclei. Deep-inelastic scattering (DIS), on the other hand, involves high-energy neutrinos that have enough energy to probe these structures. The resonant Δ production is a process where a higher-energy neutrino excites the nucleon to a higher-energy state, which then decays subsequently. This process is shown in Figure 12.

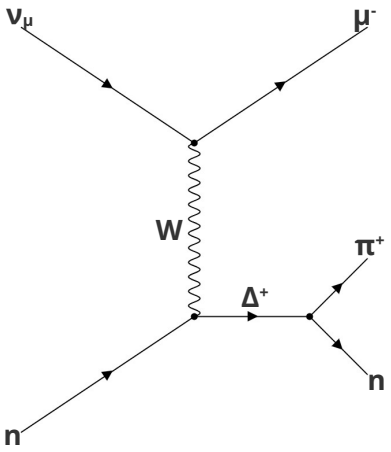

Figure 12: Feynman diagram of a resonance Δ production interaction

For these higher-energy interaction types, nuclear effects also come into play, along with Fermi motion within the nucleus, since final-state interactions usually occur there. Therefore, they are very hard to reconstruct fully. Consequently, also charged and neutral pions, neutrons, protons, etc. can be produced and detected in the final state. Hence, it is not always immediately apparent which neutrino interaction occurred, making it difficult to determine the initial neutrino energy. The initial neutrino energy is essential for calculating the oscillation probability because of the different possible interactions. More details on this can be found in the next chapter.

1.3 Kinematics of Pion Decays and Off-Axis Neutrino Beams

Neutrinos produced in charged pion decays follow the kinematics of this decay. The π^+ decay is a two-body decay resulting in an anti-muon and a muon-neutrino (analog for a π^- decay), as shown in Figure 15.

The muon and the neutrino conserve the four-momentum of the pion $\mathbf{p}_\pi = (m_\pi, 0, 0, 0)$ at rest[7]. The

[7]The rest frame is indicated by a *

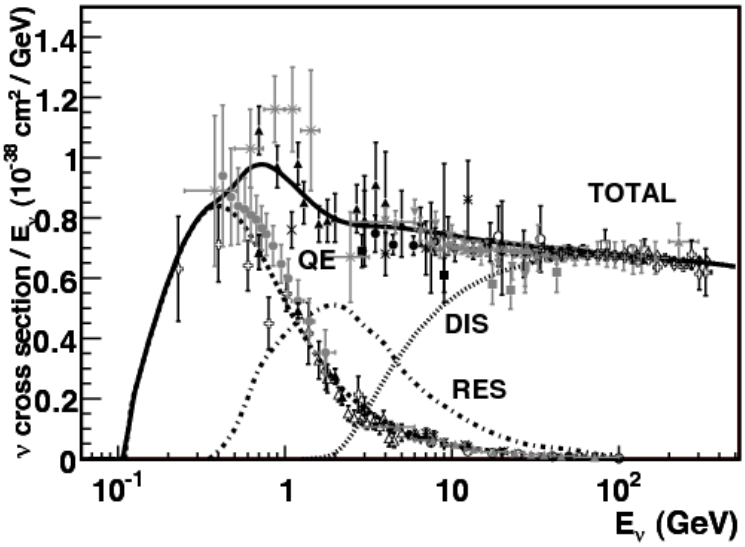

Figure 13: Neutrino cross section as a function of the neutrino energy (credit: [31])

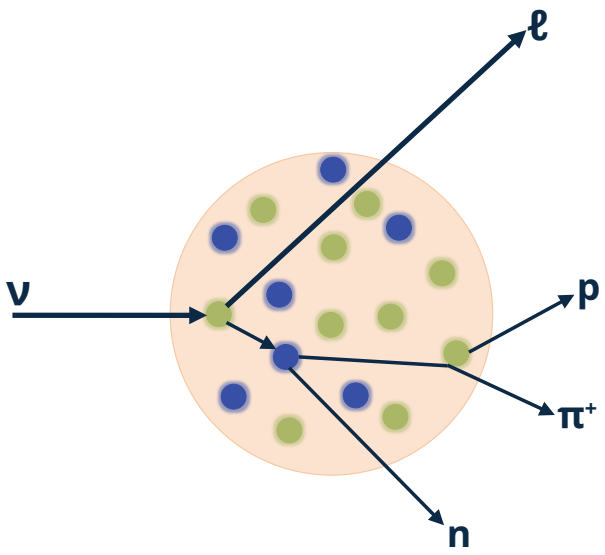

Figure 14: Schematic diagram for reaction involving final state interactions

corresponding neutrino momentum is $\mathbf{p}_\nu = (E^*_\nu, E^*_\nu \sin\theta^*, 0, E^*_\nu \cos\theta^*)$ for a movement of the pion along the z-axis in the lab frame. Boosting the neutrino's momentum from the rest to the lab frame yields $\mathbf{p}_\nu = (\gamma_\pi E^*_\nu(1 + \beta\cos\theta^*), E^*_\nu \sin\theta^*, 0, \gamma_\pi E^*_\nu(\beta + \cos\theta^*))$. From components 1 and 3, the relation for the angle θ between the neutrino and the pion in the lab frame accounts to

$$\tan\theta = \frac{E^*_\nu \sin\theta^*}{\gamma E^*_\nu(\beta + \cos\theta^*)} \approx E^*_\nu \sin\theta^*/E_\nu$$

for ultra-relativistic neutrinos and $\gamma_\pi = E_\pi/m_\pi \gg 1$.
Therefore, the neutrino angle in the lab frame depends on the neutrino energy in the pion rest frame and, of course, the pion energy.
For many pions together, this results in a neutrino flux with increasingly monochromatic energy for increasing angle relative to the 'beam' axis. The neutrino energy peak narrows and moves to lower energies for higher angles [32]. This behavior is demonstrated in Figure 16.

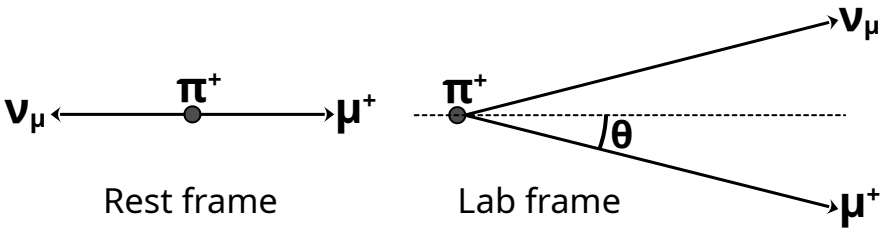

Figure 15: Pion decay at rest on the left side and in motion on the right side

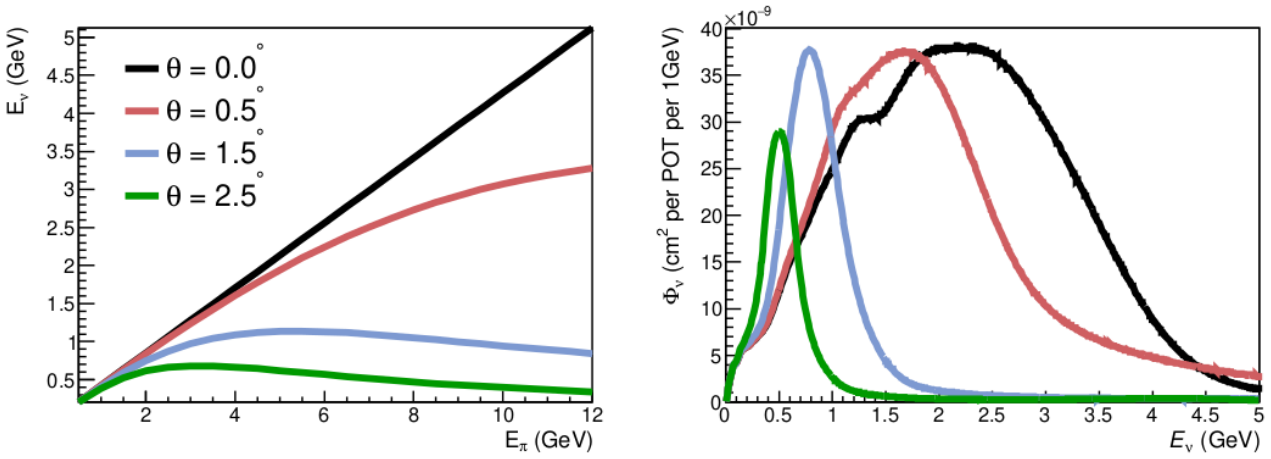

Figure 16: On the left is the neutrino energy as a function of the pion energy for different angles relative to the neutrino beam axis for the DUNE use-case. The right plot shows the corresponding neutrino flux spectra for the same four angles. [32]

1.4 Energy Loss of Particles Traveling Through Material

When particles interact with matter, they lose energy. The following sections will provide detailed descriptions of the different energy-loss mechanisms.

1.4.1 Charged Particles

Charged particles lose energy via ionization of the traversed material. This is an electromagnetic interaction with the atomic electrons. The energy loss from ionization for a given material can be calculated with the Bethe-Bloch equation shown in Equation 7 [16].

$$\left\langle -\frac{dE}{dx} \right\rangle = Kz^2 \frac{Z}{A} \frac{1}{\beta^2} \left[\frac{1}{2} \ln \left(\frac{2m_e c^2 \beta^2 \gamma^2 W_{max}}{I^2} \right) - \beta^2 - \frac{\delta(\beta\gamma)}{2} \right] \tag{7}$$

This is called the mass stopping power and has a unit of $\mathrm{MeVg^{-1}cm^2}$. z is the charge number of the incident particle, Z the atomic number of the absorber, A the atomic mass of the absorber in $\mathrm{g\,mol^{-1}}$, I the mean excitation energy, $W_{max} = 2m_e c^2 \beta^2 \gamma^2 / (1 + 2\gamma m_e / M + (m_e/M)^2)$ the maximum energy transfer of a particle of mass M in a single collision, and $\delta(\beta\gamma)$ the density effect correction to the ionization loss. K is $4\pi N_A r_e^2 m_e c^2$ with N_A as Avogadro's number, r_e as the classical electron radius, and $m_e c^2$ the electron mass.

For an increased particle energy, the E field, created by the charged particle, flattens and extends, so that the distant-collision contribution increases as $\ln(\beta\gamma)$. Real materials, however, become polarized, thereby limiting the field extension. In addition, the energy loss is higher for slower particles due to the $1/v^2$ (from $1/\beta^2$) dependence [4].

Ionization energy loss is the dominant mechanism for muons.

1.4.2 Special Case of Electrons and Photons

For electrons (and positrons), in addition to ionization, other energy-loss mechanisms come into play. Ionization is the dominant process for low energetic electrons and positrons (alongside contributions from Møller and Bhabha scattering, and e^+ annihilation) until a material-dependent, critical energy E_c is reached. Above this energy, the dominant energy loss mechanism is bremsstrahlung in the presence of a nucleus [4, 16]. The critical energy is approximately $E_c \sim 800/Z$ MeV, with Z as the charge of the nucleus.

Bremsstrahlung is a process where an electron (or positron) radiates a photon in the electrostatic field of the nucleus. The energy loss rate from bremsstrahlung is nearly proportional to the energy of the electron (or positron), while the ionization energy loss rate, as mentioned before, is only logarithmically dependent on the energy. The rate of this process is also inversely proportional to the squared mass of the particle, which suppresses this mechanism for the heavier muons.

The radiation length X_0 describes the average distance for the energy of electrons to be reduced by a factor $1/e$ through bremsstrahlung, shown in Equation 8.

$$\frac{1}{X_0} = 4\alpha r_e^2 \frac{N_A}{A}\{Z^2[L_{rad} - f(Z)] + ZL'_{rad}\} \tag{8}$$

with A as the atomic mass of the absorber, α as the fine structure constant, and tabulated values for L_{rad} and L'_{rad} [16].

Low-energy photons lose energy primarily via the photoelectric effect, Rayleigh scattering, and photonuclear absorption [4,16]. For energies above $\sim$ 1 MeV the dominant process becomes Compton scattering ($\gamma e^- \rightarrow \gamma e^-$) and above $\sim$ 10 MeV also pair production ($e^\pm$) is possible in the presence of a nucleus. The radiation length is about $7/9$ of the mean free path for pair production [4].

For high-Z materials, the radiation length can be very short. For example, for iron it is only 1.76 cm [4].

Given that both electrons (and positrons) and photons can lose energy by producing the other, electromagnetic showers can occur in materials. These showers are started by the original particle producing either a photon or $e^\pm$, which then also loses energy as described above. This creates a cascade effect that stops only when the energy of the produced and original particles falls below the critical energy. This is usually the case after

$$x_{max} = \frac{\ln E/E_c}{\ln 2}$$

radiation lengths [4]. An example of such a shower is shown in Figure 17.

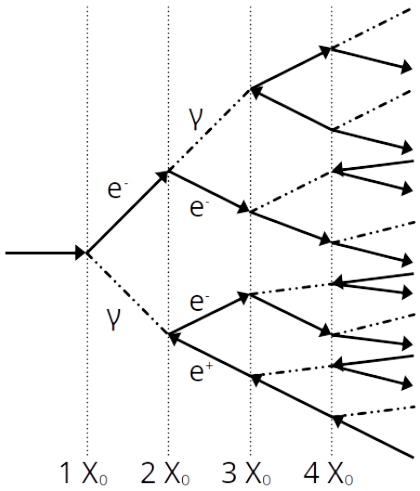

Figure 17: The cascade of an electromagnetic shower where the number of particles roughly doubles after each radiation length [4]

2 Deep Underground Neutrino Experiment – DUNE

This chapter introduces the Deep Underground Neutrino Experiment along with its physics goals. The neutrino beam production, the near detectors, and the far detectors are explained for the two planned phases of the experiment. The different near detectors are motivated and the separate physics goals are described.

2.1 Introduction

2.1.1 Overview of DUNE

The Deep Underground Neutrino Experiment (DUNE) is a next-generation neutrino oscillation experiment [33]. The predominantly muon-neutrinos are produced by the proton accelerator located at Fermilab, Illinois. They pass through the Near Detector (ND) complex and travel $\sim$ 1300 km underground to the Far Detector (FD) site at the Sanford Underground Research Facility (SURF), South Dakota. Along this distance, the muon-neutrinos oscillate according to Section 1.2.2, allowing for the appearance of electron-neutrinos in the FD. A sketch of DUNE is shown in Figure 18.

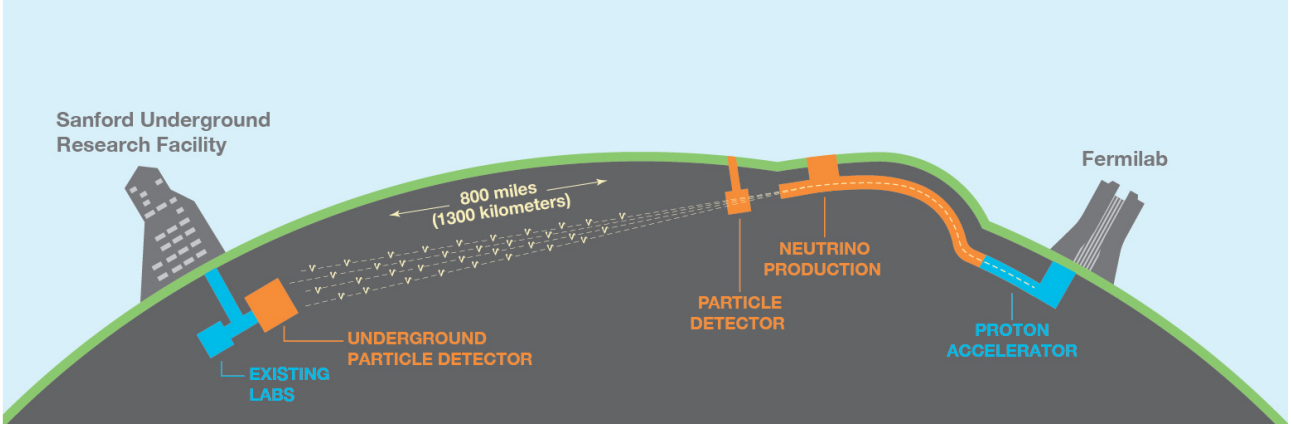

Figure 18: Sketch of the DUNE experiment with the neutrino beam traveling from Fermilab, Illinois, to SURF, South Dakota [17]

The FD site will be placed approximately 1.5 km underground to shield the modules from cosmic muons. The ND site will be located at Fermilab, Illinois, about 574 m from the neutrino beam source and 60 m underground.

2.1.2 Physics Questions and Goals

One of the main goals DUNE wants to achieve is the observation of CP violation in the leptonic sector and determination of δ_{CP} with at least 5σ certainty. This requires extensive statistics and unprecedented control of systematic uncertainties [17].
In addition to the measurement of δ_{CP}, DUNE will also perform a simultaneous measurement of the neutrino oscillation parameters θ_{13}, θ_{23}, Δm^2_{31} and the octant of θ_{23} without using external constraints. The goal here is to approach, e.g., θ_{13}, the precision of reactor neutrino experiments such as Daya Bay [25] and Jiangmen Underground Neutrino Observatory (JUNO) [28]. The precision measurement of the oscillation parameters will be used to test the unitarity of the PMNS matrix, which could indicate Beyond the Standard Model (BSM) physics if not true.
DUNE will also be able to determine the neutrino mass ordering with more than 5σ certainty. This can be done, even if there would be a degeneracy near maximum CP violation of $\delta_{CP} = \pm\pi/2$, for all possible values of δ_{CP} within a relatively short time frame of a couple of years with the current beam time plan.

Both CP violation and the neutrino mass ordering influence the oscillation probability, however, in different ways.
With the high level of precision that is achievable, DUNE is also sensitive to astrophysical neutrinos produced by potential Core-Collapse Supernova bursts as well as solar neutrinos produced in the fusion reactions in the Sun. The supernova neutrinos are predominantly ν_e with energies between 5 and 100 MeV which have a relatively large cross section in the $\nu_e + {}^{40}Ar \rightarrow e^- + {}^{40}K^*$ process. This allows to test different Supernova (SN) models. Supernova neutrinos can also be used to limit the neutrino mass via time-of-flight measurements with the distance of the source to Earth as the oscillation baseline, as well as for neutrino mass ordering measurements. With the excellent ν_e flavor sensitivity, DUNE can also probe the neutrino component of the diffuse supernova neutrino background. On the solar neutrino side, DUNE is sensitive to neutrinos from ${}^8B$ and hep processes within the Sun. The first enables a measurement of the squared mass difference Δm^2_{12} via the day-night[8] neutrino flux asymmetry from solar neutrinos induced by Earth's matter.
DUNE will also be able to detect ν_τ via τ decay final states [34]. In the FD ν_τ would appear either via oscillation from ν_μ and enable constraint of the τ elements of the PMNS matrix, or via anomalous effects opening the door to BSM physics. The latter also applies to ND, as the baseline to the beam source is too short for ν_τ to appear from 'standard' neutrino oscillation, but could originate from oscillation of sterile neutrinos.

2.1.3 Phase 1 and 2

DUNE will follow a staged construction plan, divided into two phases: Phase 1 and Phase 2. The average beam power is planned to be 1.1 MW in the first year of operation and increase to 1.6 MW during the second year with hardware upgrades [34]. The plan is to achieve 2.3 MW beam power after $\sim$ 15 y of operation with further hardware upgrades.
The far detector side will have two modules for the first three years, with a third added in year four and another in year six. The two modules (three and four) added in Phase 2 are supposed to be fully functional at the given times.
Phase 1 will use the systematic uncertainty constraints from the ND. Phase 2 will then begin after the six years of Phase 1, and use the improved uncertainty limits obtained with new and upgraded detector components.
The detector details of Phase 1 and the upgrades of Phase 2 will be discussed in the following sections.
The physics goals of Phase 1 are a subset of the full goals for DUNE, due to the different capabilities of DUNE in Phases 1 and 2. The neutrino mass ordering can still be determined with $> 5\sigma$, while CP violation can only be determined to 3σ with near maximal mixing ($\sim \pm\pi/2$) values of δ_{CP}. Improvements to the current uncertainties of Δm^2_{32} and θ_{23} are also possible during Phase 1.
DUNE will be able to accumulate about 100 kt(*LAr*) · MW(*beam power*) · year data in five years which corresponds to about 400 ν_e and 150 $\bar{\nu_e}$ candidates in the FD, which statistically limits the sensitivity to the octant of θ_{23} and CP violation in a scenario with not the most favorable case. With the base beam intensity of $1.1 - 1.6$ MW and only the two FD modules planned for Phase 1, the required time to achieve the necessary exposure would be $24 - 40$ years. The achievable integrated exposure with Phase 1 and 2 can be seen in Figure 19.
Additional upgrades to the FD modules would also enable the detection of a higher number of ν_e events with better pointing resolution and an increased sensitivity range to SN neutrinos, as well as enable the study of the CNO cycle of the Sun. The latter allows for testing different metallicity models. With a lower visible energy detection threshold, MSW matter effects (see [16]) could be studied in the Sun.

[8] During the day, the neutrinos from the Sun can hit the detector directly. At night, on the other hand, the neutrinos from the Sun have to travel through the Earth first to be detected.

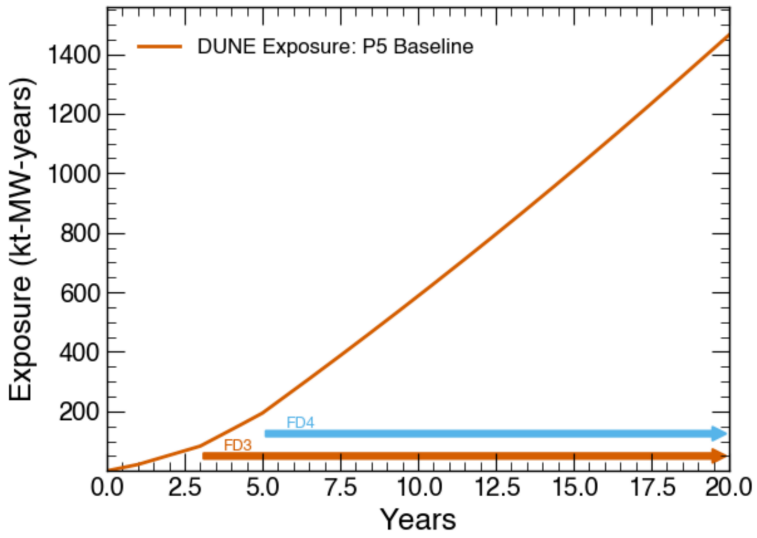

Figure 19: DUNE integrated exposure, in kt · MW · yr units, as a function of time. The integrated exposure is built from the beam power and the FD mass staging assumptions [34]

2.2 Details of Phase 1

2.2.1 Neutrino Beam Production

In general, a neutrino beam is created by shooting protons from a proton accelerator onto a graphite target, which produces predominantly charged pions. By employing magnetic horns, the sign of the produced pions can be selected. The pions then decay in a decay tunnel into muons, producing neutrinos (ν_μ for π^+ and $\bar{\nu}_\mu$ for π^-) alongside muons. The muons and other particles are filtered out of the beam in a beam dump and subsequent rocks, leaving only the neutrinos traveling forward. A sketch of this process is shown in Figure 20.

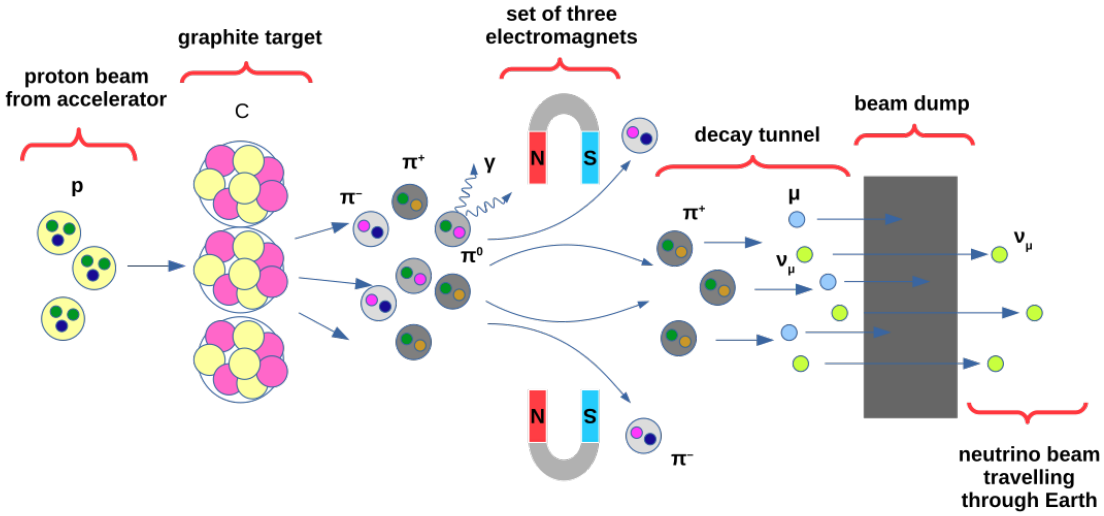

Figure 20: Sketch of muon neutrino beam production. On the left side enter protons from an accelerator and hit a graphite target. The produced pions travel between sets of electromagnets, which allows for a sign selection of the charged pions. They then enter a decay tunnel, where pions decay into muons and neutrinos. The muons are filtered out by the beam dump on the right side, leaving only the neutrinos. (Credit: [35])

For DUNE, the neutrino beam is produced by the Fermilab accelerator complex using the proton accelerator with a 120 GeV proton beam [36, 37]. About $3 \cdot 10^{13}$ protons are accelerated every 1.87 s. The used graphite target is 95 cm long and the decay volume 194 m, filled with Helium [38]. A three-horn

configuration will be used to focus the beam and select either positively or negatively charged pions. Alongside pions, kaons are also produced in the graphite target. Both decay predominantly via $\pi^+ \rightarrow \mu^+ + \nu_\mu$ and $K^+ \rightarrow \mu^+ + \nu_\mu$ (vice versa for negative charge). Subdominant decay modes of kaons produce a background of ν_e among others.

2.2.2 Far Detector Complex

In Phase I, the far detector side consists of two modules of Liquid Argon TPC (LArTPC) [33]. One module will use a horizontal drift approach, while the other uses a vertical drift approach. A visualization of the FD site is shown in Figure 21.

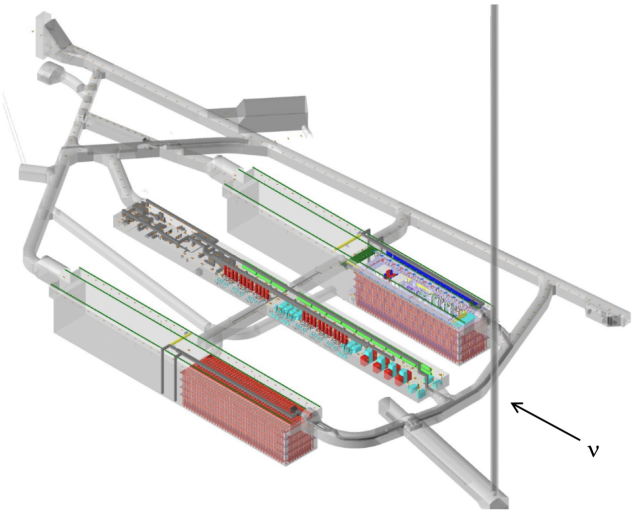

Figure 21: Underground caverns for DUNE FD and cryogenics systems at SURF in Phase 1. The two modules in their cryostats are shown in red. The gray space behind the two modules is planned for the additional modules in Phase 2. Also shown is the shaft system. The neutrino beam enters from the right side as indicated by the arrow. [17]

2.2.2.1 Horizontal Drift Module

The horizontal drift (HD) module consist of a cryostat with outer dimensions 18.9 m $\times$ 17.8 m $\times$ 65.8 m, which can be seen in Figure 22a. This cryostat will hold liquid Argon with a total mass of about 17.5 kt. The LArTPC technology used in this module has been demonstrated and used by other experiments such as ICARUS, MicroBooNE, and SBND [39]. It has also successfully been installed and tested in ProtoDUNE at CERN [40]. Charged particles traversing the detector ionize the Argon, and the charges drift horizontally, guided by an electric field, towards a vertical anode. The maximal drift length amounts to 3.5 m with a drift speed of 1.6 mm/μs. There are multiple drift volumes, as shown in Figure 22b, as the drift length is limited due to the lifetime of the drift electron. The anode consists of three planes. Each plane is built out of two stacks of 25 anode plane assembly (APA) of the size 6 m $\times$ 2.3 m each for a total size of 58.2 m $\times$ 12 m. The APAs consist of an aluminum frame holding three layers of active wires at different angles. The U and V wires (see Figure 23) are transparent to charges and mounted at angles of $\pm$35.7°, while the X wires (see Figure 23) collect the charges. This structure allows for two-dimensional information with a spatial resolution of $\sim$ 1 mm. The function of the wires and the TPC can be seen in Figure 23. With a $\sim$ 5 mm spacing between the modules, the total size of the TPC is 12 m $\times$ 14 m $\times$ 58.2 m holding 10 kt of liquid Argon in the fiducial volume.

The necessary electric field for the drift is provided by the combination of APA and cathode plane. This plane is formed by cathode plane assembly (CPA) arrays with 150 CPAs per array and two arrays per plane. Each CPA is a 1.2 m $\times$ 4 m resistive panel with its own power supply of 0.16 mA at $-$180 kV. This combination of APA and CPA results in a uniform electric field of 500 V/cm. The field uniformity is ensured by a field cage (FC), which also defines the drift volumes.

The readout of the APAs is performed with electronics embedded in the liquid Argon to achieve a good signal-to-noise ratio (S/N) by reducing the cable lengths, capacitance, and electronic noise. A good S/N

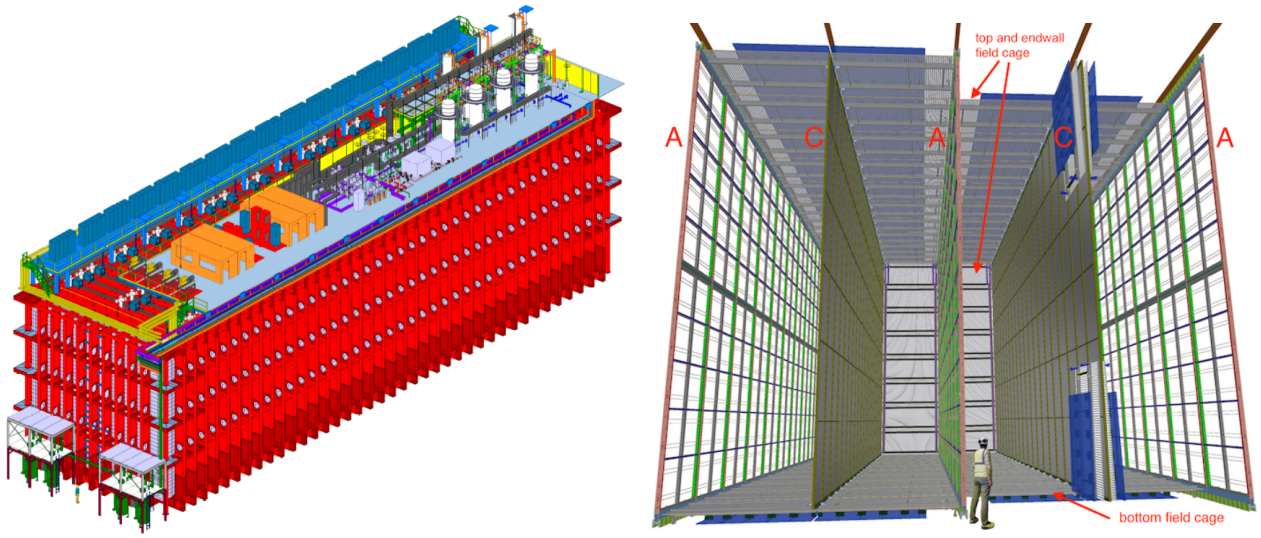

(a) Cryostat for the far detector

(b) HD module from the inside

Figure 22: Cryostat of the far detector module in 22a. At the lower left, a person indicates the scale. The inside of the HD module in 22b shows the anode (A) and cathode (C) planes, as well as the drift region surrounding field cage (FC) in between [33]

is necessary, as no additional signal amplification is used and the measured ionization is directly proportional to the energy loss per unit distance (dE/dx). This enables calorimetry and particle identification (PID) of the charged particles in the detector.

In addition to the ionization, charged particles produce scintillation light with a wavelength of 128.6 nm in the Argon. About 24,000 scintillation photons are produced per MeV in the setup. This scintillation light is detected with a photon detection system called X-ARAPUCA and used to determine the start time t_0 of the events with a 1 μs timing resolution. Knowing t_0 allows the determination of the third dimension of the event topology from the time difference of the scintillation light and the drift time. The X-ARAPUCAs are mounted in groups of 24 onto the photon detection (PD) modules with total dimension of 209 cm $\times$ 2 cm $\times$ 12 cm. Ten of the PD modules are placed between the wire layers of each APA. The inner-most PD modules detect light from both directions, while the outer modules only detect the light from one direction and also serve as cosmic muon detectors at the edges. The X-ARAPUCAs function as "light traps" with a light-collection area of 600 $\times$ 600 mm^2, and 160 Silicon Photo-Multiplier (SiPM) to detect the light. The signals from 80 of those are summed into a single output signal, with a total of two output signals per X-ARAPUCA.

An example of an event in this setup is shown in Figure 24 from the ProtoDUNE horizontal drift (single-phase) prototype.

2.2.2.2 Vertical Drift Module

The vertical drift (VD) module simplifies detector construction and installation, reducing overall cost compared to the HD modules [34], while maximizing the active volume with an extended drift distance. The drift medium is also liquid Argon [42].

While the cryostat design uses the one from the HD modules, the anode planes or charge readout plane (CRP) are now located at the top and bottom of the drift volumes as shown in Figure 25. They consist of 3.2 mm thick, double-sided, and perforated printed circuit board (PCB) connected in pairs to build a charge-readout unit (CRU). Two of these are attached on a composite frame to form a CRP of size 3.4 m $\times$ 3 m. An entire readout plane then consists of 80 of these CRPs. The top and bottom charge readouts differ slightly due to their locations. While the bottom plane is read out with the same electronics as the horizontal drift modules, the top anode readout is based on the ProtoDUNE Dual Phase

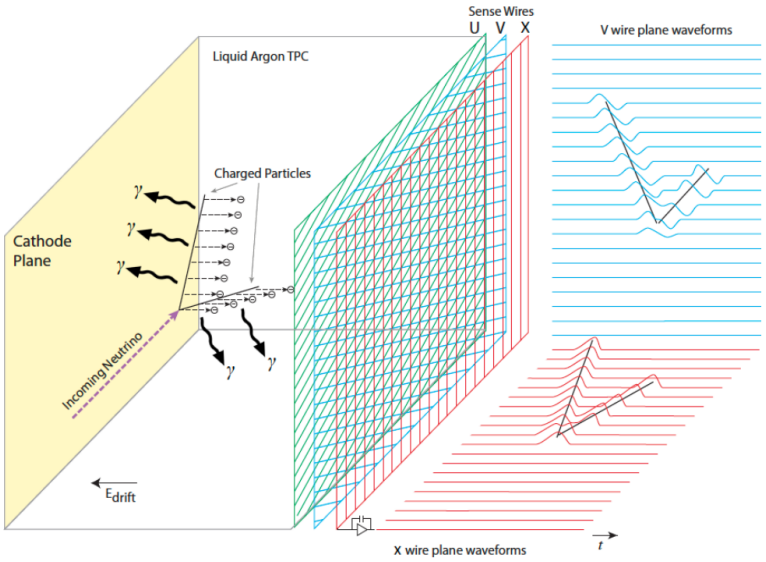

Figure 23: The general operating principle of the LArTPC in 23. Negatively charged ionization electrons drift horizontally in response to the E field in LAr and are collected on the anode, which consists of the U, V, and X sense wires. The right-hand side represents the time projections in two dimensions as the event occurs [33]

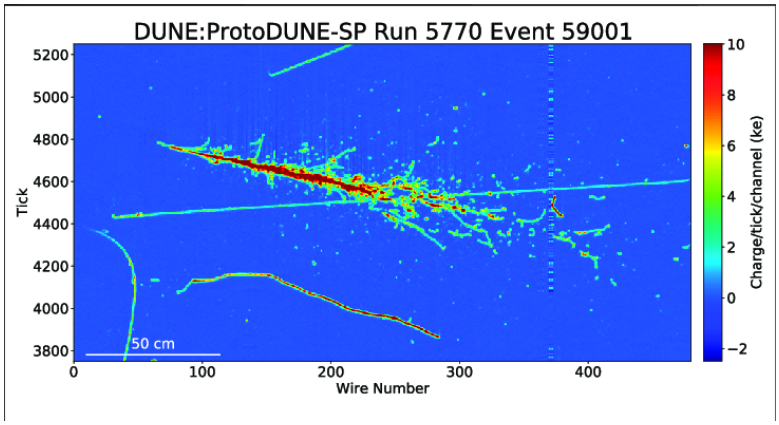

Figure 24: The example of an electron event with 6 GeV/c in the ProtoDUNE horizontal drift (single phase) prototype at CERN [41]. The incident electron creates a shower visible in the plot by the deposited charge. The scale of the plot is shown in the bottom left corner

(ProtoDUNE-DP) design, making the electronics fully accessible [34].
The cathode is a vertical mid-plane suspended from the top. It subdivides the detector into two vertically stacked 6.5 m drift volumes with a uniform 450 V/cm electric field. The cathode consists of 80 modules with the same footprint as a CRP, each with 4 X-ARAPUCAs for the PD system.
The field cage is modular and consists of aluminum electrode profiles stacked vertically at a 6 cm pitch. In the region within 4 m of the anode plane, the profiles are narrow with a width of 15 mm to allow for X-ARAPUCAs being mounted on the cryostat membrane walls behind them. Otherwise, the profiles are 46 mm wide.

2.2.3 Near Detector Complex

The ND site consists of a LAr near detector (ND-LAr), a muon spectrometer for muons not contained in ND-LAr, a system to move these two off-axis, and a permanent on-axis detector.
In the following, the need for a near detector is first explained, followed by details of the different detectors and the system.

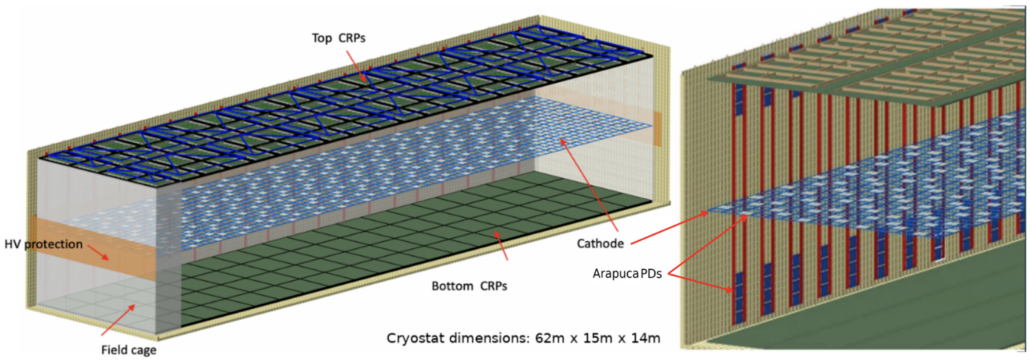

Figure 25: The layout of the vertical drift FD modules. The top and bottom CRPs are shown on the left with the cathode shown on both sides. Also, the HV protection and field cage are indicated on the right. On the left side, the X-ARAPUCAs are shown. [42]

2.2.3.1 Motivation and Purpose of the Near Detector

One of the main goals of the ND of DUNE is to measure the unoscillated neutrino spectrum. It is also supposed to constrain systematic uncertainties in the flux, neutrino interaction modeling, and the detector response modeling. The near detector is, in addition, necessary to verify the neutrino energy dependence of these effects, to characterize the relevant backgrounds, and to measure and verify the beam stability [43]. It serves as a guard against the "unknown unknowns" that are not predictable [17]. Without a near detector, there could be an undetectable, significant bias in the measured values of δ_{CP}, which could reduce sensitivity, as seen in Figure 26.

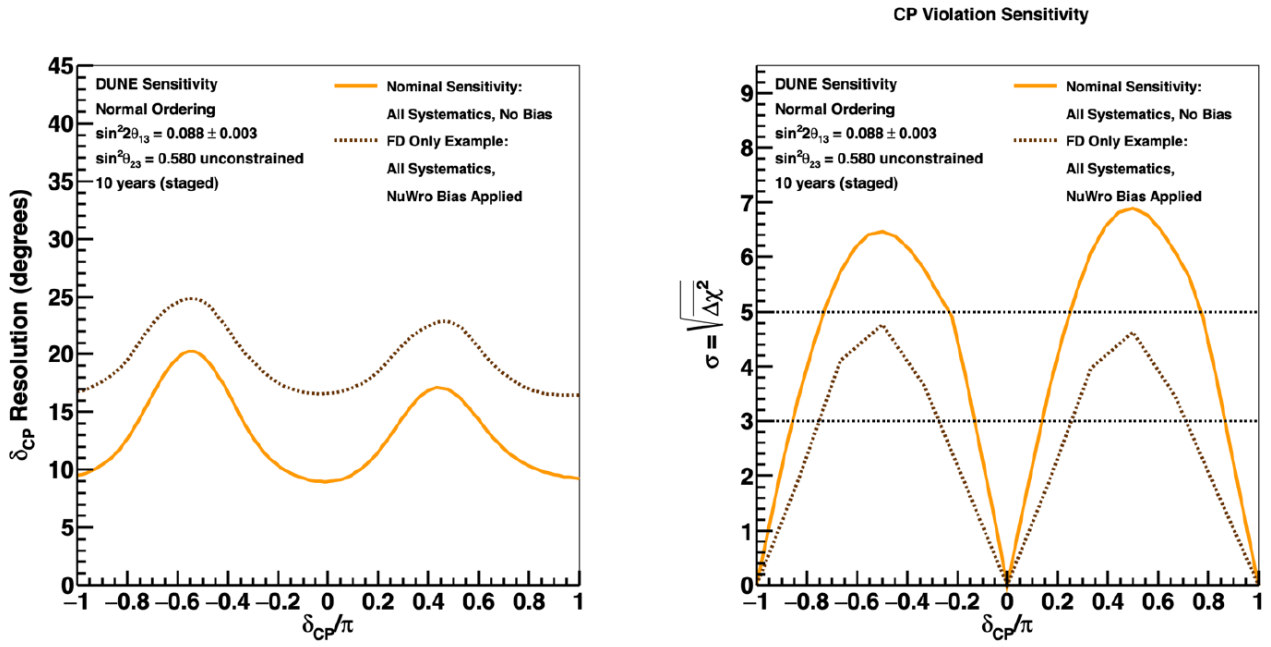

Figure 26: The CP violation sensitivity for a FD-only scenario. The δ_{CP} resolution (left) and CP violation sensitivity (right) are compared to the results from the nominal ND+FD analysis [17]

Measuring the unoscillated neutrino energy spectrum allows for the determination of the oscillation parameters by fitting the prediction at the FD. The ND also provides better background characterization than the FD [33]. Incorporated in this is the beam monitoring to check for instability in the neutrino beam and building confidence in the neutrino flux model.

The FD can not constrain the neutrino flux directly; it can, however, measure the neutrino interaction rate for different neutrino flavors as a function of the reconstructed neutrino energy [33]. The measurements

in the near and far detectors are formalized in Equations 9 and 10 for neutrinos[9]

$$\frac{dN_x^{FD}}{dE_{rec}} = \int \Phi_{\nu_\mu}^{FD}(E_\nu) P_{\nu_\mu \to x}(E_\nu) \sigma_x^{Ar}(E_\nu) T_x^{FD,Ar}(E_\nu, E_{rec}) dE_\nu \tag{9}$$

$$\frac{dN_x^{ND}}{dE_{rec}} = \int \Phi_{\nu_\mu}^{ND}(E_\nu) \sigma_x^{m}(E_\nu) T_x^{ND,m}(E_\nu, E_{rec}) dE_\nu \tag{10}$$

with $x = \nu_e, \nu_\mu$, m as the interaction target/material (e.g. H, C, or Ar), E_ν for the true neutrino energy, E_{rec} for the reconstructed neutrino energy, T for the true-to-reconstruction transfer function, σ for the neutrino interaction cross section, Φ for the unoscillated neutrino flux, and dN/dE_{rec} for the measured differential event rate per target.
The neutrino flux at the FD can be expressed with the near-to-far flux ratio $R(E_\nu) = \Phi_{\nu_\mu}^{FD}(E_\nu)/\Phi_{\nu_\mu}^{ND}(E_\nu)$ [33], as shown in Equation 11. The near-to-far flux ratio can be constrained.

$$\frac{dN_x^{FD}}{dE_{rec}}(E_{rec}) = \int \Phi_{\nu_\mu}^{ND}(E_\nu) R(E_\nu) P_{\nu_\mu \to x}(E_\nu) \sigma_x^{Ar}(E_\nu) T_x^{d,Ar}(E_\nu, E_{rec}) dE_\nu \tag{11}$$

The near detector complex, shown in Figure 27a, is especially useful for tuning models of neutrino interactions with Argon, nuclear effects of free nucleons, and the detector response [33]. As heavy nuclei, Argon nucleons interact with each other and therefore exhibit Fermi motion, which must be correctly implemented in the models. Also, the models for neutron production in neutrino interactions, which, if not detected, result in "missing energy", need to be tuned for precise neutrino energy reconstruction.
On the nuclear effects side, the cross sections of neutrinos on free nucleons in the DUNE specific energy range remain mostly unknown [33]. The uncertainties of the nuclear effects can be reduced by using DUNE's large statistics in the near detector complex. One major aspect here is Final-State Interactions (FSI) (compare Figure 14), which can also lead to the above-mentioned "missing energy" via e.g. neutron production in interactions.
The detector response model is necessary to control the FD model. The model is tuned by building a functionally equivalent ND for comparison.
The neutrino flux, interaction (cross sections), and detector response, each with its own neutrino energy dependence, are entangled [33]. This makes it difficult to reduce their respective systematic uncertainties. DUNE allows for disentangling the energy dependence by taking measurements at different positions perpendicular to the beam (off-axis positions) using the DUNE-PRISM method. This movement changes the neutrino flux spectrum, as described in Section 1.3, with the mean neutrino energy decreasing with increasing distance from the on-axis position, as shown in Figure 27b. Sampling different neutrino fluxes allows a linear combination of them to reproduce the FD oscillated neutrino spectrum. In this way, the energy dependence of the entanglement can be deconvoluted using a data-driven approach with minimal cross-section dependence. Without the DUNE-PRISM option, the measured oscillation parameters Δm^2_{32} and θ_{23} from the fit could be biased and significantly incorrect [17].
In addition to the above-mentioned tasks, the near detector complex also has a stand-alone physics program focusing on BSM searches and cross-section measurements, enabled by the high-intensity environment near the neutrino beam production point. The cross-section studies focus on model tuning of nuclear effects, NC neutrino interactions with pions in the final state (NC$\pi^{\pm,0}$), quasi-elastic (QE), multi-nucleon, resonant, and deep-inelastic scattering of neutrinos as well as the nuclear structure of Argon nuclei. The overall cross section of neutrino-Argon interactions as well as neutrino interactions on hydrogen will be measured, alongside electroweak precision measurements, the s-quark contribution in the nucleus, and more QCD specific studies with SAND [43]. On the BSM side, sterile neutrinos, exotic searches, e.g., heavy meson decays, right-handed neutrinos, and heavy neutral leptons are searched for, as well as an improved measurement of neutrino tridents. The latter serves as a direct probe of a

[9] equivalently for antineutrinos

parameter space of new BSM physics.

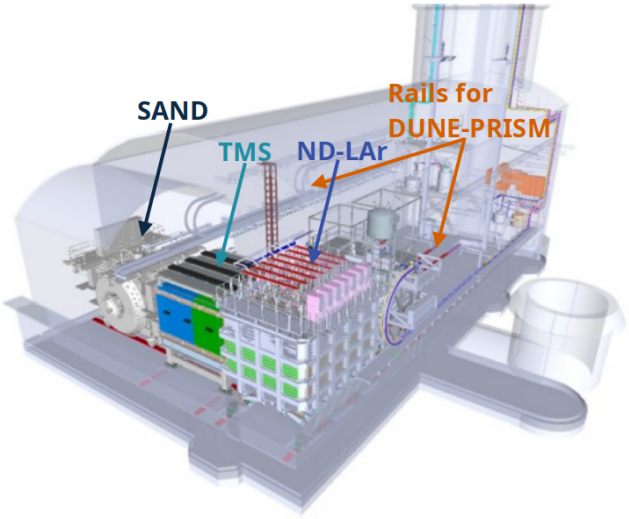

(a) DUNE Near Detector hall [43]

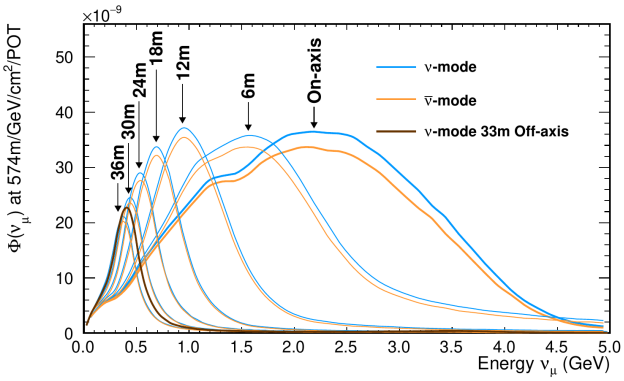

(b) Neutrino energy spectrum as a function of detector off-axis position [33]

Figure 27: 27a shows the DUNE Near Detectors in the ND Hall. The neutrino beam enters from the right, intercepting ND-LAr and TMS on the right and middle, and then TMS on the left side. Here ND-LAr+TMS are in their on-axis position, but they can be moved with DUNE-PRISM off-axis (towards the shaft in the upper right of the plot) with energy chains holding services that travel alongside the detectors as they move [43]. 27b shows the variation in the neutrino energy spectrum as a function of detector off-axis position [33]

2.2.3.2 Liquid Argon Near Detector

To provide a, to the FD, functionally equivalent near detector, ND-LAr is also a LArTPC but due to the space limitation only of the dimension $7 \times 3 \times 5$ m^3 [43]. In this way, it can match the FD in the containment of electromagnetic and hadronic showers, as well as of wide-angle muons with an energy of less than 1 GeV. The full detector on the rails is shown in Figure 28a.

ND-LAr itself is a modular system with 7×5 LArTPC modules of dimensions $1 \times 3 \times 1$ m^3. Each of these modules has dual 50 cm drift volumes, each optically segmented. An example of a beam spill showing the module structure is shown in Figure 28b. The fiducial volume excludes the volume 50 cm from the sides and the upstream edge, and 150 cm from the downstream edge. The final fiducial volume is $6 \times 2 \times 3$ m^3. Due to its smaller size, the readout could be changed to a pixel readout, which naturally provides three-dimensional spatial information from a 3.7 mm^2 pixel area and a 4 mm equivalent sampling in the drift direction. The pixel readout is also needed due to the higher instantaneous occupancy.

Expected are between $\mathcal{O}(10-100)$ neutrino interactions per 10 μs time window.

As with the far detector, the LArTPC is placed into a cryostat that is capable of supporting a $10.2 \times 6.3 \times 7$ m^3 LAr volume. It consists of a membrane insulation and an outer steel warm structure with a low mass muon window of an average density of $< 23.9 \frac{\text{g}}{\text{cm}^2}$ over an area of 8.4×4.1 m^2 to allow muons an easier exit towards TMS. Without this window, a muon acceptance gap at about 1 GeV would open.

2.2.3.3 The Muon Spectrometer

The Muon Spectrometer (TMS) is a magnetized steel scintillator range stack with the main purpose of measuring the charge and energy of ND-LAr exiting muons with 1 to 4.5 GeV by ranging them out [43, 44]. A visualization of TMS can be seen in Figure 29a. TMS is able to do this due to the higher dE/dx = 11.43 MeV/cm of steel compared to dE/dx = 2.105 MeV/cm of LAr. The active volume for TMS is $7.4 \times 3.2 \times 7$ m^3.

To get a $\sim$ 5% momentum resolution, the steel has different thicknesses throughout the detector, with

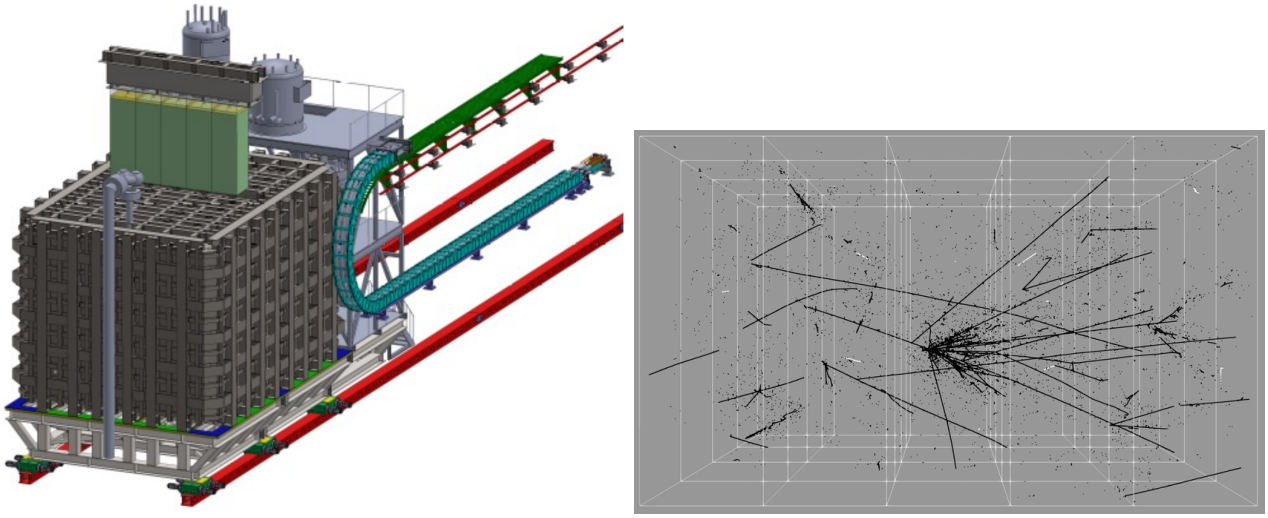

(a) ND-Lar and its cryostat

(b) Beam spill with ND-LAr module structure

Figure 28: 28a ND-LAr and its cryostat, showing a row of 5 ND-LAr modules extracted from the cryostat, and cryogenic services on a platform next to the cryostat. The rails of DUNE-PRISM are shown in red, rollers in green, and the energy chain in teal. The beam enters from the lower right [43]. 28b A beam spill in the LAr component of the DUNE ND. Fast-neutron induced recoiling proton tracks, with an energy threshold greater than $\sim$ 10 MeV, are shown in white. The black tracks are all other energy deposits sufficient to cause charge collected at the pixel planes. Also visible is the module structure of ND-LAr [33].

the first 50 layers of 1.5 cm, the next 34 layers of 4 cm, and the last 8 layers of 8 cm thickness.[10] The steel is mounted in 4 parallel rows longitudinal to the beam, indicated in Figure 29a by the red cone.
Between each steel layer is a layer of plastic scintillator. This scintillator layer consists of 6 modules of 32 bars each that are 3.6 cm wide, 1.6 cm thick and $\sim$ 3.2 m long. The modules are alternatively (by layer) tilted by $\pm 3°$ from the vertical to add some rough information in the vertical direction (U and V layers or stereo layers). In addition to these U and V layers, some layers consist of horizontally oriented modules (horizontal or X layers) to provide additional information in the vertical direction. Information in the vertical direction is necessary to achieve a good track matching between ND-LAr and TMS and to distinguish between bottom exiting or contained muons in TMS. The bar width provides sufficient spatial resolution for muon charge identification.
The charge identification of muons is made possible by a 1 T magnetic field with opposite field direction in the inner and outer steel region of TMS[11]. This field-direction switch minimizes fringe fields to neighboring detectors.
The scintillation light in each bar is read out via wavelength-shifting (WLS) Kuraray Y11 fibers and SiPMs at one end of the bars.
The readout with SiPMs allows a $\mathcal{O}$(1ns) timing resolution, allowing to separate different neutrino interactions in a single spill. In addition to the muons exiting ND-LAr, 120 neutrino interactions per spill are expected on the TMS steel.

2.2.3.4 DUNE Precision Reaction-Independent Spectrum Measurement

DUNE Precision Reaction-Independent Spectrum Measurement (DUNE-PRISM) provides the means to move ND-LAr and TMS off the beam-axis center by up to 28.5 m at the center [17, 43].
This movement allows for deconvolving the neutrino beam flux from the interaction cross-sections and detector responses, all of which are energy-dependent. All three of these effects are in addition to energy-dependent effects. By moving the detectors to different off-axis positions (changing the angle to

[10] For the following studies. The current design has 34 thin layers, 22 thick layers, and 24 double-thick layers.
[11] The magnetic field is always $\sim$perpendicular to the neutrino beam axis

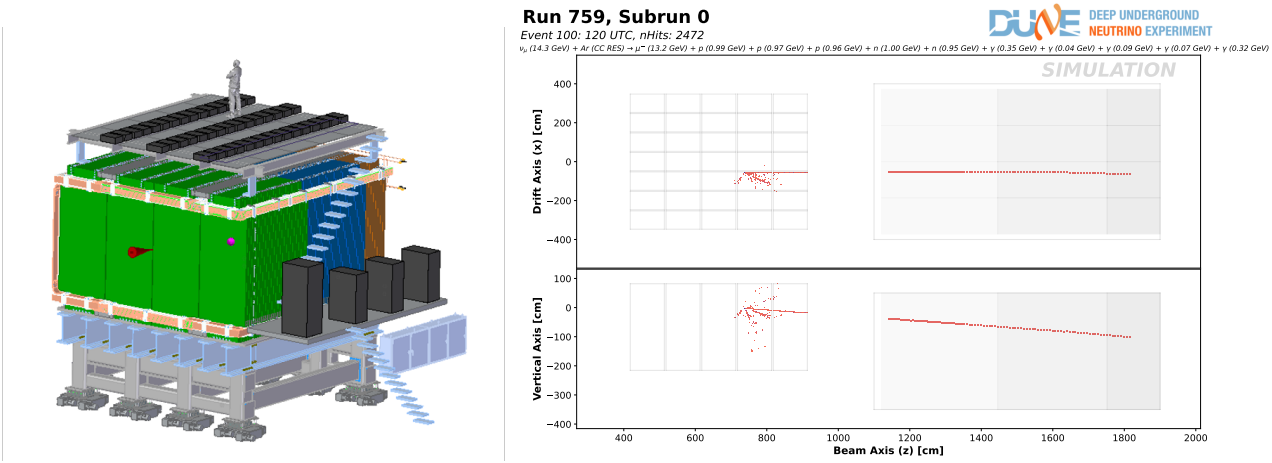

(a) TMS detector

(b) ND-LAr+TMS event display

Figure 29: 29a shows the range stacks in three longitudinal regions of increasing steel thicknesses (green, blue, red), the magnetization coils in light orange, and the DUNE-PRISM roller system at the bottom. The red cone indicates the beam direction [43]. 29b shows a neutrino interaction in ND-LAr (left) with an outgoing μ^- into TMS (right) (credit: L. Cremonesi)

the neutrino beam), the neutrino beam flux changes as shown in Figures 16 and 27b, allowing for the measurement of the influence of the neutrino energy directly. The different off-axis measurements can then be linearly combined, allowing a reproduction of the predicted FD oscillated flux. Doing so reduces the model dependence of the measurement of oscillation parameters.
Usually, this movement is done in tandem; however, for installation purposes, the two can also move separately. This movement is made possible by rails and motorized rollers, along with an energy chain that services the detectors at all positions. The movement is closely monitored by the monitoring system to precisely measure the detectors' positions and serve as a safety mechanism.

2.2.3.5 System for On-Axis Neutrino Detection

System for on-Axis Detection (SAND) is a magnetized tracking detector, surrounded by a calorimeter. It contains a liquid Argon target, and is meant to stay on the neutrino beam axis [43]. A sketch of the full detector is shown in Figure 30.

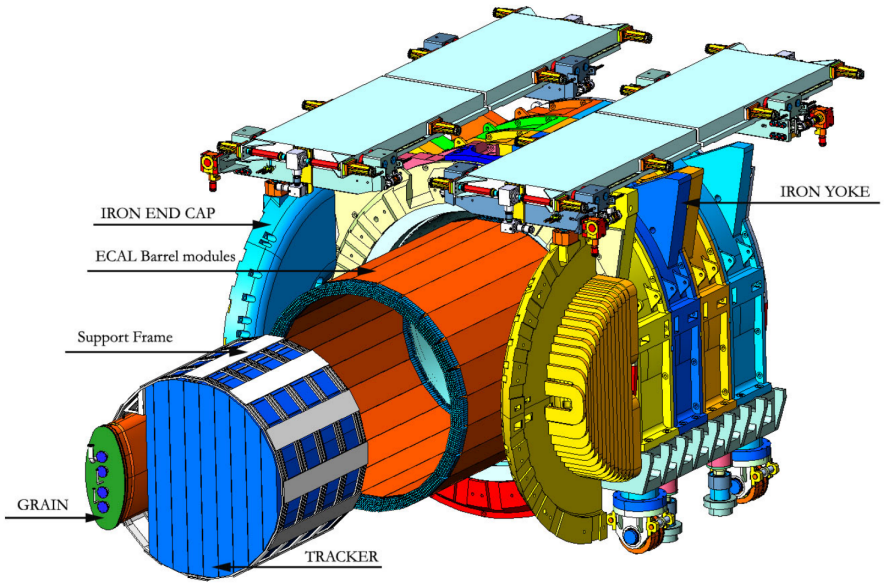

Figure 30: The SAND detector with (from inside to outside) the GRAIN optical LAr detector (green) and low density inner tracker (blue), the barrel electromagnetic calorimeter (orange), and the magnet yolk. The endcap yolk is shown in its open position in light blue and yellow, with the mounted endcap calorimeter facing outwards [43]

It contains an inner tracker consisting of straw tubes. These are arranged in an alternating pattern of

$\sim$ 5 mm thick planar nuclear targets (made from e.g. C, CH_2), transition radiators, and 5 mm diameter straw tubes up to 4 m long and arranged in two horizontal and two vertical layers with a density of 0.17 g/cm^3 (presenting $\mathcal{O}(1\%)$ of a radiation length).
The LAr target is provided by GRAIN. It is contained in a cryostat with a 148 cm (horizontal) and 49 cm (vertical) elliptical transverse profile with a length of 148 cm, holding about 1 t of LAr. Optical photons from scintillation are detected by arrays of SiPM matrices, enabling them to be matched to tracks within the inner tracker volume.
The calorimeter as well as the magnet for SAND are refurbished from the KLOE experiment[12]. The calorimeter is made from a lead-scintillating fiber matrix read out by photomultiplier tubes (PMT). It lines, as a barrel section perpendicular to the beam, the inner volume of the magnet with 24 modules of 23 cm (15 X_0) thickness with an inner radius of 4 m and 4.3 m in length. The endcaps consist of 32 vertical modules. For KLOE, the calorimeter achieved a $\sim$ 150 ps timing and $\sim$ 10% energy resolution for electromagnetic showers with less than 1 GeV.
The magnet surrounding the other parts is a superconducting solenoid producing an axial magnetic field of 0.6 T in a 4.8 m $\times$ 4.3 m cylindrical volume.

2.3 Details of Phase 2

2.3.1 Changes in Neutrino Beam Production

As mentioned in the staging plan of Phases 1 and 2, the beam power is planned to increase. This itself will happen in two main stages [37].
The first stage is the Accelerator Complex Evolution Main Injector Ramp and Target (ACE-MIRT) upgrade. In this era, the Main Injector cycle time will be reduced from $1.2 - 1.4$ s to 0.65 s and therefore increasing the beam power to 2.1 MW.
This requires a significant increase in voltage and electric power, which can be achieved only by enhancing power supplies, transformers, and feeders, increasing the size of service buildings, implementing additional cooling, adding more tunnel penetrations, and modifying the RF accelerator system. In addition, an upgrade to the Main Injector collimators is necessary. These steps will not be taken all at once, resulting in 1.6 MW in the second year of DUNE operation and gradual improvement thereafter.
The second stage is the Accelerator Complex Evolution Booster Replacement (ACE-BR) upgrade. In this era, the Booster synchrotron will be replaced to achieve beam powers above 2.4 MW and enable the accelerator complex to serve as a reliable platform in the future as well. The options for this are currently under investigation.

2.3.2 Changes for Near Detectors

2.3.2.1 Gaseous Argon Near Detector

In Phase 2, the plan is to replace TMS with a more capable detector [45]. Given the requirements for this phase, the most likely approach is to use Gaseous Argon (GAr). Using GAr yields a lower detection threshold than for LAr, which results in better particle separation as well as longer travel distances [34]. For a track length of 2 cm in LAr a proton of 46 Mev required, while it only needs 4 MeV in GAr.
On the other hand, the lower density of the gas ($\lambda \sim 90$ m) also means a lower neutrino interaction rate. To counter this, the GArTPC is planned to operate at a pressure of 10 bar to hold $\sim$ 1 t of GAr in the 5 m (diameter) $\times$5 m (length) drift volume. Research and Development (R&D) for the operating stability and gain are ongoing.
The readout is still under consideration, with plans to either use multi-wire proportional chambers, as used by the ALICE experiment, or GEMs. The multi-wire proportional chambers function well but still

[12] KLOE is a e^+e^- collider detector spectrometer operated at DAFNE, the ϕ-meson factory at Frascati, Rome. [33]

need to be tested on their long-term performance; the GEMs are currently in R&D [34]. The same goes for the readout electronics, which need to be cost-effective regardless of the number of channels.
Surrounding the GArTPC, which will serve as the tracker, will be a calorimeter responsible for neutral-particle (n, $\pi^0 \rightarrow \gamma\gamma$) detection. Given the large surface area around the TPC, it is important to balance the physics goals with the cost. A solution to this is to use a plastic scintillator sampling calorimeter as demonstrated by the CALICE R&D Collaboration. It would feature in a depth of about 44 cm 8 layers of 5 mm $\times$ 2.5 cm $\times$ 2.5 cm scintillator tiles in the inner part and 52 layers of 5 mm $\times$ 4 cm scintillator strips with copper absorber layers of 2 mm in between. The tiles are directly coupled to an SiPM, while the strips would be read out via incorporated WLS fibers and SiPMs. The copper in between ensures the compactness of the calorimeter as well as the energy and energy resolution.
To achieve the particle identification as well as the momentum resolution, the calorimeter and the GArTPC are planned to be in a uniform magnetic field of 0.5 T. The design for the superconducting solenoid is based on the solenoid for the MPD for the Nuclotron-based Ion Collider Facility (NICA) at JINR [45]. It is an integrated magnet design that uses the solenoid's vacuum vessel as the pressure vessel and the iron return yoke to support the flat end caps, eliminating the need for the usual domed heads. This allows the design to be cost-effective. The yoke is, in addition, asymmetrical to limit the material between ND-LAr and ND-GAr, making it a solenoid with a partial return yoke. A view of the full ND-GAr detector system is shown in Figure 31.
Outside of the magnet and pressure vessel is a space for a muon-tagging system to separate between μ and $\pi^{\pm}$. The plan is to have a single active layer out of scintillator extrusions, resistive plate chambers, or MicroMegas [45].
Currently unclear is the need for a potential photon detection system within the TPC, which might be implemented using LAPPDs or SiPMs. R&D is ongoing for this.

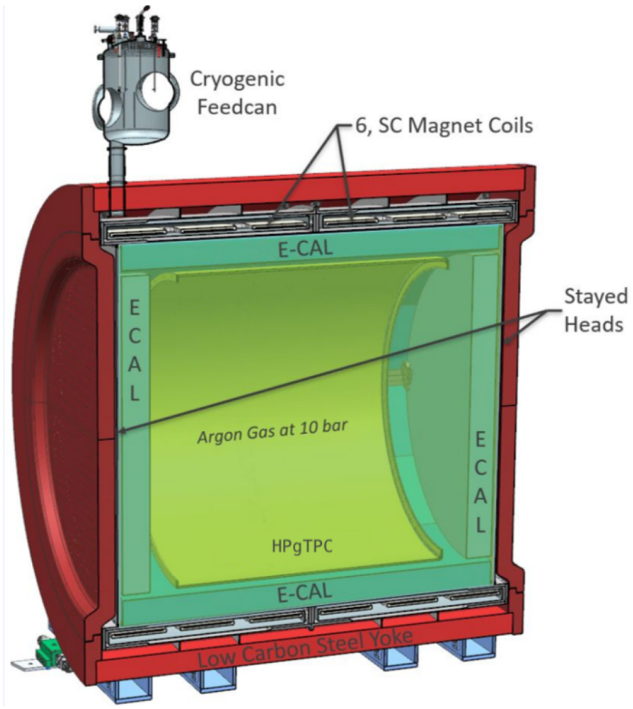

Figure 31: Cutaway view of the full ND-GAr detector system showing the High Pressure gaseous Argon TPC (HPgTPC), the calorimeter, the magnet, and the iron yoke. The detectors for the muon-tagging system are not shown [45]

2.3.2.2 Improvements to ND-LAr and SAND

While both ND-LAr and SAND are not replaced in Phase 2, R&D is ongoing for potential updates of both [34].
For ND-LAr, the options can generally be categorized into the need to empty ND-LAr or not. In the emptying case, potential updates focus on the optical detectors, including replacing the charge tiles with a ^6Li-glass scintillator, adding photosensitive dopants, and using radio-pure underground LAr. In the less

disruptive, non-emptying case, options include Xe doping, upgrading the off-detector electronics, adding a rock muon tracker at the front, and a calibration system based on ^{222}Rn injections. Whether any of these will be implemented and whether they are necessary is still under investigation.
For SAND, an update is foreseen, substituting all GRAIN matrices with backside illuminated SiPMs that are currently in the R&D state. This update would enhance light collection, improve fill factor, and enhance the anti-reflective coating on the entrance window.

2.3.3 Changes for Far Detectors

As previously described, the FD will be expanded by two modules to achieve the required exposure.

2.3.3.1 Third module — Vertical Drift

For the third far detector module, another VD module is planned. As mentioned before, this simplifies detector construction and installation, reducing overall cost compared to the horizontal-drift modules of Phase 1 [34]. The drift medium will still be LAr.

2.3.3.2 Fourth module — "Module of Opportunity"

The fourth module is planned to target new physics with more advanced technologies [34] and is still in the R&D stage; therefore, it is referred to as the "Module of Opportunity". The focus is on optimizing the readout techniques for charge and light. Still, potential LAr doping or a hybrid approach[13] to detect Cherenkov and scintillation light are also considered for a low-energy physics program.

[13] non-LArTPC

3 Detector optimization for The Muon Spectrometer

3.1 Introduction

This chapter explains TMS in more detail and discusses a study to optimize the module orientation plan, as well as the procedure to support this study.
First, the purpose of the detector is explained as well as the implications on the detector geometry design. After this, the simulation and reconstruction flows are discussed and developed in detail, as they are the key elements enabling the optimization study. Following this explanation, the effect of the module orientation plan and the studied geometries is explained. To compare the different geometries, metrics for comparison are developed and used. After the broad scan study, a small fine-tuning study is performed and evaluated.

3.1.1 Requirements for ND and TMS

During Phase 1, with a data taking period of about 200 kt · MW · yrs[14] and an expected equal split between neutrino and anti-neutrino modes, the statistics of the FD are sufficient to resolve the neutrino mass ordering at $> 5\sigma$ within a few years, to make a world-leading measurement of Δm^2_{32}, and to achieve 3σ sensitivity to maximal CP violation [44] in the longer run.
The ND needs to confirm the neutrino event rate as well as constrain systematic uncertainties, so that they do not limit the necessary precision for the neutrino oscillation measurement. Therefore, the ND needs to match the statistical uncertainty of the FD as well as determine the charge, given the limited capabilities of ND-LAr in this regard [44].
Similar to the charge, the FD is expected to have a momentum resolution of $\sim$ 5% for muons in the energy range important for the neutrino oscillation physics of 0.5 to 5 GeV. This sets a design goal for the energy resolution of the ND-LAr-TMS combination in this energy range for muons [44].
Summarizing this and deriving the overarching requirements for the ND-LAr-TMS combination yields [44]:

- The ND measurements need to be transferable to the FD and need to be usable to predict the observed neutrino spectrum at the FD, including backgrounds.
- The ND data needs to be usable to measure the neutrino flux and to make measurements with different fluxes via off-axis movements.
- ND-LAr and TMS both need to be operable in the expected high-rate environment and monitor the time variations in the neutrino beam.
- The data must be usable to constrain the neutrino interaction model in LAr.

These translate into measurement and capability requirements for the design of TMS. The two measurement requirements for TMS are the ability to move as part of the DUNE-PRISM system and to enable measurement of the wrong-sign background in Reverse Horn-Current (RHC) running to 25% [44]. An excerpt of the capability requirements for TMS with respect to this work are [44]

- TMS needs to measure the range of forward-going muons with an energy at the vertex in ND-LAr above 1 GeV and up to 4.5 GeV, to reconstruct them without a gap in kinematic coverage.
- TMS needs to measure the energy for forward-going muons that stop within TMS with $<$ 5% resolution, as this is an essential component of the reconstruction of ν_μ CC events.
- TMS needs to have sufficient 2D spatial resolution to match forward-going muons that enter its front face with the corresponding track in ND-LAr.

[14] This translates to about 10 years with some assumptions about the schedule and beam intensity.

- TMS needs to determine if a muon entering its front face stops within the detector or exits, as the muon energy is determined by range.
- TMS needs to separate between μ^- and μ^+ to measure the μ^- contamination in RHC to $<$ 25% of itself.
- ND-LAr and TMS need to have a combined muon energy resolution of $<$ 10% for the energy range of $\sim$ 1 to 5 GeV, to precisely measure the neutrino spectrum.

3.1.2 TMS Detector Design

TMS is, at the point of writing this, in the process of being redesigned to fulfill the described requirements.[15] It is vital to have a magnetic field in a way that allows for charge identification to distinguish between μ^- and μ^+, as well as having enough steel to stop the muons in the expected energy range. These two factors are outside the scope of this work and, in the following, are assumed to be fixed to a magnetic field of 1 T in the y direction, as well as the $50-34-8$ steel layout described previously.[16] The direction of the magnetic field results, owing to the $\vec{v}\times\vec{B}$ in the Lorentz force [4], in a deflection of incident charged particles along the x axis. The coordinate system is z approximately as the beam direction[17], x as the left-to-right direction perpendicular to z-axis, and y as the down-to-up direction perpendicular to both x and z.
As with the energy resolution, spatial resolution for matching tracks with ND-LAr, containment of muons, and charge identification are highly interconnected with the reconstruction of the individual muon tracks; hence, it is necessary to study the performance of TMS with different options of the detector geometry. In this work, this is done with the module orientation plan in mind, which influences the amount and precision of available information in the x and y directions of TMS.

3.2 Simulation Flow

The interaction of neutrinos from the neutrino beam at the ND complex is simulated using a multi-step approach that splits the process into generation, particle propagation, and detector response stages. Each stage uses a description of the ND geometry in the gdml format.
The first stage generates the neutrino interactions using Genie version 3.04.00. Here only neutrino interaction vertices within the fiducial volume of ND-LArThe exact volume is called ArgonCubeDetector75 and contains all the 35 ND-LAr modules as well as some steel on top, volume of x = [$-$350.0 cm, 350.0 cm], y = [$-$218.191 cm, 124.233 cm] and z = [415.7559 cm, 918.2441 cm]. are generated. This is done due to limitations in computational resources. Subsequent optimization work will enable generation across the entire ND complex, enabling future detailed studies of backgrounds from particles originating outside ND-LAr.
In the second stage, particle propagation through detector materials is simulated using edep-sim[18], a toolkit that enables straightforward interfacing with the GEANT4 software (version 10.2). Afterwards, the multiple output files from the energy deposition simulation (edep-sim, for short) are merged into a single file during the hadd step.
At the generation stage, neutrino interactions are produced one by one with an arbitrary timing structure. It is therefore necessary to perform a spill-building step, in which the timing information for each interaction is modified so that the events are organized into 'groups' with sizes reflecting the beam intensity. Within each group, the timing structure reflects that of the neutrino beam, including the splitting

[15] The results of this study also influence this process.
[16] There will be changes to the magnetic field strength and amount of steel, as well as the distribution of the steel, in the future. This will then require a re-evaluation of some of the other components of the design.
[17] The beam is tilted slightly downwards compared to the actual z-axis of the detector.
[18] Energy Deposition Simulation

into 'buckets'.
The full simulation flow is shown in Figure 32. The geometry used in the simulation for this work is limited to a rough detector layout, excluding WLS fibers, SiPMs, and electronics within the detectors.

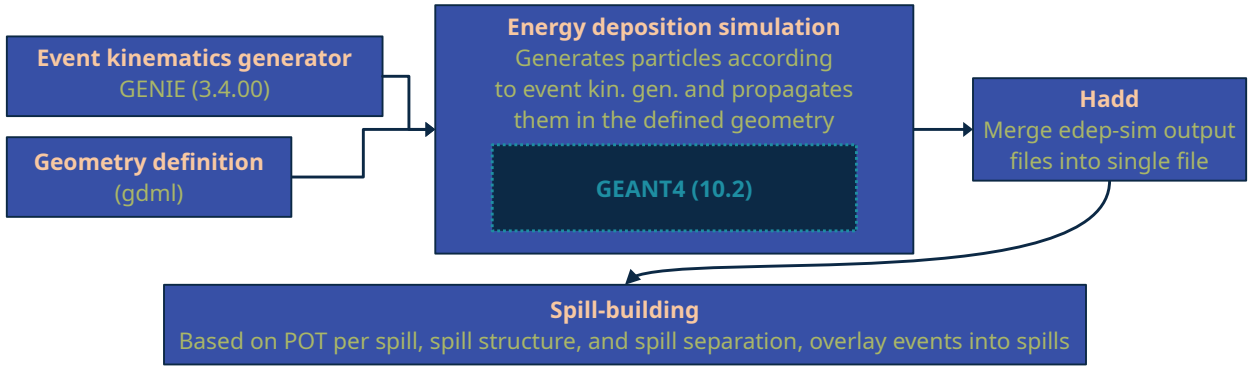

Figure 32: Flow chart of the simulation flow used for TMS. GENIE performs the physics simulation that generates neutrino interactions, the event kinematics generator. These events, along with the detector geometry definition, are then passed to the energy-deposition simulation, which uses GEANT4. The output files of this step are condensed in the hadd step before overlaying the events into spills

3.3 Reconstruction Flow

The reconstruction for TMS consists roughly of three primary parts. The first part is grouping hits by time in the time-slicing step. This is followed by the pattern recognition shown in Figure 33. There are multiple steps within the pattern recognition, which are explained in detail in the following sections. The last part is the track reconstruction, which employs a Kalman filter to fit the tracks found during the pattern recognition.

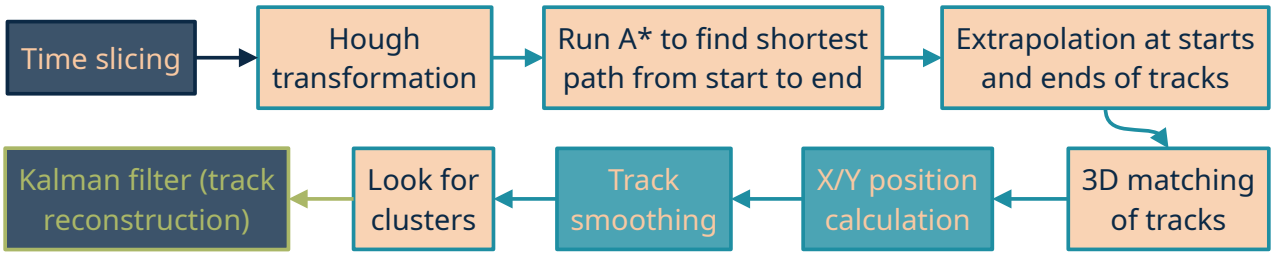

Figure 33: Flow chart of the reconstruction flow used for TMS. The main steps are the time slicing, the pattern recognition steps (shown with nude and light blue colors), and the track reconstruction step via the Kalman filter

The following sections (3.3.1 to 3.3.3.3) are adapted in large parts from [46].

3.3.1 Time Slicing

The time slicing algorithm is based on the one used by MINERvA [47]. First hits are grouped or ordered by their respective times. Starting from the start time of a spill, a 10 ns sliding window is then used to add up the respective hit energies in this window. When the summed energy goes above 10 MeV, the algorithm starts a (new) time slice with all the hits in the window. It keeps adding all hits to this time slice until the sliding-window energy drops below 5 MeV.
The minimum time slice size is 19 ns to avoid cutting too small. In addition, the rolling window stops slightly after the end of the spill to account for late hits. All hits not associated with a time slice are

bunched together in the catch-all time slice 0. The reconstruction is then presented with hits grouped into individual time slices instead of full spills, which reduces confusion from pileup. A demonstration of this can be seen in Figure 34. The plot shown is from after the complete reconstruction and therefore does not precisely reflect what the time-slicing algorithm sees. The number of hits going into the time slicer is, in reality, much higher, as the hits here are those sorted into tracks based on pattern recognition. For demonstration purposes, though, the shown plot is sufficient.

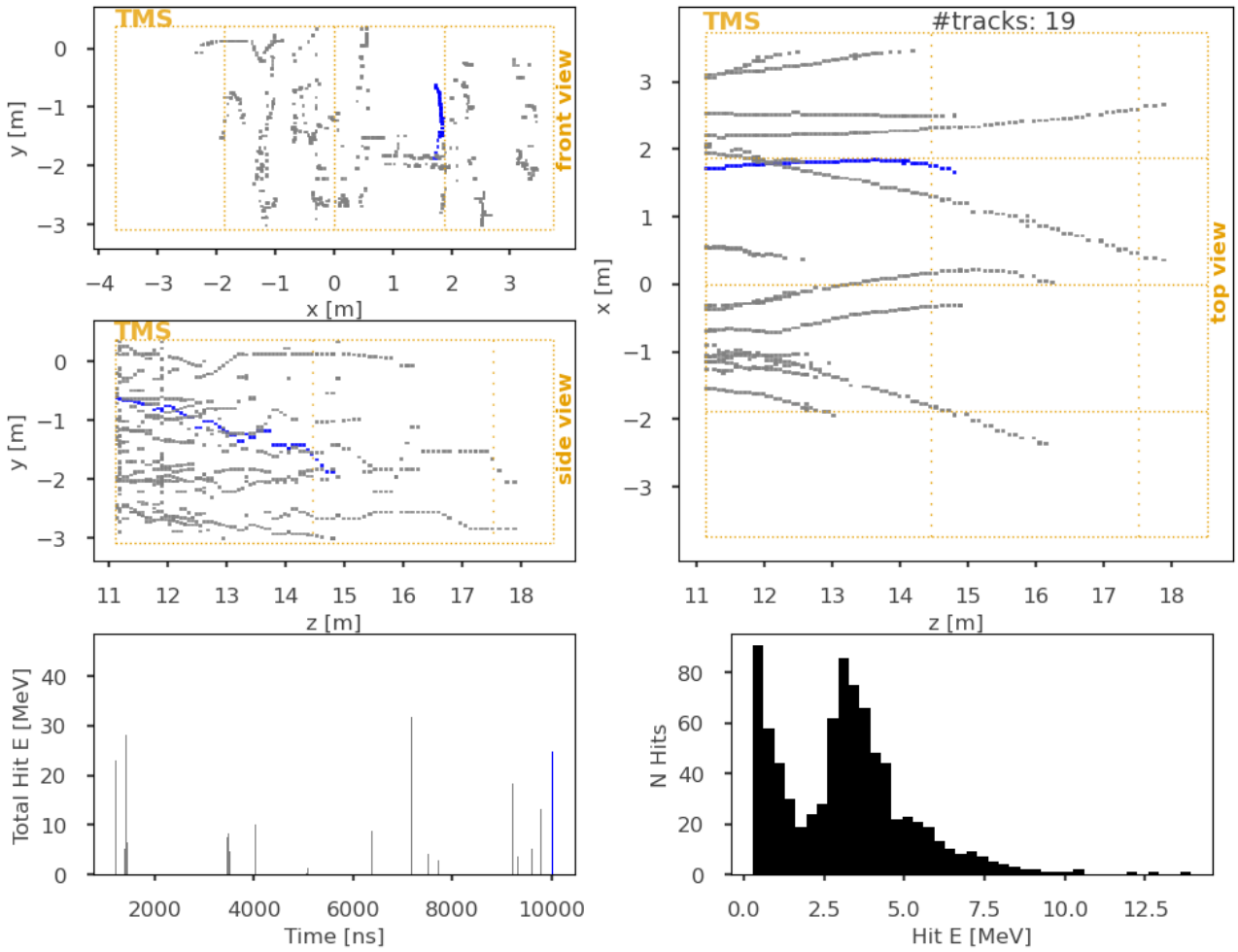

Figure 34: Demonstration of the time slicing. Shown is an example spill with one track selected (blue) to highlight the result of the time slicing. The different tracks can be seen in a top, side, and front view as well as the time and energy of the respective hits

The parameters used by the time slicing algorithm are configurable. The parameters are chosen to balance two effects. First, reduce the number of cases where two or more interactions are placed in the same time slice, resulting in pileup. Second, to maximize the amount of visible energy from single interactions captured in single time slices. These effects are quantified with cleanliness (Eq. 12) and completeness (Eq. 13) respectively,

$$\text{cleanliness} = \frac{E_{\text{vis}}^{\text{primary vertex}}}{E_{\text{vis}}^{\text{all vertice}}} \tag{12}$$

$$\text{completeness} = \frac{E_{\text{vis}}^{\text{slice}}}{E_{\text{vis}}^{\text{spill}}} \tag{13}$$

where the primary vertex is the vertex with the most visible energy in the spill. Optimizing for completeness and cleanliness is a trade-off: making the time slicer more aggressive reduces pileup but increases the chance of splitting a single event into two time slices. Several parameter sets were tested, and the current parameters were chosen because they achieve a balance between high completeness and clean-

liness (see Figure 35).

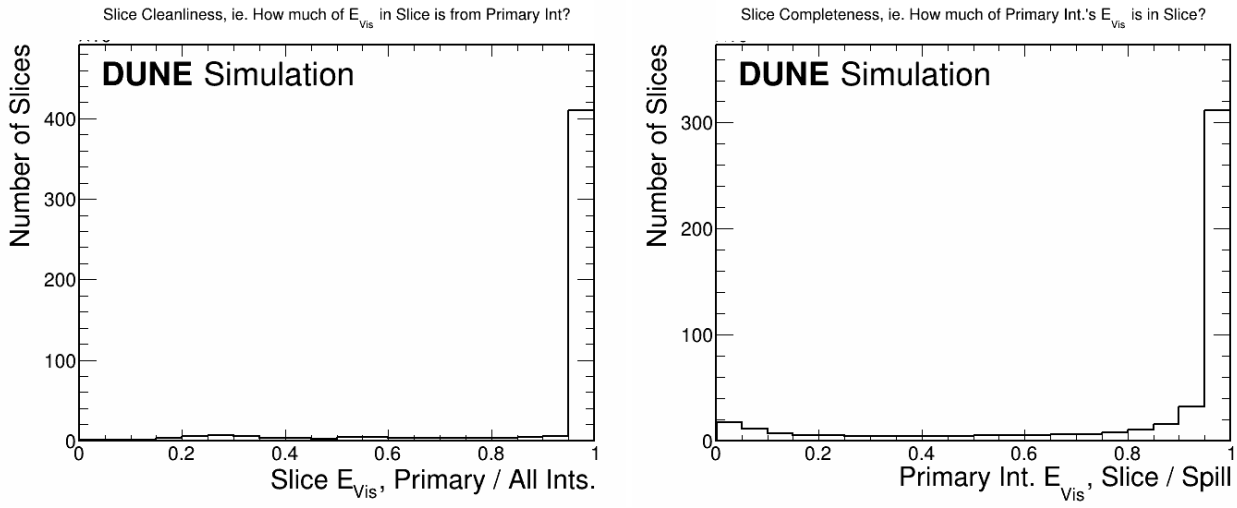

(a) Cleanliness

(b) Completeness

Figure 35: Slice cleanliness (Eq. 12) and completeness (Eq. 13) using the current time slicer parameters for an RHC full-spill simulation (but without rock muons). For completeness, the slice 0 is also included, which corresponds to the slices with very low completeness

3.3.2 Pattern Recognition

This section will describe the pattern recognition. The different steps were depicted in Figure 33, with the pattern recognition steps in nude and turquoise. The steps are now explained in more detail below.

3.3.2.1 Hough Transformation

A Hough transformation [48] takes a point in image space and transforms it into a line in parameter space, as one can see from Figure 36. Image space spans all x and y[19] coordinates while parameter space spans all slopes and intercepts.

A feature of the Hough transformation is that all points that lie on a single straight line in image space transform into straight lines in parameter space with a single point of crossing, as shown in Figure 36. This point in parameter space represents the common slope m and intercept c of all points in image space and provides a way to find this line without performing a fit.

Here, this is implemented using the x- and z-positions of hits. For all allowed slopes [20] the corresponding intercept is calculated with $c = x - m \cdot z$.

It is checked whether this intercept is allowed by ensuring it is smaller than a certain threshold, as tracks are only expected from the front face of TMS.

With the intercept calculated, the corresponding bin in a uniformly binned two-dimensional array is determined. This is done by first checking whether the input intercept is too high, then determining the bin using Equation 14. In this way, the bin is determined, and the content is increased by one.

$$\#bin = (c - c_{min})/c_{width} \tag{14}$$

This procedure is repeated for all hits, and the bin contents are raised accordingly.

To determine the Hough line now, the bin with the highest content needs to be found. The final intercept

[19] In TMS coordinates, x is the x direction for the stereo case and the y direction for the X case, and y for both cases, the z direction.

[20] The values were chosen to reflect the underlying detector geometry.

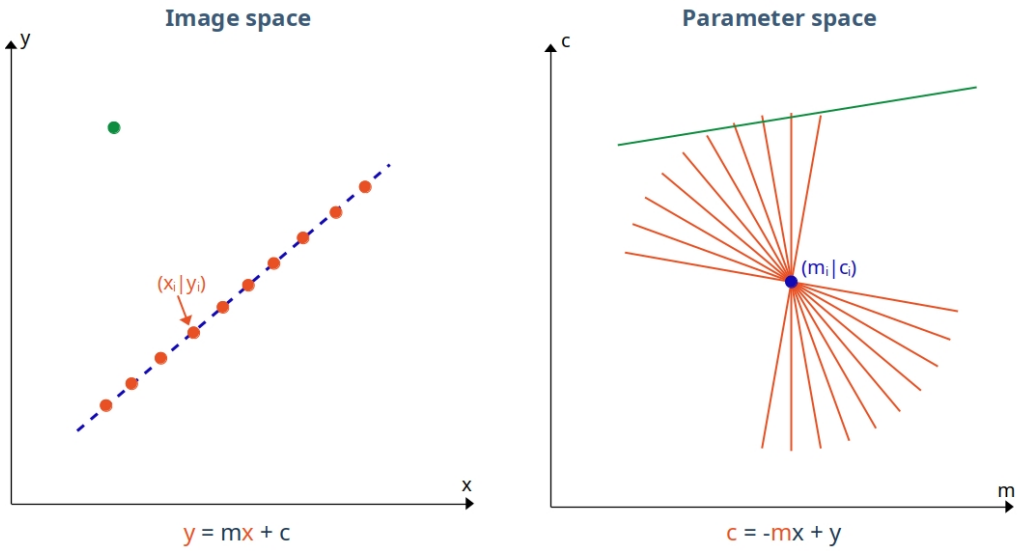

Figure 36: Illustration of the Hough transformation from image space to parameter space. A point (shown in green) in image space transforms into a line (shown in green) in parameter space, representing all straight lines crossing through this one point. Points (shown in orange) on a straight line (in blue) in the image space therefore share one crossing point (in blue) in parameter space, representing the slope m_i and intercept c_i of the 'connecting' line in image space

and slope are then calculated with Formula 15 respectively.

$$min + \#bin \cdot (max - min)/n \tag{15}$$

With this intercept and slope determined, the group of potential hits is now iterated through. For each hit, the z position, along with the slope and intercept, is used to calculate the theoretical x position, which is then compared to the actual x position. If both x positions agree within a scintillator bar width (36 mm), the hit is moved into the group of track hits.

3.3.2.2 A* Algorithm

The A* algorithm [49] is an additional method of creating a path or track of hits, but compared to the Hough transformation, it does not rely on the hits being in a certain shape (for our implementation, those are straight lines). By using two different costs that represent different distances for potentially adding hits, the A* algorithm connects hits between the given start and end points. A simple illustration of the algorithm is shown in Figure 37.

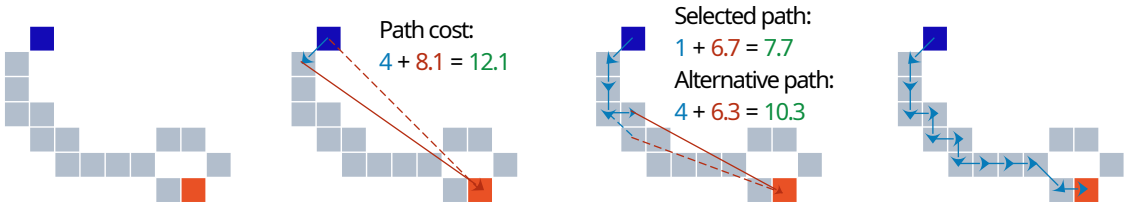

Figure 37: Illustration of the A* algorithm. On the left, the potential path is shown without any connections. The start cell is shown in blue, and the end cell is shown in red. From the start cell, the algorithm works towards the end cell by choosing the lowest sum of the heuristic cost and the connection or ground cost

In this implementation, the connection of hits is limited to the interval between the start and end of the Hough transformation output.
As mentioned, the A* algorithm works with two different costs. The first is the heuristic cost, which represents the distance to the end cell. Equation 16[21] shows how the heuristic cost is calculated.

$$Cost_{heuristic}(\mathbf{A} \rightarrow end) = \sqrt{(x_{\mathbf{A}} - x_{end})^2 + (z_{\mathbf{A}} - z_{end})^2} \tag{16}$$

A cell is here the geometry-independent phrasing for hits and represents the scintillator bar area (3.6 cm$\times$ 1.6 cm). The heuristic cost is an inherent number of each cell[22] and does not change throughout the process.
The second cost is the connection or ground cost. It represents the distance to the next potential cell and is computed for each connection using Equation 17.

$$Cost_{Connection}(\mathbf{A} \rightarrow \mathbf{B}) = \left((x_{\mathbf{A}} - x_{\mathbf{B}})^2 + (z_{\mathbf{A}} - z_{\mathbf{B}})^2\right)^2 \tag{17}$$

The algorithm then calculates the shortest path by deciding iteratively which connection to make next, with the next chosen cell having the lowest sum of both costs.[23] In this way, it iteratively works through all available hits and finds the most efficient path from a starting cell to an end cell.

3.3.2.3 Extrapolation

Due to the A* algorithm only connecting hits in between the first and last Hough hit, there exist hits outside that will not get picked up on. This is especially the case at the ends of tracks, which tend to curve much more because the particle has lost most of its energy and is curved more by the magnetic field. Because the Hough transformation uses a straight-line implementation, those hits are usually not chosen as the end of a track and are left out.
The extrapolation attempts to address this issue by looking beyond the start and end points of the simple tracks generated by the Hough transformation and the A* algorithm, and by adding nearby hits. An illustration of the method is shown in Figure 38.

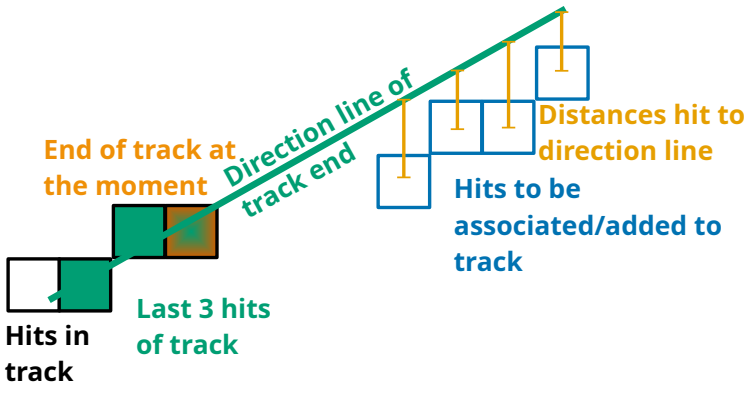

Figure 38: Illustration for the extrapolation method. From the last three hits of the track (shown in green), the direction is determined in the form of a line. All potential new candidates (blue) for the track have to be within a certain distance from this line at the respective z position (orange)

The way this is done is by determining the direction of the last part of the track by calculating a direction line from the last/first three hits of the track and then checking how far away potential hits are from this

[21] x is here again either the x direction in the stereo case, or the y direction in the X case.
[22] Indicated by A in the equation.
[23] This is not how an A* algorithm is usually implemented, and the current implementation will hopefully be checked and fixed in the future.

line. If the potential hits are within 4 (for the back) or 2 (for the front)[24] scintillator bars from the line, they are added to a group of potential hits for further investigation.
For potential hits in the group, it is then checked how far they are from the track's start or end. This is done with the A* heuristic cost.
There are two essential distances to add potential hits. The first one is the maximum distance from the end or start of the track to the closest potential hit. This is to prevent other particle tracks from being falsely added to the track. The second distance is the limit of adding potential hits to the track. This distance prevents adding hits too far away from the actual track. The total distance up to which potential hits can be added is the sum of both distances.
All potential hits that are added in this way are pushed into the existing track.

3.3.2.4 Status after Hough transformation, A* algorithm and Extrapolation

Up to this point, the pattern recognition runs separately on each orientation (U, V, and (with enough X hits) X. See details in Section 3.4.1). This allows (especially for the X modules) hits from the same orientation, with their equivalent geometry and layout, to be grouped into tracks, making the overall pattern recognition easier and reducing the computational effort.
The result of these steps can be seen in Figure 39. The different lines represent the tracks for the different orientations (U, V, and X), while the gray hits show the underlying truth information from the simulation. In addition, the start and end points, as well as hits clustered, can be seen.

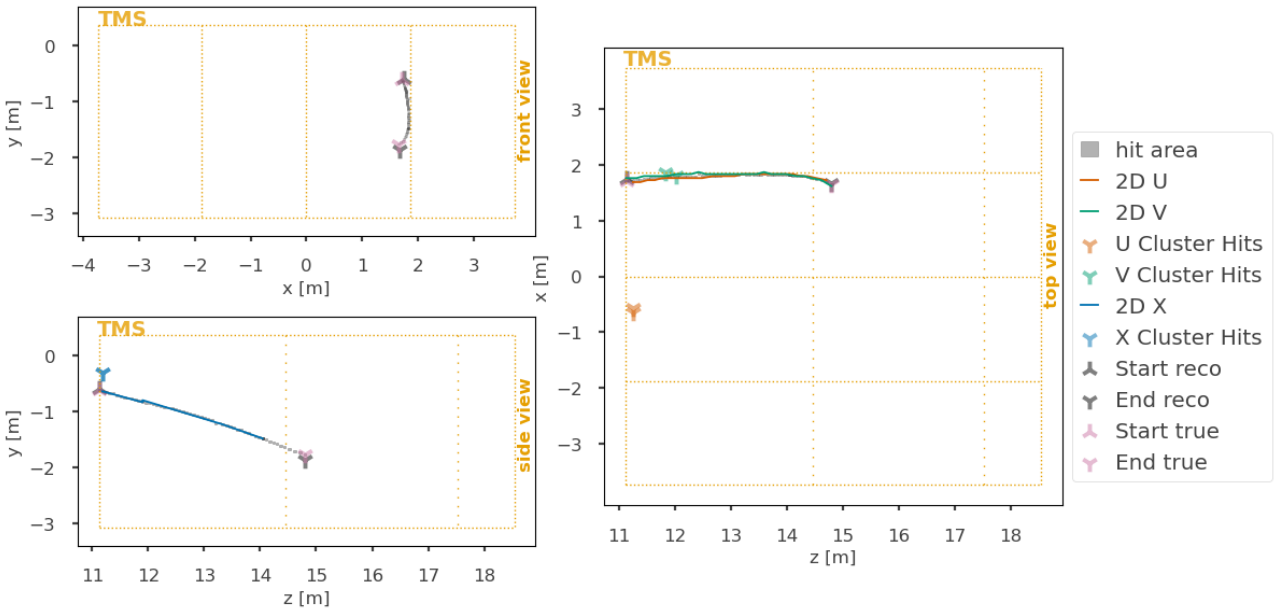

Figure 39: Event display with the separate tracks for different orientations for a geometry with U, V, and X modules. The top-left plot shows the front view of TMS, the bottom-left the side view. The plot on the right shows the top view. The dotted orange lines hint at the positions of the different steel plates (densely dotted) and thicknesses (less densely dotted). The individual hits are shown, as well as the connected tracks in two dimensions (2D lines). Also shown are the reconstructed and true start and end points of the tracks.

3.3.2.5 3D Merging of Tracks

As stated above, the pattern recognition so far runs independently for the different oriented scintillator layers. This means that the layers which are tilted by +3°are reconstructed separately from the layers tilted by −3°or the 90°(horizontal) rotated layers. This step is useful first and foremost because it allows

[24] These values were chosen due to the expected curvature of a particle in the positive z-direction traveling at the start and end of a path, which is higher at the end than at the start.

the employed reconstruction steps to be ignorant of the underlying detector geometry, ensuring that nearby hits remain nearby. In this way, changing the tilt angle or switching from a stereo layout to an orthogonal layout does not change the reconstruction.
Unfortunately, because scintillator bars are used instead of more costly tiles, the information about the hits is only two-dimensional, with an additional timestamp. To obtain three-dimensional information, we therefore need to merge the two separately reconstructed tracks and use the geometry to calculate the *y* positions of the hits/tracks.
In general, one wants to merge only tracks that are actually close. This is ensured by checking that the tracks are close at the start and ends, in both time and space. The current values for this are within three layers in *z* and within 12 bar widths in *x*. The seemingly high value of *x* is necessary to ensure that hits can be matched across the entire height of the detector. For the time constraint the tracks have to be in the same time slice and the starts and ends should have occurred within 16 ns for the two stereo orientations and within 40 ns for the horizontal orientation, taking into account the different distances to the SiPMs for this, that the light has to travel in the scintillator material.
Because the pattern recognition can struggle to pick up the correct end point (or, in rare cases, the start point), we still want the tracks merged, so a strike rule is employed. With this, the algorithm allows for one exemption from the four merging conditions (two for the front for time and space, and equivalently for the back).
In Figures 40 and 41, in-depth sketches show the full logic behind the merging.

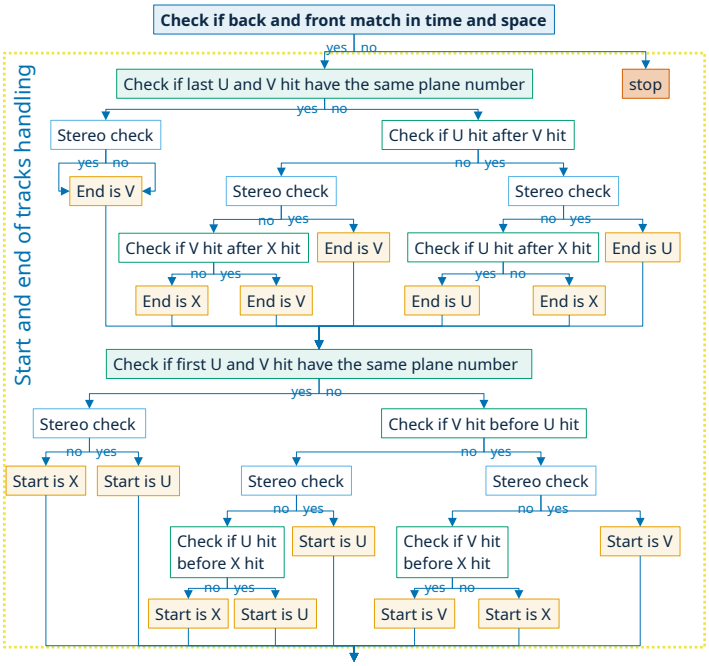

Figure 40: A detailed decision tree showing the logic for assigning the start and end of the merged 3D track. After an initial check to ensure that the front and back of the tracks from different module orientations match in space and time, the first and last hits of the combined track are determined. These are then set as the start and end of the combined track

In the case that the tracks are compatible with each other, a new 3D track object is created containing all hits from both simple tracks, and the *y* coordinates for the stereo hits are calculated, as well as the *x* coordinates for the X layer hits determined.

3.3.2.6 Calculation of *y* Positions

In the absence of hits from X layers, for the *y* coordinate to be calculated, one needs one hit each from both stereo orientations. Therefore, the calculation of *y* positions is implemented during 3D track merging. This entails that two hits share the same *y* coordinate as a calculation pair.
The calculation itself is based purely on the detector geometry and depends entirely on the tilt angle. An illustration showing the tilt and the limitations of this method can be seen in Figure 42.

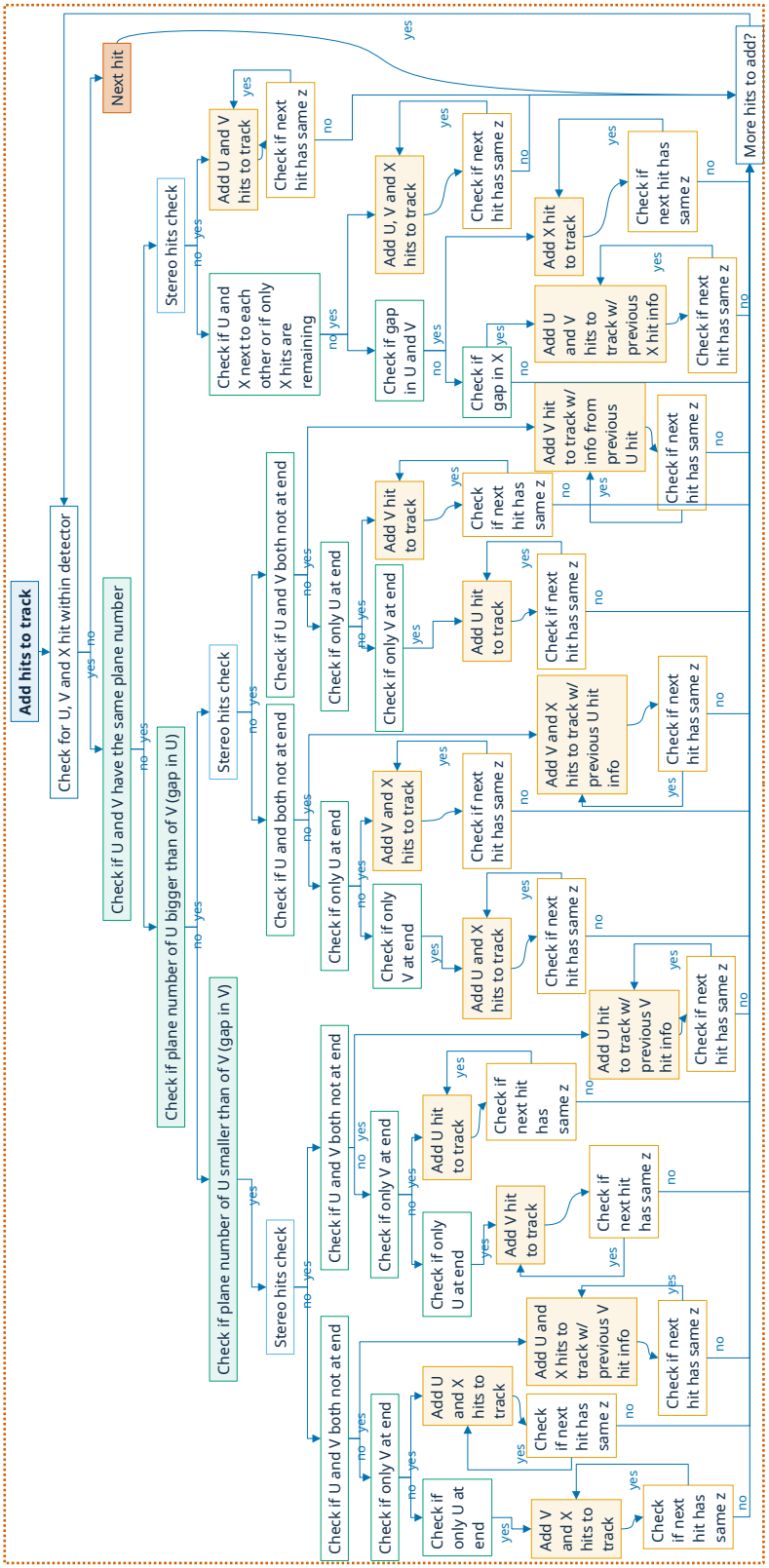

Figure 41: A detailed decision tree showing the logic for adding all hits in between the start and end hits of the U, V, and X tracks, respectively, to the merged 3D track. For hits within the detector volume, pairs from different module orientations are built to calculate the *y* position for hits from stereo layers, the *x* position for hits from X layers, and to average the *x* position of hits from U and V layers. Looping through all hits from the 'simple' tracks, also gaps in tracks per module orientation can be handled when building these pairs

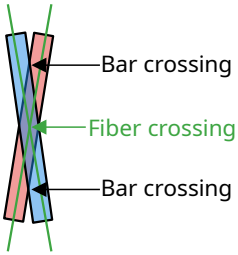

Figure 42: Illustration showing two tilted scintillator bars (red and blue) with an overlap in purple. The angle is exaggerated for better visibility. This overlap can be used to calculate the y position of the fiber (green) crossing of the hit bars

In general, the way to calculate the y position is to use an anchor point in the y direction and subtract $0.5 \cdot \tan(90° - 3°) \cdot |U_x - V_x|$ from it. The latter part describes the distance between a U and a V hit in the x direction.
Since the anchor point is in the middle of the detector, we need to determine beforehand whether we are above or below it. This is done by comparing the x positions of the U and V hits. If the U hit is further in x than the V hit, the hit is above the anchor point, otherwise below.
It is also checked if the distance makes sense in general, meaning that if the distance is bigger than 167.0 mm, therefore going beyond the detector boundaries, the y position is automatically set to either the top (above) or the bottom (below) of the detector.
For both cases[25] the formula for the y position is then as seen in Equation 18 with Y_{mid} being the middle point in y in mm.

$$y = Y_{mid} \pm 0.5 \cdot \tan\left(90° - 3°\right) \cdot |U_x - V_x| \tag{18}$$

A vital thing to keep in mind is that the actual hit can have happened anywhere in the rough area of the crossing of the two bars. This leaves us for the $\pm 3°$ tilt with an uncertainty approximation from the crossing of the fibers to the top crossing of the bars of 33.83 cm.

3.3.2.7 Track Smoothing

The reconstruction of y positions in the stereo detector leaves the tracks with non-physical jumps in y positions. These positions represent the best y-estimate given the bar pair that the particle hit, see Figure 42. However, the particle must be traveling in a smooth path. So the particle must be close to the edge of the bar when it transitions from one bar pair to another, i.e., from one y position to another.
The track-smoothing algorithm first finds all transition points where the y position jumps from one bar pair to another. From there, it assigns the average position to both hits. Then, it assumes a smooth yz slope between those points to assign new y values to all hits between these transitions. For the beginning and end of the track, the average track slope is used. The logic is shown in Figure 43.
The track smoothing reduces the uncertainty in y positions from a FWHM of about 20 cm to 12 cm. It also improves the Kalman filter step a bit as the inputs are closer to the physical reality.

3.3.2.8 Clustering

At the end of the pattern recognition, all hits that have not made their way into tracks are passed to a clustering algorithm. Clusters are compared to tracks more 'blob'-like and can group hits from e.g. showers together.
Here, the hit density-based "DB scan" clustering algorithm [50] is used. An illustration of the algorithm can be seen in Figure 44.
The algorithm starts by looking at each point to count the number of nearby points. Close-by means here within a certain distance. This can be seen in Figure 44 (a)-(j). In (b), a single point is chosen, in (c) the distance circle is shown, and in (d) the close-by points are highlighted. This is then repeated in (e) with a new point. In (h), the number of nearby points is too low for this point to qualify as a core point, which requires a certain number of neighbors. This is also the case for (i). Those two points are then shown in

[25] Below the anchor point: +, above the anchor point: −

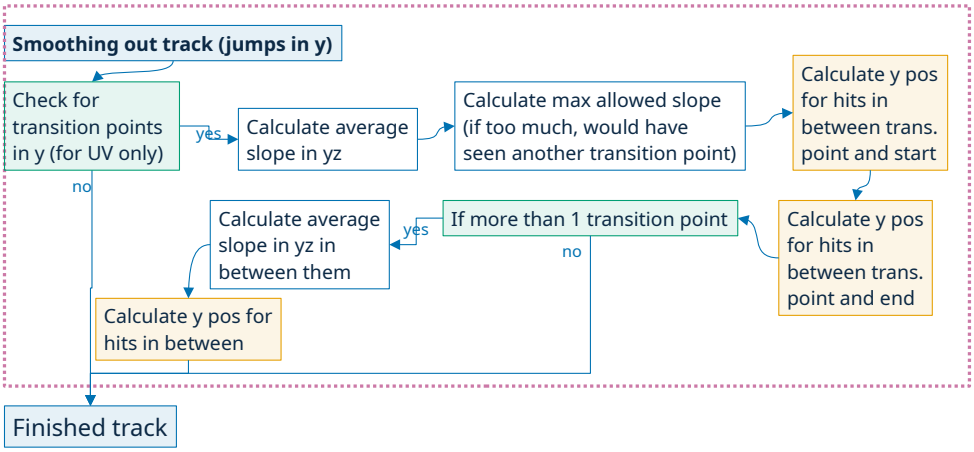

Figure 43: A detailed decision tree showing the logic for the track smoothing. The algorithm checks for jumps in the *y* position of hits and smoothes the *y* position of hits in a track, assuming the track follows a straight line in the *y* direction

(j) in a different color than the other points that have been determined to be core points before.
In (k), all determined core points are visible. From those, one is chosen in (l), and all neighboring core points are added to a cluster in (m). Iteratively, for all added core points, their neighboring core points are added as well, as can be seen in (n) and (o).
This continues until no more neighboring core points can be added, as in (p). In the next step (see (q)), all neighboring non-core points are added, but not their neighbors. This then concludes a single cluster as can be seen in (r).
In the case of more core points existing, the process of creating a cluster and adding the core and non-core points to it is then repeated as indicated in (s).
The final result with – in this example two – clusters can then be seen in (t).
To employ this algorithm, it is necessary to define appropriate values for classifying a core point and a nearby point. In Figure 45, one can see in an example the influence of the distance parameter.
This algorithm is then run on all hits that have not been added to tracks. Mostly small clusters and large tracks remain at this point. The latter have been determined in 3D as well, while the clusters stay in 2D at this point.

3.3.3 Track Fitting with Kalman Filter

The Kalman filter uses hit information from the detector, along with knowledge of the underlying physics, to converge on a series of states that approximate the particle's true path. Implicit are the assumptions that the particle does not 'loop' in the detector, and that all uncertainties are uniformly distributed. For each step, the previous state φ_{z-1} is used to produce an *a priori* estimate for state $\tilde{\varphi}_z$, and similarly an estimate for the associated error matrix is also created from the previous matrix. The detector information is then used to update the estimated quantities, allowing us to obtain φ_z from $\tilde{\varphi}_z$. Note on notation: All matrices are bolded. States are labeled with an index $_z$, where each index corresponds to a scintillator layer. Estimated or *a priori* quantities are marked with a $\tilde{}$ above. The uncertainties are assumed to show a Gaussian behavior.

3.3.3.1 Kalman State

The Kalman state at layer z, is a vector $\varphi_z = \left(x, y, \partial_z x, \partial_z y, q/p\right)$ comprising the position (x, y), direction $\left(\frac{\partial x}{\partial z}, \frac{\partial y}{\partial z}\right)$, and the 'stiffness' (q/p) of the track, where q is the particle charge and p is its momentum. Each Kalman state φ_z is associated with a corresponding error matrix $\tilde{\mathbf{C}}_z$.

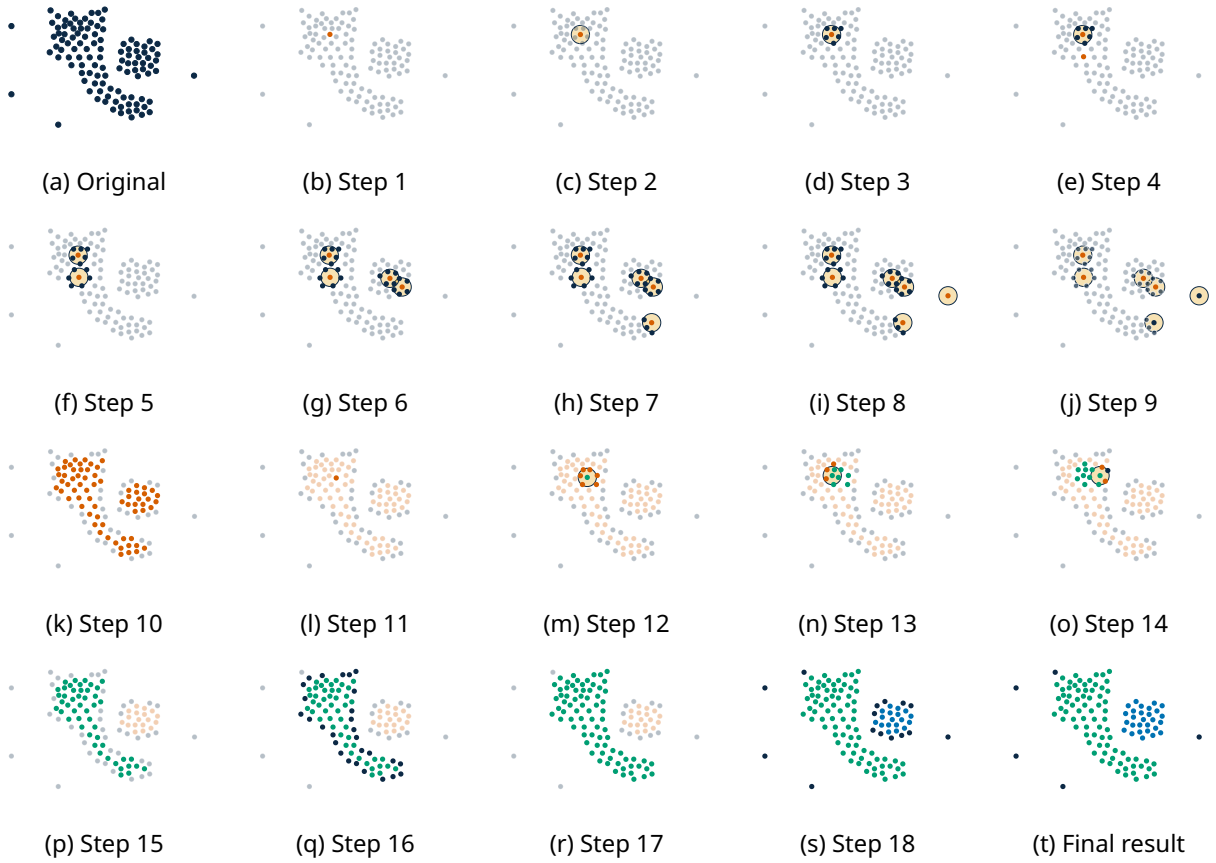

(a) Original (b) Step 1 (c) Step 2 (d) Step 3 (e) Step 4

(f) Step 5 (g) Step 6 (h) Step 7 (i) Step 8 (j) Step 9

(k) Step 10 (l) Step 11 (m) Step 12 (n) Step 13 (o) Step 14

(p) Step 15 (q) Step 16 (r) Step 17 (s) Step 18 (t) Final result

Figure 44: An in-depth illustration of the DB scan algorithm. (Images adapted from [51]

For each track, an initial state is assumed at the most downstream end of the track, seeded from the previously presented pattern recognition results. The Kalman filter itself needs[26] the pattern recognition to give a realistic initial approximation for the state vector and the covariance matrix to start a stable filtering procedure [52].
The associated covariance matrix for the initial state is set as in Equation 19,

$$\mathbf{C}_0 = \begin{pmatrix} 200\ [\mathit{length}] & & & & \\ & 1000\ [\mathit{length}] & & 0 & \\ & & 1.5 & & \\ & 0 & & 2.5 & \\ & & & & 1\ [\frac{\mathit{charge}\cdot\mathit{time}}{\mathit{length}\cdot\mathit{mass}}] \end{pmatrix} \tag{19}$$

where these values are currently preliminary. 200 and 1000 correspond to uncertainties of approximately 14 and 32 cm in x and y respectively. The uncertainties in x and $\partial_z x$ are notably smaller than their counterparts in y. This is due to the much lower y resolution in the previously discussed reconstructed quantities, resulting in a much larger uncertainty. As long as these values are sufficiently conservative (but not overly so) and the track is well-behaved, the algorithm should converge to a reasonable solution.

3.3.3.2 Propagation

To effectively propagate the particle, a method is required to propagate the state φ_{z-1} to the subsequent state φ_z. This is started with a linear transformation matrix **F**, i.e., Equation 20. In this way, the *a priori*

[26] As of the moment of writing this.

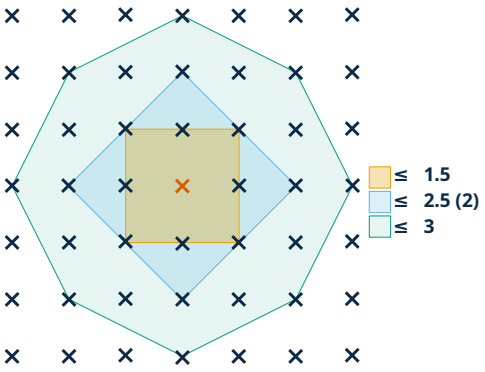

Figure 45: Illustration of the influence of the distance parameter in a discrete use case like TMS. The colored areas enclose the points considered close for different distance values. From the total number of possible close-by points, one can then conclude the ratio of coverage needed to classify an area as cluster- or track-like

estimate ($\tilde{\varphi}_z$) for the state vector at the next step gets calculated.

$$\tilde{\varphi}_z = \mathbf{F}\varphi_{z-1} \tag{20}$$

Without any magnetic field effects, the propagation matrix **F** only takes into account the z distance (the amount of traversed material) to the next layer, as well as the offsets in x and y based on the state's direction, and can be seen in Equation 21. The momentum change due to energy loss in the traversed material is added 'manually' after each Kalman step by comparing it across different hits.

$$\mathbf{F} = \begin{pmatrix} 1 & 0 & dz & & 0 \\ 0 & 1 & 0 & dz & \\ dz & 0 & 1 & 0 & 0 \\ & dz & 0 & 1 & 0 \\ 0 & & 0 & 0 & 1 \end{pmatrix} \tag{21}$$

The magnetic field deflects particles in the x direction and only affects the momentum (direction) in the state vector. The deflection Δp_x can be calculated from the Lorentz force via a Taylor expansion, which results in Equation 22. B stands for the magnetic field direction per region and is therefore either -1 T in the inner part or +1 T in the outer part[27]. q stands for the assumed charge.[28] $|start - stop|$ determines the distance between the previous and the current hit[29].

$$\Delta p_x = 0.303 \cdot q[\mathrm{e}] \cdot B[\mathrm{T}] \cdot 1.95 \cdot |start - stop|[\mathrm{mm}] \cdot 0.5 \tag{22}$$

This deflection is then applied to the x direction $\delta x/\delta z$ of the state vector φ_{z-1} as shown in Equation 23 determining the deviation in x direction from the momentum. $\varphi_{z-1,x}$ stands here for the specific entry x in the Kalman state vector.

$$\varphi_{z-1,2,(\partial_z x)} = \varphi_{z-1,2} - \Delta p_x \cdot \varphi_{z-1,4} \tag{23}$$

Using this updated direction estimation, the *a priori* estimate for the state vector at the next step is calculated using Equation 20.[30] The *a priori* estimate for the covariance matrix is calculated using Equation 24. $\mathbf{Q} = cov(\epsilon_z)$ is here the correction to the covariance matrix and ϵ_z the 'process noise' from multi-scattering processes.

$$\tilde{\mathbf{C}}_z = \mathbf{F}\tilde{\mathbf{C}}_{z-1}\mathbf{F}^T + \mathbf{Q} \tag{24}$$

[27] The factor 1.95 is the conversion factor into natural units for T.
[28] Assumed charge here refers to the charge assumption of this try. More about this in 3.3.3.5.
[29] The factor 0.5 is the conversion factor into natural units for mm.
[30] This could in principle be expressed as a matrix as the Kalman filter only encodes linear effects. Due to the existing non-linear effects, it was decided not to do so.

3.3.3.3 Updating with Hit Information

When the estimated state and covariance, $\tilde{\varphi}_z, \tilde{\mathbf{C}}_z$, are available, these values can be 'filtered' with the hit information in layer z. This update minimizes the covariance of the new state [52], which leads to the filtering equations 25 and 26,

$$\varphi_z = \tilde{\varphi}_z + \tilde{\mathbf{C}}_z \left(\mathbf{R}_z + \tilde{\mathbf{C}}_z\right)^{-1} \left(m_z - \tilde{\varphi}_z\right) \tag{25}$$

$$\mathbf{C}_z = \left[\mathbf{I} - \tilde{\mathbf{C}}_z \left(\mathbf{R}_z + \tilde{\mathbf{C}}_z\right)^{-1}\right] \tilde{\mathbf{C}}_z \tag{26}$$

where m_z is a vector of the position of the hit x/y bar $(x_{\text{meas.}}, y_{\text{meas.}})$[31], and $\mathbf{R}_z$ is the process noise matrix. In TMS, the process noise is the covariance matrix of the x, y position measurement for a given layer. As the bars are slightly rotated relative to the x, y axes, the exact location of the hit within the bar will vary the x, y values in a correlated way[32], with the x and y values being lightly correlated by the tangent of the angle (0.00275 for the nominal 3°design), with the sign of the correlation determined by the orientation, see Section 3.3.2.6. Therefore, the noise matrix varies for the different module orientations. The general form is shown in Equation 27.

$$\mathbf{R}_z = \begin{pmatrix} \sigma_x^2 & \rho\sigma_x\sigma_y \\ \rho\sigma_x\sigma_y & \sigma_y^2 \end{pmatrix} \tag{27}$$

In this equation σ_x represents the bar width in mm and σ_y the uncertainty in bar length direction. For this work σ_x is 36 mm and σ_y = 2000 mm. The parameter ρ then introduces the different module orientations: for U modules it is -1, for V modules +1, and for X modules 0.
A schematic representation of the Kalman filter, taken from [53], is shown in Figure 46.

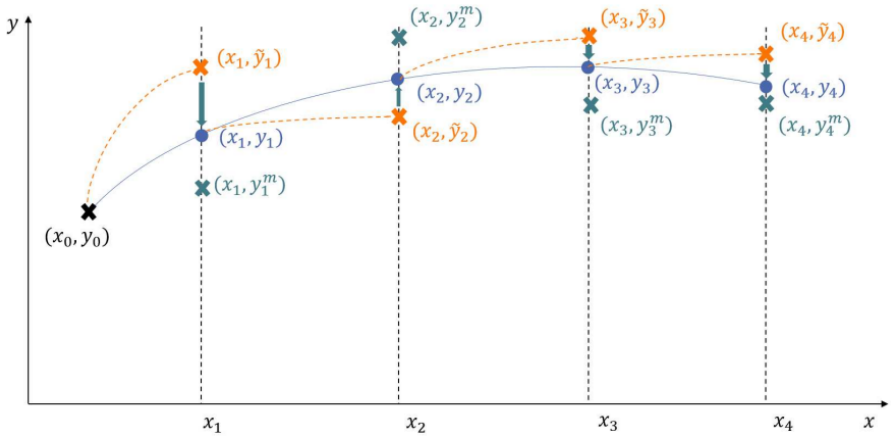

Figure 46: A schematic representation for the Kalman filter: y represents one of the variables of the state vector φ_z, which is a function of the free parameter x. x_k are points of intersection between the detector and the particle trajectory. The seeding algorithm determines the first estimate (x_0, y_0). From this, the Kalman filter produces an *a priori* estimate of the following point $(x_1, \tilde{y_1})$, shown in orange. Next, this result is compared with the measurement (x_1, y_1^m), shown in green, and with the filtering equations 25 and 19, and an updated estimate (x_1, y_1) is produced. This procedure is repeated until no more track hits are available. Credit: [53]

3.3.3.4 Rauch-Tung-Striebel Smoothing

To further improve the Kalman filter's performance, the Rauch-Tung-Striebel smoothing algorithm [54] is applied. This method uses the Kalman filter described previously and adds a backwards pass[33] on the saved *a priori* and *a posteriori* state vectors and covariance matrices.
Similar to the above-described forward pass, the first step is to define or initialize the state vector $\hat{\varphi}_n$

[31] This vector gets 'padded out' with more 0's in order to have the same dimension as $\tilde{\varphi}_z$.
[32] For tilted bars, the longitudinal position of a hit within a bar will influence both the x and y value.
[33] Forward pass: end of track to start of track. Backward pass: start of track to end of track.

and the covariance matrix $\hat{\mathbf{C}}_n$, where n is the last iteration of the forward pass. For the smoothing, this is trivial as this has already been computed and can be taken from the last step of the forward Kalman filter, i.e., $\hat{\varphi}_n = \varphi_n$ and $\hat{\mathbf{C}}_n = \mathbf{C}_n$.
From this step on, the algorithm works its way back through the states with Equations 29 and 30 using $\mathbf{K}_z$ defined in 28.

$$\mathbf{K}_z = \mathbf{C}_z \mathbf{F}^T \tilde{\mathbf{C}}_{z+1}^{-1} \tag{28}$$

$$\hat{\varphi}_z = \varphi_z + \mathbf{K}_z(\hat{\varphi}_{z+1} - \mathbf{F}\varphi_z) \tag{29}$$

$$\hat{\mathbf{C}}_z = \mathbf{C}_z + \mathbf{K}_z(\hat{\mathbf{C}}_{z+1} - \tilde{\mathbf{C}}_{z+1})\mathbf{K}_z^T \tag{30}$$

By applying the smoothing algorithm, the Kalman filter's state estimation is retrospectively improved, allowing it to overcome the intrinsic spatial resolution of the bar width.

3.3.3.5 Charge Identification with the Kalman Filter

Using the assumed charge in the magnetic field deflection described in Section 3.3.3.2, the Kalman filter can test the two charge hypotheses (positive or negative) via a χ^2 approach. The χ^2 for both charge hypotheses is the iteratively summed up squared distance in *xy* between the updated state from Equation 20 with the magnetic deflection and the *a priori* estimate of the next state.
Comparing the χ^2 of the two hypotheses, the one with the more realistic (usually lower) χ^2 is chosen as the charge estimation. The χ^2 from the less likely hypothesis can then be used to understand the confidence of this result. The difference between the two χ^2 values hints at the confidence, with the difference being small relating to a bad or more uncertain result, and vice versa.

3.3.4 Results after the Kalman Filter

As an example, Figure 47 shows an event display of the status after the entire reconstruction. Shown are the different hits and the overall Kalman track. The different hits are colored by their module orientation, or in green for the start and end point of the reconstruction. A green dotted line indicates the Kalman track. In the front and side views, some of the hit areas for the U and V bars are enlarged, reflecting the uncertainty in the *y* position from the geometry without a neighboring X hit.

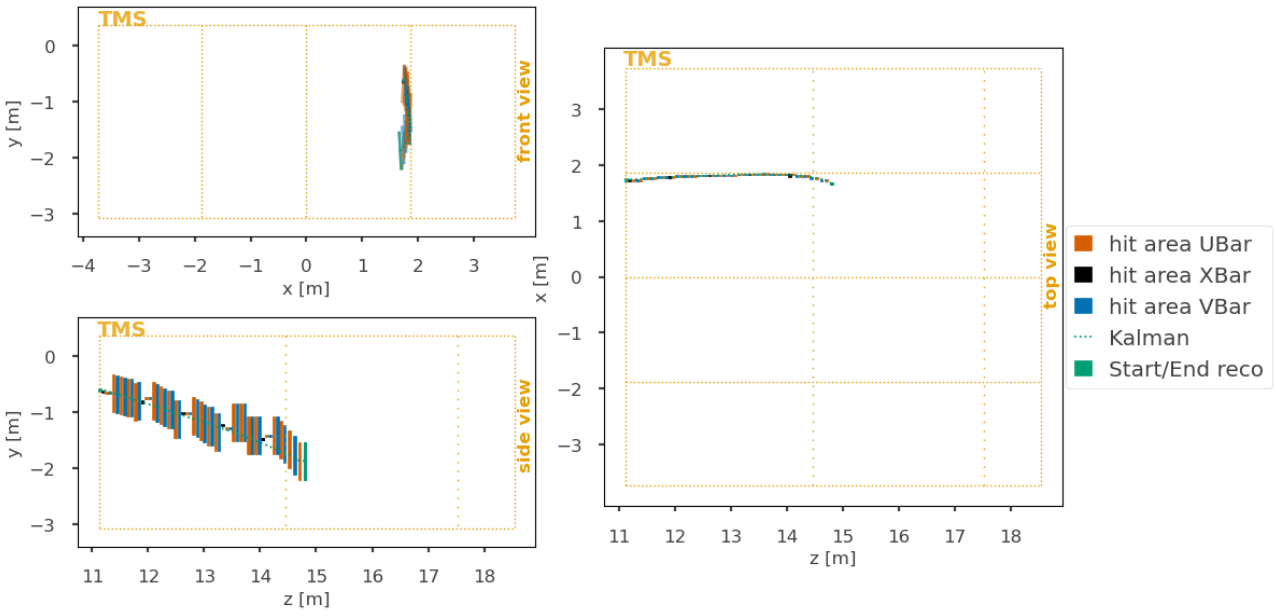

Figure 47: Event display of a simulated muon event in a geometry with every 11^{th} layer being an X layer

The overall performance of the reconstruction can be measured by the reconstruction efficiency, defined

as the number of ND physics sample muons with reconstructed tracks divided by the total number of ND physics sample muons. ND physics sample muons are muons which start in ND-LAr's active volume and end in the TMS.
The reconstruction efficiency is shown in Figure 48. At low energies, the efficiency is low because the muon deposits energy in too few planes to reconstruct a track. After that initial low, the overall efficiency rises to about $85 - 95\%$.

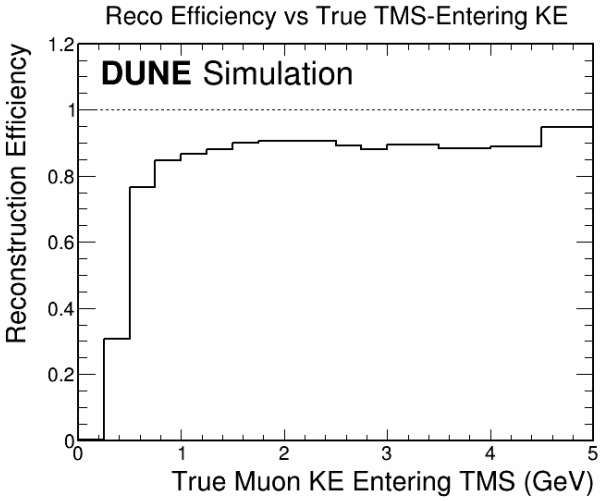

Figure 48: Reconstruction efficiency of muons in TMS. Shown is the reconstruction efficiency for muons entering TMS originating from ND-LAr and ending in TMS(contained)

3.3.5 Muon Charge Identification

Based on the task for TMS of characterizing muons from CC interactions in ND-LAr, the typical step of particle identification is omitted at this point. Instead, all particles making their way into TMS are assumed to be either muons or anti-muons. Therefore, the only necessary step in particle identification is to determine their charge.
The method used for this is the Signed Distance Method and is explained in detail in [55].[34] It uses the geometric properties of the reconstructed hit positions and is depicted in Figure 49.
It works by connecting the start and end of a track with a straight line and summing the distances of each hit in the track to the straight line at the respective *z* position. Only the *x* distance is used, since the magnetic field affects only this direction, enabling charge identification in the first place.
Special attention is paid to the direction of the magnetic field, as this changes throughout the detector (compare 2.2.3.3). Therefore, only for tracks with few crossings of these boundaries can the charge be properly identified. Up to a maximum of two boundary crossings, the sign of the sum of the distances for a specific region is flipped depending on the respective magnetic field direction of this region.
For μ^-, the Signed Distance will be positive and negative for μ^+ due to the effect of the Lorentz force. This allows for correct charge identification of about 95% of all reconstructed tracks, averaged over the entire energy spectrum, which is better than the current performance of the Kalman filter charge identification and therefore the preferred method in the following sections.

3.3.6 Muon Energy Reconstruction

As described before in Section 3.1.1, TMS is charged with determining the muon momenta and is designed to do this by determining the range of the track in the detector.

[34] This method will most likely be improved in the future.

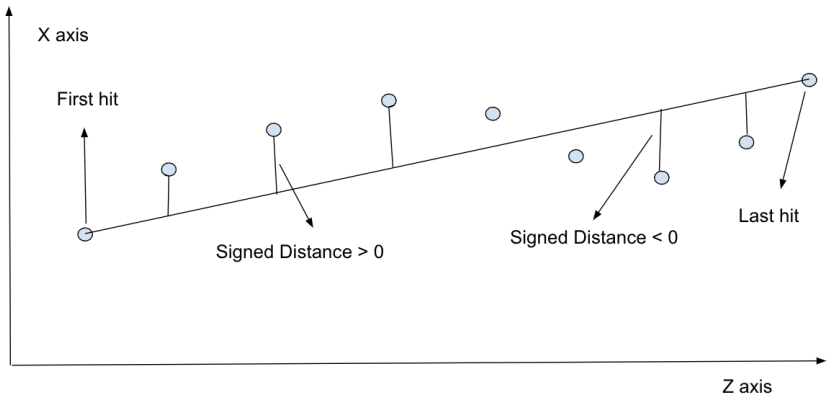

Figure 49: Schematic depiction of the Signed Distance Method [55]. The distance of hits in the x direction to a straight line connecting the first and last hit of a track is determined. These distances are then summed up over the entire track with the sign of the addition corresponding to the magnetic field direction of the respective area of TMS

The method used for reconstructing the energy is described in detail in [56] and uses the areal density between hits. For energies between 100 MeV and 100 GeV, the dominant energy loss mechanism of muons is ionization, which is described by the Bethe-Bloch equation in Equation 7. Ionization approximately depends linearly on the areal density of a muon [56], as the muons have an approximately constant energy loss in the expected energy range for TMS [57]. Sub-leading-order effects include inelastic interactions of muons with nuclei in the traversed material and the production of delta rays, which are secondary high-energy electrons.
The areal density of a track is calculated by determining the material density between neighboring pairs of hits, which is multiplied by the distance between them. These are then summed up over the entire track. In addition, a correction is made after the last reconstructed hit. On average, a muon travels through half the downstream steel plate after its previous hit in a scintillator layer before coming to a complete stop in the detector. This additional material and distance are added to the final areal density. An important point to keep in mind with this method is that only tracks contained within TMS can have their energy appropriately reconstructed.
The energy resolution distribution is shown in Figure 50b as the red dotted line. It mainly follows a Gaussian behavior, but also shows a tail on the left side, following a power-law. This behavior is described by the Crystal Ball function in Equation 31.

$$f(x) = N \begin{cases} \exp\left(-\frac{(x-\bar{x})^2}{2\sigma^2}\right), & \text{if } \frac{x-\bar{x}}{\sigma} > -\alpha \\ A\left(B - \frac{x-\bar{x}}{\sigma}\right)^{-n}, & \text{if } \frac{x-\bar{x}}{\sigma} \leq -\alpha \end{cases} \tag{31}$$

Here $\bar{x}$ represents the mean and σ the standard deviation of the Gaussian distribution, α is the transition point between the Gaussian distribution and the power-law tail, n is the exponent of the power-law, N is the normalization factor, and A and B are constants for continuity and normalization.
For a given dataset, the energy resolution distribution is sliced into true-energy slices of 250 MeV from 0 to 5 GeV and fitted with the Crystal Ball function. The mean obtained in this manner and the standard deviations are then overlaid onto a 2D-histogram of the true kinetic energy and the initial approximation of the reconstructed kinetic energy, as shown in Figure 50a.
The red line shown in this plot (50a) is the result of a linear fit for the $\bar{x}$ and σ of each slice from 0.5 to 4 GeV. This final linear fit yields the relation between the areal density $\rho_{areal,Reco}$ and the reconstructed

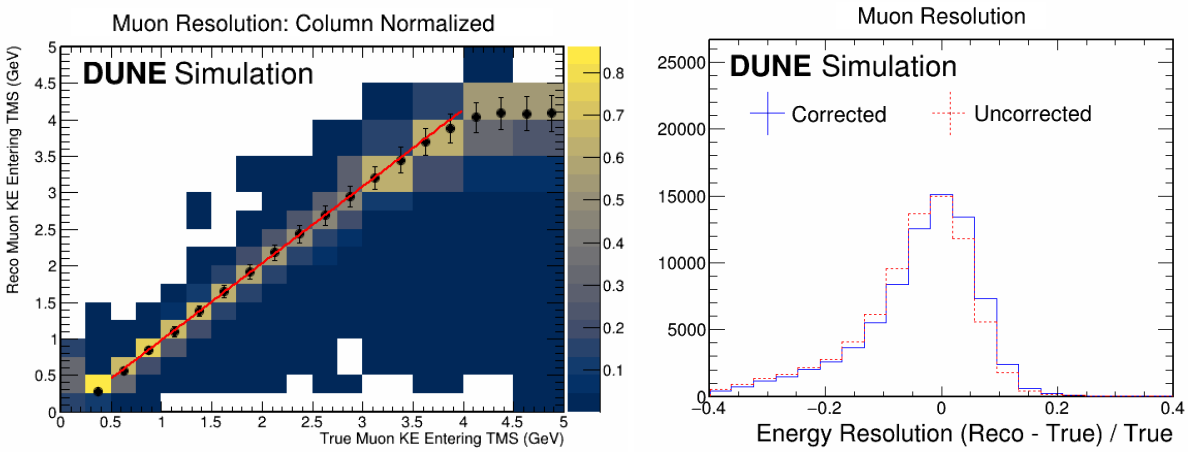

(a) True vs reconstructed muon energy

(b) Energy resolution distribution

Figure 50: 50a True vs reconstructed muon energy in a column normalized histogram overlaid with the individual fit $\bar{x}$ and σ of each slice (shown in black dots with errorbars), along with the overall fit result shown in red [56]. 50b The muon energy resolution distribution before the corrected relation between the areal density and the kinetic muon energy in red (dotted) and after in blue (solid)

kinetic muon energy $E_{Reco,kin}$ in Equation 32.

$$E_{Reco,kin} = 91.80\ \text{MeV} + 1.75 \cdot \rho_{areal,Reco} \cdot 0.9460\ \text{MeV}/(\text{g}/\text{cm}^2) \tag{32}$$

The factor 1.75 is approximately the relationship between the areal density and the energy and serves as a starting point of the final fit. The energy resolution from the fit is shown in Figure 51 and in a comparison to the distribution before the fit in Figure 50b as the blue line.

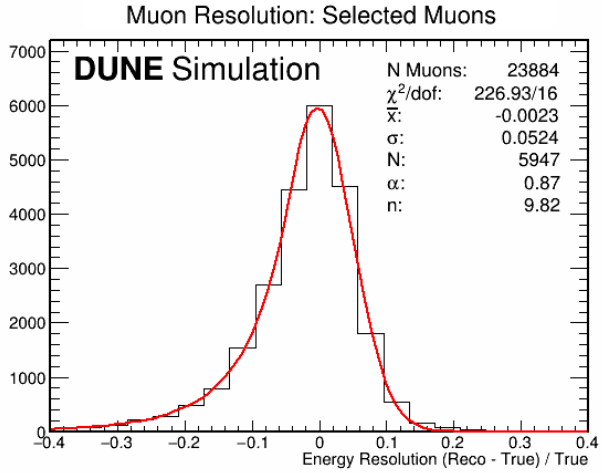

Figure 51: Energy resolution of all (selected) muons after the fit. The mean of the energy resolution is close to 0. Also, the values for the other fit parameters of the Crystal Ball function are shown [56]

Equation 32 is used as is for the following sections, even though this fit was performed for an older geometry version with a different steel layout. Given this difference, the peak of the energy resolution might be offset from 0.[35]

[35] This will have to be redone at some point in the future.

3.4 Module Orientation Plan Optimization

3.4.1 Module Orientations

For ease of handling the scintillator bars with dimensions 36 mm x 17 mm x 3300 mm (stereo) or 36 mm x 17 mm x 3500 mm (horizontal) are clustered into modules of 32 bars each and glued together. These bundles of bars are then called 'modules'. One layer consists of 6 modules.
In the U or V case (stereo), the modules are placed side-by-side in a module frame that holds them in place within the detector. Figure 52a shows the modules in a U installation, while a V installation would be tilted in the opposite direction.

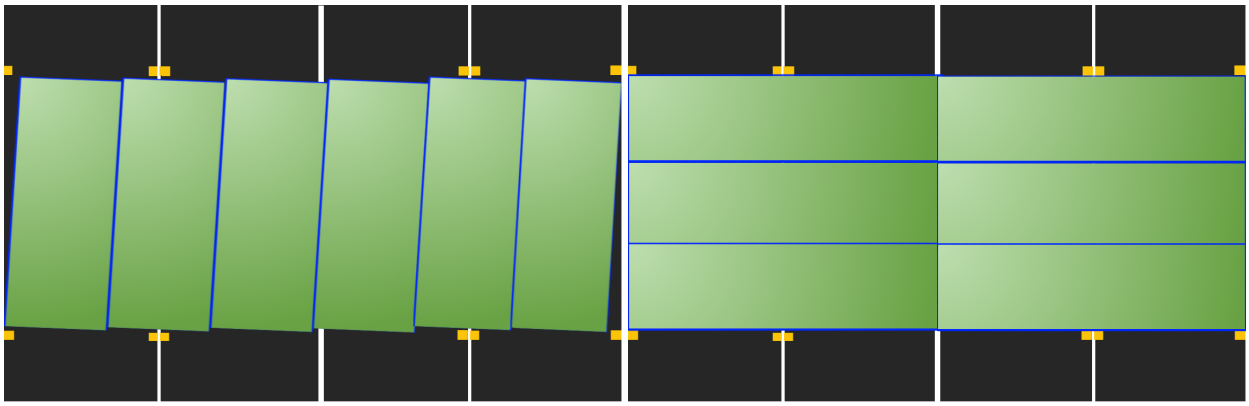

(a) U module layer layout, tilt-angle exaggerated (b) X module layer layout

Figure 52: Sketch of the different module orientations in TMS. 52a shows the layout for U modules and 52b for X modules

In the X layer case, the modules are stacked horizontally in two groups of three, as shown in Figure 52b.

3.4.2 Effect of Different Module Orientations

The stereo approach was initially chosen because it offers the highest spatial resolution in the bend direction of charged particles (mostly muons) deflected by the magnetic field. Information in this direction (x direction) is crucial to determine the charge of particles. On the other hand, this design layout sacrifices y spatial resolution (up-down) to achieve high resolution in the x direction.
This approach also allows the readout to be on one side only. In this way, the readout would be at the top, making cable management and building, etc., easier and more cost-efficient.
As described above, the charge is determined from the curvature by adding up the deviations for each hit from a straight line connecting the first and last point of the track [55]. Therefore, at the current stage, effective charge identification relies heavily on the amount of available data. ND-LAr is not capable of determining the charge due to a lack of a magnetic field and relies on TMS to determine this.
While charge identification is a major requirement, TMS also needs to determine other things. These are:

- The end point, to determine whether a particle was contained
- The start direction and position, to point back to ND-LAr
- The track length, to determine the particle's momentum and energy

The momentum is determined by the material traversed, so by range in TMS.
In the case of a particle leaving the detector, only a minimum momentum can be determined from the traversed distance. These events may be excluded from analyses, but must be reliably identified to do so.
As the neutrino beam for DUNE is slightly down-turned to reach the far detectors, there will be a slight

bias towards bottom-exiting (negative *y*) muons and anti-muons being produced in ND-LAr. However, on the other sides particles might also leave uncontained. To first order, the containment can be studied with good enough information in *x*, *y*, and *z* though.[36]
Unfortunately, in the stereo layout, the *y* direction is the weakest spatial resolution. This can be balanced by adding X layers to obtain more precise information in the *y* direction while maintaining the high information density in the bend direction achieved in the stereo layout.
Figure 53 shows the conceptual effect of adding more X layers into the TMS. The more X layers added (in place of stereo layers), the less information is gained in the bend direction. As such, the pure stereo layout is expected as the best for the charge identification, as its performance drops with more X layers. The determination of whether the particle stopped improves with more X layers. The effect of X layers on momentum reconstruction is a bit more difficult to assess. At first, the performance improves as the distance traveled in the *y* direction becomes more precise. However, the loss of the stereo layers results in a lower precision in the *x* direction. Therefore, at some point, the loss of information in *x* supersedes the information gain in *y*, so the momentum resolution decreases. [58]

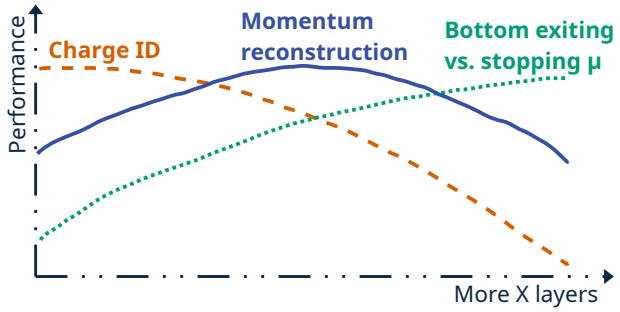

Figure 53: Conceptual plot of the effect of adding more X-layers into TMS. Adding more X layers reduces charge identification performance, as it requires replacing stereo layers. The performance for determining a top or bottom containment of muons, on the other hand, increases with more X layers. The momentum reconstruction, which represents the muon energy, is dependent on information from all directions, and therefore improves until a certain number of X layers by having more information in the *y* direction. After a certain number of X layers, though, the less amount of information in the *x* direction results in a lower performance for the momentum reconstruction when adding even more [58]

3.4.3 Considered Geometries

To study the effect of different X layer amounts, two options were initially created: a pure stereo layout that does not contain any X layers and keeps the stereo layers, and the maximum possible number of X layers, in every third layer, starting from the first layer. Both of them are depicted in Figure 54.

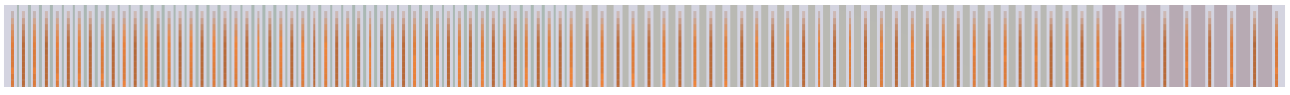

(a) Stereo

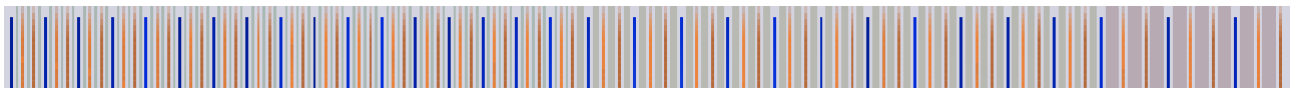

(b) Stereo and X layers (3^{rd} w/o)

Figure 54: Stereo layout in 54a and opposite with X modules (shown in blue) in every third layer in 54b. The two orange-shaded layers are the stereo scintillator layers. The increasing space from the left to the right shows in the change in steel thickness

[36] The criteria for 'good enough' are studied in the following indirectly.

Considering that TMS is mainly focusing on ND-LAr exiting muons, which therefore need to get matched back to the ND-LAr event, it is good to have good position resolution at the start of tracks as well. Given the space constraints imposed by the steel layers, the easiest way to do this is to add a second scintillator layer in front of the first steel layer. This layout is called a double first scintillator layer.
Under the assumption that this double layer will be implemented, several geometries with this option were created, and a wide range of possible X layer placement options was scanned. To keep the number of stereo layers balanced, only options with even numbers of UV pairs were considered. These geometries therefore span from every third layer to every 17^{th} layer being an X layer as depicted in Figure 55.

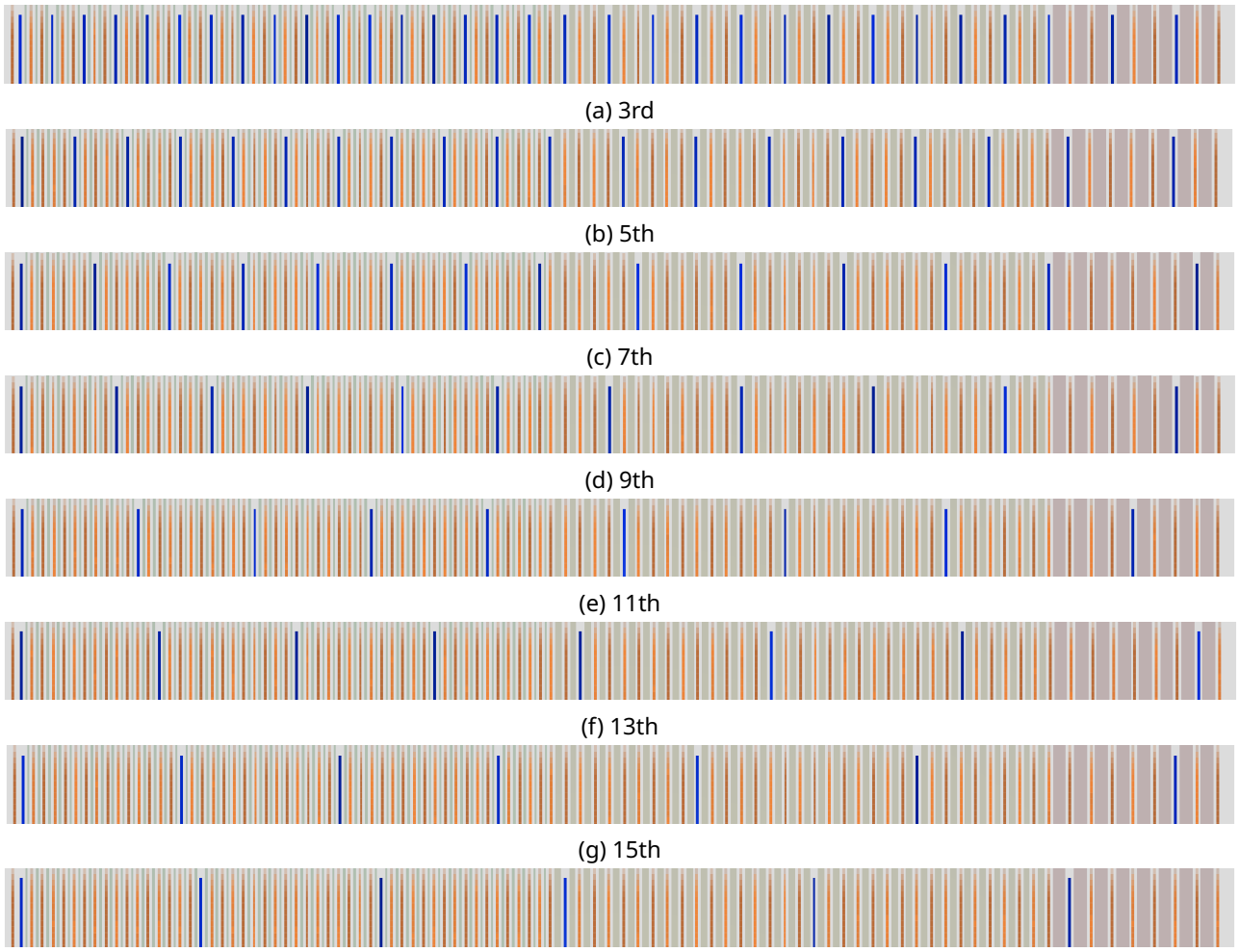

(a) 3rd

(b) 5th

(c) 7th

(d) 9th

(e) 11th

(f) 13th

(g) 15th

(h) 17th

Figure 55: Cutouts of the different double first scintillator layer geometries studied. The number in the subcaptions stands for how many scintillator layers after, another X layer (shown in blue) follows

For each of these ten geometries a total of 10^{18} protons on target (POT) were simulated and reconstructed resulting in about 100, 000 events each in TMS with full reconstruction.

3.4.4 Metrics for Comparison

To quantitatively determine the performance of the different geometries, metrics for comparison are necessary. These metrics largely follow the list from 3.4.2 and reflect the ability of the geometries to answer the questions whether a particle was contained, which neutrino interaction in ND-LAr it originated from, and what its energy is.
To allow for a sensible comparison between the different geometries, only tracks with more than 14 hits were considered. 15 hits is the minimum required number of hits to allow geometries with every 3^{rd} layer as an X layer to have reconstructed tracks for all three different module orientations, as the pattern recognition per module orientation only starts if there are at least 5 hits in this orientation found. To ensure similar conditions for all geometries and avoid potential bias at lower energies, which have shorter tracks, this lower limit of hits was chosen.
The following sections explain the different metrics in detail.

3.4.4.1 Start Point

The starting points of tracks have indirect influences on the above-mentioned questions. It may not be constructive for containment determination, but it assists in matching to ND-LAr and in estimating the energy via the track length.
Qualitatively, the starting-point resolution was determined in the *x* and *y* directions, allowing a comparison of the effect in both directions when adding X layers. The resolution is obtained by comparing the reconstructed start point with the simulated true start point and subtracting the true start point from the reconstruction for all reconstructed events. An example of this is shown in Figure 56.

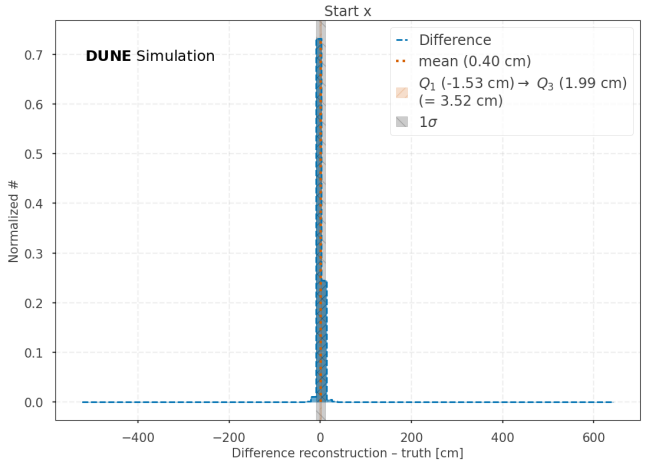

Figure 56: Not-zoomed-in start point resolution for the *x* direction for the geometry shown in 55a. In addition, the mean, standard deviation, and quartiles are shown

To allow for consistent comparison, the following distributions are plotted only in the range −50 to 50 cm for the *x* direction and −200 to 200 cm for the *y* direction. The result of this is shown in Figure 57 for the above-mentioned geometries.
For each of the shown distributions, the arithmetic mean as well as the first and third quartiles are determined. The quartiles mark the 25% and 75% points of the distributions, respectively. An example of this is shown in Figure 58. The quartiles are used here instead of the more common standard deviation, as the standard deviation is very sensitive to the small number of outliers in the distributions. The full distribution for this example is shown in Figure 56, showing the standard deviation as well as the quartiles. The metrics for comparison between the different geometries are then the mean and the distance between the two quartiles.
Due to issues still in the reconstruction, which will hopefully be fixed in the future, the reconstruction can sometimes get unreasonable results, introducing a 'reconstruction bias'. To counter this bias as much as possible, different selections are applied to all geometries. The first one is a selection of only tracks

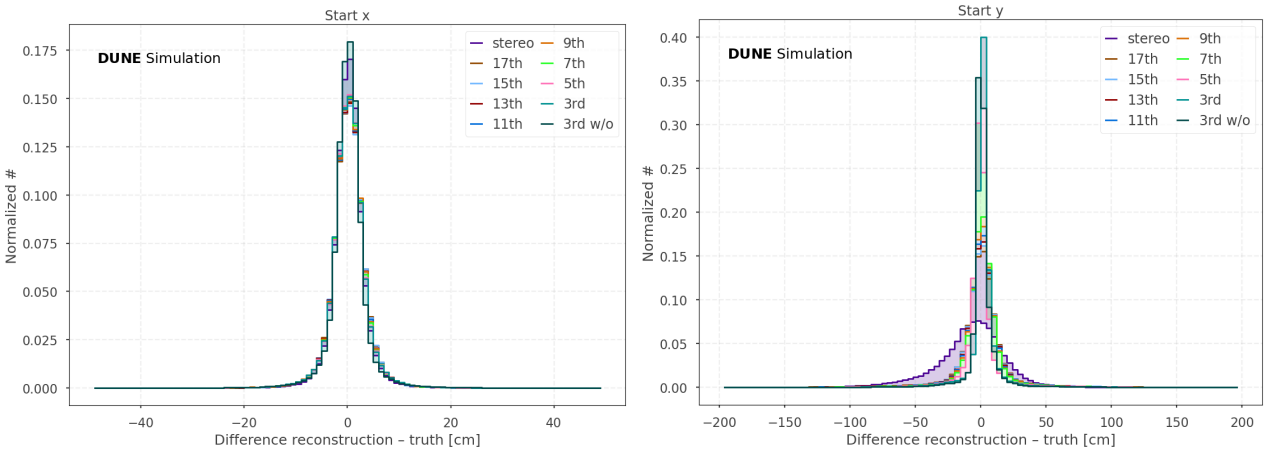

(a) x (b) y

Figure 57: Zoomed in start point resolution for the x direction in 57a and y in 57b for all geometries. In the x direction, the two geometries without the double scintillator layer in the front have the narrowest peak. In contrast, the peak for the other geometries is slightly lower, and the distribution is slightly broader. In the y direction, the stereo geometry has the broadest distribution with the lowest peak. For more X layers, the distribution narrows and peaks higher, with the opposite behavior to the stereo geometry, with the two geometries every 3^{rd}

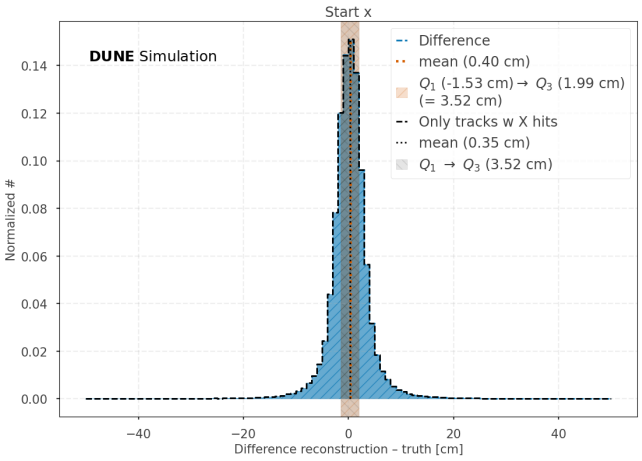

Figure 58: An example for the determination of the mean and quartiles of the start position in x. This is the result for the geometry shown in 55a

with hits from X layers[37] as this is the effect to be studied here, reducing the number of events for this example by 0.08%. This is shown in Figure 58 with black lines.

3.4.4.2 End Point

Similar to the start point, the end point resolution is calculated for the x and y direction and shown fully in Figure 59 as an example for the geometry shown in 55a.

As for the start point resolution, for an easy comparison the following distributions are plotted for an area between -200 and 200 cm for the x direction, and -300 to 300 cm for the y direction, as seen in Figure 60 for all geometries.

In addition to selecting only tracks with X hits, further selections were applied to the end point. The first selection is a containment selection, choosing only tracks whose true end point lies within the fiducial[38] detector volume and reducing the amount of events by 0.1%[39]. This is done to allow for a proper comparison of the true and reconstructed end point, as the true end point would be outside the detector for not contained tracks, without an option for the reconstruction to reflect this. It also makes it easier to

[37] Apart from the stereo case, of course.

[38] Fiducial in a more hardware-based sense. This volume has not been tuned so far and only ensures a fully contained track on the sides (x) and top/bottom y.

[39] This number includes the selection of only tracks with X hits.

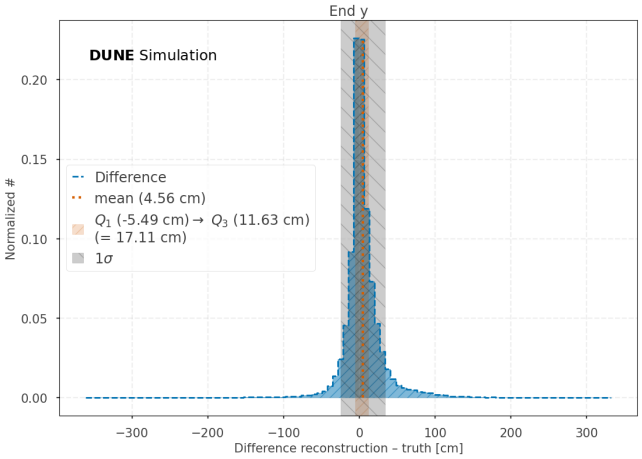

Figure 59: Not-zoomed-in end point distribution for the *y* direction for the geometry shown in 55a. In addition, the mean, standard deviation, and quartiles are shown

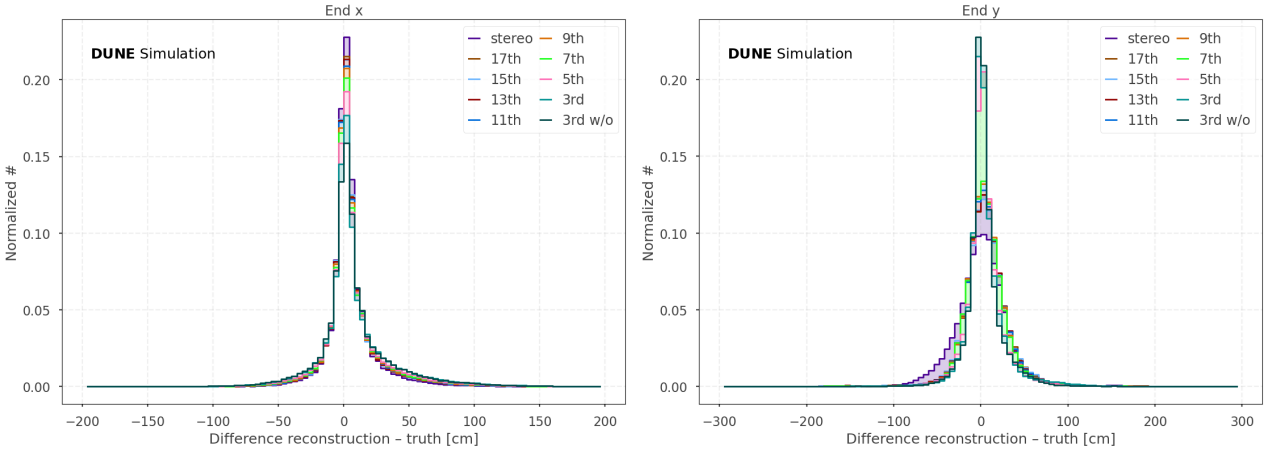

(a) End *x*

(b) End *y*

Figure 60: Zoomed in end point resolution for the *x* direction in 60a and *y* in 60b for all geometries. In the *x* direction, the opposite behavior of the start-point resolution in *y* is observed, with the stereo distribution being the narrowest and broadening slightly as more X layers are added. For the *y* direction, the same pattern from the start-point resolution in *y* repeats

compare end point resolution and energy resolution, which only contained tracks can be used for. The distributions shown in Figure 60 show the result for this selection.

The fiducial volume itself is sketched for the *x* and *y* direction in Figure 61. The exact volume is defined by $x = [-3419,\ 3419]$ mm, $y = [-2976.23,\ 291.77]$ mm, and $z = [11134,\ 18535]$ mm.

The second selection was to eliminate another reconstruction bias. When particles stop in the detector, they have lost almost all their energy by the end of their tracks. This can result in small shower-like shapes, making it difficult to determine the correct end of the track in the reconstruction, as visible in Figure 62. To counter this, the selection chooses only tracks where the reconstructed end point in the *z* direction is within ± 1 layers of the truth end point, reducing the amount of events by 59.1%[40]. The result of this selection is shown in Figure 63 for all geometries, and its influence on the means and quartile distances is shown in Figure 64b.

Equivalently to the start point resolution, the means and quartile distances are then chosen after these two additional selections as the metrics for comparison between the different geometries.

3.4.4.3 Start Direction

The track's start direction can help match the muon track in TMS to the neutrino interaction in ND-LAr. This would be done according to [59] by extrapolating from TMS to ND-LAr, using the *xz* and *yz* direction

[40] For the geometry in 55a. Other geometries are slightly more or slightly less impacted by this selection (deviation of $\mathcal{O}(1\%)$ to this value)

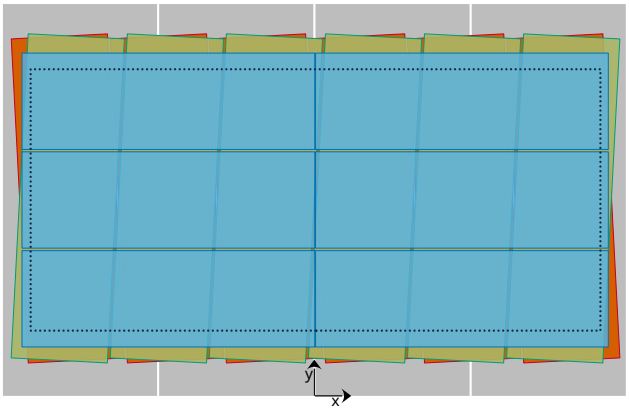

Figure 61: Sketch of the front view of the fiducial volume for TMS. Shown is the steel in gray, the two stereo layers in orange and green, and the X layer in blue. The dotted dark blue line indicates the fiducial volume

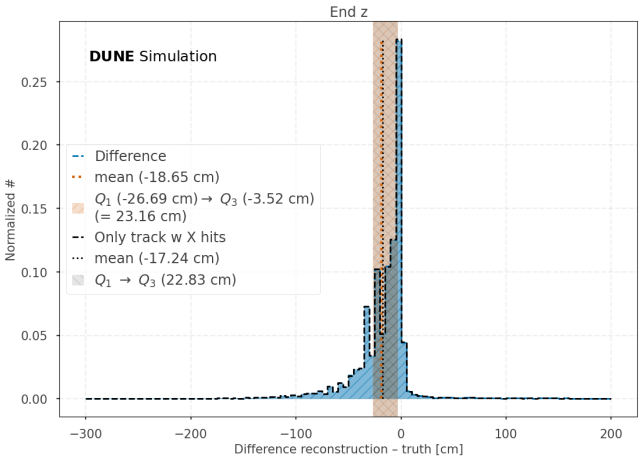

Figure 62: End point resolution for the *z* direction for the geometry shown in 55a

from the muon track to point back to ND-LAr.
Using the Kalman filter results, these values are given by the third and fourth entries in the Kalman state for the start position. They then get normalized together with the pure *z* direction, set to 1, to a vector sum of 1 according to Equation 33 with an additional normalization factor *N*.

$$|\vec{d}| = N \left| \begin{pmatrix} \frac{\delta x}{\delta z} \\ \frac{\delta y}{\delta z} \\ \frac{\delta z}{\delta z} = 1 \end{pmatrix} \right| = N \sqrt{\left(\frac{\delta x}{\delta z}\right)^2 + \left(\frac{\delta y}{\delta z}\right)^2 + 1} \equiv 1 \tag{33}$$

The two directions, or angles, *xz* and *yz*, can then be compared to the simulation truth in a manner similar to the above-described start and end point resolutions. An example of this is shown in Figure 65 for the geometry in 55a.
As before, the following distributions are then only plotted in the areas between ±20°for the *xz* direction and ±75°for the *yz* direction, as seen in Figure 66 for all geometries, with the same event selection as for the start point but only for true muon or anti-muon tracks.
For the comparison between the different geometries, as before, the mean and quartiles are determined for each geometry option, using the same selections as described for the end point resolution. This can be seen exemplarily in Figure 67 for the geometry seen in 55a. In addition to this, Figure 68 shows the relation of the mean and quartiles and the kinetic energy of the different muon tracks.

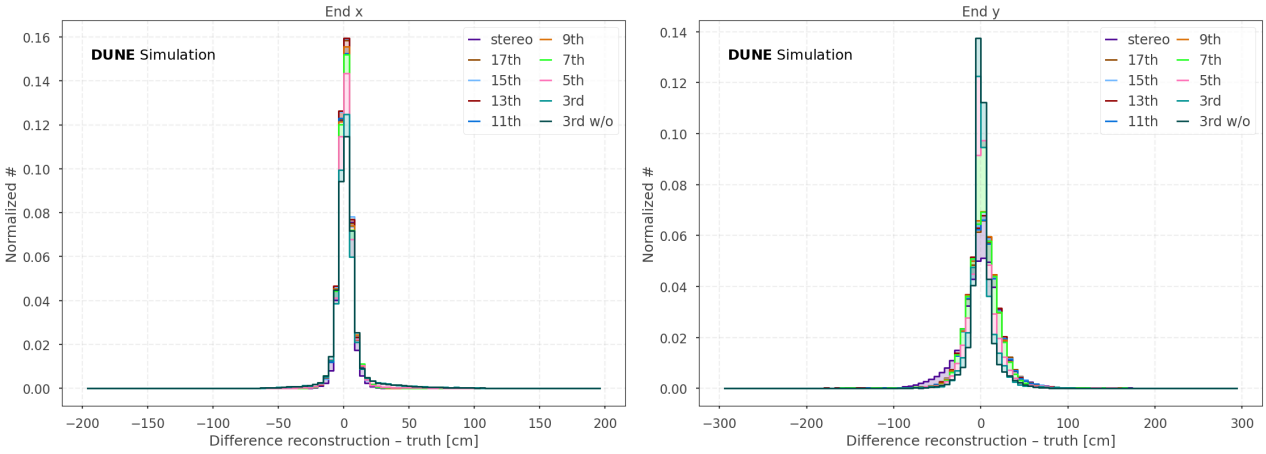

(a) End *x*

(b) End *y*

Figure 63: End point distribution for the *x* direction in 63a and *y* in 63b for all geometries with the end point selection. In the *x* direction, the distributions narrow considerably compared to before the selection. The stereo distribution remains the narrowest, while the other distributions are slightly wider, with minimal differences in peak heights. In the *y* direction, the same behavior as before can be seen, with the narrowest distribution being the 3^{rd} without the double scintillator layer in the front and then widening towards the stereo distribution. In contrast to the distributions in the *x* direction, the distributions do not narrow as much

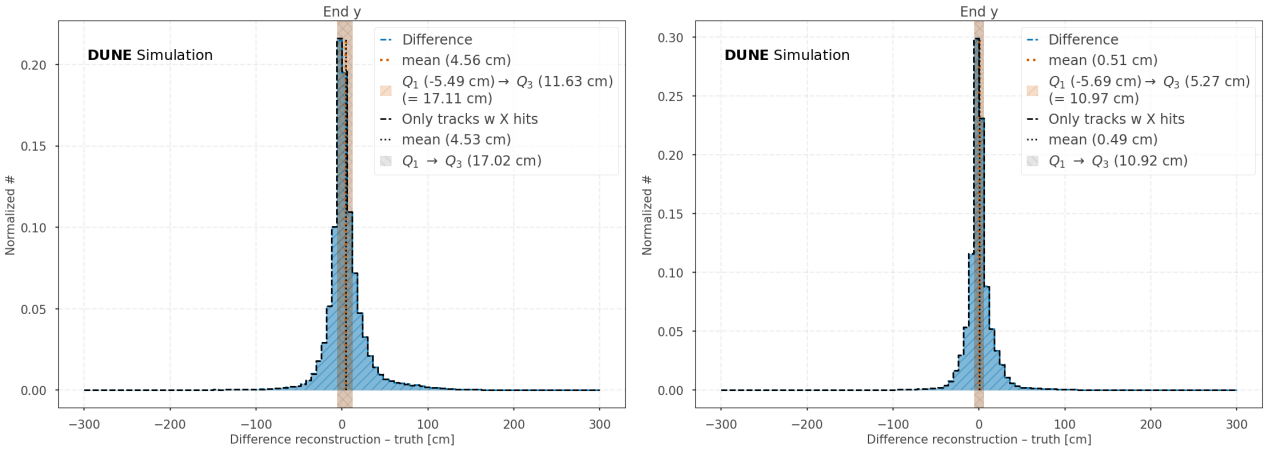

(a) End *y*

(b) End *y* with the end point selection

Figure 64: The end point resolution in *y* for the geometry shown in 55a. In 64a for without the end point selection and in 64b with the selection

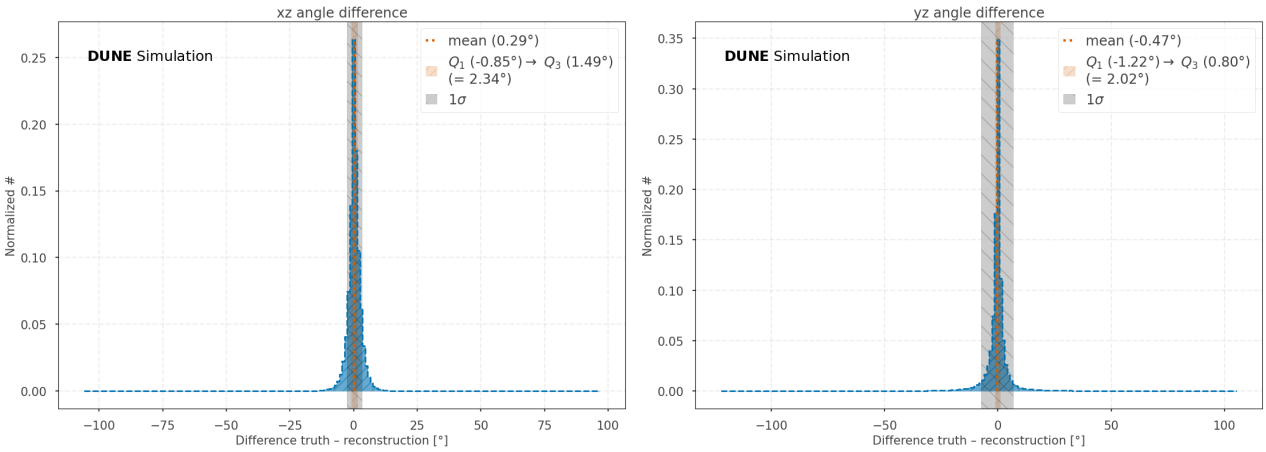

(a) Angle *xz* (b) Angle *yz*

Figure 65: Not-zoomed-in start direction resolution for the *xz* angle in 65a and *yz* in 65b for the geometry shown in 55a. In addition, the mean, standard deviation, and quartiles are shown

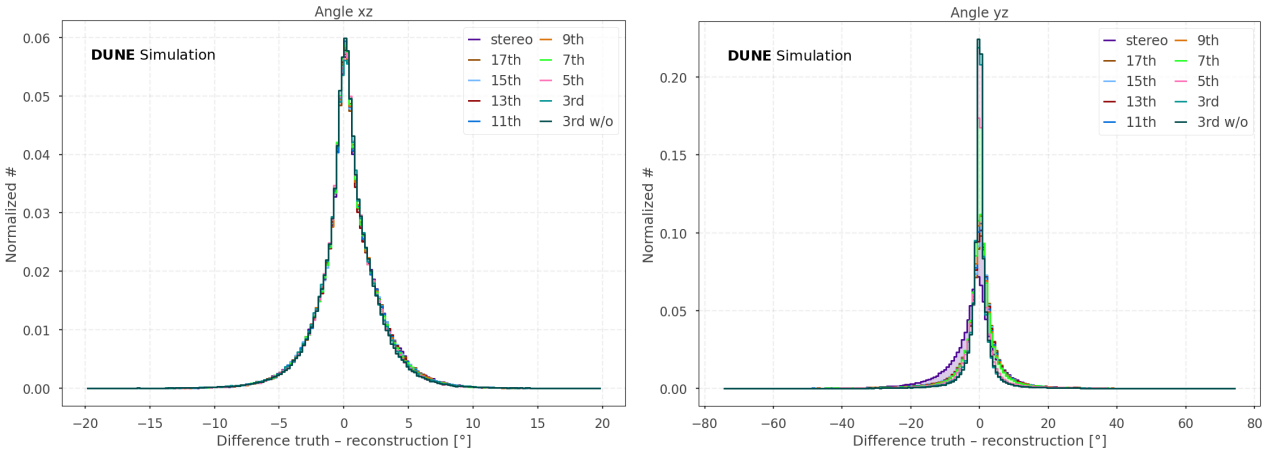

(a) *xz* (b) *yz*

Figure 66: Zoomed in start direction resolution for the *xz* angle in 66a and *yz* in 66b. For the *xz* angle, barely any differences between the different geometries are visible. For the *yz* angle, the same pattern as for the start point resolution in *y*, with a broader stereo distribution and increasingly narrower ones for geometries with more X layers

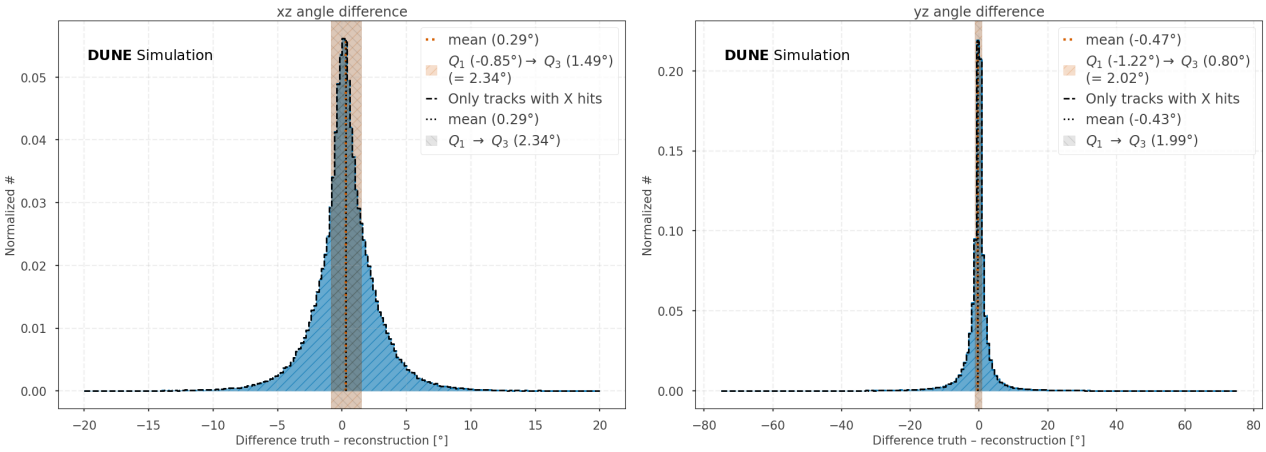

(a) Angle *xz* (b) Angle *yz*

Figure 67: The start direction resolution for the geometry shown in 55a. In 67a for the *xz* angle and in 67b for *yz*.

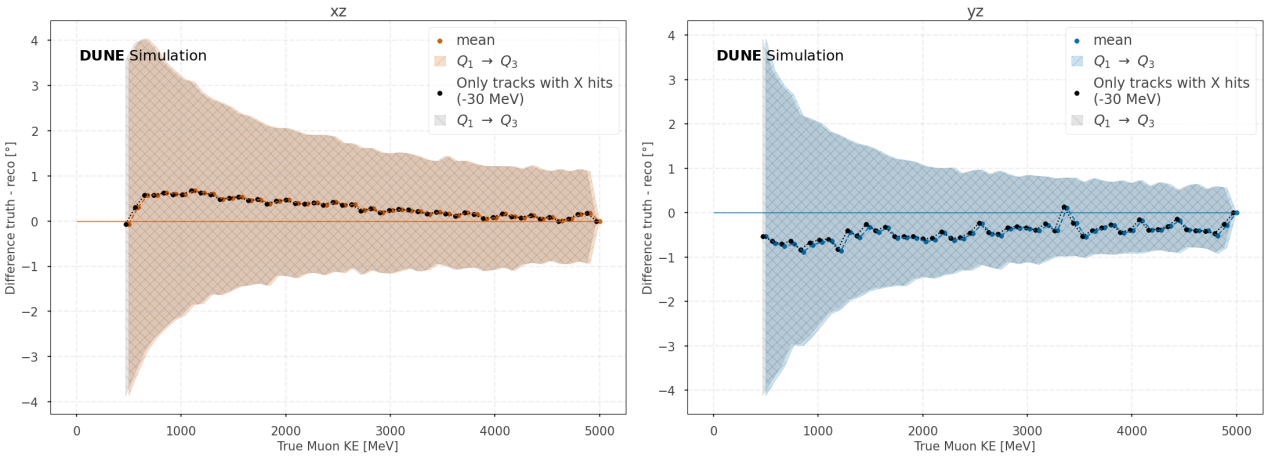

(a) Angle *xz* resolution for true kinetic energies

(b) Angle *yz* resolution for true kinetic energies

Figure 68: Start direction resolution against the true kinetic energy of muon tracks for the *xz* angle in 68a and *yz* in 68b for the geometry shown in 55a. The small positive bias in the *xz* angle in 68a likely originates from the curvature of the predominantly μ^- in the samples, which curve towards negative *x*-values. This curvature is currently not perfectly reconstructed, resulting in a small positive bias across all geometry layouts. The small negative bias in the *yz* angle in 68b comes from the neutrino beam pointing slightly downwards. This is reconstructed better in some geometries than others; for this geometry, it is not well reflected

3.4.4.4 Charge Identification

For comparison of the charge identification performance, the same selections as described for the end point resolution were used.

Given the nature of only two possible hypotheses for the charge (either positive or negative), the metric for the charge identification comparison is different from the ones described so far. There are four possible outcomes of the charge identification: a true muon being reconstructed as such (in the following referred to as true positive (TP)), or misidentified as an anti-muon (false negative (FN)) and vice versa for a true anti-muon (-> true negative (TN) and false positive (FP)). A schematic of this is shown in Figure 69.

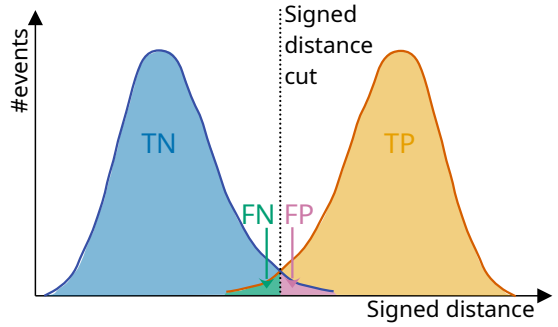

Figure 69: Schematic drawing of the charge reconstruction classification. TP and FP would be reconstructed as μ^- and TN and FN as μ^+. T stands for true, meaning the reconstruction agrees with the simulated truth, and F for false, meaning the reconstruction falsely identified the particle with another sign than the simulated truth

With this classification, it is now possible to determine the identification efficiency with Equation 34[41], purity with Equation 35[42] and accuracy with Equation 36[43] for all reconstructed events.

$$efficiency = \frac{TP}{TP + FN} \tag{34}$$

$$purity = \frac{TP}{TP + FP} \tag{35}$$

$$accuracy = \frac{TP + TN}{TP + TN + FP + FN} \tag{36}$$

In Figure 70 the charge identification efficiency can be seen against the true kinetic energy of the tracks and Figure 71 shows this for the exemplary geometry shown in 55a with the uncertainties on the efficiency obtained from a simple Gaussian error propagation and the uncertainty of the respective parameter (TN, TP, FN, FP) assumed to be the square root of its value. In this last plot, the correctly identified fraction of $\mu^\pm$ is also shown, with a focus on the kinetic energy expected to be contained within TMS.

The accuracy, reflecting the identification performance for both μ^- and μ^+, is calculated for the whole energy range (500 MeV to 5 GeV), for the neutrino flux spectrum peak at 2 ± 0.1 GeV and for the low energy part of up to 1 GeV for the different geometries and then used as the metric for comparison.

3.4.4.5 Energy Resolution

The final metric for comparison is the energy resolution. For this, the true muon energy is subtracted from the reconstructed energy for each event, and the result is then divided by the true muon energy. As before, the same selections are made, resulting in the distribution seen in Figure 72 for the example geometry from 55a. One event with an undetermined energy (assigned to $-999,999$) from the reconstruction entered this plot, resulting in the large scale of the x-axis, even though the entry remains largely invisible in the shown plot. The results for all geometries are shown in Figure 73, with only areas between -0.75 and 0.5 shown to exclude undetermined events. The end point selection shown in Figure 73b, in addition, minimizes the power-law tail of the distributions, which is mainly from events with a too short reconstructed track (either too late start or too early end).

[41] For the μ^- case. Vice versa for μ^+
[42] For μ^- case. Vice versa for μ^+
[43] For both cases

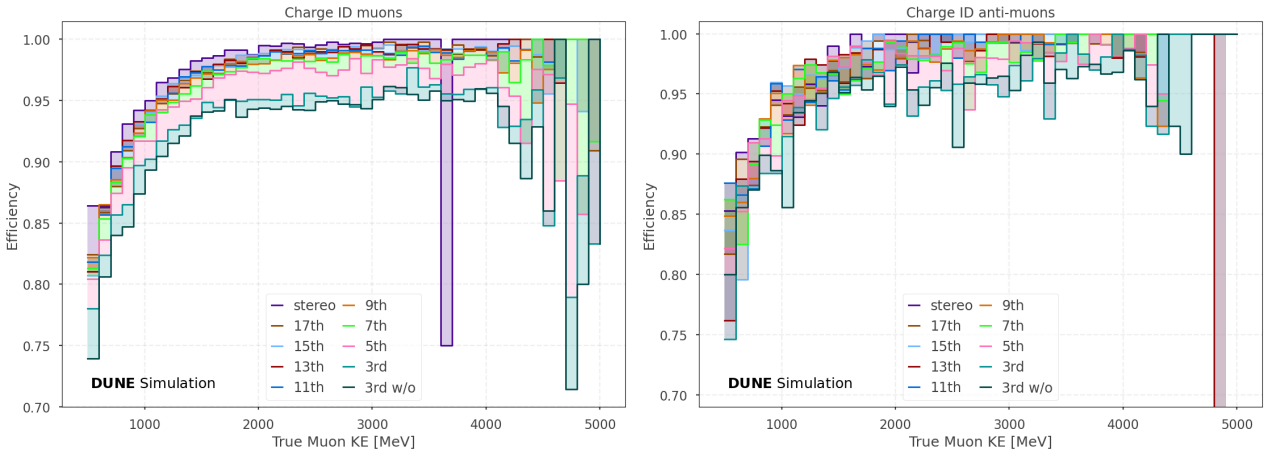

(a) Charge identification efficiency for μ^- of all geometries. The efficiency to identify μ^- decreases with more X layers. For all geometries, the efficiency starts lower for lower energetic muon tracks, rises to about 1.5 GeV, and stays stable afterwards

(b) Charge identification efficiency for μ^+ of all geometries. Roughly the same pattern as for μ^- can be observed, but harder to identify due to the lower amount of μ^+ in the data set simulating a ν_μ-beam

Figure 70: Charge identification efficiency for μ^- in 70a and for μ^+ in 70b

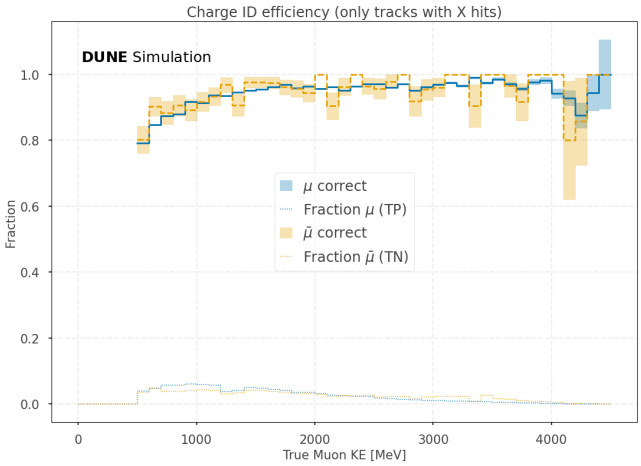

Figure 71: Charge identification efficiency and normalized distribution of correctly identified particles for the geometry shown 55a

As seen in these plots, the distributions do not peak at 0, but are slightly offset. This is due to the fit for the areal density-kinetic energy relation being performed on a detector geometry with a different steel distribution, thereby slightly changing the conditions. This will have to be done correctly in the future. From these distributions, the median and quartiles are determined for comparison. The median represents the 50% point of the distributions and is chosen, due to the unreasonable outliers, as seen in Figure 72, shifting the mean outside the actual distributions. Figure 74 shows an example of the median and quartiles for the geometry from 55a.

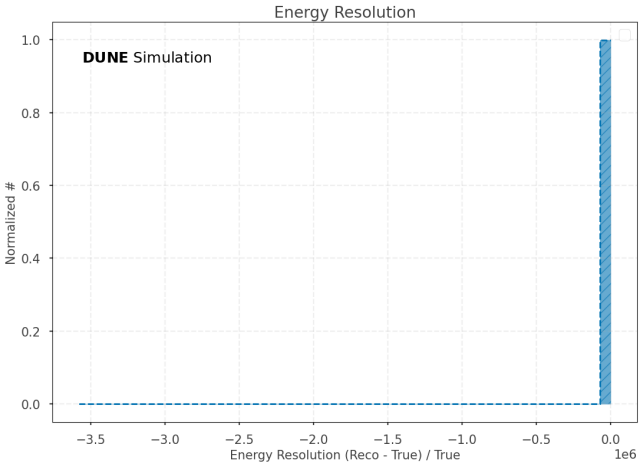

Figure 72: Not-zoomed-in energy resolution for the geometry shown in 55a. The x-axis was scaled automatically during plotting and includes a single entry at around $-3.6e6$

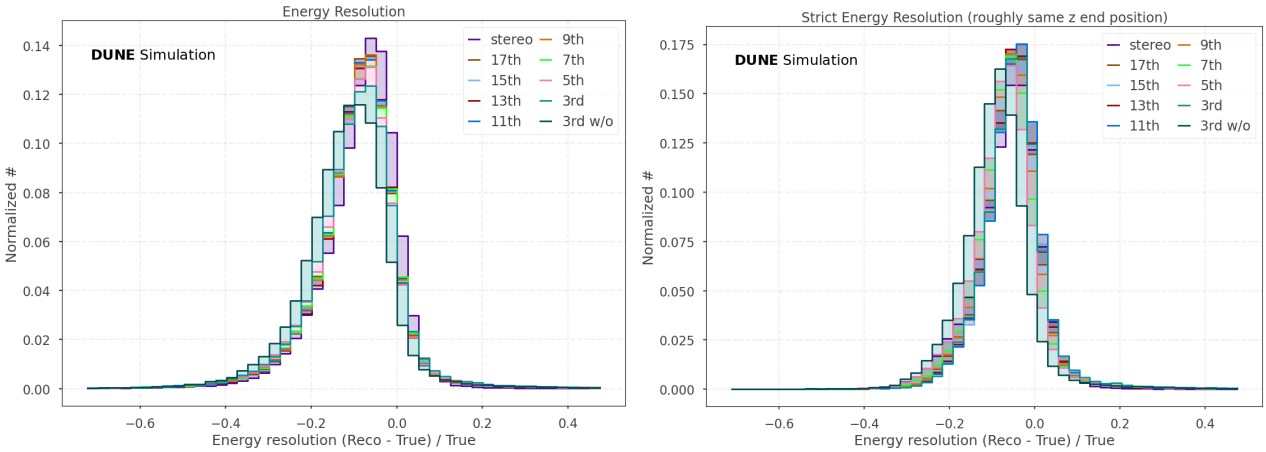

(a) Contained

(b) Contained and end point selection

Figure 73: Zoomed in energy resolution for contained tracks in 73a and contained and with the end point selection in 73b. For the strict selection, all geometries show similar distributions, with only small differences; only the 3^{rd} w/o shows a larger difference in peak position and moves further away from 0. For the non-strict selection, the geometries with the double scintillator layer in the front also behave very similarly and perform between the geometry with X layers (worse) and the stereo geometry (better)

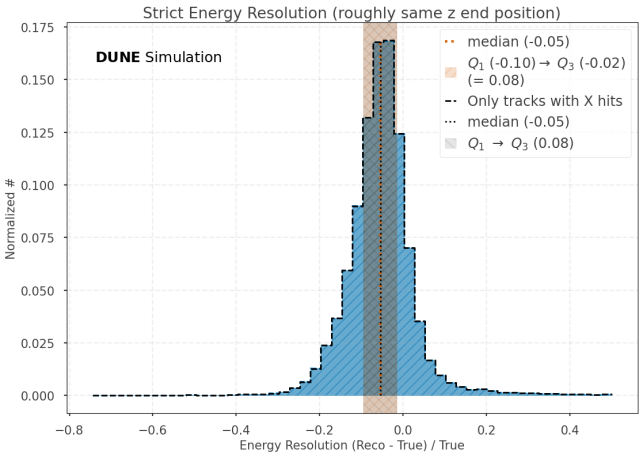

Figure 74: An example for the determination of the median and quartiles of the energy resolution. This is the result for the geometry shown in 55a

3.4.5 Comparison

In the following, the different metrics are evaluated separately and then examined together.

3.4.5.1 Start Point

Having determined the mean and quartiles for all geometries, they are summarized in Table 2 and plotted in Figure 75a. Stereo (w/o) and every 3^{rd} w/o stand here, and in all following cases for the geometries shown in Figures 54a and 54b, with w/o standing for without a double scintillator layer in the front. The other geometries in Figure 55 all include a double scintillator layer at the front.

Geometry	*x*			*y*		
	mean [mm]	$Q_1 \rightarrow Q_3$ [mm]	IQR [mm]	mean [mm]	$Q_1 \rightarrow Q_3$ [mm]	IQR [mm]
stereo w/o	3.2	$-13.6 \rightarrow 18.0$	31.6	-85.5	$-212.7 \rightarrow 80.5$	293.2
17^{th}	3.4	$-15.4 \rightarrow 20.9$	36.3	1.0	$-66.2 \rightarrow 76.6$	142.8
15^{th}	3.5	$-15.4 \rightarrow 21.0$	36.4	3.3	$-63.1 \rightarrow 77.9$	141.0
13^{th}	3.2	$-15.4 \rightarrow 20.6$	36.0	4.2	$-59.8 \rightarrow 72.8$	132.6
11^{th}	3.0	$-15.1 \rightarrow 20.5$	35.6	6.2	$-56.1 \rightarrow 70.8$	126.9
9^{th}	2.9	$-15.2 \rightarrow 20.3$	35.6	7.9	$-52.1 \rightarrow 68.2$	120.3
7^{th}	2.9	$-15.1 \rightarrow 20.1$	35.2	10.7	$-46.8 \rightarrow 66.3$	113.1
5^{th}	2.8	$-15.0 \rightarrow 19.8$	34.8	-2.0	$-41.7 \rightarrow 25.3$	67.0
3^{rd}	3.5	$-15.3 \rightarrow 19.9$	35.2	14.4	$-8.7 \rightarrow 41.4$	50.1
3^{rd} w/o	2.5	$-13.3 \rightarrow 16.3$	29.6	11.6	$-19.1 \rightarrow 29.1$	48.2

Table 2: Mean, quartiles, and inter-quartile distances (IQR) for the start point resolution of all geometries

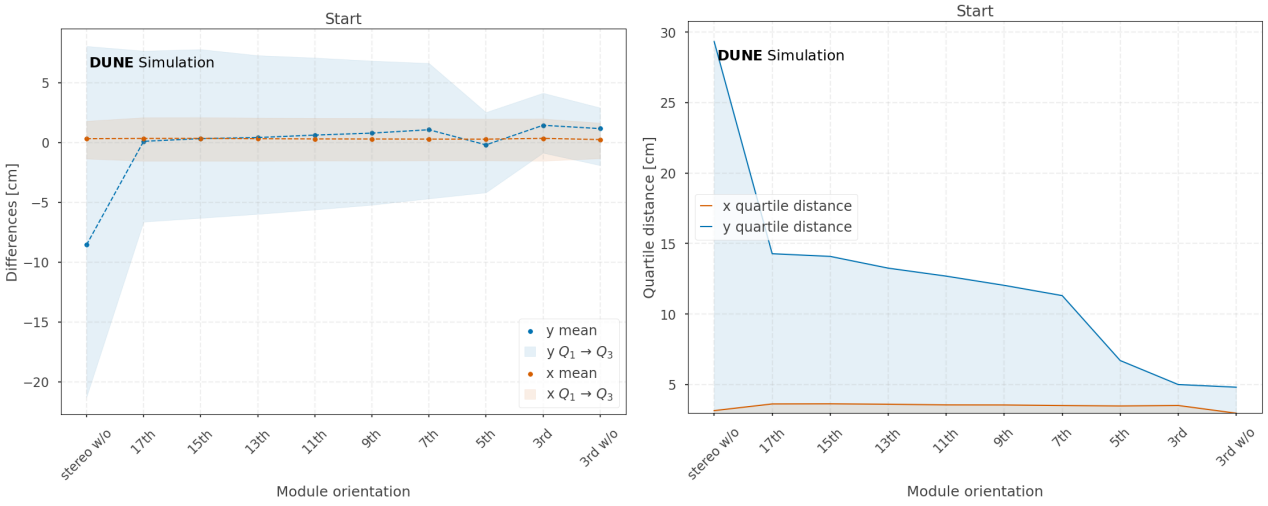

(a) Mean and quartiles

(b) Quartile distances

Figure 75: Start point resolution in comparison for all geometries. 75a shows the mean along with the quartiles, 75b just the distance between the quartiles. Both include the resolution for the *x* (in orange) and *y* (in blue) directions

The consistent positive bias for the *x* direction has likely the exact origin as for the start direction, explained in Figure 68.

From both the plot and the table, it is immediately clear that there are only minimal differences in the start-point resolution in *x*, with the best resolution for the two geometries without the double scintillator layer at the front. In this layout, the next scintillator layer in the *x* direction is closer to the first layer, resulting in a marginally better resolution for the start point in the *x* direction. In the *y* direction, on the other hand, the stereo geometry performs worse than the other geometries, which is to be expected.

The general trend is that the resolution in *y* becomes better the more X layers are introduced into TMS, which proves the effect of them. Figure 75b shows, compared to Figure 75a, only the difference in the distance between the quartiles, referred to as the quartile distance in the following. This distance, divided by two, can be understood as the actual start point resolution in the absence of a standard deviation obtained from a fit.
The quartile distance plot proves the stability of the resolution in the *x* direction at about 3.5 cm. Also, it reveals a plateau-like behavior for the *y* direction between every 17^{th} and 7^{th} layer of about 13 cm. Before this plateau, the resolution in *y* is only about 30 cm; afterwards, it improves to 5 cm in the extreme case of every 3^{rd} layer being an X layer. This indicates that a threshold amount or ratio of X layers must be reached before further improvement in resolution in the *y* direction is possible. Another explanation could be an effect of the minimum hit requirement in the reconstruction, which was attempted to be countered by selecting only tracks containing hits from X layers. An effect arising from the underlying particle energy distribution could be excluded by comparing the distributions across the different geometries.
From the start point resolution comparison alone, the optimal module orientation plan would be a layout with every 3^{rd} layer an X layer, with or without the double-scintillator layer in the front. While the resolution in the *x* direction is slightly better without the double layer, the difference is small enough that it could be due to statistical fluctuations.

3.4.5.2 Start Direction

The mean and quartiles for the start direction can be seen in Table 3 and Figure 76a.

Geometry	*xz*			*yz*		
	mean [°]	$Q_1 \rightarrow Q_3$ [°]	IQR [°]	mean [°]	$Q_1 \rightarrow Q_3$ [°]	IQR [°]
stereo w/o	0.38	$-0.81 \rightarrow 1.62$	2.43	-2.09	$-5.04 \rightarrow 1.73$	6.77
17^{th}	0.37	$-0.81 \rightarrow 1.60$	2.41	-0.18	$-2.20 \rightarrow 2.60$	4.80
15^{th}	0.36	$-0.81 \rightarrow 1.61$	2.42	-0.14	$-2.11 \rightarrow 2.53$	4.64
13^{th}	0.35	$-0.81 \rightarrow 1.58$	2.39	-0.21	$-2.09 \rightarrow 2.29$	4.38
11^{th}	0.35	$-0.81 \rightarrow 1.56$	2.37	-0.21	$-2.02 \rightarrow 2.36$	4.38
9^{th}	0.34	$-0.80 \rightarrow 1.55$	2.37	-0.22	$-2.00 \rightarrow 2.23$	4.23
7^{th}	0.33	$-0.80 \rightarrow 1.53$	2.35	-0.25	$-2.00 \rightarrow 2.11$	4.11
5^{th}	0.31	$-0.82 \rightarrow 1.49$	2.31	-0.43	$-1.63 \rightarrow 1.15$	2.78
3^{rd}	0.29	$-0.85 \rightarrow 1.49$	2.34	-0.43	$-1.19 \rightarrow 0.80$	1.99
3^{rd} w/o	0.28	$-0.81 \rightarrow 1.44$	2.25	-0.23	$-1.05 \rightarrow 0.83$	1.88

Table 3: Mean, quartiles, and inter-quartile distances (IQR) for the start direction resolution of all geometries

While the performance in the *xz* angle remains almost constant for all different geometries, it gets better for the *yz* angle, the more X layers are introduced into the geometry.
In Figure 76b, only the quartile distances are shown. As before, the resolution in *xz* remains almost the same across all geometries at about 2.5°, while in *yz* there is again a plateau between every 17^{th} and 7^{th} layer at about 4.5°. For the stereo case, the resolution in *yz* is at about 7°only, and after the plateau, the resolution goes down to about 2°for every 3^{rd} layer being X.
Overall, the start direction behaves very similarly to the start point, with the optimal module orientation plan for this metric being every 3^{rd} with or without the double scintillator layer in the front.

3.4.5.3 End Point

For the end point, the mean and quartiles are summarized in Table 4 and plotted in Figure 77a.

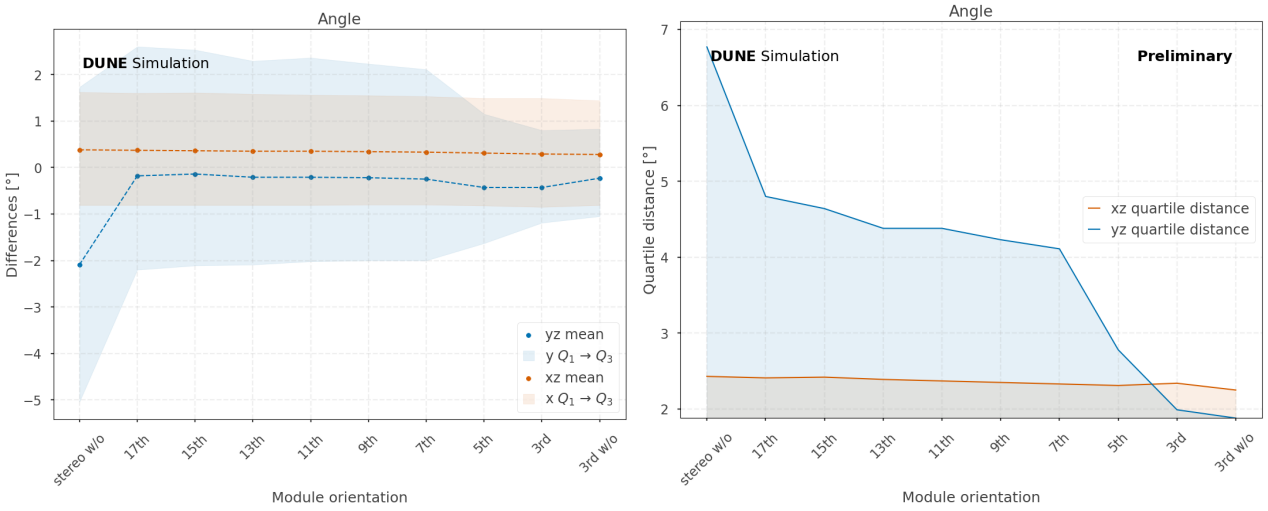

(a) Mean and quartiles

(b) Quartile distances

Figure 76: Start direction resolution in comparison for all geometries. 76a shows the mean along with the quartiles, 76b just the distances between the quartiles. Both include the resolution for the *xz* (in orange) and *yz* (in blue) directions

Geometry	*x*			*y*		
	mean [mm]	$Q_1 \to Q_3$ [mm]	IQR [mm]	mean [mm]	$Q_1 \to Q_3$ [mm]	IQR [mm
stereo w/o	11.0	$-17.2 \to 38.1$	55.3	1.6	$-130.7 \to 144.1$	274.8
17^{th}	11.1	$-20.0 \to 39.5$	59.5	25.5	$-92.5 \to 140.5$	233.0
15^{th}	11.0	$-20.2 \to 39.8$	60.0	28.3	$-92.1 \to 137.6$	229.7
13^{th}	11.2	$-20.3 \to 39.9$	60.2	26.3	$-92.8 \to 136.8$	229.6
11^{th}	11.1	$-20.6 \to 39.9$	60.5	27.7	$-90.7 \to 137.2$	227.9
9^{th}	12.0	$-20.6 \to 40.5$	61.1	23.3	$-90.0 \to 129.9$	219.9
7^{th}	12.3	$-20.9 \to 40.5$	61.4	21.2	$-91.5 \to 128.1$	219.6
5^{th}	15.2	$-20.9 \to 41.2$	62.1	13.8	$-64.9 \to 83.7$	148.6
3^{rd}	29.3	$-22.5 \to 47.2$	69.7	5.0	$-56.9 \to 52.3$	109.2
3^{rd} w/o	27.8	$-26.1 \to 53.0$	79.1	8.2	$-40.7 \to 48.3$	89.0

Table 4: Mean, quartiles, and inter-quartile distances (IQR) for the end point resolution of all geometries

The resolution in both directions roughly follows the same behavior as at the start point, but with a lower overall resolution. This smearing can be explained by the increased difficulty of reconstruction with low-energy hits, which are expected at the ends of contained tracks.
In the *x* direction, the performance appears best for the stereo layout, very slightly worse with the introduction of some X layers, but without any big changes until every 5^{th} layer is X. Then the performance drops off slightly. The differences between the last two layouts show the positive impact of the double scintillator layer at the front, even in the *x* direction at the end point.
In the *y* direction, the same pattern from the start point can be observed with a stable performance for all geometries with every 17^{th} to 7^{th} layer a X layer, improving from the stereo layout and further improving when introducing even more X layers.
Figure 77b summarizes this behavior again by only showing the quartile distances. The resolution in the *x* direction for the end point is about 6 cm in the plateau part, and improves to about 5 cm for the stereo case and 8 cm for every 3^{rd} layer without the double scintillator layer. In the *y* direction, the resolution plateau is even more pronounced than for the start point at around 23 cm and improves to about 9 cm for every 3^{rd} layer without the double layer in the front.
The difference between the two layouts with every 3^{rd} layer X for the end point resolution hints at a prob-

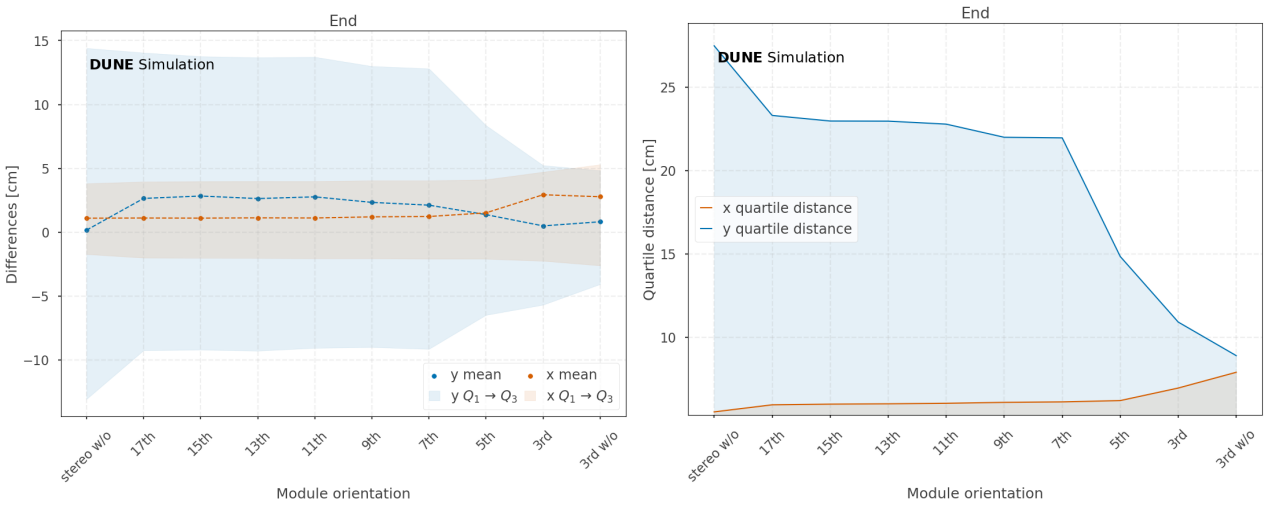

(a) Mean and quartiles

(b) Quartile distances

Figure 77: End point resolution in comparison for all geometries. 77a shows the means and quartiles, 77b the quartile distances. Both include the resolution for the *x* (in orange) and *y* (in blue) directions

lem within the reconstruction, as this small change in geometry at the front of TMS should not impact the resolution of the end point this much.
From the end-point comparison alone, the optimal module orientation plan would be to have every 5^{th} layer be an X layer, balancing the resolutions in the *x* and *y* directions.

3.4.5.4 Charge Identification

The accuracy for the charge identification for the entire energy range from 0.5 to 5 GeV, below 1 GeV, and at 2 GeV can be seen in Table 5 and Figure 76a.

Geometry	**Accuracy**		
	< 1 GeV [%]	2 ± 0.1 GeV [%]	total [%]
stereo w/o	90.37 ± 0.250	99.16 ± 0.163	95.90 ± 0.093
17^{th}	89.53 ± 0.254	99.09 ± 0.166	96.55 ± 0.082
15^{th}	89.73 ± 0.266	99.20 ± 0.166	96.78 ± 0.082
13^{th}	89.80 ± 0.260	98.85 ± 0.186	96.47 ± 0.085
11^{th}	89.52 ± 0.262	98.55 ± 0.214	96.31 ± 0.087
9^{th}	89.17 ± 0.255	98.63 ± 0.201	96.31 ± 0.084
7^{th}	88.95 ± 0.268	98.93 ± 0.186	96.42 ± 0.086
5^{th}	88.15 ± 0.277	98.32 ± 0.241	95.94 ± 0.093
3^{rd}	86.60 ± 0.315	96.05 ± 0.374	94.54 ± 0.113
3^{rd} w/o	84.81 ± 0.326	96.50 ± 0.349	94.51 ± 0.109

Table 5: Accuracies for the charge identification of all geometries

The accuracy for 2 GeV muons of mostly about 99% is better than the total accuracy of about 96%. In comparison, for the very low energetic muons, it is even lower at about 89%. In all three energy range cases, the accuracy remains mostly stable with the addition of more X layers up until every 5^{th} or more layer is X. For these geometries, the accuracy goes down. For low energy muons, every 13^{th} being X has the highest accuracy apart from the stereo layout, with the differences being statistically insignificant, which can be very clearly seen in Figure 78b displaying the difference in percentage points from the accuracy of the stereo case.

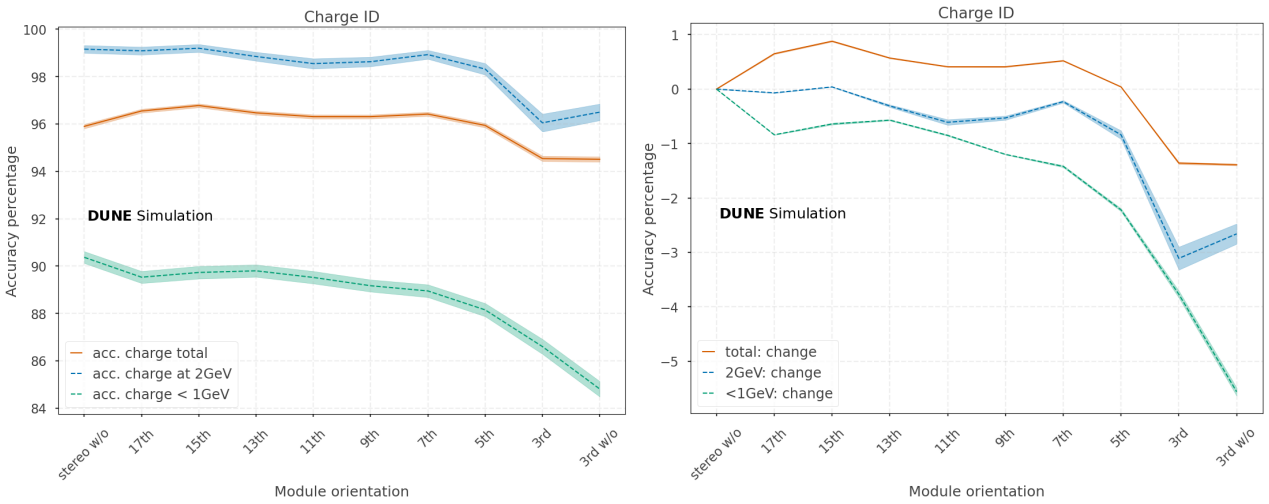

(a) Accuracy

(b) Accuracy change

Figure 78: Charge identification accuracy in comparison for all geometries. 78a shows the accuracy; 78b shows only the change in accuracy with respect to the stereo layout. Both include the charge identification performance for the full energy range (in orange), for an energy of 2 GeV (in blue), and for the low energy area (in green)

For 2 GeV the highest accuracy on the other hand is achieved with every 15^{th} layer X, even slightly better than for the stereo layout, and a second high peak[44] for every 7^{th} layer X. These peaks stem most likely from reconstruction effects changing the sample phase space and would not be expected if repeating this study on a truth level. For more X layers, the accuracy drops by at least 2% across all energies.
Over the total energy range, the highest accuracy is also achieved with every 15^{th} layer X, with all layouts between every 17^{th} and every 5^{th} performing better than the stereo case. A possible explanation for this effect might be given by Figures 34 and 79. Compared to all the other geometries, the fraction of $\mu^{\pm}$ for the stereo case drops off way sooner. So fewer high-energy muons appear to be in the selection of this data set. In this way, the number of lower-energy muons, which are less efficiently identified, is higher, lowering the overall accuracy for this layout.

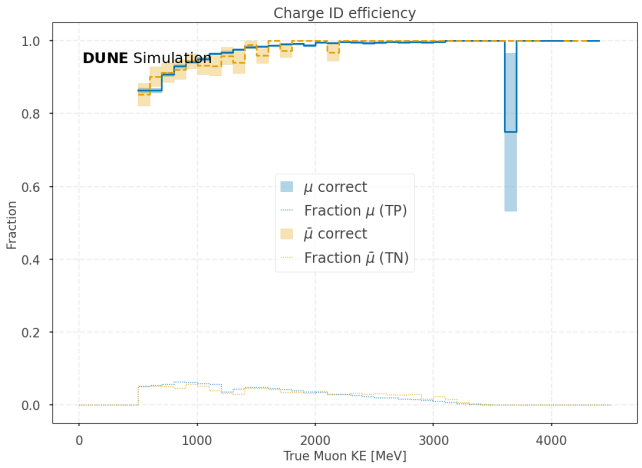

Figure 79: Charge identification efficiency and fraction of correctly identified particles for the stereo geometry

Assuming a higher accuracy for the stereo case from a more similar data set, as it can be observed for the smaller energy ranges, the accuracy for the total energy range behaves similarly to the performance of the 2 GeV curve.
For the charge identification alone, the optimal module orientation plan for the entire energy range (500 MeV to 4.5 GeV) targeted by the current TMS design would be either the stereo layout or every 15^{th}

[44] Apart from the stereo layout

layer being a X layer[45].

3.4.5.5 Energy Resolution

The medians and quartiles for all geometries of the energy resolution (relative residuals) are shown in Table 6 and Figure 80a.

Geometry	median	$Q_1 \rightarrow Q_3$	IQR
stereo w/o	-0.063	$-0.114 \rightarrow -0.023$	0.091
17^{th}	-0.055	$-0.096 \rightarrow -0.018$	0.078
15^{th}	-0.054	$-0.095 \rightarrow -0.017$	0.078
13^{th}	-0.054	$-0.096 \rightarrow -0.018$	0.078
11^{th}	-0.054	$-0.095 \rightarrow -0.017$	0.078
9^{th}	-0.055	$-0.095 \rightarrow -0.017$	0.078
7^{th}	-0.053	$-0.095 \rightarrow -0.016$	0.079
5^{th}	-0.056	$-0.100 \rightarrow -0.018$	0.082
3^{rd}	-0.054	$-0.095 \rightarrow -0.016$	0.079
3^{rd} w/o	-0.120	$-0.182 \rightarrow -0.074$	0.108

Table 6: Median, quartiles, and inter-quartile distances for the energy resolution of all geometries

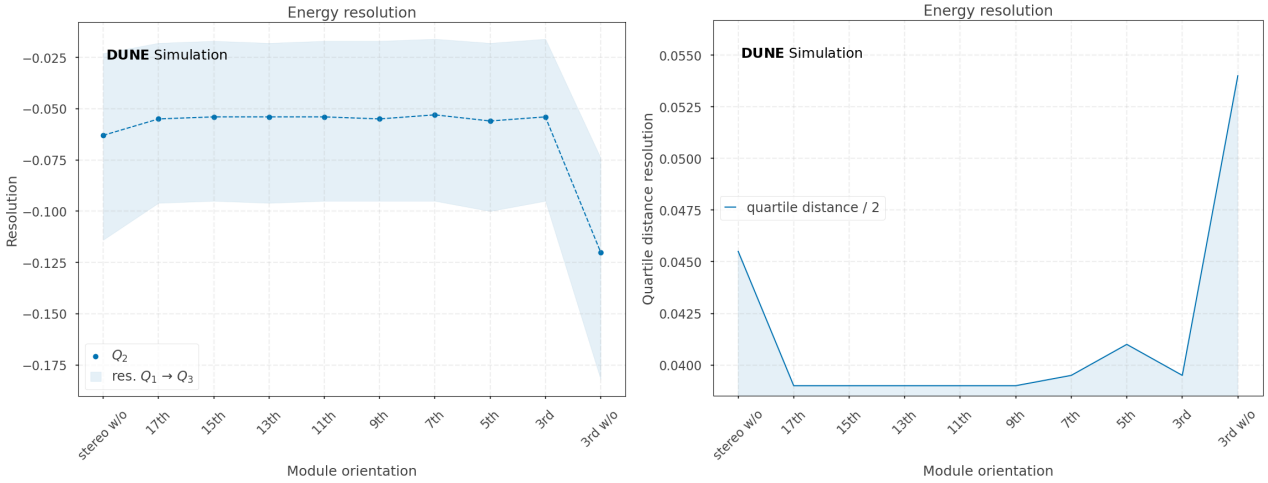

(a) Median and quartiles

(b) Quartile distances divided by 2

Figure 80: Energy resolution in comparison for all geometries. 80a shows the median and the quartiles, 80b just the half distance between the quartiles

A very stable energy resolution behavior is observed across most geometries. A small outlier is the stereo geometry with a median energy resolution of -0.06, dropping slightly below the average median plateau of close to -0.50. The biggest change is observed at every 3^{rd} without the double layer in the front, with the median dropping below -0.1.

The quartile distances divided by two are shown in Figure 80b. This division is done to allow easier comparison with the standard deviation, given in the requirements, which reflects the actual energy resolution. Apart from the outliers already seen in Figure 80a, a constant energy resolution between every 17^{th} and 9^{th} layer, with X, is visible, with a rise in resolution with more X layers. In addition, the positive effect of the double scintillator layer in the front becomes very clear when comparing the two different geometries with every 3^{rd} layer being X.

For the energy resolution alone, the optimal module orientation would be any of the options between 17^{th} and 9^{th}.

[45] Depending on a more comparable data set for the stereo layout.

3.4.5.6 Combining the Metrics

The different metrics yield different optimal module orientation plans.

- Start point: every 3^{rd} layer with or without a double scintillator layer in the front
- Start direction: every 3^{rd} layer with or without a double scintillator layer in the front
- End point: every 5^{th} layer with a double scintillator layer in the front
- Charge identification: every 15^{th} layer or every 7^{th} layer with a double scintillator layer in the front
- Energy resolution: any of the geometries between every 17^{th} and every 9^{th} layer with a double scintillator layer in the front

The optimal module orientation therefore has to balance the different metrics to achieve the best possible performance of TMS. The main task for TMS is to distinguish μ^- and μ^+ through the charge identification and determining the energy of contained muons. Hence, these two metrics carry the most weight in the decision.
Considering this, the optimal module orientation among those studied here is for every 7^{th} layer to be an X layer, balancing energy resolution with the end point while maintaining good charge identification performance. This is also a good choice for the start point and start direction, being, in both cases, the end of the stable performance plateau for the *y* direction and the *yz* angle.

3.4.6 Fine Tuning of Geometries

The module orientation options looked at so far all have the same number of scintillator layers between two X layers. However, this is not the only option to consider. For example, having different (constant) ratios of X to stereo layers in the parts with different steel thicknesses, having the same amount of steel density-wise in between X layers, or non-constant distributions of X layers throughout the detector are all interesting options to consider.
In the following, a variation of the latter option is considered, with a higher ratio of X layers at the very front, then moving to the identified best module orientation plan, with every 7^{th} layer being X for the rest of the detector. The higher ratio in the front is achieved by adding sets of one X, one U, and one V layer in the front. Three variations of this are shown in Figure 81, with one set in 81a, two sets in 81b, and three sets in 81c.

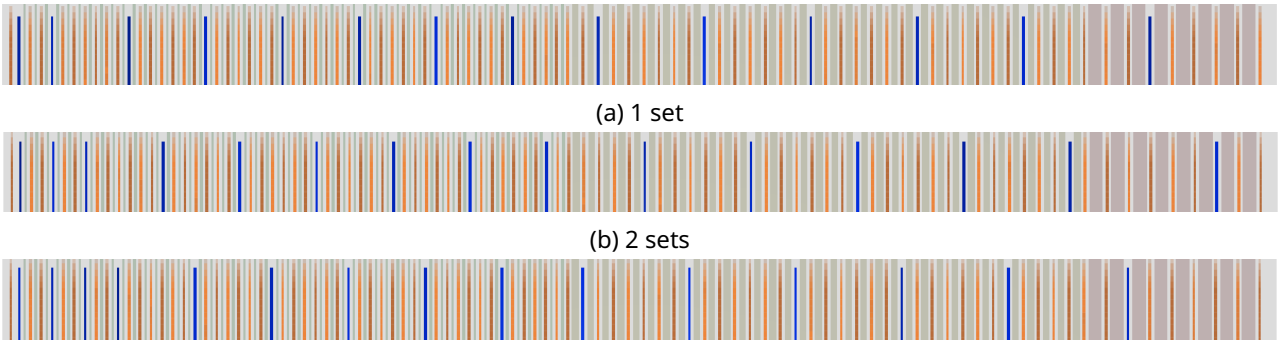

(a) 1 set

(b) 2 sets

(c) 3 sets

Figure 81: Cutouts of the different geometries with XUV sets in the front. X layers are shown in blue, stereo layers in orange. After the sets in the front, the rest of the scintillator layers use the module orientation plan with every 7^{th} layer being X

The comparison metrics are the same as those used before. The same selection as for the pure every 7^{th} layer being X layout is used as well, allowing for an easy performance comparison.

3.4.6.1 Start Point

The start point distributions in the *x* and *y* directions for the three options, as well as for the base pure layout, are shown in Figure 82.

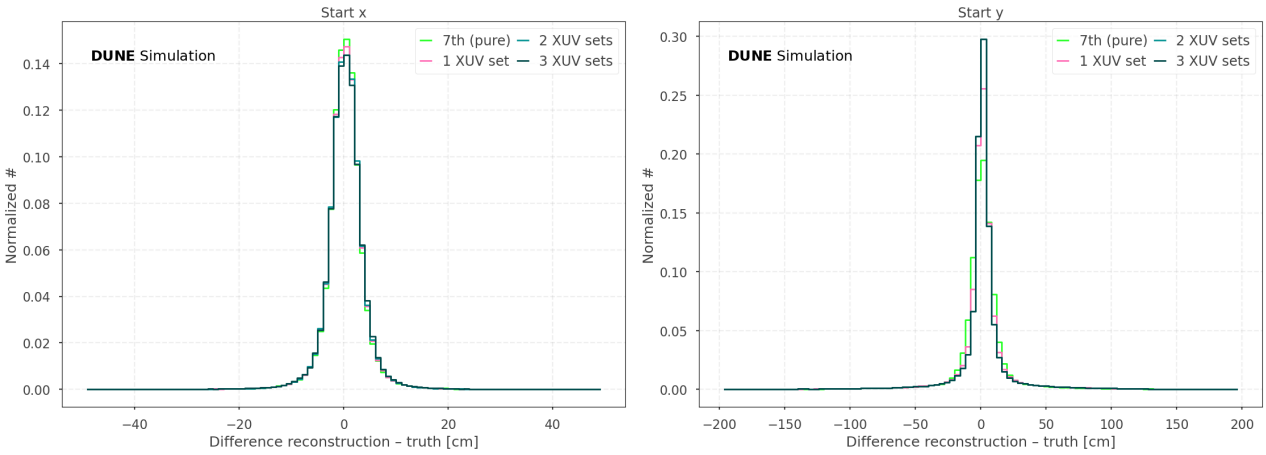

(a) *x* (b) *y*

Figure 82: Start point resolution in *x* direction in 82a and *y* in 82b for the three geometries with added XUV sets in the front and the pure every 7^{th} layout. The distributions in 82a broaden and have lower peak heights as more sets are introduced at the front. For the *y* direction, the opposite of the *x* direction holds, with better performance for more sets introduced. Overall the changes in *x* are small compared to the changes for *y*

As before, the distributions for the *x* direction differ only slightly. The pure layout is slightly narrower with a higher peak. The more sets are introduced at the front, the wider the distributions become and the lower the peaks. In the *y* direction, the opposite is the case, with more sets in the front making the distributions narrower and peak higher.
The mean and quartiles are shown in Table 7 and Figure 83.

Geometry	*x*			*y*		
	mean [mm]	$Q_1 \rightarrow Q_3$ [mm]	IQR [mm]	mean [mm]	$Q_1 \rightarrow Q_3$ [mm]	IQR [mm]
7^{th} pure	2.86	$-15.07 \rightarrow 20.06$	35.13	10.69	$-46.82 \rightarrow 66.27$	113.12
1 set	3.08	$-15.36 \rightarrow 20.67$	36.03	15.33	$-29.55 \rightarrow 56.45$	86.00
2 sets	3.49	$-15.48 \rightarrow 21.13$	36.61	17.53	$-21.55 \rightarrow 51.38$	72.93
3 sets	3.81	$-15.58 \rightarrow 21.48$	37.06	18.77	$-17.43 \rightarrow 48.84$	66.27

Table 7: Mean, quartiles, and inter-quartile distances for the start point resolution of all geometries

The performance for the start point remains the same in the *x* direction, with a minimal broadening of the quartile distance with more introduced sets of about 2 mm. In the *y* direction, on the other hand, the introduction of sets steadily narrows the quartiles by about 4 cm from pure to three sets.
Given the minimal worsening in the *x* direction, the optimal layout for the start point resolution is the one with three XUV sets.

3.4.6.2 Start Direction

The distributions for the start directions in *xz* and *yz* are shown in Figure 84.
The distributions of the four layouts differ only slightly in both directions. In the *xz* direction, the pure layout is slightly narrower and taller, and in the *yz* direction, the ones with sets are slightly taller. The mean and quartile distances are shown in Table 8 and Figure 85.
Similar to the start point resolution, the performance at the *xz* angle remains very similar. The resolution from the quartile distance broadens by 0.13°. In the *yz* angle, performance improves as well, but the

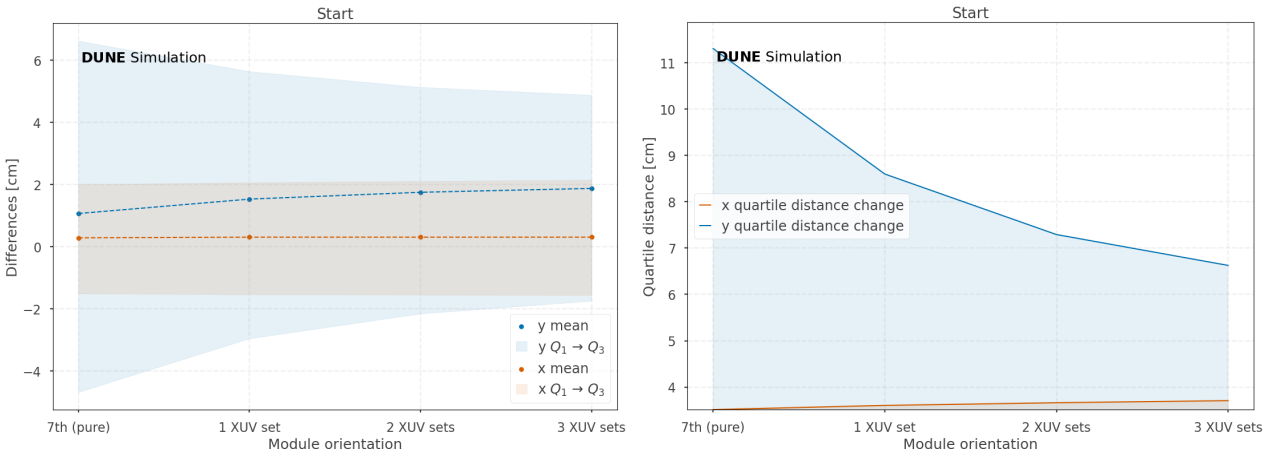

(a) Mean and quartiles

(b) Quartile distances

Figure 83: Mean and quartiles of the start point for all geometries in 83a and the quartile distances in 83b. The performance in the *x* direction is shown in orange, and that in the *y* direction in blue. The increase in the mean of the *y* direction is caused by the addition of more XUV groups in the front, which on their own perform slightly worse in reflecting the neutrino beam pointing downwards than the pure 7^{th} geometry, as explained in Figure 68

Geometry	*xz*			*yz*		
	mean [°]	$Q_1 \rightarrow Q_3$ [°]	IQR [°]	mean [°]	$Q_1 \rightarrow Q_3$ [°]	IQR [°]
7^{th} (pure)	0.33	$-0.80 \rightarrow 1.53$	2.33	-0.25	$-2.00 \rightarrow 2.11$	4.11
1 set	0.33	$-0.81 \rightarrow 1.56$	2.37	-0.07	$-1.74 \rightarrow 2.14$	3.88
2 sets	0.34	$-0.83 \rightarrow 1.58$	2.41	-0.09	$-1.73 \rightarrow 2.05$	3.78
3 sets	0.35	$-0.84 \rightarrow 1.62$	2.46	-0.21	$-1.87 \rightarrow 1.94$	3.81

Table 8: Mean, quartiles, and inter-quartile distances for the start direction resolution of all geometries

smallest quartile distance between the two sets is only slightly smaller. The quartile distance resolution improves here from about 4.1° to about 3.8°.
In this way, the optimal layout for the start direction is the one with two XUV sets.

3.4.6.3 End Point

The distributions of the end points are shown in Figure 86.
For the end point, even though the front module orientation layout should not have a significant impact, small differences are still visible. In the *x* direction, as for the start point, the pure layout performs best, and the distribution becomes wider and the peak lower with more sets introduced. In the *y* direction, though, the best performance comes from the pure and one set geometries, while the other two are slightly wider and have lower peaks.
The differences seen here could either be caused by (probably the same) reconstruction effect as seen in the comparison of every 3^{rd} with and without a double scintillator layer in the front, or, a bit less likely, by very low energetic muons entering TMS from the front and only traveling very short paths. This second explanation is less likely due to requiring at least 14 hits in a track to be used in the analysis, as well as only very few muons making it out of ND-LAr in this energy range. For muons with an energy of 500 MeV, about 30 hits within the thin steel part of TMS are expected. This makes the other explanation more likely.
The mean and quartile distances are shown in Table 9 and Figure 87.
As expected, the changes from the layout differences at the front of the detector are minimal for the end point resolution. For both directions, the resolution stays almost the same. In the *y* direction, a small dip in resolution is observed in one set, followed by a small increase across more XUV sets. Reconstruction

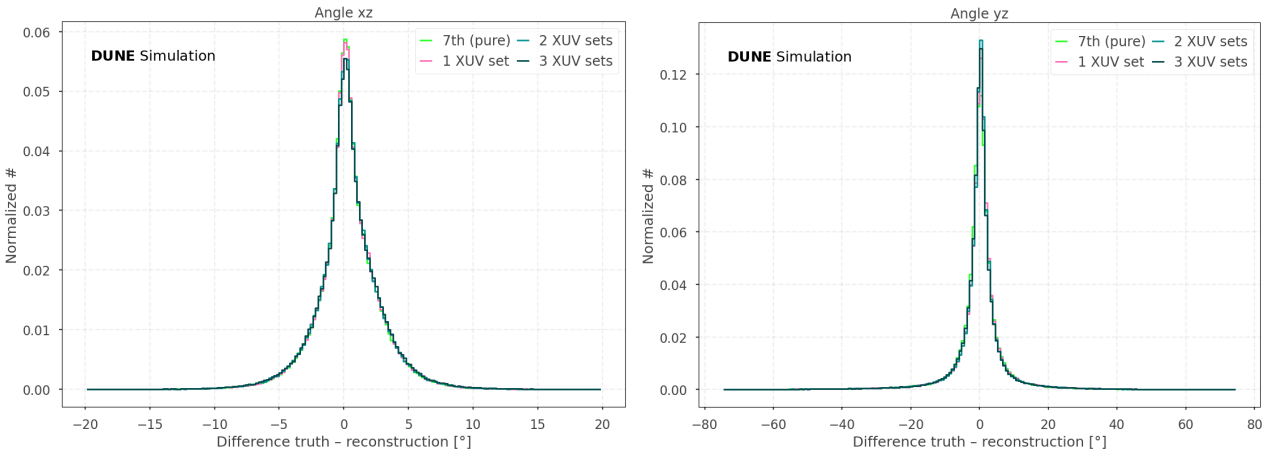

(a) *xz* (b) *yz*

Figure 84: Start direction resolution for *xz* in 84a and *yz* in 84b for all geometries. The distributions for *xz* broaden and have lower peaks as more sets are introduced, whereas the opposite is mostly true for *yz*. The layout with two sets has a slightly higher peak than the one with three sets in the front. Overall, the differences are minimal

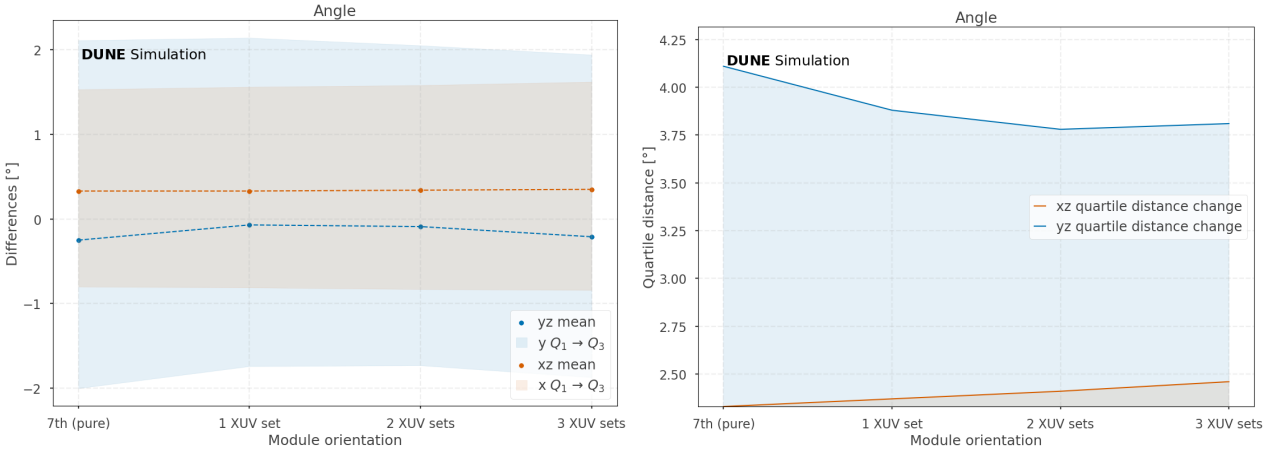

(a) Mean and quartiles (b) Quartile distances

Figure 85: Mean and quartiles for the start direction resolution in 85a and the quartile distances in 85b for all geometries. The *xz* direction is shown in orange, *yz* in blue

effects could well explain this difference.
From the end point alone, either the pure layout or the one with one set is optimal.

3.4.6.4 Charge Identification

The efficiencies for identification of μ^- and μ^+ are shown in Figure 88.
There are some differences between the layouts; however, they fall well within the range of statistical noise, as shown in Figure 89.
The usual trend of better performance with more or fewer introduced sets is not evident in the plots. In the lower-energy range, while having one set seems better than having more, as expected for lower-energy muons, having three sets is more efficient than two, which is slightly unexpected. For the 2 GeV bins, it is tough to say from the plots alone. Overall, it seems that having two sets has a slightly higher efficiency than one or three sets. All these differences might stem from reconstruction effects, though, as seen before.
The accuracies and their changes are shown in Table 10 and Figure 90.
Overall, the accuracy for all layouts stays very stable. The changes are on the order of $< 1\%$. The accuracy

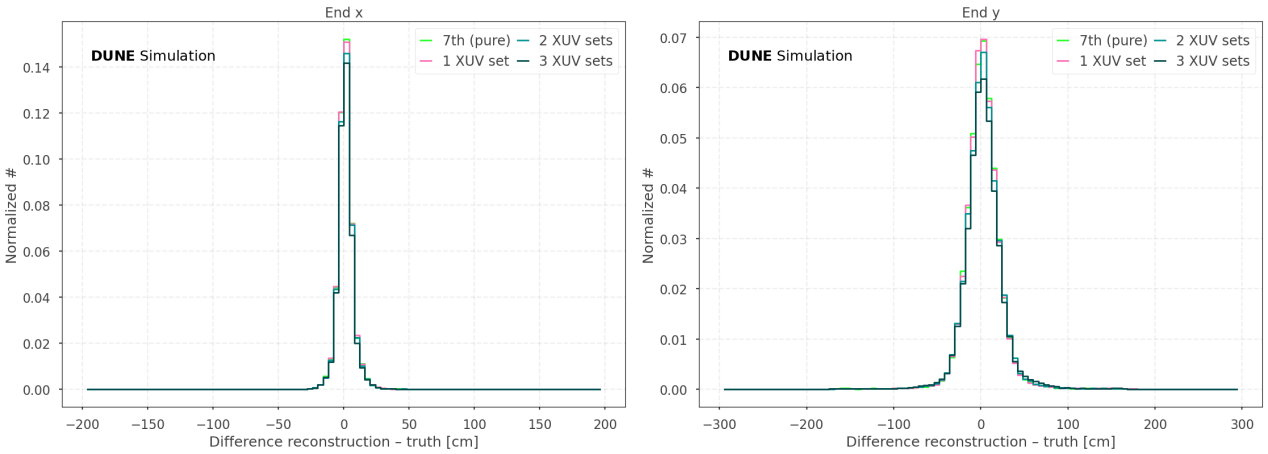

(a) x (b) y

Figure 86: End point resolution for all geometries for x in 86a and y in 86b. The more XUV sets are introduced in the front, the lower the peak in x and y. One set has a similar peak height as the pure layout in both directions

Geometry	x			y		
	mean [mm]	$Q_1 \rightarrow Q_3$ [mm]	IQR [mm]	mean [mm]	$Q_1 \rightarrow Q_3$ [mm]	IQR [mm]
7^{th} (pure)	12.29	$-20.88 \rightarrow 40.45$	61.33	21.17	$-91.48 \rightarrow 128.10$	219.58
1 set	13.09	$-21.11 \rightarrow 40.89$	62.00	21.70	$-89.52 \rightarrow 126.79$	216.31
2 sets	13.50	$-21.06 \rightarrow 41.14$	62.74	24.41	$-90.46 \rightarrow 133.24$	223.66
3 sets	12.27	$-21.08 \rightarrow 39.85$	60.93	26.08	$-91.77 \rightarrow 135.60$	227.37

Table 9: Mean and quartiles for the end point resolution of all geometries

is the highest for the pure layout. For two sets, although the low-energy accuracy is the lowest and the accuracy at 2 GeV is not peaking, the total accuracy is excellent, driven by the charge identification performance at higher energies. For three sets, although the low-energy accuracy and that for 2 GeV are increasing, the total accuracy drops slightly from before, also due to the higher-energy performance. All these changes are minimal, though, and could easily be due to reconstruction effects.
The optimal layout for the charge identification is not to introduce XUV sets into the detector at the front.

3.4.6.5 Energy Resolution

The energy resolution from strict end point selection is shown in Figure 91.
A noticeable difference between the layouts is that the introduction of XUV sets at the front seemingly shifts the energy-resolution distributions further toward 0. Even though the peak positions of the distributions move only marginally, there is a shift of events from the left to the right. The differences between the three different layouts are then small though.
The medians and quartile distances are shown in Table 11 and Figure 92.
The energy resolution performance remains the same across the different layouts. Compared to the previous scan study, the changes shown in 92b are minimal and not statistically significant.
Based solely on the energy resolution, the optimal layout would be one with two XUV sets added at the front.

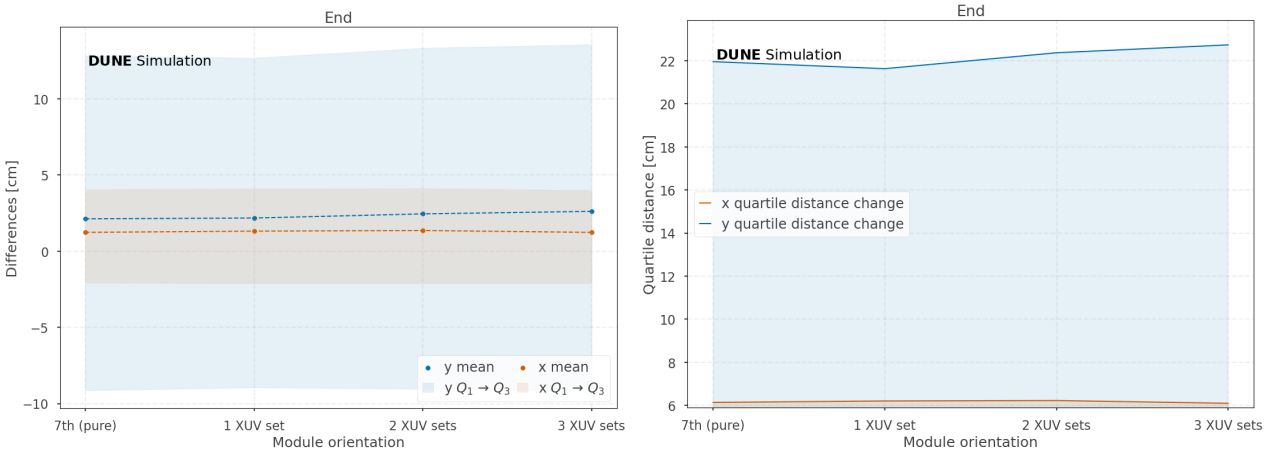

(a) Mean and quartiles

(b) Quartile distances

Figure 87: Mean and quartiles for all geometries of the end point in 87a and the quartile distances in 87b. The performance in the *x* direction is shown in orange, *y* in blue

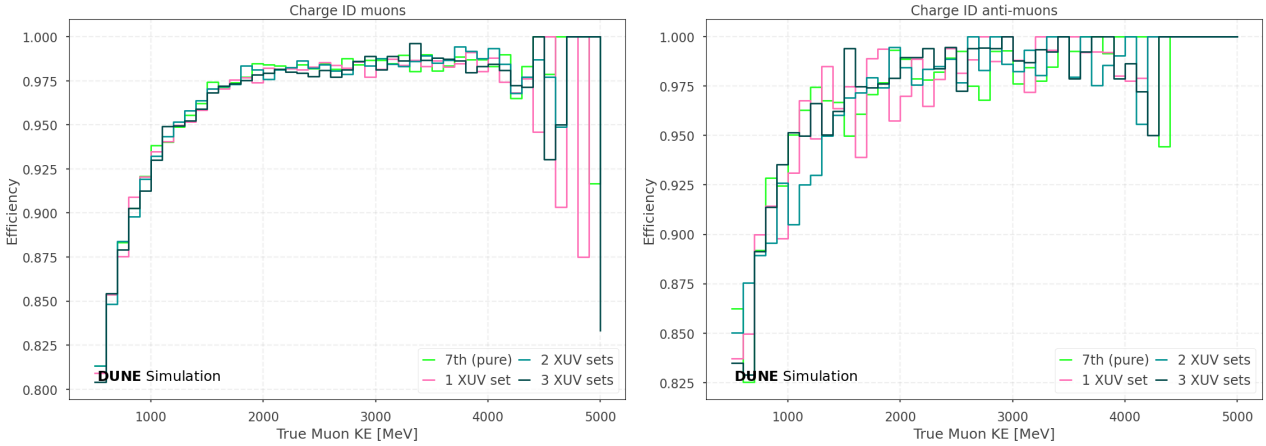

(a) μ^-

(b) μ^+

Figure 88: The charge identification efficiencies for μ^- in 88a and for μ^+ in 88b. The efficiencies for the different true kinetic muon energies are all similar, with only small changes between the different geometries

3.4.6.6 Combining the Metrics

The different metrics yield different optimal module orientations.

- Start point: three sets
- Start direction: two sets
- End point: pure or one set
- Charge identification: pure
- Energy resolution: two sets

As before, all metrics must be considered and weighed against one another. Given the small changes in charge identification performance, the improvement in the *yz* angle of the start direction, and the energy resolution for two XUV sets, the two XUV sets layout is slightly better suited for TMS than the layout without the sets added to the front.

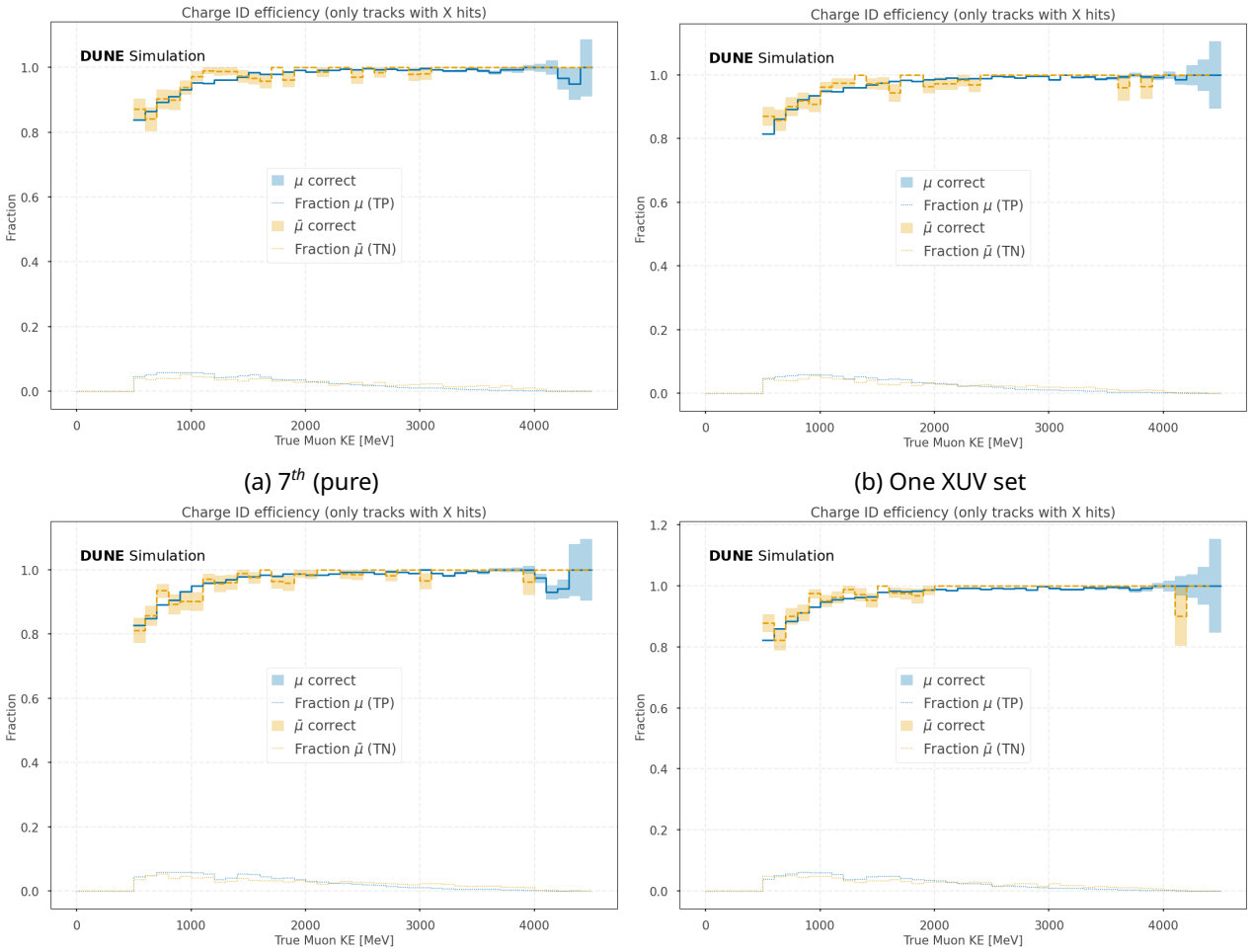

(a) 7^{th} (pure)

(b) One XUV set

(c) Two XUV sets

(d) Three XUV sets

Figure 89: The charge identification efficiencies along with their uncertainties and the respective fraction of $\mu^{\pm}$ for each energy bin between 500 MeV and 4.5 GeV for the different geometries. Blue shows the performance for true μ^{-}, orange for μ^{+}. The pure layout is shown in 89a, one set in 89b, two sets in 89c and three sets in 89d

3.5 Conclusion and Outlook

TMS is required to measure the energy and determine the charge of forward-going muons entering its front face from ND-LAr with energies between $\sim$ 1 and 5 GeV. It is also necessary to match TMS tracks with ND-LAr events as well as determine whether a muon stopped in TMS or left it on the sides (*x* and *y*). To test if these requirements are met, neutrino events were simulated with GENIE and GEANT4 in ND-LAr with muons traveling into TMS. These muon hits were then reconstructed using time slicing, pattern recognition, and a Kalman filter to produce tracks. From these tracks, the muon charge, energy, start and end positions, and start direction were then determined.

To test how well the requirements were met for different module orientation plans, about 100, 000 muon events were generated for each geometry. These geometries were a stereo layout with only U and V modules, a layout with every third layer an X layer, and U and V layers in between. Also, a layout with a double scintillator layer in front was studied for X layers ranging from every third to every 17th.

The performances of these geometries were then compared in identifying the start and end points in the *x* and *y* directions, the start direction in the *xz* and *yz* directions, and the charge, as well as determining the energy resolution with respect to the truth information from the simulation. The best balance between the different metrics was achieved with every 7th layer an X layer, and it was concluded that the double scintillator layer in the front is improving the performance as well.

Afterwards, a fine-tuning study of this geometry was performed by examining the insertion of XUV sets

Geometry	Accuracy		
	< 1 GeV [%]	2 GeV [%]	total [%]
7^{th} (pure)	88.95 ± 0.268	98.93 ± 0.186	96.42 ± 0.086
1 set	88.75 ± 0.219	98.47 ± 0.259	95.98 ± 0.087
2 sets	88.32 ± 0.268	98.57 ± 0.209	96.30 ± 0.085
3 sets	88.60 ± 0.271	98.71 ± 0.200	96.27 ± 0.087

Table 10: Accuracies for the charge identification of all geometries

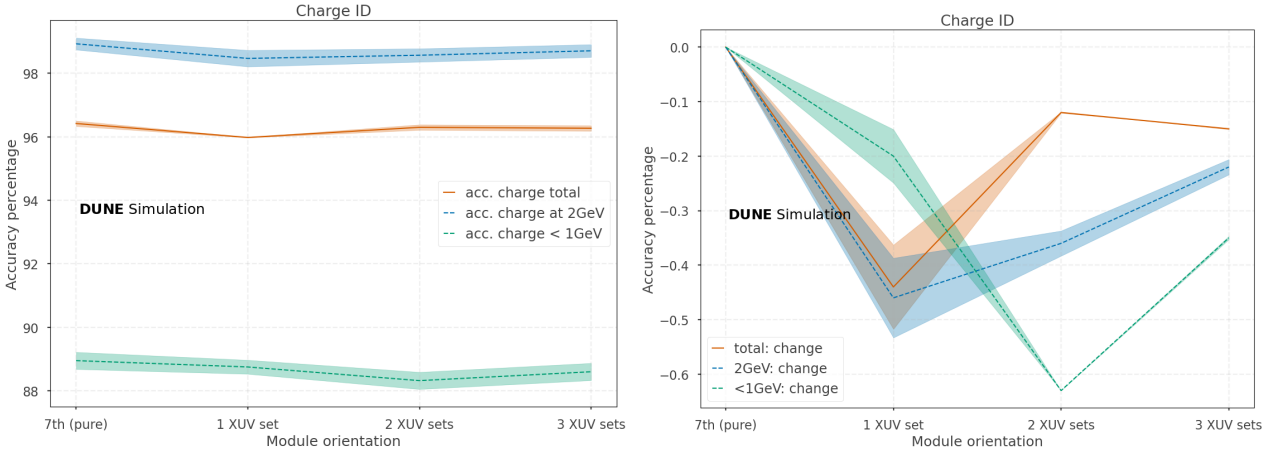

(a) Accuracy

(b) Accuracy change

Figure 90: The charge identification accuracy for all geometries is shown in 90a and the accuracy changes compared to the pure layout in 90b

at the front. One, two, and three sets were tested, where, after the last layer of each set, the geometry 'returns' to every 7^{th} layer an X layer. The performance of these geometries was tested using the same metrics as before, yielding the result that two sets in the front perform best. The performance of this geometry can be seen in Table 12.

Due to a reinvestigation of the stopping power, the steel layout of TMS has been revised with now 34 thin, 22 thick, and 24 double thick steel layers. This reduces the total number of scintillator layers from 94 to 82, while keeping the double layer at the front and a single layer at the back after the last steel layer. The physics performance with the here-developed metrics will need to be re-evaluated. In addition, a study without a filter for only contained muons would be interesting.

The reconstruction is expected to improve in the future. This will most likely enhance the energy resolution and charge identification performances. Current ideas for improvement include fine-tuning the extrapolation parameters, incorporating hits into clusters in the Kalman filter stage, and reworking the pattern recognition using a pure A* algorithm. Reconstruction based on Machine Learning with Pandora or SPINE is also in development and could drastically improve the current performance.

In the future, the geometry may change further. The performance metrics of this work will enable easy comparison with previous geometry iterations.

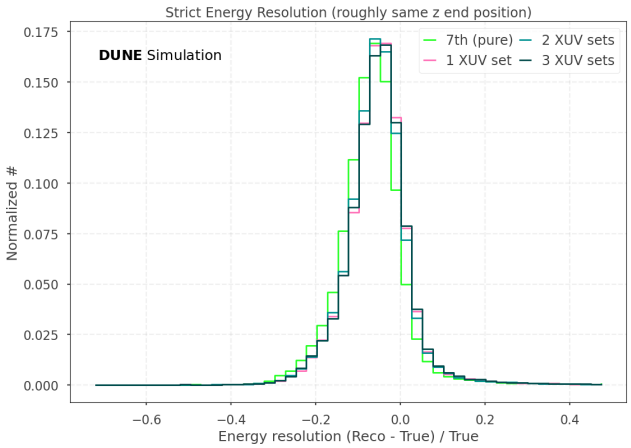

Figure 91: The energy resolution for all geometries. The layouts with XUV sets introduced in the front are shifted slightly to the right towards 0 than for the pure layout. The peak heights stay roughly the same

Geometry	**median**	$Q_1 \to Q_3$	**IQR**
7^{th} (pure)	-0.053	$-0.095 \to -0.016$	0.079
1 set	-0.053	$-0.095 \to -0.015$	0.080
2 sets	-0.053	$-0.093 \to -0.015$	0.078
3 sets	-0.051	$-0.094 \to -0.013$	0.081

Table 11: Median, quartiles, and inter-quartile distances for the energy resolution of all geometries

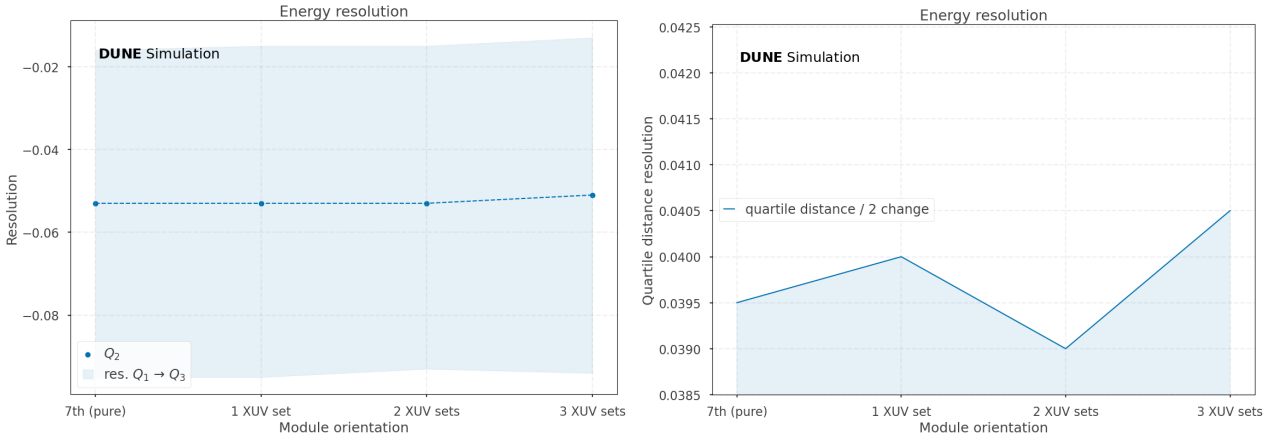

(a) Median and quartiles

(b) Quartile distances divided by 2

Figure 92: The median and quartiles for all geometries for the energy resolution in 92a and the quartile distances divided by two in 92b

Metric	**Value** 1	**Value** 2	**Value** 3
Start point (x)	mean: 3.49 mm	IQR: 36.61 mm	
Start point (y)	mean: 17.53 mm	IQR: 72.93 mm	
Start direction (xz)	mean: 0.34°	IQR: 2.41°	
Start direction (yz)	mean: -0.09°	IQR: 3.78°	
End point (x)	mean: 13.50 mm	IQR: 62.74 mm	
End point (y)	mean: 24.41 mm	IQR: 223.66 mm	
Charge ID accuracy	$<$ 1 GeV: 88.32 ± 0.268 %	2 GeV: 98.57 ± 0.209 %	total: 96.30 ± 0.085 %
Energy resolution	median: -0.053	IQR: 0.078	

Table 12: Performance of every 7th layer being an X layer, two sets of XUV in the front, and a double scintillator layer in the front

4 Neutron and Gamma Tagging with Pulse Shape Discriminating Plastic Scintillator

In the following, a more detailed introduction to scintillator physics is given, with a different use case than in the Introduction chapter. Based on this, a study on neutron and gamma tagging in a plastic scintillator is described. This study describes the setup and data-taking procedures. Finally, the data handling and analysis are presented. The analysis has multiple steps and different methods. At first, the first analysis method is explained and fully explored, and discussed afterwards in detail. Then another analysis method is studied and discussed. At last, the two methods are combined, and the result is discussed in detail again. Also, a potential cosmic muon background is studied.
The tagging and analysis methods described could potentially also be used in a DUNE Phase 2 detector.

4.1 Introduction to Scintillator Physics

Scintillation is the emission of UV or visible light from a material under excitation from high-energy photons (X-rays, γ-rays) or energetic particles ($e^{\pm}$, α, n, p, ions, etc.). A material that exhibits this behavior is called a scintillator. For electrons, positrons, and gammas, the amount of scintillation light is proportional to the deposited energy in the material [4].
In general, the scintillation process has three main stages: conversion, transport and energy transfer, and luminescence [60]. In the conversion stage, the energy from incident radiation is absorbed. For organic scintillators, delocalized π-electrons from π-orbitals are excited by the radiation.
In the transport and energy transfer stage, following the absorption stage, the molecule undergoes a transition to the S_1 (singlet) or T_1 (triplet) state via molecular vibrations. A sketch showing this process is shown in Figure 93.

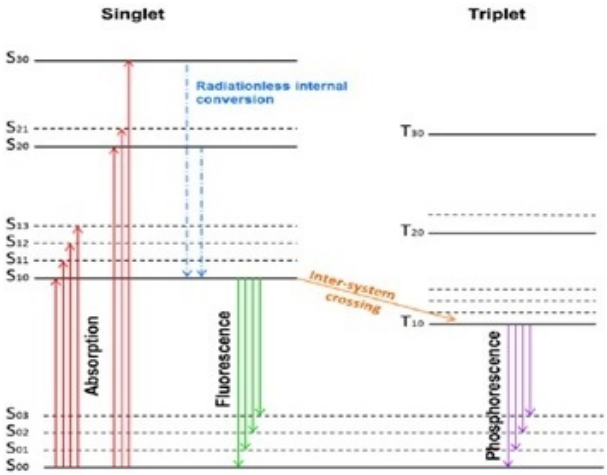

Figure 93: π-electronic energy levels of an organic molecule. Energy is first absorbed in the conversion stage, transported and transferred, and then finally emitted in the luminescence stage. The luminescence stage, fluorescence and phosphorescence are possible, depending on the state of emission (singlet or triplet). S_0 is the ground state. S_1, S_2, S_3 are excited singlet states. T_1, T_2, T_3 are excited triplet states. S_{00}, S_{01}, S_{10}, S_{11}, etc. are vibrational sublevels [61]

The third stage of the scintillation process is the de-excitation to the S_0 state. For the singlet states, this is immediate and therefore referred to as fluorescence, as shown in Figure 93. In triplet states, this decay can occur over a much longer time and is called phosphorescence. The fluorescence is often called the fast component, while the phosphorescence is called the slow component.
Depending on the particular energy loss of a certain particle, the singlet and triplet states are occupied in different proportions. The differences in light yield, due to the different energy loss mechanisms, are empirically described by Birk's Law [62]

$$\frac{dL}{dx} = S\frac{\frac{dE}{dx}}{1 + kB\frac{dE}{dx}}$$

where L is the light yield, S the scintillation efficiency, dE/dx the specific energy loss per path length, and kB the material-dependent Birk's coefficient with units of distance per energy.

The differences in light yield and timing can enable particle identification via pulse shape discrimination (PSD).
In the following study, the energy-loss processes for photons and neutrons are of particular interest. Photons with an energy below 60 keV lose energy predominantly via the photoelectric effect [63]. Above this energy, the dominant process is Compton scattering [64]. For an energy above 1022 keV, which is twice the rest mass of electrons, also pair-production comes into play and becomes dominant for energies above 8 MeV [65]. The different effects are shown in sketches in Figure 94.

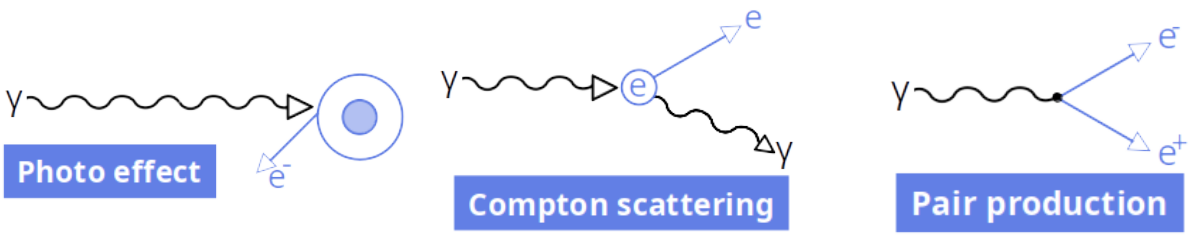

Figure 94: Sketches of the different energy loss mechanisms of photons

The AmBe source, used in the following study, produces photons/gammas with an energy of about 4.4 MeV and neutrons with energies about 4.6 MeV [66–68]. The energy loss is therefore from a mixture of Compton scattering and pair-production.
For fast neutrons with an energy above 0.5 MeV, detection via ionization in scintillators happens primarily via proton recoil from (n,p) reactions. Neutrons, via the protons, therefore, have a higher energy loss in scintillators than gammas, which results in a higher occupation of the triplet states, meaning an enhanced slow component [69]. As organic plastic scintillators are rich in hydrogen, they are preferred for neutron detection.

4.2 Idea for Neutron and Gamma Tagging

Using the signal differences of a PSD material, the idea for neutron and gamma tagging in this study is to use the number of late light signals, from the triplet states, and compare this to the height of the early light, also referred to as the first peak in the following sections, from the singlet state. Using a radioactive source that produces both neutrons and gammas in coincidence, the different types can be tagged and identified.
The number of late light signals approach might have advantages over a method that integrates the amplitude over time (see [70]), as it does not require correction for potential undershoots in the measured waveform. This undershoot is often observed when a pre-amplifier, which causes a negative dip after a peak, is used for a SiPM.
The approach used in the following study counters the negative dip by directly counting late light signals; however, it requires storing the full measured waveform.

4.3 Setup

To test the tagging idea, a small test setup was designed and built. This setup contained two PSD tiles ($3 \times 3 \times 0.5$ cm^3), a radioactive AmBe source emitting neutrons and gammas (in coincidence in about $55 - 60\%$ of decays [71, 72]), and a muon veto in the form of four plastic scintillator strips. The decay of AmBe is detailed in Figure 95. The entire setup is shown in Figures 96 and 97.
The material for the PSD tiles used here is the EJ-276G with properties shown in Table 13, taken from [74].

Two PSD tiles were used to allow for a coincidence measurement of a neutron in one tile and a gamma in the other. In this way, an event-by-event analysis was possible. To allow for as many events as possible

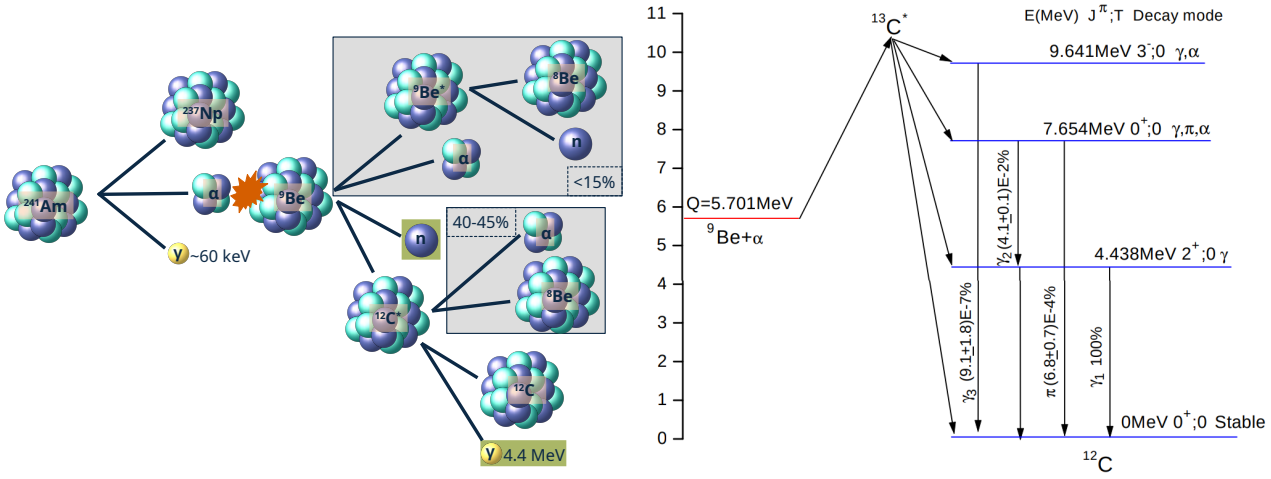

(a) Decay diagram for AmBe

(b) Energy level diagram for ^{12}C

Figure 95: Details of the decay of AmBe. 95a shows the different sub-processes with the initial decay of ^{241}Am to ^{235}Np with an emitted α. This α then interacts with the ^{9}Be into different outcomes indicated. The grey boxes around some processes highlight the ones not of interest for this work. The green boxes highlight the emitted neutron and photon. 95b shows in addition different energy levels for the $^{9}Be + \alpha$ process' results (credit: [73]). As the photon is emitted from the excited ^{12}C sub-process almost instantaneously, the neutron and photon are emitted in $55 - 60\%$ of initial ^{241}Am decays in coincidence

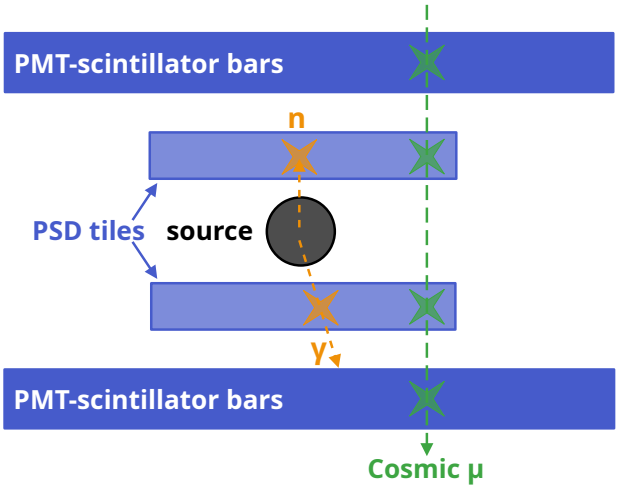

Figure 96: Sketch of the setup. Shown is the source in black, the two PSD tiles, and the PMT-scintillator bars for the muon veto. A coincidence between a neutron emitted upwards and a gamma ray emitted downwards from the source is shown in orange, and a cosmic muon in green.

with the highest acceptance, the tiles were placed as close to the source as possible, as seen in Figure 98a. They were directly read out by 2×2 mm^2 SiPMs (S13360-2050VE) mounted on the backside of the tiles, into the tiles' dimples shown in Figure 98c. The SiPMs were furthermore connected to a pre-amplifier (DS3769-A1423B). Also shown in Figure 98b is the 3D-printed holding structure for the AmBe source, PSD tile, and the SiPM and PCB placement.

The holding structure was then placed in the middle of the muon veto. Two plastic scintillator strips, connected to PMTs, were placed at the top, analog at the bottom. The space between the scintillator strips and the holding structure was minimized to ensure that no muons can cross the PSD tiles without crossing the muon veto.

The SiPMs and PMTs were connected to power sources (a stand-alone low-voltage power supply for the SiPMs and a high-voltage VME power supply for the PMTs) and to an oscilloscope (Keysight Technologies MSOS254A). The oscilloscope settings are shown in Tables 20 through 25 in the Appendix. The signals from the two PMTs per layer were joined with a T-piece, summing the input into the oscilloscope. The oscilloscope was then used to trigger the event recording on the bottom PSD tile when a positive edge of

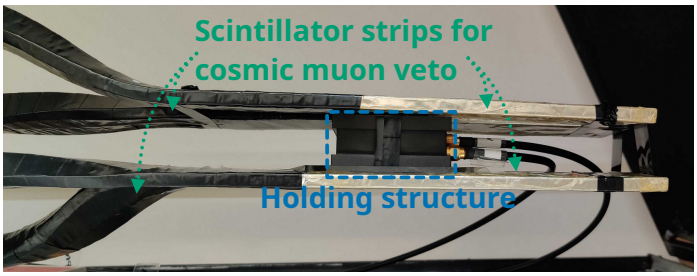

(a) Side view

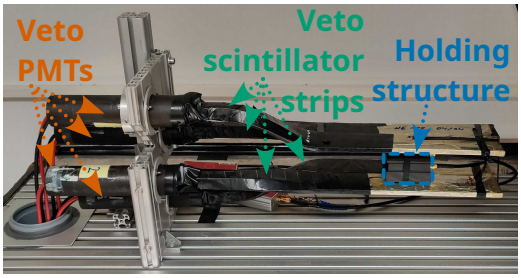

(b) Top view

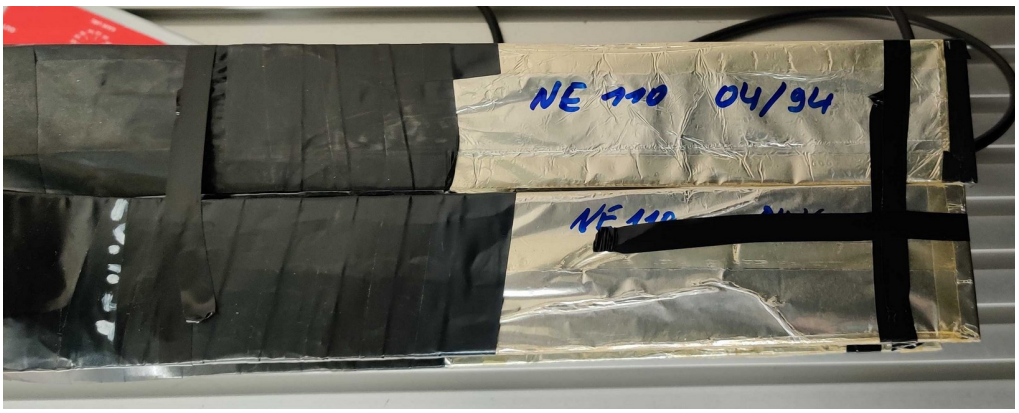

(c) Veto top view

(d) Veto front view

(e) Veto back view

Figure 97: Pictures of the setup. 97a shows the side of the setup with the holding structure (see Figure 98a for more details) and the muon veto. 97b shows the full setup including the PMTs used for the veto readout. 97c shows the two scintillator strips for the veto per 'layer' from the top, and 97d shows the two scintillator strips for the veto per 'layer' from the front. The small gap between the two scintillator strips in 97d was closed by using electrical tape as seen in 97c. 97e shows the back of the setup with the two PMTs used for one of the muon veto 'layers' inserted.

	Medium component		Long component			
	Decay const. [ns]	Intensity [%]	Decay const. [ns]	Intensity [%]	Decay const. [ns]	Intensity [%]
Gamma	13 ± 1	84	110 ± 10	7	800 ± 80	9
Fast N	14 ± 1	62	95 ± 10	13	800 ± 80	25

Table 13: Characteristics of the EJ-276G plastic scintillator [74]

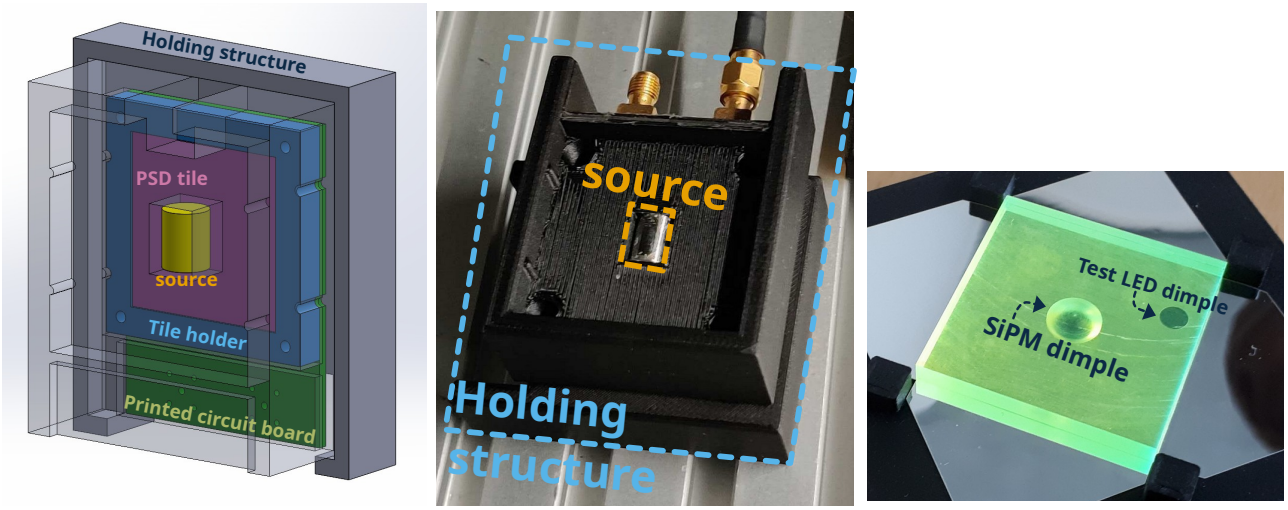

(a) Sketch of the holding structure (b) Picture of the holding structure (c) Picture of the scintillator tile

Figure 98: The holding structure of the PSD tiles, the AmBe source, the SiPMs, and the PCBs. 98a is a sketch of the holding structure and its internals: the AmBe source, one PSD tile, the tile holder, and the PCB. 98b is a picture of the 3D printed holding structure with the inserted AmBe source. The PSD tile ($3 \times 3 \times 0.5$ cm^3), holder and PCB were inserted on top of the source. The other tile is already inserted on the back. 98c shows a close-up of the PSD tile before the reflective foil was attached. Two dimples can be seen, one for the SiPM to be mounted into, and one for a test LED, which was not used in this setup

at least 35 mV was measured. Data acquisition was handled by a connected PC. A script was used to save waveforms measured with the oscilloscope and to repeat this over a specified time range or a specified number of events.
The dataset used in the following was taken over 100,000 s between June 16th and 17th, 2023, and contains a total of 754,420 triggered events, of which many are not in coincidence.

4.4 Analysis of the Individual Waveforms

4.4.1 PSD tiles

As the trigger for data taking was only on one of the two PSD tiles, the first step in waveform handling is to ensure that both tiles contain an event. For this, the highest amplitude of the waveform in the expected time window of ± 200 ns was determined. If the amplitudes for both tiles were not above the required threshold of 76.85 mV[46], the event was skipped, as then no coincidence was detected.
The next step was to fit the baseline of the waveform to perform an offset correction. The fit was performed in the time range of 60 ns to 2400 ns after the trigger and used an exponential decay function with a linear function shown in Equation 37.

$$f(t) = e^{-\frac{t}{a}} \cdot (b + c \cdot t) + d \tag{37}$$

[46] This was a trigger applied during the analysis, not online during the data taking, reducing the number of events quite a bit.

The parameter a describes the decay constant, b and c are for the linear function, and d is a constant offset. This fit was necessary to determine the heights of the late light signals accurately. An example of a fitted waveform is shown in Figure 99a.

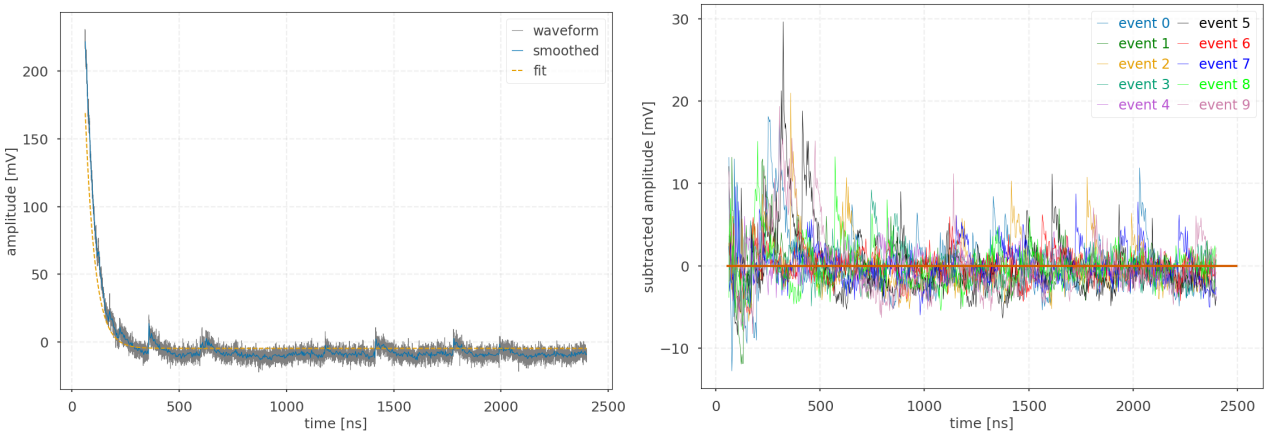

(a) Plot of waveform

(b) Plot of 10 subtracted events

Figure 99: 99a Plot of a waveform (gray) with the smoothing by average (blue) and the fit result (orange). 99b Plot of 10 events with the baseline fit subtracted from the smoothed waveform, indicating the goodness of the fit

In addition to the baseline fit, a smoothing step was taken to 'filter out' noise in the waveforms. The waveform in the fitted time range was split into slices of three time steps each[47], then averaged within each slice. The mean of the slice is assigned as the new time, and the averaged amplitude as the new amplitude. An example of the result of this step can also be seen in Figure 99a.

Figure 99b also shows, for 10 events, the smoothed waveform with the baseline fit subtracted. This shows that the fit performs reasonably well.

Using these smoothed and baseline-fit-subtracted waveforms, the individual late light signals were identified using the scipy.signal.find_peaks function. This function finds local maxima by comparing neighboring values. The peak-finding was tuned to properly identify the single late light signals using the available parameters for peak height, distance between neighboring peaks, peak prominence, and width, evaluated in the given order. The peak height was set at 3 mV as a minimum above the mean of the given waveform, motivated by the plot in Figure 99b to filter out the noise. The distance parameter was set to 5 ns after comparing the peak-finding results for different waveforms for values of 1, 5, 10, 15, and 20 ns, of which 5 ns performed the best. For a full data set of 1599 triggered events, Figure 101a shows the determined peak heights as a function of the distance between them. Here, it is clear that there is no correlation between the two parameters. Most events have a small distance between neighboring peaks and small peak heights.

Prominence can be understood as the relative height of a peak over its surrounding baseline. An illustration of this is shown in Figure 100.

As the prominence is determined over its surroundings, the function also allows for a window length in which the prominence is determined. The window length was set to 100 ns. The prominence itself was then set to 4 mV after comparing the peak-finding results for different waveforms for values of 0, 3, 4, 5, 10, and 15 mV, of which 4 mV performed the best. Figure 101b shows the expected correlation of the peak height and prominence. A higher peak correlates with a higher prominence.

The final set parameter was the peak width. The width was set to be evaluated at a relative peak height of 0.5 and set to be at least 2 ns wide after comparing the results for different waveforms for values of 1, 2, 5, and 10 ns, of which 2 ns identified the peaks, seen by eye, the best.

The outputs of the peak finding function are the time of each identified peak and its height. For the

[47] One time step is $\sim$ 0.2 ns.

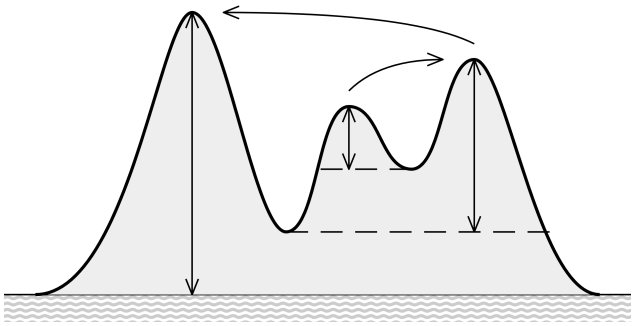

Figure 100: Illustration of prominence. The vertical arrows show the prominence of three peaks. The dashed horizontal lines show the lowest contours that do not encircle higher peaks. Curved arrows point from a peak to its parent (credit: [75])

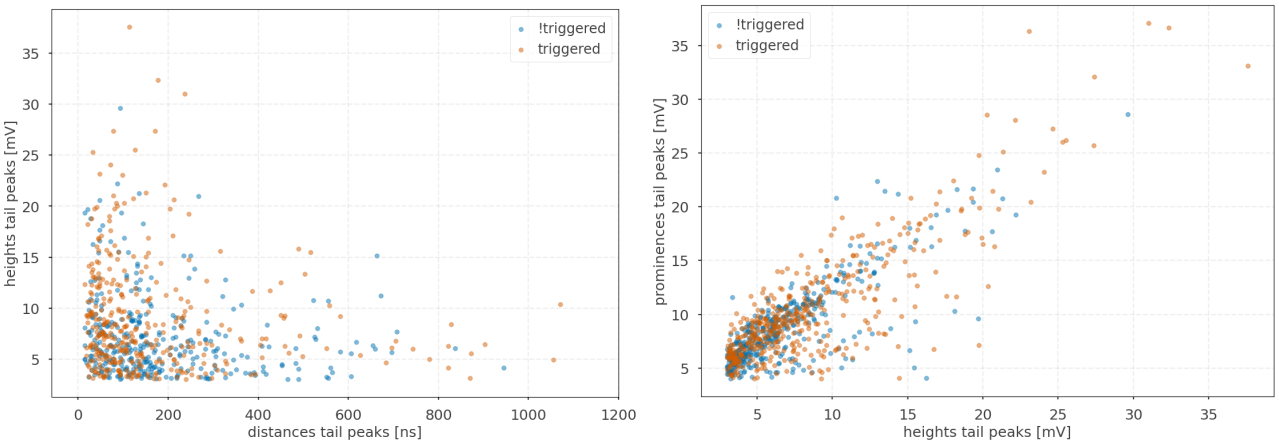

(a) Heights vs. distance

(b) Prominence vs. heights

Figure 101: 101a shows the identified peak heights against the distance to the next peak for the two tiles. 101b shows the prominences of identified peaks against their heights for the two tiles.

example waveform from Figure 99a, the result is shown in Figure 102.

4.4.2 Scintillator Strips for the Muon Veto

For the scintillator strips in the muon veto, a simple determination of the highest amplitude was sufficient. The maximum amplitude and the time of this maximum were determined. An example of this is shown in Figure 103a.

4.5 Muon Veto

So far, the information of the different oscilloscope channels has been handled largely independently. To select clear candidates for neutron and gamma coincidences, all potential cosmic muon events had to be filtered out. This was achieved by combining the information from the different channels.
The first step in this combination is determining the signal event threshold for the PMTs. This was done by calculating the mean and standard deviation of the peak amplitudes per PMT outside the big peak window ($\pm$200 ns) shown in Figure 103b. A signal was then vetoed from the analysis if it had an amplitude of at least 4σ above the mean per PMT. In addition, for an event to be tagged as a cosmic muon for further analysis, a coincidence of both PSD tiles and both scintillator bars was required.
For the following analysis, only two types of events are of interest: first, events without a veto signal from either of the two PMTs and both PSD tiles having a signal, and second, events with veto signals in both PMTs and both PSD tiles. The first type is assumed to be events with coincident neutron and gamma detection, while the second type is assumed to be cosmic muon events. A sketch of the different event types, considered in the following analysis, is shown in Figure 96.
For the selection of the neutron-gamma events, the PMTs can not have a signal above the respective

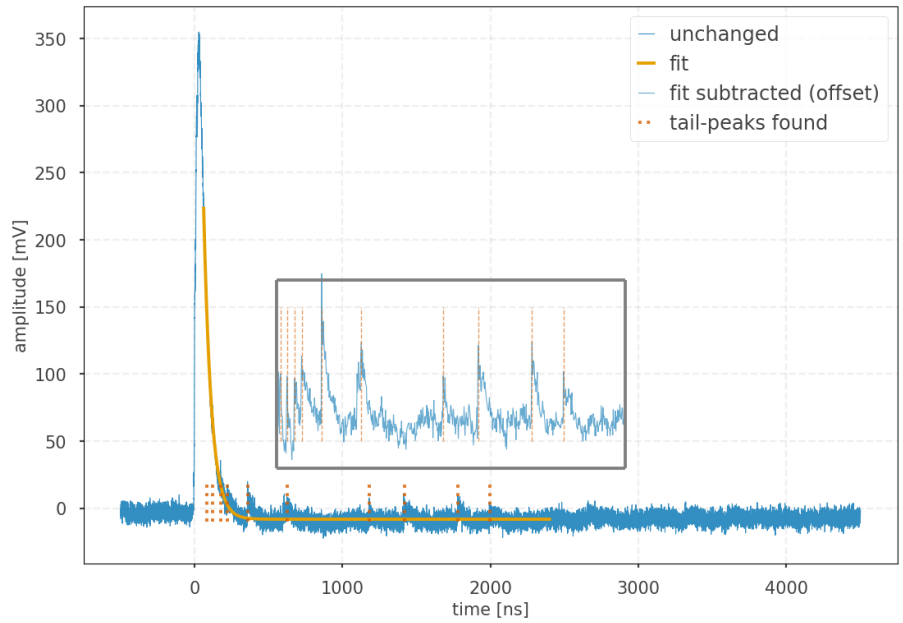

Figure 102: Plot of the original waveform (blue line outside of the box), the baseline fit (solid orange line), the baseline fit subtracted from the waveform and smoothed (blue line in the box), and the identified tail-peaks (orange dotted lines). The waveform in the box is also enlarged by a factor of 5 and offset by 70 mV

thresholds in the time window between -200 ns and 2400 ns, as this would constitute a veto signal from a potential cosmic muon. This time window fully covers the expected window of late light signals, and the waveforms would not be affected by signals outside this range.
For the selection of the muon events, an event is required from both PSD tiles and both PMTs within ± 200 ns to rule out any other event types. In this way, 9931 neutron-gamma events were selected and 2321 tagged cosmic muon events from the 15, 635 events, with coincident signals in both SiPMs and with late light signals.[48]

4.6 Amplitude of the Early Light Signal against the Number of Late Light Signals

The idea of this analysis was to use the number of individual late light signals and compare it to the amplitude of the early light signal per event.
Cosmic muons can be used as an indication of a gamma-dominated area, due to the similarity between gamma rays (in the considered energy range) and muons with respect to the interaction type. The gammas lose energy via Compton scattering (in the here expected energy range), thereby producing electrons which lose energy via bremsstrahlung (see Section 1.4.2). Muons lose energy via ionization (see Equation 7). Neutrons, on the other hand, lose energy via proton recoils, which have, compared to both gammas and muons, a much higher energy loss over distance (through ionization). Therefore, for this study, it can be assumed that gammas and muons both have a dominant scintillation light signature from singlet states. In contrast, the neutrons have a higher contribution from the triplet states.
Overlaying the neutron-gamma events with the muon events, as seen in Figure 104, shows therefore which events are more likely to be gammas and which are more likely to be neutrons.
Using this indication, high-purity selections of neutrons and gammas were made. The high-purity selection for gammas was determined with the cosmic muon distribution. For each row[49] between 7 and 19 late light signals for the triggered PSD tile, and 9 and 16 for the untriggered one, the x position of the 95

[48] Technically, also events without late light signals can be used. In the following analysis, the timing of late light signals was also used at some point, though, requiring that all events have at least one late light signal.
[49] Integer values on the y-axis

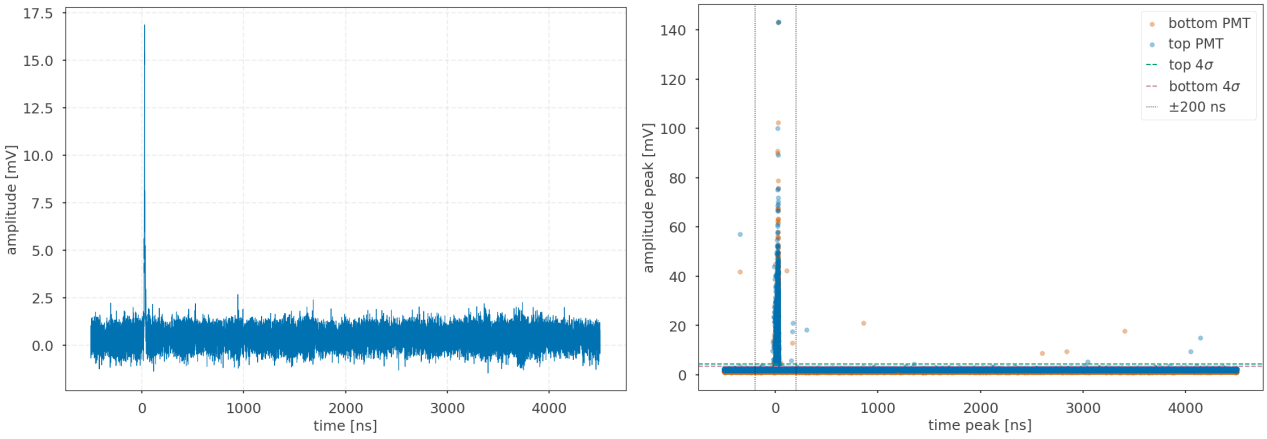

(a) Plot of one PMT signal

(b) Maximum peak height from the veto PMTs

Figure 103: 103a Plot of one PMT signal. 103b Scatter plot of the maximum peak height from the veto PMTs. Also shown are the time window for excluding the mean and standard deviation calculation, as well as the threshold lines.

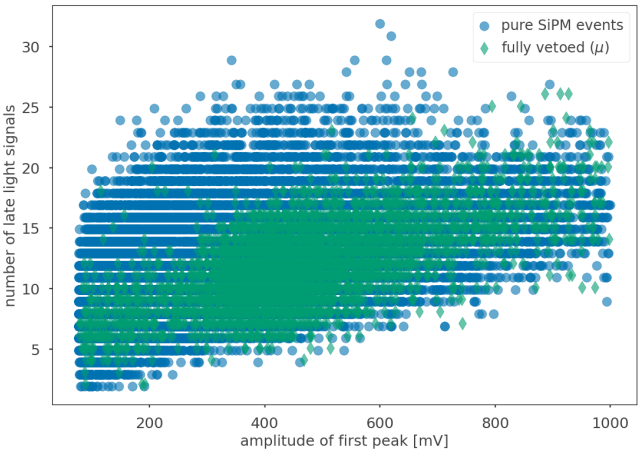

Figure 104: Plot of amplitude of the first peak against the number of late light signals of neutron-gamma candidates (blue circles) and cosmic muon events (green diamonds). The cosmic muon events populate the lower area of the neutron-gamma event distribution. This indicates that the more gamma-like events are also in this region, while the more neutron-like events are in the higher area

percentile of muon events was determined. These x positions were then used to fit a straight line shown in Figure 105a. Also shown in this figure are the fit residuals, which are the difference between the x position of the percentile points and the x position of the fitted line at the same y position.

For the triggered tile, the neutron-gamma events below this straight line are the high-purity gamma events. These events exhibit the most gamma-like behavior, as expected from the energy-loss mechanisms and scintillation light production described above. The corresponding events from the untriggered tile, therefore, are neutrons[50], selected without any bias and therefore called the unbiased events. The same is done for the untriggered tile using both the high-purity gamma selection and the unbiased neutron selection. The result can be seen in Figure 105b.

The high-purity neutron selection was performed similarly, but without the cosmic muon distribution. Using the knowledge of the cosmic muon distribution, the events furthest away from the muon distribution are the most neutron-like events. In this case, these are the events in the upper left corner of Figure 104.

To select events in this area, the x position of the 7.5 percentile for each row between 10 and 23 for the triggered tile, and 10 and 21 for the untriggered tile, was determined. The odd percentile was chosen to balance the number of events selected in both high-purity selections.

As before, a straight line was then fitted through these points and used to select the most neutron-like candidates. The corresponding events from the other tile were then again the unbiased gamma events[51].

[50] Or both signals are from untagged cosmic muon events. More on this at the end of this chapter.

[51] This time, no cosmic muon events are expected in this unbiased selection.

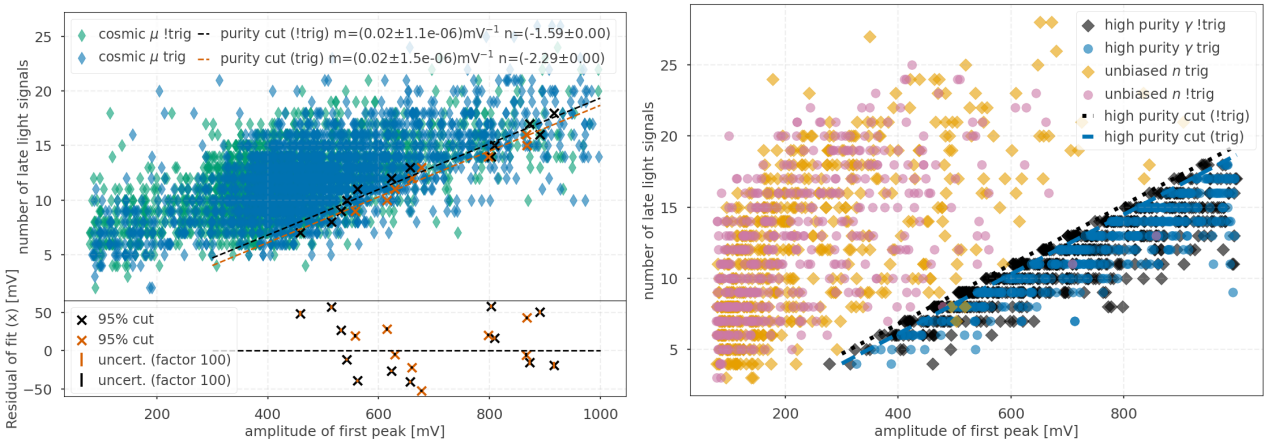

(a) Plot of the high purity cut

(b) Plot of the unbiased neutron events

Figure 105: 105a shows the cosmic muon events (blue and green diamonds), the 95 percentile positions per row (black and red X's), and the straight line fit (black and red dashed lines). The bottom plot shows the residuals for the fit, with the points' uncertainties enlarged, but still not visible. 105b shows the high-purity gamma events (black diamonds and blue circles), the high-purity cuts (black and blue lines), and the unbiased neutron events (orange diamonds and magenta circles).

This can be seen in Figures 106a and 106b.

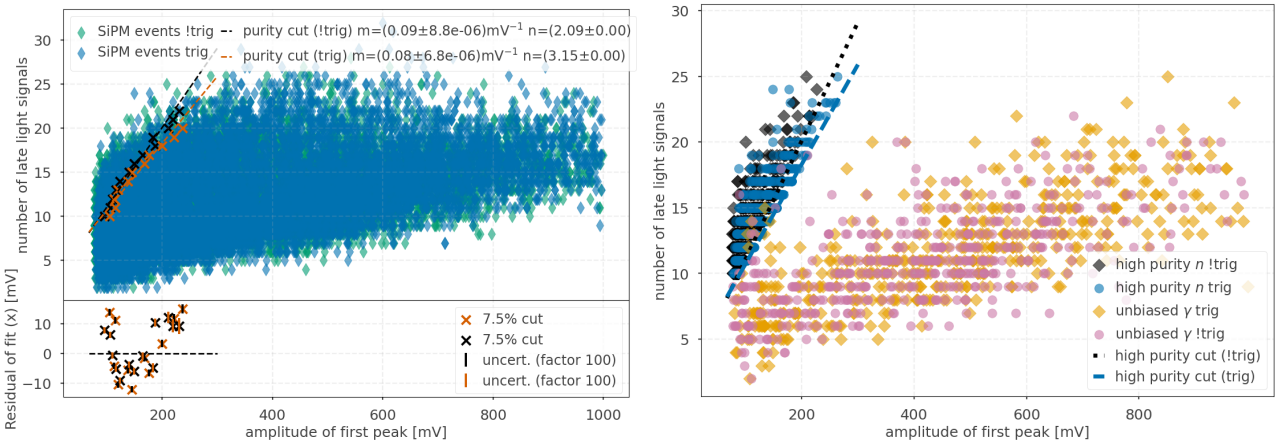

(a) Plot of the high purity cut

(b) Plot of the unbiased gamma events

Figure 106: 106a shows the SiPM events, the 7.5 percentile points per row (black and red X's), and the straight line fit (black and red dashed lines). The bottom plot shows the residuals for the fit, with the points' uncertainties enlarged, but still not visible. 106b shows the high purity neutron events (black diamonds and blue circles), the high purity cuts (black and blue lines), and the unbiased gamma events (orange diamonds and magenta circles).

In total, 581 (triggered tile) and 451 (untriggered tile) events were selected for the unbiased neutron sample, and 493 (triggered tile) and 474 (untriggered tile) for the unbiased gamma sample.
These unbiased samples were now split into training and test sets at a ratio of 5 : 1. The training sample was used to tune the separation, and the test sample was used to evaluate the performance.

4.6.1 Separation Lines

In the next step, a separation line between the two unbiased event (training) samples was determined. The line was optimized to yield the highest accuracy (see the definition in Equation 36) for determining whether an event is more neutron- or more gamma-like, as shown in Figure 107. The tested parameter

space was slopes between 0.001 and 0.1, and intercepts between −10 and +10[52]. The highest accuracy of correctly identified neutrons and gammas, based on the events being above the line (neutron) and below the line (gamma) by the number of events, was 79.6% (triggered tile) and 79.9% (untriggered tile). This was achieved by a slope of 0.0339 mV^{-1} (triggered tile) and 0.0433 mV^{-1} (untriggered tile)) and an intercept of 1.11 (triggered tile) and −0.95 (untriggered tile). These parameter combinations are indicated by a black cross in Figure 107. The correctly sorted neutron events were 300 (triggered tile) and 363 (untriggered tile), and the correctly sorted gamma events 289 (triggered tile) and 323 (untriggered tile). Incorrectly identified as neutron events were 91 events (triggered tile) and 72 (untriggered tile), and incorrectly identified as gamma events were 61 (triggered tile) and 102 (untriggered tile). The unbiased event samples with this separation line are shown in Figure 108.

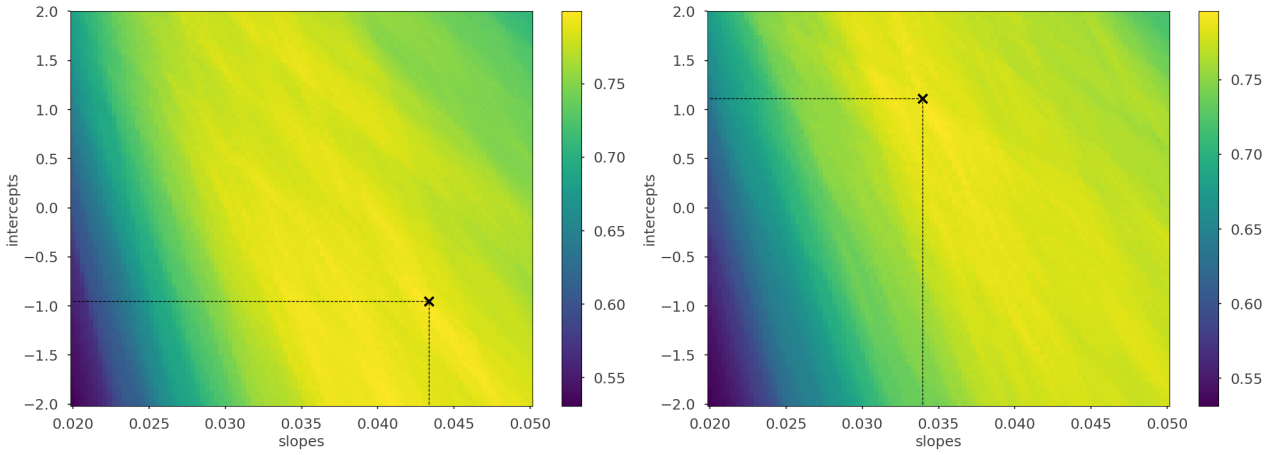

(a) Triggered tile

(b) Untriggered tile

Figure 107: Plot of the separation accuracy (as the *z*-axis, shown with the color) for different slopes and intercepts of the separation line for the two tiles. All combinations in the shown parameter spaces were tested, with the highest separation accuracy achieved for the combinations marked with a black cross

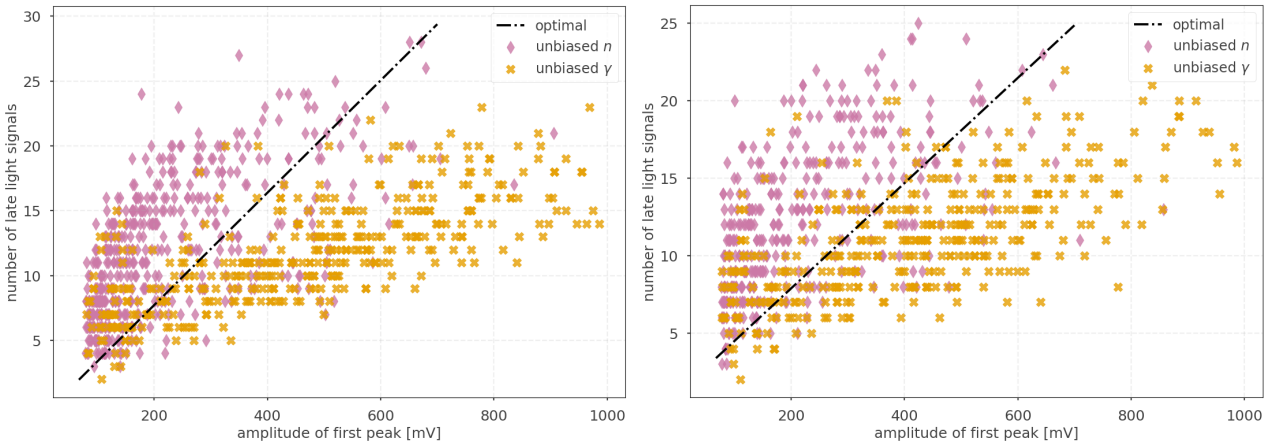

(a) Triggered tile

(b) Untriggered tile

Figure 108: Plot of the unbiased samples with the optimized separation line for both tiles. The optimal separation line is shown in black, the unbiased neutron-events with orange crosses, and the unbiased gamma-events with magenta diamonds

In addition to this straight line, a quadratic line was also considered. Instead of the overall highest accuracy across the complete training distributions, the highest separation accuracy and, therefore, the optimal point of separation were determined here per row of the number of late light signals. A quadratic

[52] A smaller parameter is shown in the following plots, which allowed for a finer selection.

function was then fitted through the optimal separation points. This can be seen in Figures 109. For this fit to work correctly, the axes were swapped.

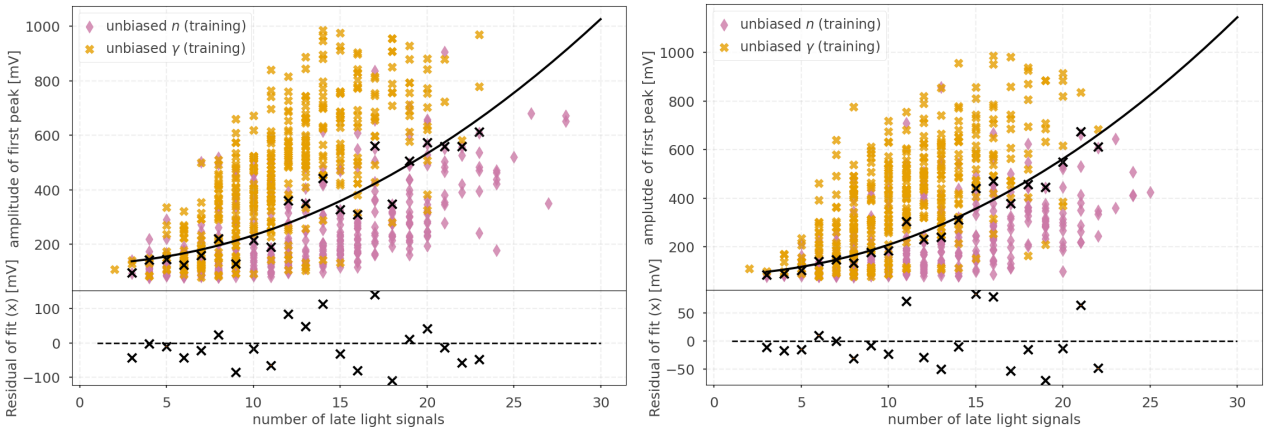

(a) Triggered tile

(b) Untriggered tile

Figure 109: Plot of the unbiased training samples with the fitted quadratic line (shown in black) for separation for both tiles. The black crosses mark the maximum separation accuracy per number of late light signals. In the bottom plot, the residuals from the quadratic fit are shown

4.6.2 Distance to Separation Line

4.6.2.1 Distance to the Straight Separation Line

The straight separation line could, at this point, be used as a tagging method; however, using the distance to the separation line also provides an additional measure of the identification's confidence. The signed distance used for this purpose is calculated with

$$d = \pm\sqrt{\frac{(m \cdot x + c - y)^2}{m^2 + 1}}$$

(+ for above the line, $-$ for below the line). m is the slope of the separation line, c the intercept, x the amplitude of the early light signal, and y the number of late light signals. This distance was determined for each event. The histogram of the signed distances per event is shown in Figures 110. It also includes plots of the efficiencies, purities, and accuracies (see Equations 34, 35, and 36) for the unbiased test neutron events identified as neutrons at different signed distances.

To obtain the identification uncertainties, the identification is treated as a Bayesian analysis to determine the success-probability of a binomial process. The prior probability distribution for this is shown in Equation 38 [76].

$$P(p; \alpha, \beta) = \frac{p^{\alpha-1}(1-p)^{\beta-1}}{(\alpha+\beta)^2(\alpha+\beta+1)} \tag{38}$$

For this binomial process, α is $k+1$, with k as the number of successes, and β is $n-k+1$, with n as the number of trials. $n-k$ then gives the number of failures. This choice results in a flat distribution in p. Therefore, the posterior probability is also a Beta distribution, and the variance, as shown in Equation 39, quantifies the uncertainty in the efficiency, purity, or accuracy (depending on the input values).

$$Var(p) = \sigma^2 = \frac{\alpha\beta}{(\alpha+\beta)^2(\alpha+\beta+1)} = \ldots = \frac{kn - k^2 + n + 1}{n^3 + 5n^2 + 7n + 12} \tag{39}$$

4.6.2.2 Distance to the Quadratic Separation Line

Also, for the quadratic separation line, the distance to it is used. For a quadratic function, however, the shortest distance of a point to the function is not analytically expressible. Therefore, the shortest distance

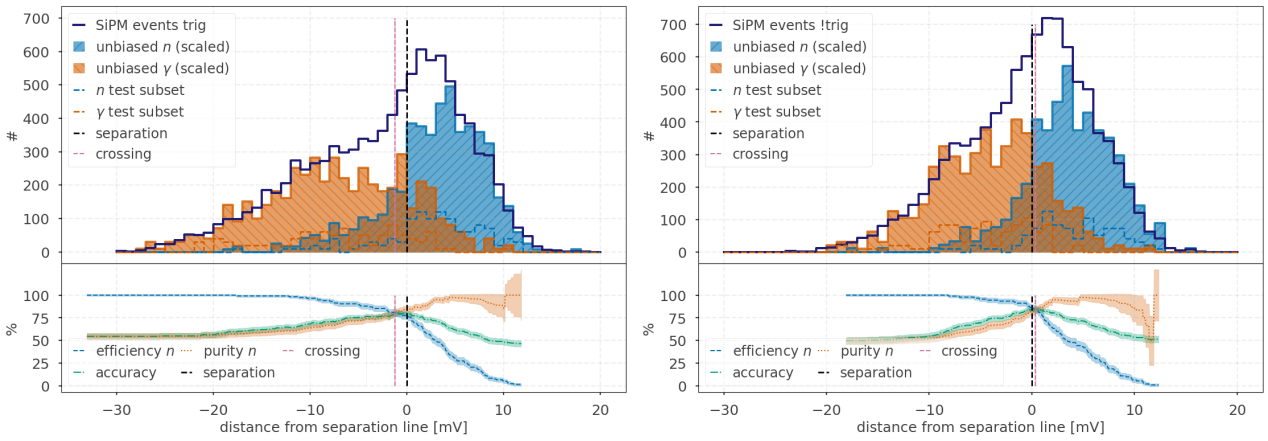

(a) Triggered tile

(b) Untriggered tile

Figure 110: Tops: Histogram of the signed distances from the linear separation line for the unbiased training samples (neutrons in blue, gammas in red) and the respective full distributions (dark blue lines) for the two tiles. Bottoms: Plot of the efficiencies, purities, and accuracies of the unbiased test events being correctly identified as neutrons at the different signed distances for the two tiles. The black, dashed line shows the separation line, and the magenta line shows the smallest difference between the efficiency and purity lines.

was determined numerically by calculating the distance to 240 homogeneously spaced points on the fitted quadratic function[53], in the range of $[3, 40]$ for both tiles, and then determining the minimum of these calculated distances.

As for the straight separation line, the signs of the distances were also taken into account. The histogram of the signed distances per event is shown in Figures 111. It also includes plots of the efficiencies, purities, and accuracies for a correct neutron identification. Again, the uncertainties were determined using the Beta distribution for binomial processes (see Equation 39).

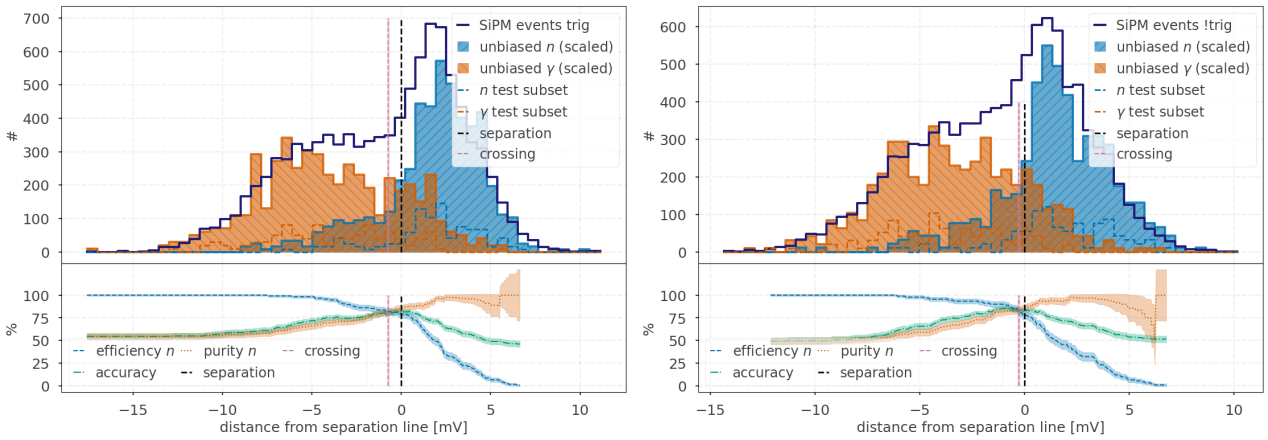

(a) Triggered tile

(b) Untriggered tile

Figure 111: Tops: Histogram of the signed distances from the quadratic line for the unbiased training samples (neutrons in blue, gammas in red) and the respective full distributions (dark blue lines) for the two tiles. Bottoms: Plot of the efficiencies, purities, and accuracies of the unbiased test events being correctly identified as neutrons at the different signed distances for the two tiles.

Comparing the distributions for the linear and quadratic separation line, the shapes for the signed distances of the quadratic separation have a more precise point of separation at a distance of 0 mV than the distances of the linear separation. For both lines, the unbiased neutron and gamma distributions

[53] Given the difference of range on the two axes, the amplitudes were weighted to give both directions the same effect on the distance.

have populations on both sides of 0 though. So it is not immediately[54] clear which type of line performs better in the neutron identification. More details on this in Section 4.6.4.

4.6.3 Log-likelihood Ratio of Distance

In the next step, these signed distance distributions were used as the likelihoods that an event with a given signed distance from the separation line is a neutron or a gamma.

4.6.3.1 Straight Line Separation

For the linear separation line, the training distributions were first normalized to the same number of events and then to the sum of 1 per bin, as shown in Figure 112. To allow for the best hypothesis test per event, the log-likelihood ratios (λ_{LR}) were then determined per event from these likelihoods by subtracting the logarithmic likelihood of an event stemming from a gamma ($\mathcal{L}_{gamma}$; the height of the gamma distribution bin in which the event falls in Figure 112) from the logarithmic likelihood of the event stemming from a neutron ($\mathcal{L}_{neutron}$; the height of the neutron distribution bin, in which the event falls in Figure 112) as shown in Equation 40.

$$\lambda_{LR} = \log(\mathcal{L}_{neutron}) - \log\left(\mathcal{L}_{gamma}\right) \tag{40}$$

For events with 100% likelihood for originating from a neutron (gamma), the log-likelihood ratio was assigned to 3.5 (neutron) -3.5 (gamma), as over- and underflow bins. For the unbiased event samples, the results are shown in Figure 113. Also shown in this plot are the efficiencies, purities, and accuracies for a correct neutron identification. Due to the almost monotonous correspondence of the likelihoods to the signed distance, no big improvement was expected here. Advantages were only expected from the not-monotonous 'dips' of the likelihoods, e.g., in Figure 112a at ~ -18 mV and $\sim +7$ mV.[55]

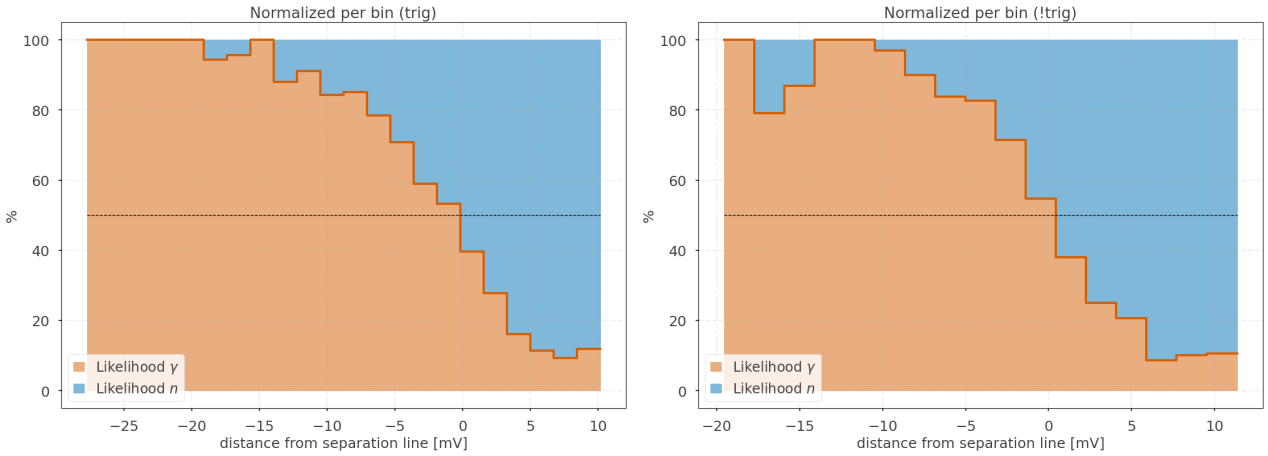

(a) Triggered tile

(b) Untriggered tile

Figure 112: Plot of the normalized unbiased signed distance distributions for the linear separation line for the two tiles

The observed 'spikiness' of the histogram is due to the limited amount of values for the log-likelihood ratio, due to the choice of bins[56]. As before, the uncertainties shown in Figure 113 were determined using the variance of the Beta distribution for binomial processes (see Equation 39).

4.6.3.2 Quadratic Line Separation

For the distance from the quadratic separation line, the same procedure was employed to determine the

[54] At least not from only looking at the plots.
[55] The choice of the histogram binning enters here as well. In this study, the binning was chosen to achieve a result at least as good as that of the signed distance method (directly).
[56] See previous footnote

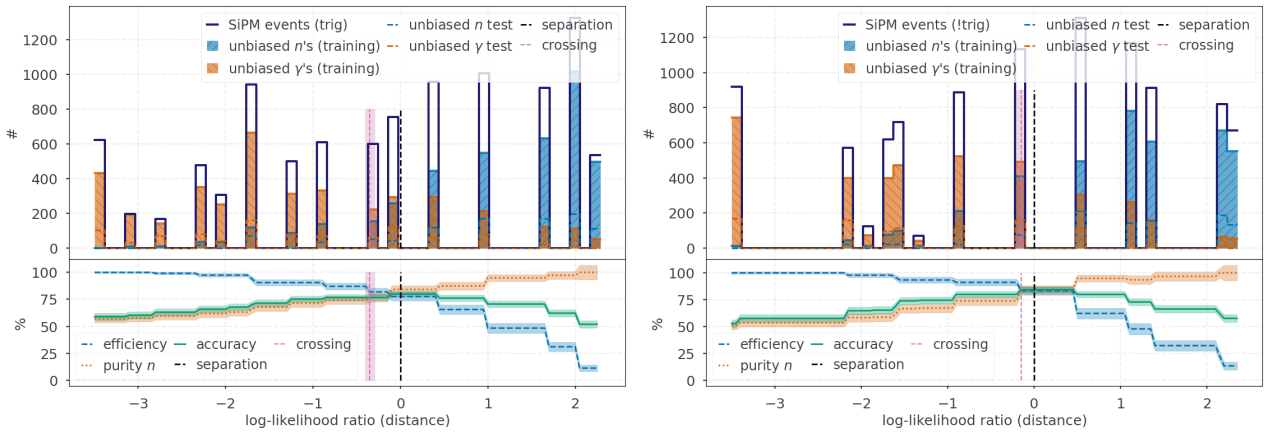

(a) Triggered tile

(b) Untriggered tile

Figure 113: Tops: Histogram of the log-likelihood ratios of the signed distances from the linear separation line for the unbiased training samples (neutrons in blue, gammas in red) and the respective full distributions (dark blue lines) for the two tiles. Bottoms: Plot of the efficiencies, purities, and accuracies of the unbiased test events being correctly identified as neutrons.

log-likelihood ratios. The normed unbiased signed distance distributions are shown in Figures 114, and the histogram of the resulting log-likelihood ratios is shown in Figures 115.

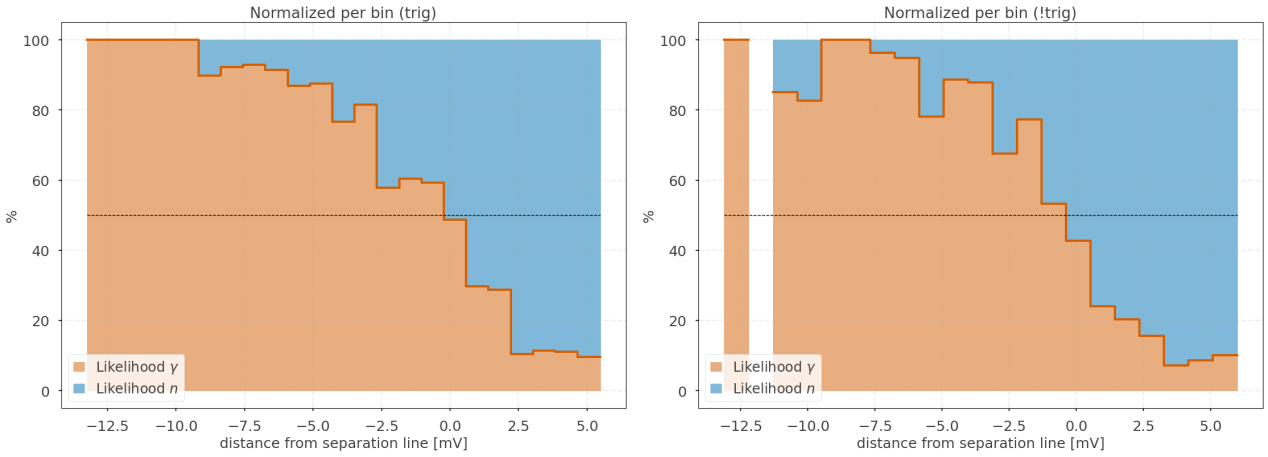

(a) Triggered tile

(b) Untriggered tile

Figure 114: Plot of the normalized unbiased signed distance distributions for the quadratic separation line for the two tiles

Due to the similarities in the normalized unbiased signed distributions for the two separation line types, the log-likelihood ratios of these two methods are somewhat similar in performance.

4.6.4 Discussion

The efficiencies, purities, and accuracies for both approaches are summarized in Table 14. For both tiles, the results are given for the test and training samples. The comparison between these two allows for checking for 'over-training'[57], which does not seem to be the case, given the only slight differences between the two results.

While the efficiency of neutron identifications is higher for the untriggered tile than the triggered tile in the linear separation approach, the effect for the purity is, as expected, reversed. This is true for both methods (direct and log-likelihood ratio). This is because the triggered tile inherently has more late light

[57] As no training was performed here, it is not really a check over-training, but rather a check for how well the test data set compares to the training data set.

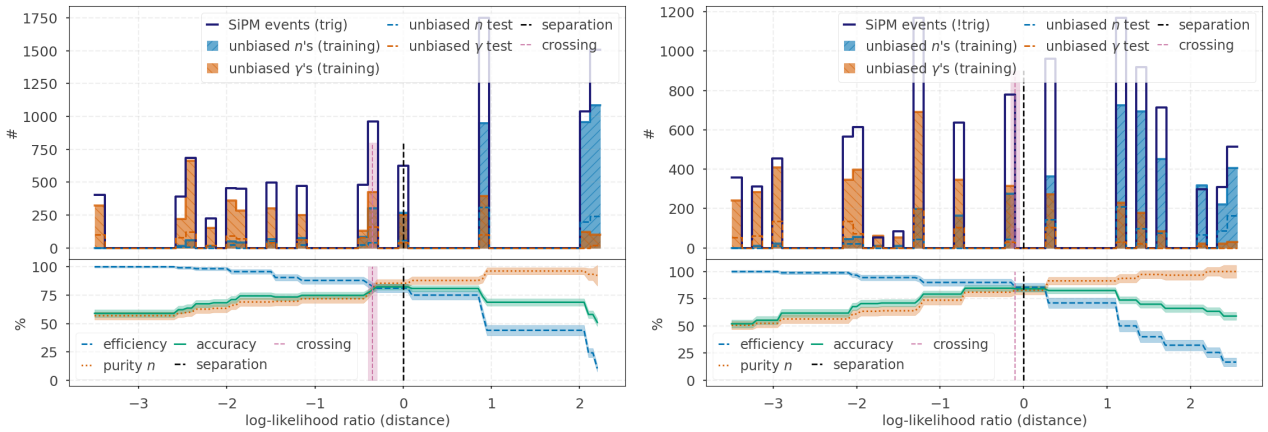

(a) Triggered tile

(b) Untriggered tile

Figure 115: Tops: Histogram of the log-likelihood ratios of the signed distances for the quadratic separation line for the unbiased training samples and the respective full distributions for the two tiles. Bottoms: Plot of the efficiencies, purities, and accuracies of the unbiased test events.

signals than the untriggered tile, as shown in Figure 116a. The untriggered tile also has fewer events with an amplitude of the early light above about 400 mV, as shown in Figure 116b.

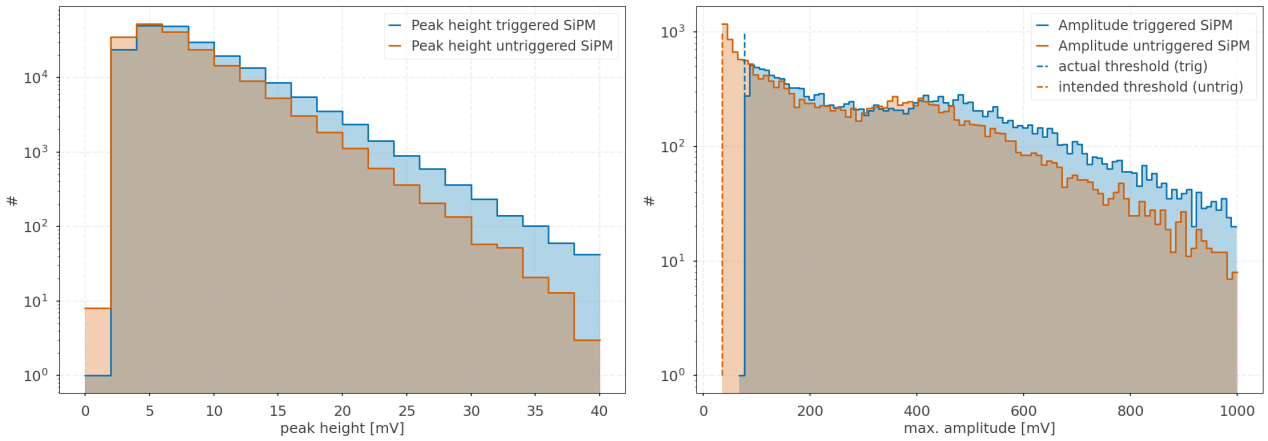

(a)

(b)

Figure 116: 116a Histogram of the heights of the late light signals for the triggered tile in blue and the untriggered tile in red. For small peak heights, an excess of events from the untriggered SiPM can be seen. For peak heights above $\sim$ 10 mV and an excess of events from the triggered SiPM is visible. 116b Histogram of the amplitudes of the early light for the triggered tile in blue and the untriggered tile in red. For events with a small maximal amplitude, an excess for events from the untriggered SiPM can be seen. This excess is mitigated by using the actual threshold (shown in blue) from the triggered SiPM. For events with an maximal amplitude above $\sim$ 400 mV, an excess from the triggered SiPM is visible, which can not be mitigated

These two facts, combined, indicate that events from the untriggered tile are, in general, more gamma-like than those from the triggered tile. This plays a role because the unbiased neutron and gamma samples are chosen from the high-purity samples on the opposite tile. The high-purity gamma selection from the untriggered tile is therefore less 'high-purity' than the one from the triggered tile; this can be seen from the comparison of Figure 117, and is also reflected in the sample sizes[58] of the unbiased distributions. As this only affects the selection of the unbiased neutron sample for the triggered tile, the performance between the two tiles is therefore slightly different, with the triggered tile having a lower neutron identification efficiency but a higher purity than the untriggered tile.

[58] 581 (triggered) and 451 (untriggered) unbiased neutron events, and 493 (triggered) and 474 (untriggered) unbiased gamma events

LINEAR	**Triggered tile**			**Untriggered tile**		
Direct	**@**0 test	**@**0 training	**@**-1.21	**@**0 test	**@**0 training	**@**0.36
Eff. [%]	77.59 ± 3.88	77.97 ± 1.72	81.03 ± 3.66	85.56 ± 3.77	83.59 ± 1.75	84.44 ± 3.87
Pur. [%]	84.91 ± 3.52	83.73 ± 1.59	81.03 ± 3.66	81.91 ± 4.00	77.73 ± 1.89	84.44 ± 3.87
Acc. [%]	80.37 ± 2.72	79.89 ± 1.22	79.44 ± 2.77	83.70 ± 2.74	80.32 ± 1.31	84.78 ± 2.67
LLR	**@**0 test	**@**0 training	**@**-0.35	**@**0 test	**@**0 training	**@**-0.15
Eff. [%]	77.59 ± 3.88	78.92 ± 1.89	81.90 ± 3.60	83.33 ± 3.97	78.12 ± 2.18	83.33 ± 3.97
Pur. [%]	84.11 ± 3.57	82.47 ± 1.81	76.61 ± 3.81	84.27 ± 3.91	77.90 ± 2.18	84.27 ± 3.91
Acc. [%]	79.91 ± 2.75	79.53 ± 1.38	76.64 ± 2.98	84.24 ± 2.70	78.54 ± 1.51	84.24 ± 2.70
QUADR.	**Triggered tile**			**Untriggered tile**		
Direct	**@**0 test	**@**0 training	**@**-0.72	**@**0 test	**@**0 training	**@**-0.27
Eff. [%]	79.31 ± 3.78	80.03 ± 1.66	81.90 ± 3.60	77.78 ± 4.40	78.27 ± 1.94	82.22 ± 4.07
Pur. [%]	85.19 ± 3.46	83.04 ± 1.59	81.90 ± 3.60	86.42 ± 3.88	81.90 ± 1.86	82.22 ± 4.07
Acc. [%]	81.31 ± 2.67	80.35 ± 1.21	80.37 ± 2.72	83.15 ± 2.77	80.97 ± 1.29	83.15 ± 2.77
LLR	**@**0 test	**@**0 training	**@**-0.25	**@**0 test	**@**0 training	**@**-0.10
Eff. [%]	81.03 ± 3.66	81.94 ± 1.79	82.76 ± 3.54	85.56 ± 3.77	80.06 ± 2.11	85.56 ± 3.77
Pur. [%]	85.45 ± 3.41	81.58 ± 1.80	80.00 ± 3.67	82.80 ± 3.95	78.32 ± 2.15	82.80 ± 3.95
Acc. [%]	82.24 ± 2.62	80.23 ± 1.36	79.44 ± 2.77	84.15 ± 2.72	79.49 ± 1.48	84.15 ± 2.72

Table 14: Efficiencies, purities and accuracies for the signed distance from the linear and quadratic separation line approaches for the two tiles. The first two columns per tile refer to the black lines; the third column to the magenta lines in Figures 110, 111, 113, and 115.

For the quadratic separation line method, on the other hand, this effect is less pronounced in the final performance. The shape of the quadratic function is at least for the triggered tile better at separating the two populations seen in Figure 117a than the straight line. Given the more smeared populations seen in Figure 117b and the greater number of events in the unclear (for separation) region, this explains the somewhat lower separation performance for the untriggered tile with the quadratic function compared to the linear separation.

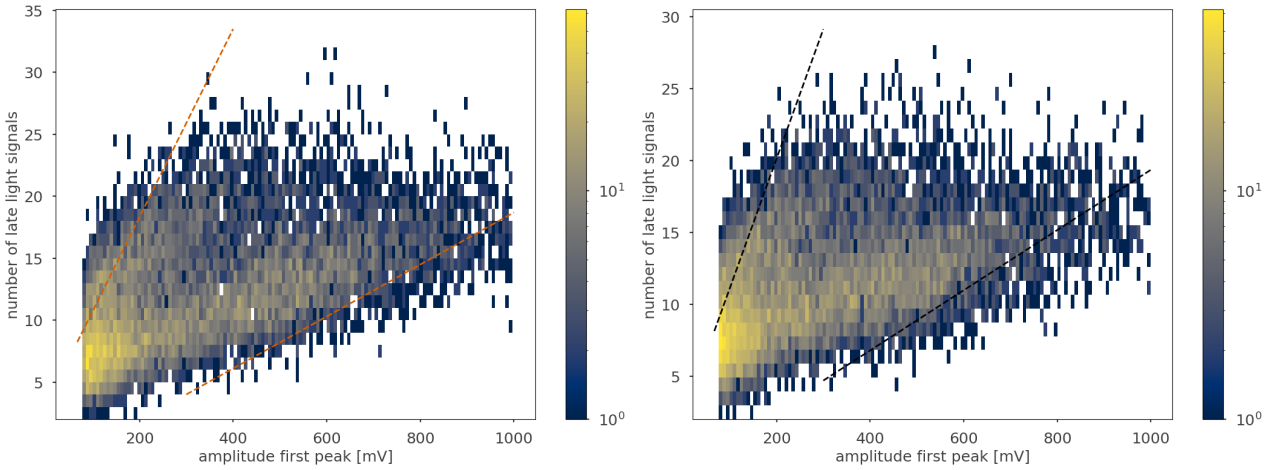

(a) Triggered tile

(b) Untriggered tile

Figure 117: 2D histograms of the event distribution for the two tiles. The lines show the high-purity cuts per tile, with the same colors as in Figures 105a and 106a.

4.7 Time Information of Late Peaks

In addition to the pure number of late light signals, one could also use the time information of the individual peaks. Given the different decay constants for neutrons and gammas (see Table 13), the time information also hints at the particle type, albeit expectedly less significant.
The first step here was to obtain, from the data alone, a probability distribution for the occurrence of late light signals from neutrons and gammas, given by a normalized histogram of the peak times of the unbiased training neutron and gamma samples.[59] These histograms are shown in Figure 118.

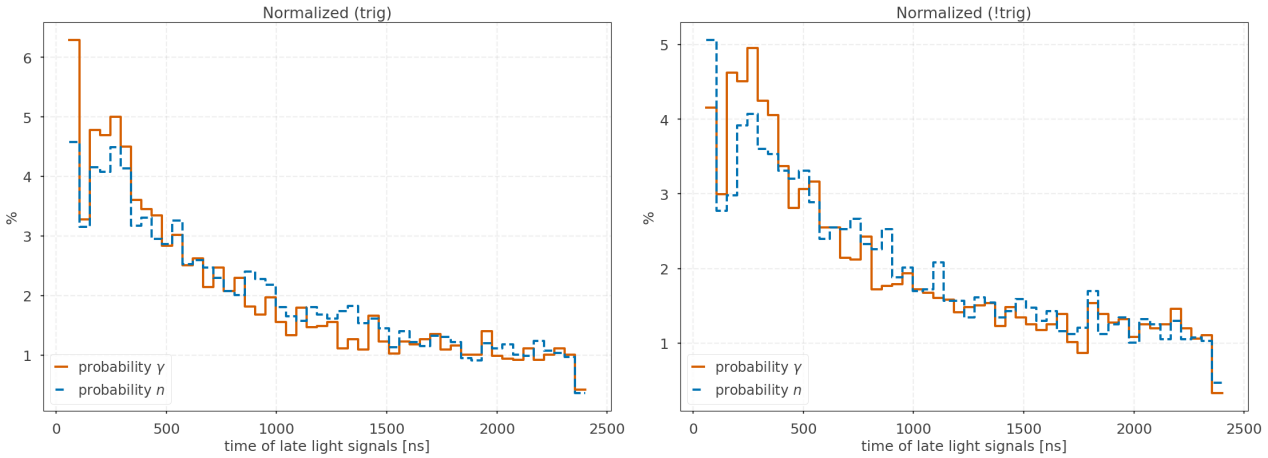

(a) Triggered tile

(b) Untriggered tile

Figure 118: Plot of the normalized unbiased training distributions for late light signal times for the two tiles

These probability distributions are used to calculate the log-likelihood ratio per event of being identified as a neutron or a gamma using Equation 41.

$$\lambda_{LR} = \sum_i \log(\mathcal{P}_{neutron}) - \sum_i \log(\mathcal{P}_{gamma}) \tag{41}$$

The probabilities $\mathcal{P}_{neutron}$ and $\mathcal{P}_{gamma}$ are then the bin heights from Figures 118 for all late light signals of

[59] It was also attempted to fit the distributions. Unfortunately, at the time of writing, no start parameters for the fit could be identified that yielded a successful fit.

an event (per respective tile).
For the unbiased neutron and gamma samples, the distributions of log-likelihood ratios, calculated per event, are shown in Figure 119 for both tiles. Also shown in this plot are the efficiencies, purities, and accuracies for a correct neutron identification for the test samples.

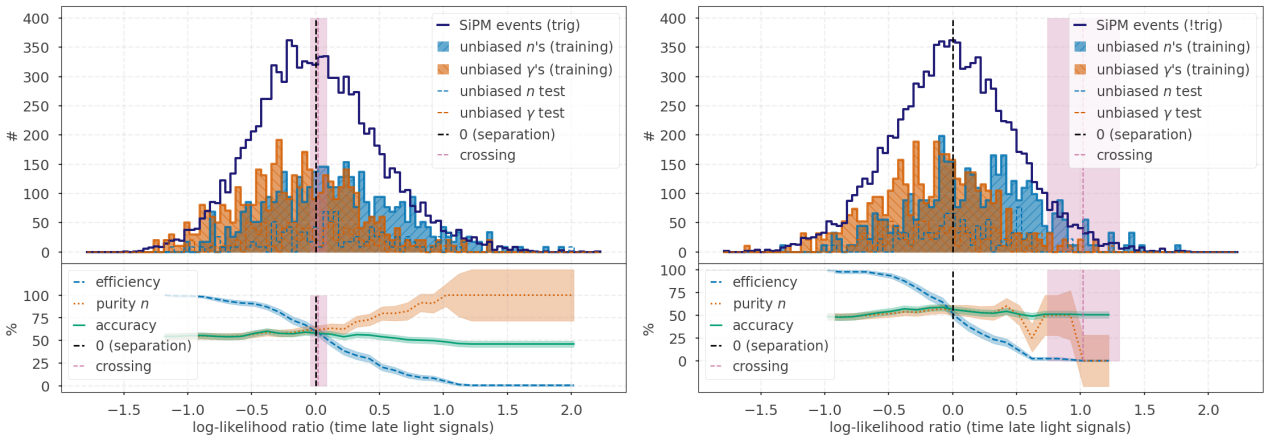

(a) Triggered tile

(b) Untriggered tile

Figure 119: Tops: Histogram of the log-likelihood ratios from the late light signal times for the unbiased training samples (neutrons in blue, gammas in red) and the respective full distributions (dark blue lines) for the two tiles. Bottoms: Plot of the efficiencies, purities, and accuracies of the unbiased test samples being correctly identified as neutrons. The black, dashed line shows the separation line (0), and the magenta line shows the smallest difference between the efficiency and purity lines.

As before, the uncertainties were determined using the variance of the Beta distribution for binomial processes (see Equation 39).
The results from this method are shown in Table 15. They are, as mentioned previously, not as decisive for an identification as the results from the signed distance. This also comes as no surprise when looking at the probability distributions of the unbiased neutron and gamma distributions. There is no significant difference between them, once they are both normalized to the same number of late light signals. The slight observed difference in the time distribution is expected from the subtle difference in the medium decay constants for neutrons and gammas given in the introduction of this chapter (compare Table 13).

	Triggered tile		**Untriggered tile**	
	@0	**@**0.02 ± 0.06	**@0**	**@**0.02 ± 0.28
Efficiency [%]	60.34 ± 4.53	58.62 ± 4.56	51.11 ± 5.24	0.00 ± 1.09
Purity [%]	61.95 ± 4.55	61.82 ± 4.62	55.42 ± 5.43	0.00 ± 28.28
Accuracy [%]	58.41 ± 3.36	57.94 ± 3.37	55.98 ± 3.65	50.54 ± 3.68

Table 15: Efficiencies, purities and accuracies for the time approach for the two tiles. The first column per tile refers to the black lines, the second column to the magenta lines in Figure 119.

4.8 Combination of Signed Distance and Time Methods

The time method alone cannot distinguish between neutrons and gammas; however, it can be combined with the signed distance method to further improve its separation performance. To ensure that no effects arise from combining correlated properties, the Pearson correlation coefficients between the log-likelihood ratios from the time method and the number of late light signals for the two unbiased distributions, as well as with the amplitude of the early light, were calculated and are shown in Table 16. As no correlation was apparent, the combination could be safely performed.

Method	Triggered tile	Untriggered tile
unbiased n λ_{time} number	0.233	0.173
unbiased γ λ_{time} number	0.108	0.047
λ_{time} amplitude	-0.060	-0.066

Table 16: Pearson correlation coefficients for the log-likelihood ratios from the time method and the number of late light signals (top two rows) and the amplitude of the early light (last row) for both tiles

As the first step of the combination, the log-likelihood ratios of both methods are plotted against each other for each event. This is shown in Figure 120 for the unbiased training samples.

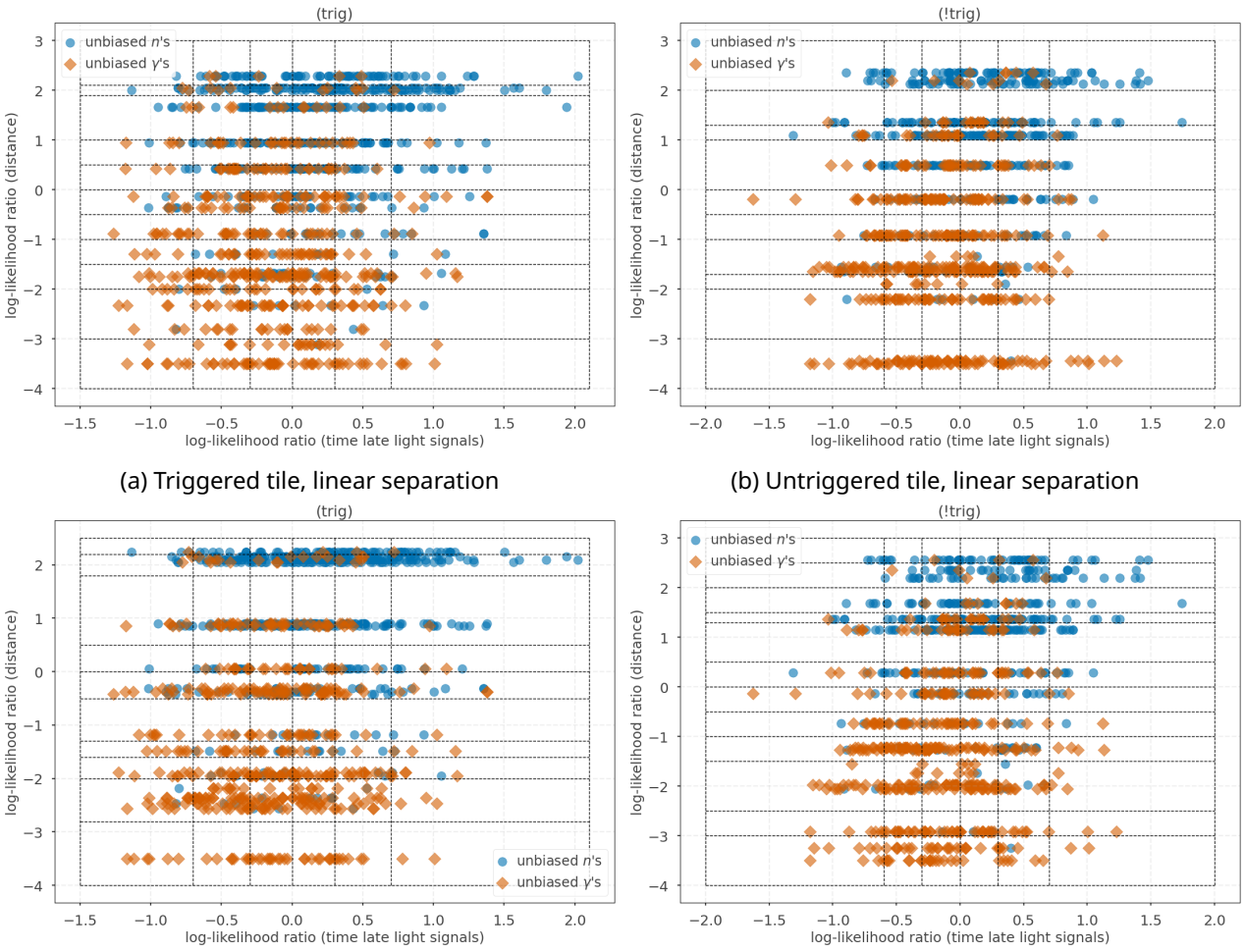

(a) Triggered tile, linear separation

(b) Untriggered tile, linear separation

(c) Triggered tile, quadratic separation

(d) Untriggered tile, quadratic separation

Figure 120: Scatter plots of the log-likelihood ratios from the time method (x axes) and the log-likelihood ratios from the signed distance methods (y axes) for both tiles. 120a and 120b show the combination for the linear separation, 120c and 120d for the quadratic separation. The black, dashed lines show the boundaries for the 2D histograms

Within this scatter plot, lines are drawn which are used as the boundaries for a two-dimensional histogram of the unbiased training distributions. The histograms for the neutron and gamma samples can be seen in Figure 121.

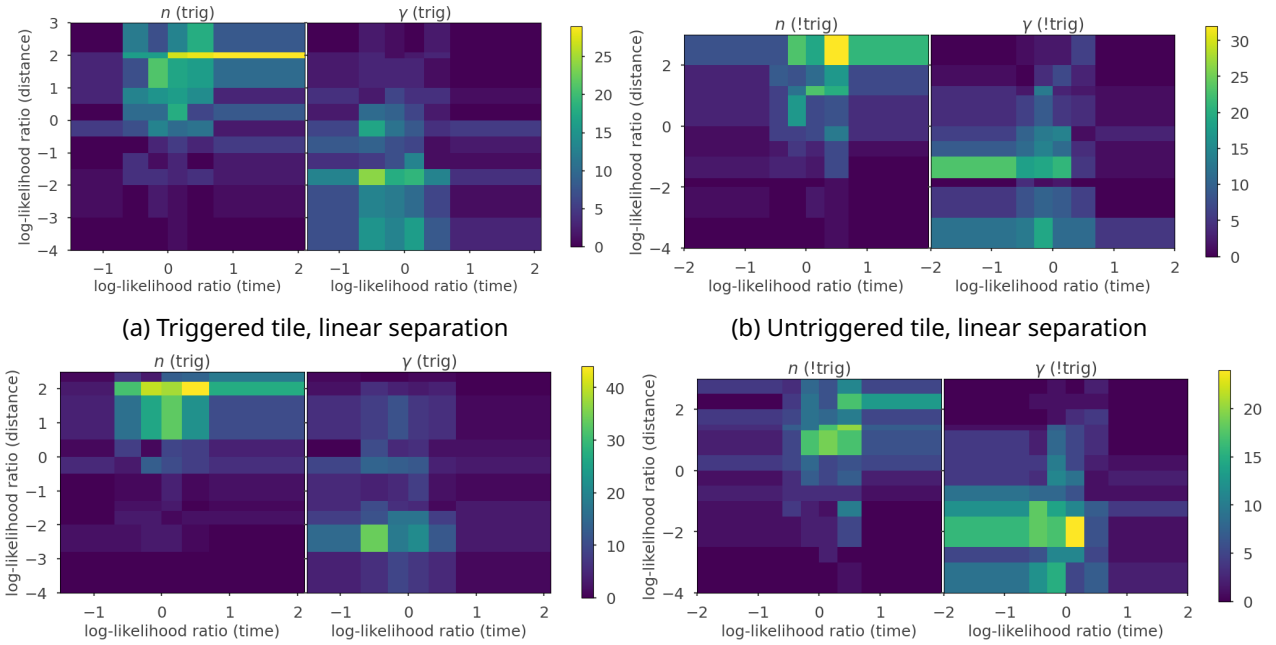

(a) Triggered tile, linear separation

(b) Untriggered tile, linear separation

(c) Triggered tile, quadratic separation

(d) Untriggered tile, quadratic separation

Figure 121: 2D histograms of the combined log-likelihood ratios for the unbiased training samples for both tiles and separation lines. The left histogram shows the distribution of neutrons; the right, of gammas.

Each of the histograms is in the next step normalized per bin to a sum of 1 after a normalization to the same number of events. The result of this normalization can be seen in Figure 122.
To determine whether a given event is a neutron or a gamma, the log-likelihood ratio is once more calculated using Equation 40, where the contents of the respective bins in both histograms represent the likelihoods. This is repeated for all events from the unbiased training and test samples, and the results are shown in Figure 123. Also shown in the plots are the efficiencies, purities, and accuracies in detecting neutrons for the unbiased test samples.
As before, the uncertainties were determined using the variance of the Beta distribution for binomial processes (see Equation 39). The results from this are shown in Table 17. Again, the results are shown for the test and training samples to monitor for overtraining, which is also not observed here.

	Triggered tile			**Untriggered tile**		
Linear	**@**0 test	**@**0 training	**@**−0.20	**@**0 test	**@**0 training	**@**0.05
Eff. [%]	76.72 ± 3.93	83.66 ± 1.72	80.17 ± 3.72	83.33 ± 3.97	79.50 ± 2.13	82.22 ± 4.07
Pur. [%]	82.41 ± 3.69	81.89 ± 1.77	78.81 ± 3.78	75.00 ± 4.34	79.28 ± 2.13	77.89 ± 4.27
Acc. [%]	78.50 ± 2.81	81.16 ± 1.33	77.57 ± 2.86	78.26 ± 3.05	79.76 ± 1.48	79.89 ± 2.96
Quadr.	**@**0 test	**@**0 training	**@**−0.30	**@**0 test	**@**0 training	**@**−0.10
Eff. [%]	79.31 ± 3.78	82.80 ± 1.75	81.90 ± 3.60	84.44 ± 3.87	85.32 ± 1.87	84.44 ± 3.87
Pur. [%]	83.64 ± 3.56	84.25 ± 1.71	78.51 ± 3.75	81.72 ± 4.07	77.78 ± 2.09	81.72 ± 4.04
Acc. [%]	80.37 ± 2.72	82.33 ± 1.30	78.04 ± 2.84	83.15 ± 2.77	80.97 ± 1.44	83.15 ± 2.77

Table 17: Efficiencies, purities and accuracies for the combination for the two tiles. The first column per tile refers to the black lines, the second column to the magenta lines in Figures 123.

As for the signed distance approaches, the untriggered tile has a slightly better separation performance

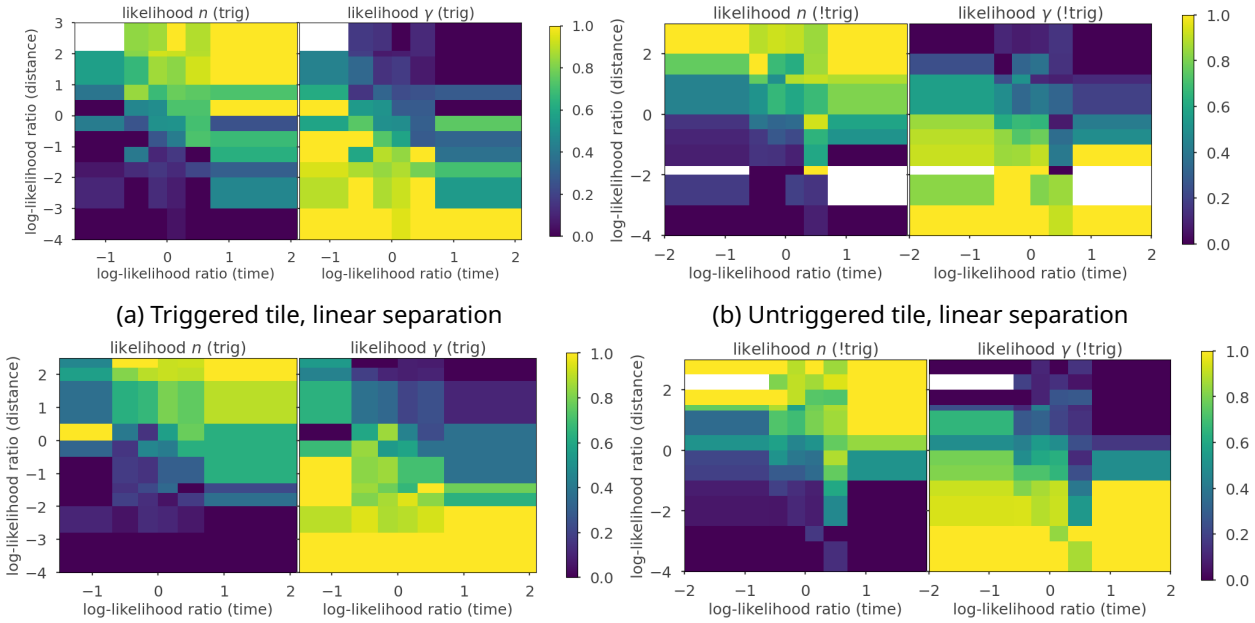

(a) Triggered tile, linear separation

(b) Untriggered tile, linear separation

(c) Triggered tile, quadratic separation

(d) Untriggered tile, quadratic separation

Figure 122: 2D normalized histograms of the log-likelihood ratios combination for the unbiased training samples for both tiles and separation lines. Each bin is used as a likelihood distribution in the following.

than the triggered tile for the quadratic separation line. For the linear separation line approach, the two tiles perform almost identically.

4.9 Comparison of the Different Methods

The performance of the individual and combined methods is summarized in Figure 124.
As mentioned before, the time method performs significantly worse than the signed distance method. Unfortunately, combining the two methods does not further improve performance beyond the signed distance method alone. Especially for the linear separation, the combination performs significantly worse than either of the two signed-distance methods. Therefore, the time method, even when combined, is not effective for identifying the particle generating the signal in the tiles.
To determine which of the signed distance methods performs best, the performances of the linear and quadratic separation approaches are shown in Figure 125.
For the triggered tile, the best performance is clearly from the log-likelihood ratios of the signed distance from the quadratic separation line with the highest efficiency, purity, and accuracy. The quadratic separation also works better for the triggered tile, and the signed distance separation performs better than the log-likelihood ratios.
For the untriggered tile, the situation is a bit more complicated. While the highest efficiency of neutron identification is achieved with the linear direct[60] signed distance method (compare Table 14), the highest purity is achieved with the quadratic direct signed distance method. The opposite is true for the purity of the linear direct and the efficiency of the quadratic direct signed distance methods. The best overall performance in identifying neutrons and gammas, e.g., in terms of accuracy, is the log-likelihood ratio for the linear signed distance, followed very closely by the quadratic one. For both log-likelihood ratios, the efficiencies, purities, and accuracies are closer together; the neutron identification efficiency is slightly better with the quadratic log-likelihood ratio. Therefore, the best method for the untriggered tile is also the quadratic log-likelihood ratio method.

[60] Direct meaning without the log-likelihood ratios.

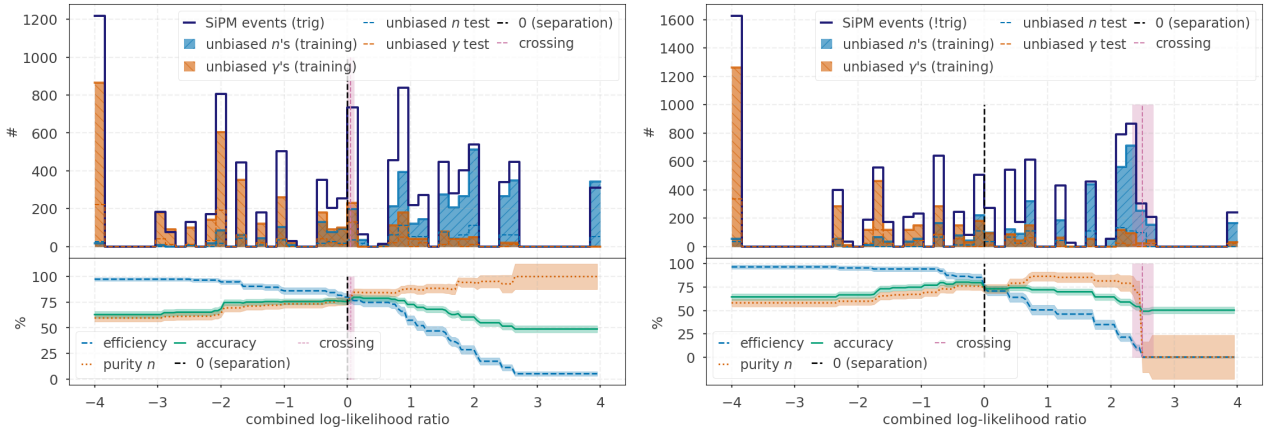

(a) Triggered tile, linear separation

(b) Untriggered tile, linear separation

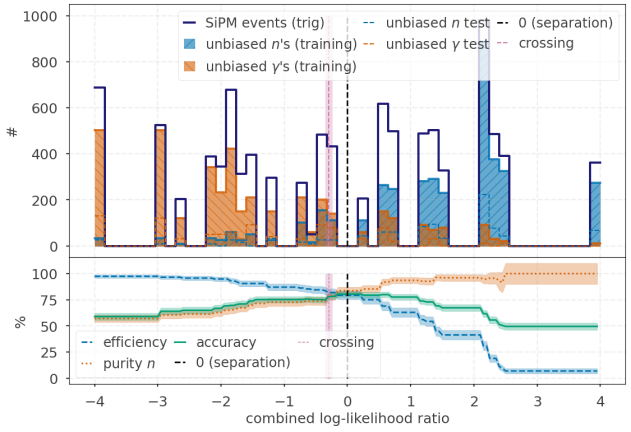

(c) Triggered tile, quadratic separation

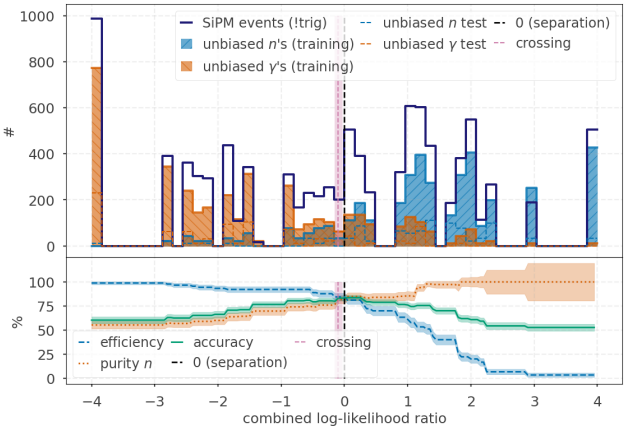

(d) Untriggered tile, quadratic separation

Figure 123: Tops: Histogram of the log-likelihood ratios of the combination for the two tiles and separation line types. Bottoms: Plot of the efficiencies, purities, and accuracies of the unbiased test events. The black, dashed line shows the separation line, and the magenta line shows the smallest difference between the efficiency and purity lines.

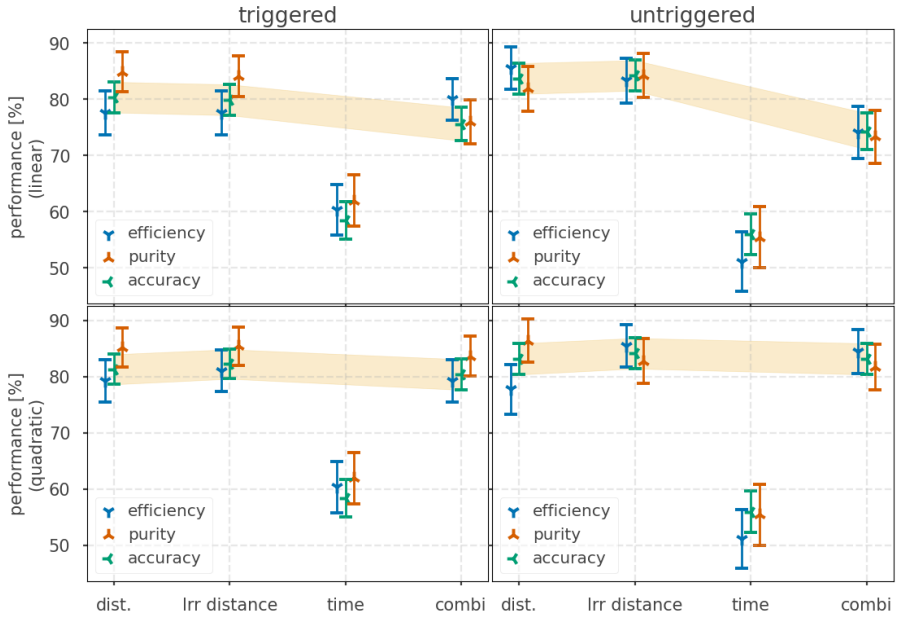

Figure 124: Comparison of the separation performance for all methods. The top two plots show the performance for the linear separation line, the bottom two for the quadratic separation line; the left two plots for the triggered tile and the right two for the untriggered tile. For each method, the neutron identification efficiency, purity, and accuracy are shown. The orange bands connect the accuracies of the different methods, leaving the time of the late light signals out

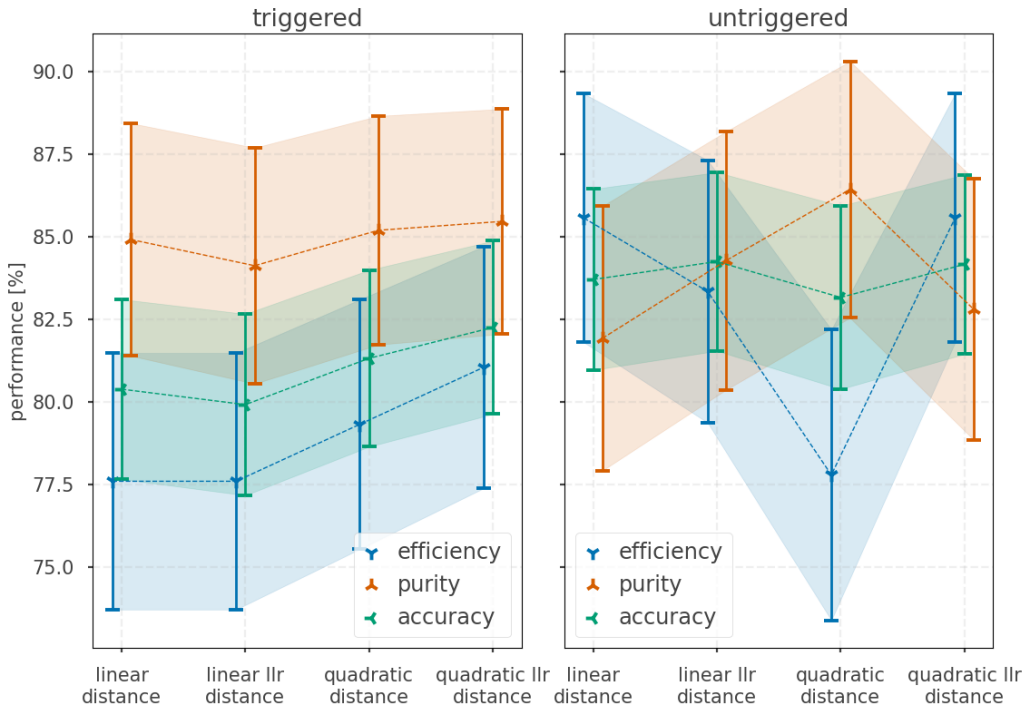

Figure 125: The efficiencies, purities, and accuracies for each of the different distance methods for the triggered and untriggered tile

4.10 Performance of Neutron and Gamma Tagging with this Method

So far, the comparison of the methods has been made only using the test portion of the unbiased distributions. In a real-life application of this method, the initial approach of choosing an unbiased distribution first might not be feasible, though. To determine the performance in this type of situation, the full event distributions, beyond the unbiased samples, for both tiles were used. The log-likelihood ratios for the quadratic distance method across the two tiles are plotted. This is shown in Figure 126. The numbers displayed in the different bins represent the number of events in each bin.

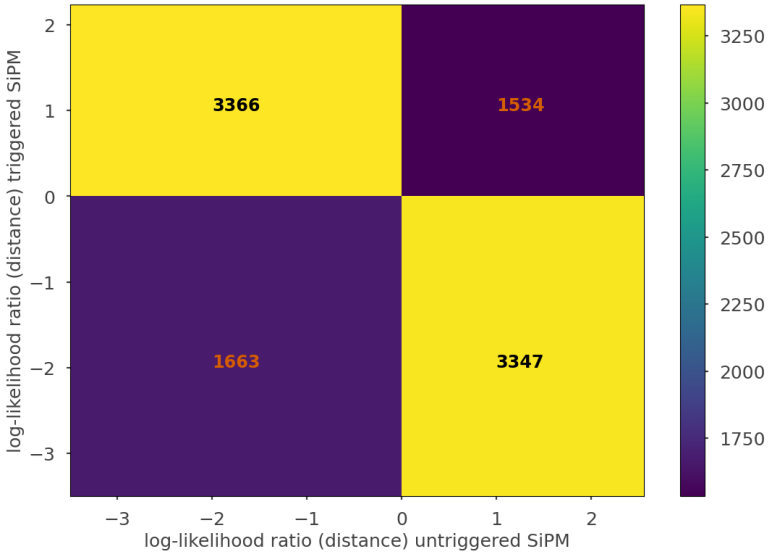

Figure 126: Log-likelihood ratios of the quadratic distance method for both tiles plotted against each other in a 2D histogram. The binning was chosen to represent neutron and gamma identification based on a log-likelihood ratio above or below 0 per event.

The bin on the bottom right contains the events with a clear indication for a neutron event in the untriggered tile and a corresponding gamma in the triggered tile. The top left bin is the equivalent of the triggered tile. Both of these bins contain about twice as many events than the two other bins and each roughly the same amount of events.
The bin on the bottom left contains the events with an indication for gamma events in both tiles, and the top right bin contains the events with an indication for neutron events in both tiles. As these two types of combination are not possible from the AmBe source, they are areas of confusion in the separation. The bins contain slightly different amounts of events.
From these values, the overall efficiency and purity of the separation per tile, and the total accuracy, can be determined using Equations 34, 35, and 36. The false negative (FN) events are in the bottom left corner (1663), as they were falsely identified as gammas for the respective tile. The false-positive (FP) events are in the top right corner (1534), as they were falsely identified as neutrons for the respective tile. The true positive (TP) events vary by tile: the untriggered (3347) tile's efficiency. For the accuracy, the TP is chosen from the untriggered tile, and the true negative (TN) from the triggered tile. The results are presented in Table 18, with uncertainties for the values obtained as before with the Beta distribution.

	Triggered tile	**Untriggered tile**
Efficiency [%]	66.93 ± 0.66	66.81 ± 0.66
Purity [%]	68.69 ± 0.66	68.57 ± 0.67
Accuracy [%]	67.74 ± 0.47	

Table 18: Efficiencies, purities, and accuracies of the neutron and gamma identification for both tiles.

The performance of the complete distributions is expectedly lower than that of the unbiased test samples, but very similar for both tiles. The total accuracy of the neutron-gamma separation is (67.74 ± 0.47) %.

4.10.1 Cosmic Muon Background

Comparing the number of events with a signal from either of the muon veto layers of 3529 (top), 3705 (bottom), and 2370 of those in coincidence, the number falls somewhat short against the expectation of cosmic muon events for the total measurement duration of 100, 000 s. Furthermore, comparing the numbers of events between the two veto layers separately and in coincidence shows that the PMTs have a suboptimal detection efficiency.
So far, the impact of the detection efficiency of the PMTs has been somewhat mitigated by using the unbiased distributions to build the separation method. Still, a small cosmic muon background was possible and expected in the unbiased neutron samples. In the unbiased gamma samples, no such background was expected. However, for the final performance evaluation, a much larger effect from completely undetected cosmic muons is expected.
To quantify this effect, the detection efficiency of the PMTs must first be determined. This can be done using the number of events with signals from only one of the two PMTs and from both, employing Equations 42 to 44.

$$N_{top} = b \cdot (1 - \epsilon_{bottom}) \cdot \epsilon_{top} \tag{42}$$

$$N_{bottom} = b \cdot (1 - \epsilon_{top}) \cdot \epsilon_{bottom} \tag{43}$$

$$N_{coincidence} = b \cdot \epsilon_{top} \cdot \epsilon_{bottom} \tag{44}$$

N refers here to the number of events, b to the background or the actual amount of cosmic muons, and ϵ to the detection efficiency. These equations can be solved for the unknowns (background and both detection efficiencies). The results are $\epsilon_{top} \approx 0.640$, $\epsilon_{bottom} \approx 0.672$ and $b \approx 5517$.
The result for b gives the actual number of cosmic muons, detected or undetected. It is, as expected, higher than the number of events in coincidence or without a coincidence. Using the actual amount of cosmic muons and the two detection efficiencies, it is now possible to estimate the number of cosmic muon events that were completely undetected by both muon veto layers. This is done with Equation 45.

$$N_{no\ signal} = b \cdot (1 - \epsilon_{top}) \cdot (1 - \epsilon_{bottom}) \approx 651 \tag{45}$$

From this number, one would need to subtract the events without tail peaks from the PSD tiles, which happens with a rate between 0.7% to 2.1 %[61]. This would decrease the number of fully untagged cosmic muon events in the final filtered distributions used for the neutron-gamma separation by 5 to 14 events. Assuming that, in the best-case scenario, these 647 to 638 events are all located in the γ confusion area of Figure 126, the efficiency and accuracy of the separation performance would improve to 72.40 ± 0.46% to 72.47 ± 0.46%, as shown in Table 19.

	Triggered tile	**Untriggered tile**
Efficiency [%]	76.56 ± 0.66 to 76.71 ± 0.66	76.66 ± 0.66 to 76.81 ± 0.66
Purity [%]	68.69 ± 0.66	68.57 ± 0.67
Accuracy [%]	72.40 ± 0.46 to 72.47 ± 0.46	

Table 19: Efficiency, purity, and accuracy of the neutron and gamma identification for both tiles with the cosmic muon pollution taken into account (best-case scenario). The two numbers given refer to the range of events without tail-peaks.

[61] These values were calculated from the data distributions directly and do not reflect an underlying detection efficiency, etc.

With these numbers, it is also possible to calculate the expected cosmic muon background in the unbiased neutron sample. For the triggered tile this amounts to $\sim$ 37 events ($\sim$ 5.9%), for the untriggered tile to $\sim$ 29 events ($\sim$ 4.5%).

4.11 Conclusion and Outlook

The idea for tagging neutron and gamma signals in PSD material was to count the number of late light signals and compare it to the height of the early light signal. This idea was tested with a small setup which used two PSD tiles for coincident neutron and gamma measurements from an AmBe source. The setup also included layers of standard non-PSD plastic scintillator coupled to PMTs, which were used to tag cosmic muon events and serve as a muon veto.
The first step was to determine the individual peaks of the late light signals in the SiPM signals. After this, the amplitude of the early light signal could be compared to the total number of late light signals per event. Using the cosmic muon events as an indicator for the gamma-dominated region of the resulting distribution, it was possible to determine unbiased gamma and neutron samples from high-purity selections for each PSD tile.
Using these unbiased neutron and gamma samples, a separation was performed based on the distance to separation lines of two different shapes per event. To improve these approaches also the log-likelihood ratios were determined.
It was also investigated whether the addition of timing information for the different late light signals further improved the separation performance. This was found not to be the case, neither in the pure approach nor in the combination of the log-likelihood ratios from both methods.
Finally, the separation performance of the full, cosmic-filtered[62] distributions was tested, yielding a separation accuracy of (67.74 ± 0.47)%. In addition, the impact of the detection efficiency of the PMTs was taken into account. The suboptimal detection efficiencies resulted in a cosmic muon background in the cosmic-filtered distributions. Subtracting these untagged cosmic muon events, the total separation accuracy improved to (in the best case scenario) (72.40 ± 0.46)% to (72.47 ± 0.46)%, depending on the rate of SiPM events without late light signals.
The result of this analysis is currently being prepared for publication, and the methods and PSD scintillators could be used for future neutrino detectors that require neutron identification.

[62] Not only the unbiased distributions

5 Conclusion

In the first part of this thesis, the TMS detector was introduced, and the need for optimizing the module orientation plan was described. To do so, the event reconstruction was explained and refined to a sufficient degree. This included extrapolating the start and end points of tracks from separate module orientations and matching them. Afterwards, a Kalman filter was employed to smooth and improve the identified track. With this, the study of different module orientation plans was conducted, including a comparison between no addition of X layers and X layers at different densities throughout the detector, with a double scintillator layer in the front. The best-performing plan was to place an X layer in every 7^{th} layer, which was further improved by adding XUV sets at the very front. Two sets performed best for this. This result was adopted by the TMS Consortium. However, due to ongoing geometry optimization studies, the current design foresees only vertical and horizontal layers, with an optimized distribution throughout the detector. The study, however, was primarily influenced by this work.
In the last chapter, a study of neutron and gamma tagging using an PSD plastic scintillator was described. The methods studied used the individual late light signals directly, either counting them per event or using their timing. These properties were then compared to the amplitude of the early light signal, allowing for a neutron and gamma separation. Using the log-likelihood ratio of the signed distance of each event the number of late light signals against the amplitude of the early light signal from a quadratic curve performed best for this separation. In a second step, the separation performance on a data set without prior knowledge (in the form of unbiased neutron and gamma distributions) was tested, and the detection efficiency of the PMTs in the presence of a cosmic muon background in this data set was studied. The results are currently being prepared for publication. The detection technique and analysis method could be employed in a DUNE Phase 2 detector.

A Neutron and Gamma Tagging with Pulse-Shape Discriminating Plastic Scintillator

The following tables show the exact settings for the oscilloscope used in Chapter 4.

	Channel 1	Channel 2	Channel 3	Channel 4
Display	1	1	1	1
Commmonmode?	0	0	0	0
Differential	0	0	0	0
Input	DC50	DC50	DC50	DC50
BW Limit	0	0	0	0
Probe	1.00000E+00,RAT	1.00000E+00,RAT	1.00000E+00,RAT	1.00000E+00,RAT
Probe Skew	0.0E+00	0.0E+00	0.0E+00	0.0E+00
Invert	0	0	0	0
Label	1	2	3	4
Units	VOLT	VOLT	VOLT	VOLT
Offset	6.00E-01	6.00E-01	-6.00E-02	-6.00E-02
Scale	1.60E-01	1.60E-01	2.00E-02	2.00E-02
Range	1.28E+00	1.28E+00	1.60E-01	1.60E-01

Table 20: Channel information

View	Main
Reference	Cent
Reference Percent	5.000e+01
Position	2.0000000E-06
Scale	5.00E-07
Range	5.00E-06

Table 21: Timebase information

Mode		Edge		
Edge Source		CHAN2		
Edge Coupling		DC		
Edge Slope		POS		
Level CHAN	5.35E-03	35.00E-03	0.0E+00	0.0E+00

Table 22: Trigger information

Bandwidth	2.50E+09
Bandwidth frame	2.500E+09
Bandwidth testlimits	1,<numeric>5.0E+08:2.50E+09
Srate	5.000E+09
Srate testlimits	1,<numeric>1.0E+01:1.000E+10
Points	25003
Points testlimit	1,<numeric>16:50048
HResolution	Auto
Interpolate	0
Average	0
Count	16
Mode	SEGM
Segmented count	1599
Segmented index	0
Segmented ttags	1

Table 23: Acquire information

Bandpass	0E+00,2.60000E+09
View	all
Byteorder	LSBF
Streaming	1
Points	50003
Format	WORD
Type	RAW
Coupling	DC
Count	1
Source	CHAN4
Segmented all	1
Segmented count	0
XDisplay	-5.00000000000E-07
XIncrement	1.00000000E-10
XOrigin	-5.00069864246E-07
XRange	5.00000E-06
XReference	0
XUnits	Second
YDisplay	-6.00000E-02
YIncrement	2.63501E-06
YOrigin	-5.73439E-02
YRange	1.60000E-01
YReferenc	0
YUnits	Volt

Table 24: Waveform information

Acquisition target	events = 0 / time = 100000.0 s
Individual runs are limited to	events = 1599 / time = 900.0 s
Will readout channels	[1, 2, 3, 4]

Table 25: Data taking information

References

[1] S. L. Glashow, "Partial-symmetries of weak interactions," *Nuclear Physics* **22** no. 4, (1961) 579–588.

[2] S. Weinberg, "A Model of Leptons," *Phys. Rev. Lett.* **19** (Nov, 1967) 1264–1266.

[3] A. Salam, *Weak and electromagnetic interactions*, pp. 244–254. https://www.worldscientific.com/doi/pdf/10.1142/9789812795915_0034.

[4] M. Thomson, *Modern Particle Physics*. Cambridge University Press, 2013.

[5] L. M. Brown, "The idea of the neutrino," *Physics Today* **31** no. 9, (09, 1978) 23–28.

[6] O. Kofoed-Hansen, "Nuclear recoil and detection of the neutrino," *Physica* **18** no. 12, (1952) 1287–1301.

[7] C. L. Cowan, F. Reines, F. B. Harrison, H. W. Kruse, and A. D. McGuire, "Detection of the Free Neutrino: a Confirmation," *Science* **124** no. 3212, (1956) 103–104, https://www.science.org/doi/pdf/10.1126/science.124.3212.103.

[8] T. Li, X. Xia, X. Huang, J. Zou, W. Li, T. Lin, K. Zhang, and Z. Deng, "Design and Development of JUNO Event Data Model," *Chinese Physics C* **41** (02, 2017) .

[9] G. Danby, J.-M. Gaillard, K. Goulianos, L. M. Lederman, N. Mistry, M. Schwartz, and J. Steinberger, "Observation of High-Energy Neutrino Reactions and the Existence of Two Kinds of Neutrinos," *Phys. Rev. Lett.* **9** (Jul, 1962) 36–44.

[10] G. Abbiendi et al., "Precise determination of the Z resonance parameters at LEP: "Zedometry"," *The European Physical Journal C* **19** no. 4, (Mar, 2001) 587–651.

[11] J. N. Bahcall and R. Davis, "Solar Neutrinos: A Scientific Puzzle," *Science* **191** no. 4224, (1976) 264–267, https://www.science.org/doi/pdf/10.1126/science.191.4224.264.

[12] B. T. Cleveland, T. Daily, R. Davis, Jr., J. R. Distel, K. Lande, C. K. Lee, P. S. Wildenhain, and J. Ullman, "Measurement of the Solar Electron Neutrino Flux with the Homestake Chlorine Detector," *The Astrophysical Journal* **496** no. 1, (Mar, 1998) 505.

[13] **Super-Kamiokande** Collaboration, Y. Fukuda *et al.*, "The Super-Kamiokande detector," *Nucl. Instrum. Meth. A* **501** (2003) 418–462.

[14] A. Bellerive, J. Klein, A. McDonald, A. Noble, and A. Poon, "The Sudbury Neutrino Observatory," *Nuclear Physics B* **908** (07, 2016) 30–51.

[15] **Super-Kamiokande** Collaboration, "Evidence for Oscillation of Atmospheric Neutrinos," *Phys. Rev. Lett.* **81** (Aug, 1998) 1562–1567.

[16] **Particle Data Group** Collaboration, R. L. Workman *et al.*, "Review of Particle Physics," *PTEP* **2022** (2022) 083C01.

[17] **DUNE** Collaboration, "Deep Underground Neutrino Experiment (DUNE), Far Detector Technical Design Report, Volume II: DUNE Physics," arXiv:2002.03005 [hep-ex].

[18] https://en.wikipedia.org/wiki/Neutrino_oscillation#/media/File:Oscillations_muon_short.svg. accessed: 2025-12-02.

[19] T2K and NOvA collaborations, "Joint neutrino oscillation analysis from the T2K and NOvA experiments," *Nature* **646** no. 8086, (10, 2025) 818–824.

[20] M. Prado Rodriguez, "Neutrino Mass Ordering with IceCube DeepCore," *Physical Sciences Forum* **8** no. 1, (2023) .

[21] **Particle Data Group** Collaboration, S. Navas *et al.*, "Review of particle physics," *Phys. Rev. D* **110** no. 3, (2024) 030001.

[22] M. Redchuk, *Looking inside the Sun with the Borexino experiment: detection of solar neutrinos from the proton-proton chain and the CNO cycle*. PhD thesis, RWTH Aachen U., 12, 2020.

[23] https://www.hawc-observatory.org/science/cosmicrays.php. accessed: 2025-12-10.

[24] T. Kajita, "Atmospheric Neutrinos and Discovery of Neutrino Oscillations," *Proc. Japan Acad. B* **86** (2010) 303–321.

[25] **Daya Bay** Collaboration, "Precision measurement of reactor antineutrino oscillation at kilometer-scale baselines by Daya Bay," 2022.

[26] X. Qian and J.-C. Peng, "Physics with reactor neutrinos," *Reports on Progress in Physics* **82** no. 3, (02, 2019) 036201.

[27] **MicroBooNE** Collaboration, "Search for light sterile neutrinos with two neutrino beams at MicroBooNE," *Nature* **648** no. 8092, (Dec, 2025) 64–69.

[28] **JUNO** Collaboration, "First measurement of reactor neutrino oscillations at JUNO," 2025.

[29] **KamLAND** Collaboration, "First Results from KamLAND: Evidence for Reactor Antineutrino Disappearance," *Physical Review Letters* **90** no. 2, (Jan, 2003) .

[30] **T2K** Collaboration, "Constraint on the matter–antimatter symmetry-violating phase in neutrino oscillations," *Nature* **580** no. 7803, (04, 2020) 339–344.

[31] J. A. Formaggio and G. P. Zeller, "From eV to EeV: Neutrino cross sections across energy scales," *Reviews of Modern Physics* **84** no. 3, (Sep, 2012) 1307–1341.

[32] C. Hasnip, *DUNE-PRISM - a new method to measure neutrino oscillations*. PhD thesis, Oxford University, Oxford U., 2023.

[33] **DUNE** Collaboration, "Volume I. Introduction to DUNE," *Journal of Insrumentation* **15** no. 08, (Aug, 2020) T08008.

[34] **DUNE** Collaboration, "DUNE Phase II: Scientific Opportunities, Detector Concepts, Technological Solutions," arXiv:2408.12725 [physics.ins-det].

[35] Batmann. https://en.wikipedia.org/wiki/Accelerator_neutrino#.

[36] P. e. a. Adamson, "The NuMI neutrino beam," *Nuclear Instruments and Methods in Physics Research Section A: Accelerators, Spectrometers, Detectors and Associated Equipment* **806** (01, 2016) 279–306.

[37] S. Gori, N. Tran, K. DiPetrillo, B. Echenard, J. Eldred, R. Harnik, P. Machado, M. Toups, R. Bernstein, I. Bigaran, C. Cesarotti, B. Dutta, C. Herwig, S. Jindariani, R. Plestid, V. Shiltsev, M. Solt, A. Sousa, D. Stratakis, Z. Tabrizi, A. Thapa, J. Zettlemoyer, and J. Zupan, "ACE Science Workshop Report," 2024.

[38] V. Papadimitriou, K. Ammigan, J. A. Jr., K. E. Anderson, R. Andrews, V. Bocean, C. F. Crowley, N. Eddy, B. D. Hartsell, S. Hays, P. Hurh, J. Hylen, J. A. Johnstone, P. Kasper, T. Kobilarcik, G. E. Krafczyk, B. Lundberg, A. Marchionni, N. V. Mokhov, C. D. Moore, D. Pushka, I. Rakhno, S. D. Reitzner, P. Schlabach, V. Sidorov, A. M. Stefanik, S. Tariq, L. Valerio, K. Vaziri, G. Velev, G. Vogel, K. Williams, R. M. Zwaska, and C. Densham, "Design Of The LBNF Beamline," 2017.

[39] R. Acciarri *et al.*, "A Proposal for a Three Detector Short-Baseline Neutrino Oscillation Program in the Fermilab Booster Neutrino Beam," arXiv:1503.01520 [physics.ins-det].

[40] **DUNE** Collaboration, "First results on ProtoDUNE-SP liquid argon time projection chamber performance from a beam test at the CERN Neutrino Platform," *Journal of Instrumentation* **15** no. 12, (12, 2020) P12004–P12004.

[41] M. Wang, T. Yang, M. A. Flechas, P. Harris, B. Hawks, B. Holzman, K. Knoepfel, J. Krupa, K. Pedro, and N. Tran, "GPU-Accelerated Machine Learning Inference as a Service for Computing in Neutrino Experiments," *Frontiers in Big Data* **Volume 3 - 2020** (2021) .

[42] O. Lantwin, "The DUNE vertical drift TPC," in *Proceedings of 41st International Conference on High Energy physics — PoS(ICHEP2022)*, ICHEP2022, p. 332. Sissa Medialab, 11, 2022.

[43] **DUNE** Collaboration, "DUNE Near Detector Preliminary Design Report," *DUNE DocDB DUNE-doc-33925-v2, (available upon request)* (2026) .

[44] **DUNE** Collaboration, "Deep Underground Neutrino Experiment (DUNE) LBNF/DUNE-US Near Detector Preliminary Design Report," *DUNE DocDB* (2026) .

[45] **DUNE** Collaboration, "A Gaseous Argon-Based Near Detector to Enhance the Physics Capabilities of DUNE," arXiv:2203.06281 [hep-ex].

[46] J. Kleykamp, A. Nehm, and L. O'Sullivan, "TMS reconstruction tech note," *dune-docdb 32805* (2025) .

[47] L. Aliaga, L. Bagby, B. Baldin, and et al., "Design, calibration, and performance of the MINERvA detector," *Nuclear Instruments and Methods in Physics Research Section A: Accelerators, Spectrometers, Detectors and Associated Equipment* **743** (2014) 130–159.

[48] P. V. Hough, "Method and Means for Recognizing Complex Patterns," U.S. Patent 3069654, Dec. 1962.

[49] P. E. Hart, N. J. Nilsson, and B. Raphael, "A Formal Basis for the Heuristic Determination of Minimum Cost Paths," *IEEE Transactions on Systems Science and Cybernetics* **4** no. 2, (1968) 100–107.

[50] M. Ester, H.-P. Kriegel, J. Sander, and X. Xu, "A Density-Based Algorithm for Discovering Clusters in Large Spatial Databases with Noise," *KDD-96 Proceedings* (1996) .

[51] Josh Starmer. https://www.youtube.com/watch?v=RDZUdRSDOok.

[52] B. Batyunya and Y. Belikov, "Kalman filtering application for track recognition and reconstruction in ALICE tracking system," *CERN Internal Note/PAT* **ALICE/97-24** (1997) .

[53] F. Battisti, M. Ivanov, and X. Lu, "A Kalman Filter for track reconstruction in very large time projection chambers," *arXiv* **2404.08614** (2024) .

[54] J. W. Miller, "Lecture Notes on Advanced Stochastic Modeling," *Duke University, Durham, NC* (2016) .

[55] X. Huang", "TMS charge ID tech note," *dune-docdb 32806* (2025) .

[56] J. Kleykamp, "TMS Energy Resolution Tech Note," *dune-docdb 32788* (2025) .

[57] D. E. Groom, N. V. Mokhov, and S. I. Striganov, "Muon stopping power and range tables 10-MeV to 100-TeV," *Atom. Data Nucl. Data Tabl.* **78** (2001) 183–356.

[58] A. Nehm, "Module Orientation," *dune-docdb 32803* (2025) .

[59] K. Hildebrandt, "Track Matching Study," *dune-docdb 34245* (2025) .

[60] A. Di Chicco, *Characterization of a stilbene organic scintillator for use as a broadband neutron spectrometer in mixed radiations fields*. PhD thesis, 03, 2023.

[61] J. Mdhluli, H. Jivan, R. Erasmus, Y. Davydov, V. Baranov, S. Mthembu, B. Mellado, E. Sideras-Haddad, O. Solovyanov, C. Sandrock, G. Peter, S. Tlou, N. Khanye, and B. Tjale, "Neutron induced radiation damage of plastic scintillators for the upgrade of the Tile Calorimeter of the ATLAS detector," *Journal of Physics: Conference Series* **878** (07, 2017) 012008.

[62] J. B. Birks, "Scintillations from Organic Crystals: Specific Fluorescence and Relative Response to Different Radiations," *Proceedings of the Physical Society. Section A* **64** no. 10, (Oct, 1951) 874.

[63] H. Hall, "The Theory of Photoelectric Absorption for X-Rays and γ-Rays," *Rev. Mod. Phys.* **8** (Oct, 1936) 358–397.

[64] P. Eisenberger and P. M. Platzman, "Compton Scattering of X Rays from Bound Electrons," *Phys. Rev. A* **2** (Aug, 1970) 415–423.

[65] J. Hubbell, "Electron–positron pair production by photons: A historical overview," *Radiation Physics and Chemistry* **75** no. 6, (2006) 614–623. Pair Production.

[66] M.-M. Bé, V. Chisté, C. Dulieu, X. Mougeot, E. Browne, V. Chechev, N. Kuzmenko, F. Kondev, A. Luca, M. Galan, A. Nichols, A. Arinc, and X. Huang, *Table of radionuclides (Vol. 5 - A = 22 to 244)*, vol. 5 of *Table of radionuclides*. 2010.

[67] A. W. Obst, T. B. Grandy, and J. L. Weil, "Reaction ^{9}Be(α, n)^{12}C from 1.7 to 6.4 MeV," *Phys. Rev. C* **5** (Mar, 1972) 738–754.

[68] K. Geiger and L. Van Der Zwan, "Radioactive neutron source spectra from ^{9}Be(α, n) cross section data," *Nuclear Instruments and Methods* **131** no. 2, (1975) 315–321.

[69] C. Holroyd, M. Aspinall, and T. Deakin, "Pulse shape simulations for organic scintillation detectors using Geant4," *EPJ Web of Conferences 253, 11002* (2021) .

[70] M. Roush, M. Wilson, and W. Hornyak, "Pulse shape discrimination," *Nuclear Instruments and Methods* **31** no. 1, (1964) 112–124.

[71] K. Geiger and L. Van Der Zwan, "Radioactive neutron source spectra from ^{9}Be(α, n) cross section data," *Nuclear Instruments and Methods* **131** no. 2, (1975) 315–321.

[72] S. Croft, "The use of neutron intensity calibrated ^{9}Be(α, n) sources as 4438 keV gamma-ray reference standards," *Nuclear Instruments and Methods in Physics Research Section A: Accelerators, Spectrometers, Detectors and Associated Equipment* **281** no. 1, (1989) 103–116.

[73] A. A. Mowlavi and R. Koohi-Fayegh, "Determination of 4.438MeV γ-ray to neutron emission ratio from a ^{241}*Am*–^{9}*Be* neutron source," *Applied Radiation and Isotopes* **60** no. 6, (2004) 959–962.

[74] M. Grodzicka-Kobylka, T. Szczesniak, M. Moszyński, K. Brylew, L. Swiderski, J. Valiente-Dobón, P. Schotanus, K. Grodzicki, and H. Trzaskowska, "Fast neutron and gamma ray pulse shape discrimination in EJ-276 and EJ-276G plastic scintillators," *Journal of Instrumentation* **15** no. 03, (Mar, 2020) P03030.

[75] `https://upload.wikimedia.org/wikipedia/commons/3/3e/Prominence_definition.svg`. accessed: 2025-11-25.

[76] N. L. Johnson, S. Kotz, and N. Balakrishnan, *Continuous Univariate Distributions*. Wiley, 1995.